GEOSPATIAL MODELING OF SNOW-MET PARAMETERS AND ESTIMATION OF ENERGY FLUXES

Ph.D. THESIS

by

HEMENDRA SINGH GUSAIN

DEPARTMENT OF CIVIL ENGINEERING
INDIAN INSTITUTE OF TECHNOLOGY ROORKEE
ROORKEE – 247 667 (INDIA)

JUNE, 2014

GEOSPATIAL MODELING OF SNOW-MET PARAMETERS AND ESTIMATION OF ENERGY FLUXES

A THESIS

Submitted in partial fulfilment of the requirements for the award of the degree

of

DOCTOR OF PHILOSOPHY

in

CIVIL ENGINEERING

by

HEMENDRA SINGH GUSAIN

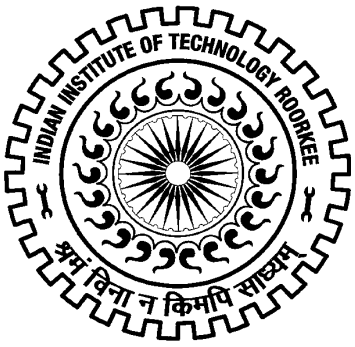

DEPARTMENT OF CIVIL ENGINEERING
INDIAN INSTITUTE OF TECHNOLOGY ROORKEE
ROORKEE – 247 667 (INDIA)

JUNE, 2014

INDIAN INSTITUTE OF TECHNOLOGY ROORKEE
ROORKEE

CANDIDATE'S DECLARATION

I hereby certify that the work which is being presented in this thesis entitled "GEOSPATIAL MODELING OF SNOW-MET PARAMETERS AND ESTIMATION OF ENERGY FLUXES" in partial fulfilment of the requirements for the award of the Degree of Doctor of Philosophy and submitted in the Department of Civil Engineering of the Indian Institute of Technology Roorkee is an authentic record of my own work carried out during a period from July, 2010 to June, 2014 under the supervision of Dr. Manoj K. Arora, Professor, Department of Civil Engineering, Indian Institute of Technology Roorkee, Roorkee (currently on lien to PEC University of Technology, Chandigarh as Director), and Dr. V. D. Mishra, Scientist 'E', Snow and Avalanche Study Establishment (Defence Research & Development Organisation), Chandigarh.

The matter presented in the thesis has not been submitted by me for the award of any other degree of this or any other Institute.

(HEMENDRA SINGH GUSAIN)

This is to certify that the above statement made by the candidate is correct to the best of our knowledge.

(V. D. Mishra)
Supervisor

(Manoj K. Arora)
Supervisor

Date: June , 2014

The Ph.D. Viva-Voce Examination of **Mr. Hemendra Singh Gusain**, Research Scholar, has been held on _____.

Signature of Supervisor's Signature of Chairman, SRC Signature of External Examiner

Head of the Department/Chairman, ODC

ABSTRACT

Surface energy fluxes of the cryospheric regions have many applications in climatology, hydrology, glaciology, snow avalanche forecasting and other snow/ice related studies. The components of the surface energy fluxes are net shortwave radiation flux, net longwave radiation flux, sensible heat flux, latent heat flux and sub surface heat flux. A number of snow-meteorological parameters may be used in estimation of these components of surface energy fluxes. These include air temperature, surface temperature, relative humidity, wind speed, atmospheric pressure, snow depth, albedo, cloud amount etc.. Cryospheric regions have limitations of poor monitoring using sparse *in situ* snow-met observations, which may therefore not characterize spatial variation of energy fluxes over a large snow/ice covered regions. Attempts are being made to model snow-met parameters at spatial scale and to estimate surface energy fluxes of large snow/ice covered regions using satellite remote sensing in conjunction with *in situ* observations.

The present research focuses on geo-spatial modeling of snow depth, albedo, surface temperature and estimate surface energy fluxes using *in situ* as well as remote sensing observations for the snow/ice covered cryospheric regions of Antarctica and Western Himalaya.

The work carried out in this thesis consists of three parts. The first part covers the geospatial modeling of few snow-met parameters e.g. snow depth, albedo and surface temperature. The second part focuses on the estimation of surface energy fluxes using *in situ* recorded snow-met data and presents analysis of the temporal variability of energy fluxes for four years. The third part presents the spatial estimation of surface energy fluxes, their evaluation using *in situ* recorded data and analysis of spatial variation in north and south aspect slopes in the mountain topography.

A novel algorithm for geospatial interpolation of snow depth in Western Himalaya has been developed using snow depth data of manual observatories and digital elevation model. The algorithm improves upon the limitations of earlier published snow depth interpolation algorithm. The algorithm has been used to produce snow depth maps at spatial resolution of 0.5 km. These maps have been validated at few remote locations of the study area and an overall correlation coefficient of 0.71 and RMSE of 42 cm between estimated and *in situ* collected snow depth have been obtained. The proposed algorithm has advantages over the previous models of snow depth in Western

Himalaya by having higher spatial resolution and applicable for all snow thicknesses.

Algorithms for direct retrieval of snow broadband albedo using AWiFS and MODIS data have been developed and presented. *In situ* measurements of spectral reflectance and transmitted solar irradiance using data collected from spectroradiometer in field have been used for the development of snow broadband albedo from narrow band AWiFS and MODIS data. The retrieved albedo from AWiFS and MODIS data has been validated with *in situ* measurements. The overall R^2 and RMSE values between estimated and *in situ* recorded albedo values for AWiFS sensor have been observed as 0.94 and 0.03. The corresponding values for MODIS sensor have been observed as 0.88 and 0.026 respectively. The algorithm developed for estimation of broad band albedo using narrow band reflectance of AWiFS images is probably one of the first attempts in this direction.

Another algorithm has been developed for the estimation of surface temperature in the study area of Antarctica using split-window technique. The R^2 and RMSE of 0.99 and 0.8°C respectively have been obtained between estimated and *in situ* recorded surface temperature.

Surface energy fluxes have been estimated using *in situ* as well as remote sensing data. *In situ* data have been used to estimate surface energy fluxes at the edge of the Antarctic ice sheet. A four-year analysis of the meteorological parameters, radiative and turbulent energy fluxes have been presented. The energy fluxes have been analysed for summer season, winter season and transition periods. It has been observed that the meteorological conditions at the observation site have generally been characterised by mild air temperature (annual mean -10.2 ˚C), low relative humidity (annual mean 50%) and high katabatic winds (annual mean 8.3 m s^{-1}). Net radiative flux has been the main heat source to the glacier during summer (summer mean 46.8 Wm^{-2}) and heat sink during winter (winter mean -42.2 Wm^{-2}). Sensible heat flux (annual mean 32 Wm^{-2}) has been the heat source and latent heat flux (annual mean -61 Wm^{-2}) has been the heat sink to the glacier surface throughout the year. The study highlights the high latent heat flux at the edge of the ice sheet compared to other coastal locations in Dronning Maudland of Antarctica. This may be due to mild temperature, low relative humidity and high katabatic wind compared to other locations. High latent heat flux causes high sublimation rate equivalent to 5.29 cm w.eq per month at the study site. This may contribute to higher rate of ablation of the ice sheet at the location.

Surface energy fluxes estimated using *in situ* recorded data do not characterize spatial variation of energy fluxes of large snow/ice covered regions. So, energy fluxes have been estimated at spatial level using MODIS data and *in situ* recorded snow-meteorological data in Western Himalaya and Antarctica. Incoming shortwave radiation flux and net shortwave radiation flux have been estimated at spatial resolution of 0.5 km whereas net longwave radiation flux and net radiation flux have been estimated at spatial resolution of 1.0 km. These estimated energy fluxes have been evaluated at sampled locations using automatic weather stations data. RMSE in estimation of incoming shortwave radiation flux, net shortwave radiation flux and net radiation flux have been found to be 75 W m^{-2}, 84.9 W m^{-2}, 90 W m^{-2} respectively in Western Himalaya and 105 W m^{-2}, 75 W m^{-2}, 81 W m^{-2} respectively in Antarctica. In this research, the incoming shortwave radiation flux has been estimated at higher spatial resolution than those reported in earlier studies and at a comparable accuracy of 14-27% of the mean values. As there is no access to data from any other source on spatial estimation of net shortwave radiation and net radiation fluxes for snow/ice covered region, the results of this study therefore have not been evaluated any further.

Spatial and temporal variations of energy fluxes on north and south aspect slopes of mountain topography in Western Himalaya have also been assessed. Incoming shortwave radiation flux on south aspect slopes has been observed to be higher than those observed on north aspect slopes for the study period. This may be due to low incidence angle (i) of solar radiation on south aspect slopes as compared to that on the north aspect slopes. Temporal variation in the incoming shortwave radiation flux has been found to be in accordance with the variation of solar zenith angle. However, the temporal variation of net shortwave radiation flux has been found to depend on incoming shortwave radiation flux and the albedo of the snow cover.

The significant findings of this research include,

1. Development of algorithm for geospatial interpolation of snow depth, which has advantages over the previously reported algorithms. The algorithm shall have direct applications in spatial estimation of sub-surface heat flux, avalanche forecasting, hydrological and glaciological studies.
2. Development of an algorithm for broad band albedo of snow cover from narrow bands reflectance of MODIS and AWiFS images. The algorithm can be used in various snow studies for estimating radiative energy fluxes and snowmelt run-off modeling. The

study has focused on estimation of the sublimation and melt of the ice sheet for four years using *in situ* recorded snow-met parameters. The study highlights the high ablation rate of the ice sheet near Schirmacher Oasis, compared to other parts of East Antarctica.

3. Estimation of surface energy fluxes at spatial level using remote sensing technique and validation with *in situ* recorded data. The results may be directly applicable to various snow/ice studies in the cryospheric regions.

ACKNOWLEDGEMENTS

In the name of **ALMIGHTY GOD**, most Gracious, most Merciful.

I wish to express my sincere appreciation to those who have contributed to this thesis and supported me in one way or the other during this amazing journey.

First of all, I am extremely grateful to my main supervisor, **Dr. Manoj K. Arora**, Professor in Civil Engineering at IIT Roorkee and currently on lien to PEC University of Technology, Chandigarh as Director, for his wise guidance, invaluable suggestions and constant encouragement during my thesis work. I always enjoyed the discussions and brainstorming sessions with him. His scientific acumen has made him as a continuous source of ideas which inspired and enriched my growth as a student, a researcher and a scientist. I really appreciate his willingness to meet me at short notice every time and going through several drafts of my thesis.

I wish to express my sincere gratitude to my supervisor **Dr. V. D. Mishra,** Senior Scientist, Snow and Avalanche Study Establishment (SASE), Defence Research and Development Organisation, Chandigarh, for his outstanding support, wise guidance and invaluable suggestions both professional and personal. He is the person who inspired me for the Ph.D. registration at I.I.T. Roorkee. He encouraged me at every step of this journey.

This research would not have been possible without an active support of my both the supervisors.

I owe my most sincere gratitude to the members of the student's research committee, **Dr. N. K. Goel**, Professor, Department of Hydrology and **Dr. B. R. Gurjar**, Professor, Department of Civil Engineering, IIT Roorkee for their detailed review, constructive criticism and excellent advice during the preparation of this thesis. ***I am grateful to faculty and staff members, Geomatics Engineering Group, for providing all kind of help during the course of this work.***

Very special thanks to my establishment **Snow and Avalanche Study Establishment (SASE)** and my organisation **Defence Research and Development Organisation (DRDO)** for giving me the opportunity to carry out my doctoral research and for sponsoring me. Special thanks to **Mr. Ashwagosha Ganju**, Director SASE for extending all kind of support throughout this journey. I am thankful to **SASE Data**

Centre for providing me all the required data to complete this research.

During this work, I have collaborated with many of my colleagues for whom I have great regards, and I wish to extend my warmest thanks to **Dr Mohit Srivastava**, Assistant Professor, Bharat Institute of Technology, Meerut, **Dr Kamal Kumar**, Assistant Professor, Punjab Engineering College, Chandigarh, **Mr Prem Datt** and **Mr. S K Dewali**, Scientists, SASE, Chandigarh.

I would further like to thank **Mr. N. Prabhu, Mr. Manoj Kuri, Mr. Reet Kamal Tiwari, Ms. Deepti Yadav, Ms. Varinder Saini, Mr. Danie, Dr H S Negi, Dr Atanu Bhattacharya, Dr J. C. Kapil, Mr. Kamal Kant, Mr. Dan Singh, Mr. Piyush Joshi, Mr. Chaman Chandel, Mr. Jagdish Joshi, Mr. R. K. Das, Mr. Manoj Kumar, Mr. Gursewak Singh, Mr. Avinash Negi, Ms. Kavita Mitkari** and all those who have helped me directly or indirectly in my work.

I want to express my gratitude and deepest appreciation to **my parents and my parents-inlaws** for their great patience and understandings. Their encouragement and contribution lifted me to reach this place. My sincere, heartfelt gratitude and indebtedness is due to **my wife, my kids, my brothers, my brother-in-law, my sister, my sister-in-law and my mamaji** for their sincere prayers and constant encouragement. I also warmly thank and appreciate my relatives, friends and well wishers for their moral support in all aspects of my life.

I dedicate this thesis to my adoring parents and my sweet family.

(Hemendra Singh Gusain)

CONTENTS

List of Figures

List of Tables

List of Notations

T_a	Air temperature
T_s	Surface temperature
RH	Relative humidity
w	Wind speed
P	Atmospheric pressure
α	Albedo
r	Correlation coefficient
$NDVI$	Normalised Difference Vegetation Index
μm	Micro meter
$L_{sat\lambda}$	Spectral Radiance at wavelength λ
$L_{max\lambda}$	Maximum value of spectral radiance at wavelength λ
$L_{min\lambda}$	Minimum value of spectral radiance at wavelength λ
$DN_{max\lambda}$	Maximum value of digital number at wavelength λ
$DN_{sat\lambda}$	Digital number value recorded at satellite sensor at wavelength λ
R_λ	Spectral reflectance corrected for path radiance
L_p	Path radiance
t_v	Atmospheric transmittance along the path from ground to sensor
t_z	Atmospheric transmittance along the path from Sun to ground
E_0	Exo-atmospheric spectral irradiance
θ	Solar zenith angle
D	Earth-Sun distance in Astronomical Units
E_d	Downwelling diffused radiation
R^t_λ	Topographically corrected spectral reflectance
I	Local incidence angle
Φ	Slope angle
α_s	Aspect angle
α_a	Solar azimuth angle
C_λ	Normalization coefficient at wavelength λ
$S_\lambda^{'}$	Mean reflectance value on sunlit slopes after first stage normalization
N_λ	Mean reflectance value on shady slopes in uncorrected image
$N_\lambda^{'}$	Mean reflectance value on shady slopes after first stage normalization
$R_{n\lambda ij}$	Normalized reflectance values for image pixel *ij* at wavelength λ
$R_{\lambda ij}$	Original reflectance on the tilted surface for image pixel *ij* at wavelength λ
h	Planck's constant
c	velocity of light
k	Boltzmann's constant
T	Brightness temperature
$SHW\downarrow$	Incoming shortwave radiation flux
$SHW\uparrow$	Outgoing shortwave radiation flux
SHW_{net}	Net shortwave radiation flux
$LW\downarrow$	Incoming longwave radiation flux

$LW\uparrow$	Outgoing longwave radiation flux
LW_{net}	Net longwave radiation flux
R_{net}	Net radiation flux
SHF	Sensible heat flux
LHF	Latent heat flux
G	Sub surface heat flux
ΔQ	Net change in energy storage of a glacier or ice sheet
ϵ_{m}	Emissivity of the atmosphere
w_p	Precipitable water content
e_{a}	Vapour pressure
σ	Stephan Boltzmann constant
ϵ_{s}	Surface emissivity
ρ_a	Density of air
C_{p}	Specific heat of air
K_{H}	Coefficient of turbulent diffusivity
Γ	Adiabatic lapse rate
ρ_{a0}	Density of air at the standard atmospheric pressure P_0
P	Mean atmospheric pressure
K_{n}	Dimensionless transfer coefficient
k_v	Von Karman's constant
z_{a}	Air temperature sensor height above ground
z_0	Aerodynamic roughness length
K_{c}	Coefficient depending on the type and height of clouds
L_{v}	Latent heat of vaporization
e_{s}	Saturation vapour pressure at the glacier surface
R_{i}	Bulk Richardson number
T_{ad}	Daily averaged air temperature
T_{sd}	Daily averaged surface temperature
HS_j	Snow depth at grid cell location j
G_b	Base value of snow depth obtained from mathematical function
A_i	Compensation factor in estimation of snow depth
h_e	Elevation above mean sea level
we_i	Weight assigned to i^{th} location
u_i	Difference between observed snow depth and estimated snow depth at i^{th} location
p	Weighting factor
$\rho_{\Delta\lambda}$	Narrowband reflectance in wavelength interval $\Delta\lambda$
$\sum E_{s\Delta\lambda}$	Integrated downward irradiance
f	Adjustment factor in estimation of broadband albedo
R^2	Coefficient of determination
S_0	Solar constant
a	Elevation angle of the Sun
T_d	Dew point temperature

List of Abbreviations

A P	Arunachal Pradesh
AAN	Asian AWS Network
ABL	Atmospheric Boundary Layer
AMSR-E	Advanced Microwave Scanning Radiometer -EOS
ARM	Atmospheric Radiation Measurement
ART	Atmospheric Radiative Transfer
ASTER	Advanced Spaceborne Thermal Emission and Reflection Radiometer
AT	Air Temperature
ATSR	Along Track Scanning Radiometer
AVHRR	Advanced Very High Resolution Radiometer
AWiFS	Advanced Wide Field Sensor
AWS	Automatic Weather Station
BBA	Broad Band Albedo
BRDF	Bidirectional Reflectance Distribution Function
BSRN	Baseline Surface Radiation Network
CASPR	Cloud and Surface Parameter Retrieval
CERES	Clouds and the Earth's Radiant Energy System
DEM	Digital Elevation Model
DN	Digital Numbers
DOS	Dark Object Subtraction
DRDO	Defence Research and Development Organisation
ELR	Environmental Lapse Rate
ERA-40	European Centre for medium range weather forecast 40-Year Reanalysis
ERB	Earth Radiation Budget
ERBE	Earth Radiation Budget Experiment
ERS	Earth Receiving Station
ETM^{+}	Enhanced Thematic Mapper Plus
FOV	Field of View
GCM	General Circulation Model
GC-Net	Greenland Climate Network
GCP	Ground Control Point
GERB	Geostationary Earth Radiation Budget

GIDS	Gradient-plus-Inverse-Distance-Squared
GIS	Geographic Information System
GMS	Geostationary Meteorological Satellite
GMT	Greenwich Mean Time
GOES	Geostationary Operational Environmental Satellite
GPR	Ground Penetrating Radar
H P	Himachal Pradesh
IDW	Inverse Distance Weighted
IMD	India Meteorological Department
IR	InfraRed
IRS-P6	Indian Remote Sensing Satellite-P6
ISRO	Indian Space Research Organisation
J&K	Jammu and Kashmir
LANDSAT	Land Use Satellite
LHF	Latent Heat Flux
LIDAR	Light Detection and Ranging
LISS-III	Linear Imaging Self Scanning-III
LST	Land Surface Temperature
LW	Long Wave
MAE	Mean Absolute Error
MEMLS	Microwave Emission Model of Layered Snowpack
MISR	Multi-angle Imaging SpectroRadiometer
MLR	Multiple Linear Regression
MODIS	Moderate Resolution Imaging Spectroradiometer
NBBA	Narrow Band to Broadband Albedo
NBR	Narrow Band Reflectance
NCAR	National Centers for Atmospheric Research
NCEP	National Centers for Environmental Prediction
NCEP-R2	National Centers for Environmental Prediction Reanalysis II
NDSI	Normalised Difference Snow Index
NDVI	Normalized Difference Vegetation Index
NIR	Near InfraRed
NRSC	National Remote Sensing Centre

NSIDC	National Snow and Ice Data Centre
PAM	Portable Automated Mesonet
POLDER	Polarization and Directionality of the Earth's Reflectances
REF	Residual Energy Flux
RH	Relative Humidity
RMSD	Root Mean Square Deviation
RMSE	Root Mean Square Error
S D	Standard Deviation
SASE	Snow and Avalanche Study Establishment
SEBAL	Surface Energy Balance Algorithm for Land
SHEBA	Surface Heat Budget of the Arctic Ocean
SHF	Sensible Heat Flux
SHW	Short Wave
SMARTS	Simple Model of the Atmospheric Radiative Transfer of Sunshine
SMMR	Scanning Multichannel Microwave Radiometer
SOI	Survey of India
SRB	Surface Radiation Budget
SRTM	Shuttle Radar Topographic Mission
SSM/I	Special Sensor Microwave Imager
SURFRAD	Surface Radiation Budget Network
SWE	Snow Water Equivalent
SWIR	Shortwave Infra Red
TLR	Temperature Lapse Rate
TM	Thematic Mapper
UMD	University of Maryland
UTC	Universal Time Coordinate
VIIRS	Visible Infrared Imaging Radiometer Suite
VIS	Visible
WDML	Western Dronning Maud Land
WMO	World Meteorological Organization

Chapter I

INTRODUCTION

1.1 General

The surface energy balance is an essential element of the climate in any region of the world. It has an added significance in the snow/ice covered cryospheric regions, where small changes in the surface energy fluxes can lead to changes in the overall energy balance thereby affecting the climate. In order to study the long term effect of the climate on the snow/ice fields, it is important to understand the variability of different surface energy fluxes on temporal and spatial scales. These energy fluxes are also used in various hydrological studies for estimation of snow melt run-off (Upadhyay 1995, Paterson 1994, Alam *et al.* 2011, Sharma *et al.* 2012). The components of the surface energy fluxes are net shortwave radiation flux, net longwave radiation flux, sensible heat flux, latent heat flux and sub surface conductive heat flux (Paterson 1994, Vihma 2011). The snow meteorological parameters used in estimation of surface energy fluxes of snow/ice covered regions are air temperature (T_a), surface temperature (T_s), relative humidity (RH), wind speed (w), atmospheric pressure (P), snow depth, albedo (α) etc. Snow meteorological data are generally recorded as *in situ* observations and many studies have been conducted to estimate this data at spatial scale based on various statistical techniques (Courault and Monestiez 1999, Cresswell 1999, Florio *et al.* 2004, Foppa *et al.* 2007, Kumar *et al.* 2010, Xu *et al.* 2012, Gr¨unewald *et al.* 2013). Unfortunately, *in situ* observations of these parameters in cryospheric regions are very sparse and observed at very few locations.

Geospatial science encompassing remote sensing and Geographic Information System (GIS) (Foody and Atkinson 2002) provides an opportunity to study surface energy

fluxes at spatial and temporal scales. Estimation of surface energy fluxes of a large area using remote sensing depends on accurate estimation of snow meteorological data at each pixel of the image. Snow meteorological parameters at each pixel can be estimated from *in situ* observations with appropriate interpolation technique or modeling of the parameter using physical/statistical or other methods. However, modeling of these parameters have always been a challenging task in mountain topography as compared to flat terrain due to large spatial variability. The main aim of the present research is therefore on geospatial modeling of a few snow-met parameters in mountain topography and estimation of surface energy fluxes using *in situ* as well as remote sensing observations for the snow/ice covered cryospheric regions.

1.2 Measurement and Estimation of Snow-Met Parameters

Snow meteorological (snow-met) parameters, namely, air temperature, snow/ice surface temperature, relative humidity, wind speed, atmospheric pressure, snow/ice cover albedo, snow depth etc. are important factors in processes of energy exchange between snow/ice covered surface and atmosphere (Armstrong and Brun 2008). These parameters are recorded by different instruments or sensors in the field (WMO 2008). Observations of these parameters at a specific location is known as point observation or *in situ* observation and represent a small area. *In situ* observations are sparse in snow/ice covered region as compared to other land cover regions due to inaccessibility of the terrain and harsh climatic conditions. To study a large snow/ice covered region for various snow studies, snow-met parameters are required at spatial scale. To overcome this problem, sparse point observations can be effectively integrated with remote sensing or other geo-spatial data with appropriate interpolation or modeling techniques in a GIS environment (Hernandez *et al.* 2003). In the past, many studies have been conducted to model a number of snow-met parameters (Nolin and Dozier 2000, Hall *et al.* 2002, Hall *et al.* 2004, Roy *et al.* 2004, Foppa *et al.* 2007, Negi *et al.* 2007, Das and Sarwade, 2008, Painter *et al.* 2009, Dewali *et al.* 2009, Negi and Kokhanovsky 2011, Takala *et al.* 2011, Dai *et al.* 2012 etc.) at spatial scale in different snow bound regions across the globe. Although, it may be argued that snow-met parameters estimated by the interpolation or modeling techniques are less

accurate as compared to observed parameters, but the major advantage is the availability of information on snow-met parameters at spatial scale and also at desired accuracy depending upon the application.

Snow depth is an important parameter in estimation of subsurface heat flux of the snow cover. It has also been widely studied in snow avalanche research (Bühler 2012), hydrology, glaciology and other snow studies. Generally, two approaches have been adopted by researchers for estimation of this parameter at spatial scale. In the first approach, researchers have used interpolation techniques (Elder *et al.* 1998, Erxleben *et al.* 2002, Foppa *et al.* 2007, Moreno and Bravo 2006) from *in situ* observations. In second approach, snow depth has been modelled from microwave backscattered or emitted signals (Roy *et al.* 2004, Das and Sarwade 2008, Dai *et al.* 2012). A few algorithms have been developed to model snow depth in Western Himalaya (Singh *et al.* 2007, Das and Sarwade 2008) at coarse spatial resolution using passive microwave satellite data. Airborne and terrestrial Light Detection and Ranging (LIDAR) sensors data have also been used in mapping snow depth at watershed scale (Hopkinson *et al.* 2004, Deems and Painter 2006, Deems *et al.* 2006, Nolin 2010).

Albedo is an important parameter in estimation of net shortwave radiation flux and has been studied widely (Song and Gao 1999, Liang *et al.* 1999, Liang 2000, Liang *et al.* 2002, Liang 2003, Key *et al.* 2001, Stroeve 2001, Stroeve and Nolin 2002a, 2002b) for different land covers. It has significant role in understanding and characterizing the surface energy fluxes at the earth surface. Generally two types of approaches, physically based and direct estimation, are in vogue for estimation of land surface broad band albedo, as reviewed by Liang *et al.* (2010). Moderate Resolution Imaging Spectroradiometer (MODIS) derived global albedo products MOD43B are also available based on 16 days average (http://modis.gsfc.nasa.gov). These products have been estimated using Bidirectional Reflectance Distribution Function (BRDF) in seven spectral bands at 1 km spatial resolution (Strahler *et al.*, 1999). However, these products can not be used directly to estimate surface energy fluxes of snow/ ice surfaces as albedo of snow changes rapidly with time as compared to other land surfaces due to its metamorphic processes. Therefore, for the study of surface energy fluxes of snow/ice surfaces, instant albedo at the time of satellite pass may be more useful as compared to 16 day averages.

The instant albedo can be estimated expediently using narrowband to broadband conversion algorithms.

Air temperature (T_a), relative humidity (*RH*) and surface temperature (T_s) are also important parameters in estimation of radiative and turbulent energy fluxes. These parameters are usually estimated from *in situ* observation stations manually using instruments or automatically using sensors mounted on automatic weather station (AWS). However, due to sparse observations on ground, spatial interpolation methods or modeling techniques may also be used to estimate these parameters at spatial scale (Courault and Monestiez 1999, Negi *et al.* 2007, Dewali *et al.* 2009, Kumar *et al.* 2010, Xu *et al.* 2012, Lai *et al.* 2012). A few studies to estimate these paramenters at spatial level in Indian Western Himalaya have also been reported (e.g., Negi *et al.* 2007, Dewali *et al.* 2009, Kumar *et al.* 2010).

1.3 Estimation of Surface Energy Fluxes Using *In Situ* Observations

Various physical processes at the snow/ice surface contribute to different surface energy fluxes (Anderson 1976, Azam *et al.* 2014). These energy fluxes at the surface determines the ablation and accumulation processes (Lewis *et al.* 1998). Quantification of these fluxes can contribute to better understanding of the mass exchange at the surface and subsequently the health of the glacier/ice sheet (Gusain *et al.* 2009b). Radiative energy flux, turbulent energy flux and sub surface heat flux are the main components of the surface energy balance of a snow/ice covered surface (Van Den Broeke *et al.* 2006). Incoming and reflected shortwave radiation flux, downwelling and upwelling longwave radiation flux are components of the radiative energy flux (King and Turner 1997). Radiative energy fluxes can be directly measured in the field or can be estimated using parameterization schemes. Incoming and reflected shortwave radiation flux can be measured using upward and downward looking pyranometers. Upwelling and downwelling longwave radiation flux can be measured using downward and upward looking pyrgeometers. Net radiation flux can be measured from net radiation pyrnometer. Incoming shortwave radiation flux can be estimated from parameterization schemes given by researchers for clear sky days (Bennett 1982, Moritz 1978, Zillman 1972, Iqbal 1983

etc.) as well as for cloudy sky days (Berliand 1960, Laevastu 1960, Niemelä 2001b). There are also parameterization schemes to estimate downwelling longwave radiation flux for clear and cloudy sky conditions (Idso 1981, Prata 1996, Dilley and O'Brien 1998, Jacobs 1978, Maykut and Church 1973, Niemelä, 2001a). These parameterization schemes estimate incoming shortwave radiation flux and downwelling longwave radiation flux based on screen level measurements of air temperature and relative humidity and cloud observations at the location. Upwelling longwave radiation emitted by surface is estimated by Stefan-Boltzman equation and requires surface temperature and surface emissivity information.

Turbulent transfer of heat from snow/ice surface to atmosphere and vice versa occurs in the form of sensible and latent heat fluxes (Cuffey and Paterson 2010). Sensible heat flux is the measure of heat transfer between the surface and the atmosphere above due to difference of temperature without phase change, while latent heat flux is the measure of energy exchanged in the form of phase change. These turbulent energy fluxes can be estimated over snow/ice covered surface by recording meteorological parameters e.g. air temperature, surface temperature, atmospheric pressure, relative humidity, wind speed etc. Bulk aerodynamic method is generally used to estimate turbulent energy fluxes using *in situ* measurements. However, these energy fluxes can also be measured directly using instruments based on eddy covariance technique.

Sub surface heat flux is the measure of heat transfer between glacier surface and ice underneath. Sub surface heat transfer in a glacier takes place mainly using conduction process (Lewis *et al.* 1998). Inside snowcover, conduction and diffusion are the dominant processes for heat transfer (Mc Clung and Schaerer 1993). Sub surface heat flux can be measured directly using heat flux sensors placed inside snow/ice and can be estimated from temperature at the surface and inside snow/ice.

1.4 Spatial Estimation of Surface Energy Fluxes

In situ snow-met observations in cryospheric regions are difficult to obtain due to harsh climatic and topographic conditions. Cryospheric regions have limitations of poor monitoring using sparse *in situ* snow-met observations all over the globe. Surface energy fluxes estimated from sparse snow-met observations may therefore not characterize spatial

variation of energy fluxes over a large snow/ice covered regions. To overcome this problem, remote sensing data can be effectively used in conjunction with sparse ground observations *via* suitably interpolation or modeling techniques to map energy fluxes at spatial level, as most of the area may be inaccessible for recording *in situ* observations. The additional advantage in adopting a remote sensing based approach is to retrieve the information at frequent temporal resolutions. Many studies (e.g., Bisht *et al.* 2005, Tang *et al.* 2006, Samani *et al.* 2007, Su *et al.* 2008, Tang and Li 2008, Wang and Pinker 2009, Bisht and Bras 2010a, 2010b) have been conducted to estimate incoming shortwave radiation flux, net shortwave radiation flux and net radiation flux using remote sensing techniques. Most of these studies, however, have been conducted over different land cover types other than snow/ice. Wang and Pinker (2009) proposed a forward inference scheme to estimate incoming shortwave radiation flux from top of the atmosphere to surface at different vertical levels. The scheme was implemented using MODIS data at spatial resolution of 1˚ (approximately 100 km) for 3-year period (2003-2005) at global scale and the results were evaluated for data collected at Baseline Surface Radiation Network (BSRN) sites of Arctic, Antarctic, Pacific, Atlantic, North America and Europe regions. A Root Mean Square Error (RMSE) of $\pm$14-25% in daily average incoming shortwave radiation flux in different regions was observed. Niu *et al.* (2010) evaluated the output of this scheme for high latitudes of northern and southern Polar Regions using BSRN data and other buoy observations and obtained an RMSE of $\pm$14-21% in estimation of daily incoming shortwave radiation flux. The main limitations of this scheme was that it required detailed information of atmospheric conditions e.g. water vapor, ozone, aerosol, cloud properties etc. and information derived was also at coarse spatial resolution. Moreover, there is lack of such studies on the snow/ice covered regions of Western Himalaya, which is a source of many rivers (Prasad and Singh 2007) and millions of people rely on varying extent on the water of these rivers (Bolch *et al.* 2012). Snow avalanches are also frequent in Himalayan ranges affecting lives and property severely every year (Sharma and Ganju 2000, Gusain *et al.* 2009a). It is therefore important the surface energy fluxes of large snow/ice covered regions in Western Himalaya be studied rigorously.

Further, the surface energy balance of the Antarctic ice sheet is also important as melting from the ice sheet can affect sea level rise and global climate. Many studies have

been conducted to estimate surface energy fluxes of ice sheet using *in situ* measurements at different parts of the Antarctica (Reijmer and Oerlemans 2002, Van den Broeke *et al.* 2004a, 2004b, Hoffman *et al*. 2008, Town and Walden 2009, Bliss *et al.* 2011). However, very few studies (Wang and Pinker 2009, Niu *et al.* 2010) have been reported on spatial estimation of energy fluxes. Further, these studies have been limited to estimation and evaluation of incoming shortwave radiation flux. Thus, study of other parameters of surface energy fluxes in Antarctica at spatial level is also a grey area.

1.5 Research Gaps

The brief review of literature presented here as well as in chapter II highlights that snow-met parameters are required to estimate the surface energy fluxes of snow/ice covered regions. Snow-met parameters are recorded using *in situ* measurements. These paremters can be estimated at spatial scale using various geospatial interpolation or modeling techniques using remote sensing data. Spatial maps of snow-met parameters can be used to estimate surface energy fluxes at spatial scale. Based on a review of more than 200 research articles on the subject, the following research gaps have been identified.

i) Very few attempts have been made to model snow depth in Western Himalaya. Additionally, these models have their own limitations (e.g these models have been developed for data at coarse spatial resolution from 5 km to 25 km, and also for very specific region or for shallow snow cover less than 1 meter).

ii) There appears to be lack of appropriate albedo maps of the snowcover in Western Himalaya for better estimation of net shortwave radiation flux.

iii) Literature is silent on estimation of surface energy fluxes in complex mountain topography of Western Himalaya using remote sensing techniques. Only a few studies based on point observations have been reported.

iv) Estimation of surface energy fluxes by integrating remote sensing techniques with *in situ* observations is required in cryospheric regions.

v) Spatial variability of surface energy fluxes in different aspects of mountain topography has to be explored.

vi) Many studies have been reported on surface energy fluxes of ice sheets using point observations but there appears to be lack of studies at the edge of the ice sheet from where melt water contribute to ocean.

1.6 Research Objectives

The main objective of this research is to assess the potential of geospatial models for estimation of a few snow-met parameters and the surface energy fluxes of snow/ice covered regions. The specific research objectives are:

i) Development of an approach for geospatial interpolation of snow depth in Western Himalaya.

ii) Development of an approach for broad band albedo of snow cover from narrow bands reflectances using moderate and high resolution satellite data.

iii) Estimation of surface energy fluxes at the edge of the Antarctic ice sheet using point observations and studying their temporal variability.

iv) Estimation and evaluation of incoming shortwave radiation flux, net shortwave radiation flux, net longwave radiation flux and net radiation flux of snow/ice covered regions of Western Himalaya and Antarctica using remote sensing technique.

v) Study of spatial variability of surface energy fluxes on different aspects of mountain topography.

1.7 Scope of Work and Overall Methodology

In the present research work, an approach has been developed for spatial interpolation of snow depth in Western Himalaya using sparse *in situ* snow depth observations. An approach for estimation of broad band albedo of snow/ice covered region has been developed using narrow band reflectances of moderate spatial resolution Moderate Resolution Imaging Spectroradiometer (MODIS) and medium spatial resolution Advanced Wide Field Sensor (AWiFS) sensors. In case of AWiFS images, it is one of the pioneer algorithms developed for narrow band to broad band conversion of snow/ice albedo. Surface energy fluxes at the edge of the ice sheet have been estimated using *in situ* observations. Information on seasonal and diurnal variation of energy fluxes, melt and sublimation of ice sheet have been presented. Energy fluxes have been estimated at spatial scale using MODIS images and evaluated from *in situ* AWS recorded data. Probably, the estimation and evaluation of energy fluxes of snow cover using remote sensing technique in Western Himalaya in the present research is also one of the initial attempts. Spatial variation in energy fluxes of snow covered north and south aspect slopes in mountain topography have been studied and presented. The broad overall methodology of the work done in the present research is given in the Figure 1.1.

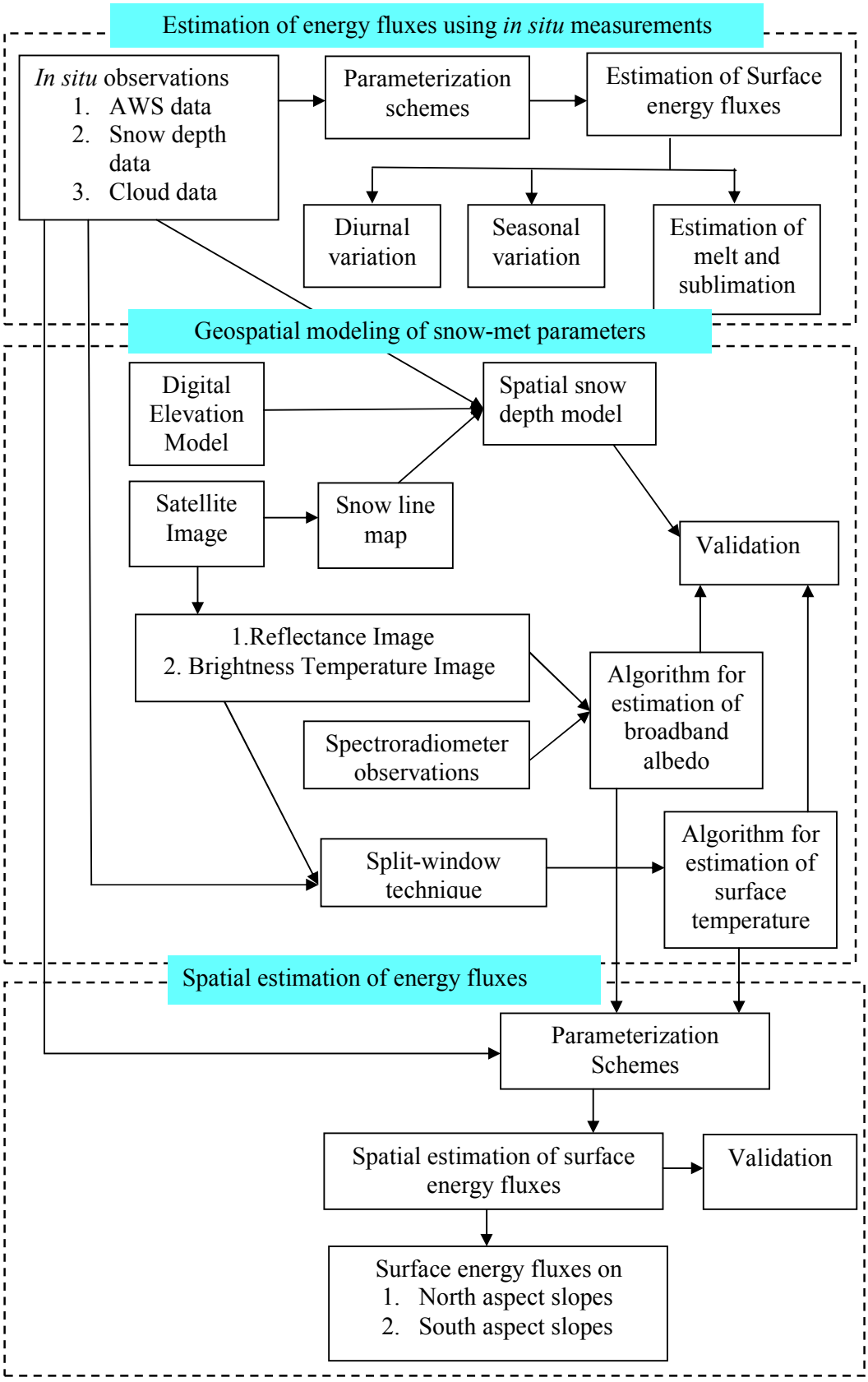

Figure 1.1: Broad overall methodology of research work

1.8 Organization of the Thesis

In order to accomplish the objectives of this research, *in situ* snow-met data recorded at manned observatories, AWS data, spectroradiometer data, remote sensing data from AWiFS and MODIS sensors, and Shuttle Radar Tropographic Mission (SRTM) Digital Elevation Model (DEM) have been used for development of approaches, their implementation, analysis and validation. All these aspects have been compiled as a thesis, which has been organized into seven chapters,

Chapter I highlights the importance of surface energy fluxes in the snow/ice covered region and summarises estimation of surface energy fluxes using *in situ* observations and remote sensing data in the form of a brief review. It also highlights the importance of snow-met parameters in estimation of surface energy fluxes and techniques to estimate these parameters at spatial scale. The chapter presents the existing research gaps in the literature, formulation of research objectives of the study, scope of work, broad overall methodology and organization of the thesis.

In chapter II, a comprehensive literature review relevant to the subject matter of this research has been provided. The review covers various methods used to interpolate and model snow-met parameters e.g. air temperature, snow depth, snow cover albedo, snow surface temperature etc. at spatial scale. The chapter also covers the methods used to estimate surface energy fluxes from *in situ* observations and remote sensing data and highlights the broad outcomes of the previous studies conducted in snow/ice covered regions.

Chapter III describes the study area and data used in the present research. Study areas have been described for their geographic location, topography and climate. The detail scheme of collecting *in situ* as well as remote sensing data used in this research has been discussed. Details on pre-processing of remote sensing data and generation of data base have also been presented in the chapter.

In Chapter IV, estimation of surface energy fluxes from *in situ* observations of snow-met parameters using AWS has been presented. Temporal variability of snow-met parameters and energy fluxes has also been described. A comprehensive discussion of the

results and the inferences drawn from the analysis are presented. Comparison of results of the study with published literature has also been discussed in this chapter.

Chapter V describes modeling of snow depth in Western Himalaya, development of algorithm for estimation of broad band albedo of snow from narrow band reflectances of satellite data and development of algorithm for estimation of surface temperature in Antarctica. The chapter discusses generation of snow depth maps from point snow depth observations using interpolation technique and validation in the study area. Development and validation of algorithms for estimation of broad band albedo of the snow/ice cover from narrow band reflectances of AWiFS and MODIS data have also been discussed. Further, development of algorithm for estimation of surface temperature in Antarctica has been presented.

Chapter VI discusses the estimation and evaluation of incoming shortwave radiation flux, net shortwave radiation flux, net longwave radiation flux and net radiation flux of snow/ice covered regions using remote sensing technique. The results have been presented in the form of maps which would be useful in hydrology and other snow studies. These results have been compared with previous studies on snow/ice covered regions. The chapter also discusses on spatial and temporal variation of surface energy fluxes in mountain topography, specifically on north and south aspect slopes.

Chapter VII presents the summary and major conclusions of the study followed with major research contributions and the scope for further research.

Chapter II

LITERATURE REVIEW

2.1 Introduction

In cryospheric regions, water is found in solid form and includes ice sheet, ice shelves, glaciers, snow cover, frozen lakes, frozen river, sea ice, permafrost and seasonally frozen ground (IPCC 2007). These regions play an important role in defining the global climate and affect the climate system due to many effects e.g. high reflectivity for incoming solar radiation, low thermal conductivity, large thermal inertia etc.. These also have the potential to affect ocean circulation, atmospheric circulation and sea level (IPCC 2007). Cryosphere interacts with atmosphere through exchange of heat, mass and momentum at the cryosphere-atmosphere interface (Vihma 2011). Heat exchange includes shortwave and longwave radiative fluxes and turbulent fluxes of sensible and latent heat (Armstrong and Brun 2008). Exchange of energy and mass at the interface results into various physical processes such as sublimation, evaporation, condensation, deposition, melt, freezing etc.. Snow/ice surface gains or loses energy by these physical processes (Upadhyay 1995). It gains heat,

i) from incoming shortwave radiation

ii) from downwelling longwave radiation from atmosphere and clouds

iii) advection of warm air over the cold surface

iv) condensation and deposition of moisture on the surface

v) sensible heat transfer if air above is warmer than surface and

vi) through conduction from ground underneath if ground is at higher temperature compared to the surface.

On the other hand it loses heat to atmosphere,

i) by emitting longwave radiation,

ii) evaporation or sublimation from the surface,

iii) sensible heat transfer if air above is colder than surface and

iv) through conduction if ground underneath is at comparatively lower temperature.

The net energy gained by the snow/ice surface is used in raising the temperature of the surface and the process of melting starts after surface temperature reaches to 0°C (Lewis *et al*. 1998, Gusain *et al.* 2014a). The study of energy balance of the snow/ice surface can be used to determine the ablation processes at the surface. The quantification of the physical precesses can be helpful in assessment of the mass loss or mass deposit over the snow/ice surface (Azam *et al.* 2014).

The physical processes can be studied quantitatively using the meteorological parameters over the snow/ice surface and in the air above. Many glacier mass balance models have been developed based on quantification of the energy exhange between the atmosphere and the glacier surface (Anderson 1976, Greuell and Oerlemans 1986, Oerlemans 1992, Oerlemans and Fotuin, 1992). Thus, the study of the surface energy balance in the cryospheric region includes the study of the snow meteorological parameters and the energy exchange between snow/ice surface and atmosphere. Many studies have been conducted to study the surface energy balance of the snow/ice media in Antarctica (e.g., Bintanja and Van den Broeke 1994, 1995b, Bintanja 1995, 1999, Bintanja *et al.* 1997, Lewis *et al*. 1998, Mishra 1999, Schneider 1999, Bintanja and Reijmer 2001, King *et al*. 2001, Van den Broeke *et al*. 2004a, 2004b, 2005, 2006, Fountain *et al*. 2006, Genthon *et al*. 2007, Hoffman *et al*. 2008, Bliss *et al.* 2011, Kuipers Munneke *et al.* 2012), in Arctic (e.g., Ohmura 1982, 1984, 2012, Lindsay 1998, Lynch *et al.* 1999) and glaciers (e.g., Brock *et al.* 2000, 2006, Wagnon *et al.* 2003, Giesen *et al.* 2008, Sicart *et al.* 2008,

Azam *et al.* 2014) all over the globe using snow-meteorological *in situ* observations.

Remote sensing techniques also have been used to estimate radiative (e.g., Duguay 1993, 1995, Hetrick *et al.* 1993, Bisht *et al.* 2005, Oliphant *et al.* 2006, Yang *et al.* 2006, Samani *et al.* 2007, Wang and Liang 2009, Journée and Bertrand 2010, Bisht and Bras 2010a, 2010b) and turbulent energy fluxes (e.g., Chehbouni *et al.* 1997, Schumugge *et al.* 1998, Bastiaanssen 2000, Garcia *et al.* 2008, Jiang and Islam 2010, Chang *et al.* 2010, Mito *et al.* 2012) spatially in a variety of land covers. However, few studies have been reported in snow/ice covered regions where remote sensing techniques can be very helpful as these regions are regarded as inaccessible and sparsely observed regions.

Estimation of surface energy fluxes at spatial scale requires knowledge of snow meteorological parameters at spatial level. These parameters can be estimated from *in situ* observations with appropriate interpolation or modeling technique. Many studies have been conducted in the past to model a number of snow-met parameters at spatial level across the globe (e.g., Nolin and Dozier 2000, Hall *et al.* 2002, Hall *et al.* 2004, Roy *et al.* 2004, Kumar *et al.* 2006, Foppa *et al.* 2007, Negi *et al.* 2007, Das and Sarwade 2008, Painter *et al.* 2009, Dewali *et al.* 2009, Negi and Kokhanovsky 2011, Takala *et al.* 2011, Bühler 2012, Dai *et al.* 2012 etc.). In the present study, the focus is on modeling of a few snow-met parameters at spatial scale and estimation of surface energy fluxes from *in situ* and remote sensing data in the cryospheric region of Western Himalaya and Antarctica. In this chapter, a comprehensive literature review on conventional snow-met observations, geo-spatial modeling techniques of snow-met parameters, estimation of surface energy fluxes using *in situ* observations and remote sensing techniques has been presented.

2.2 Estimation of Snow-Met Parameters

Meteorological observations have a long history since the establishment of first meteorological network in Italy in 1653 (IPCC 2007). Systematic weather observations had started by later part of 19th century all over the globe. The World Meteorological Organization (WMO) palys an important role in systematic observations of meteorology, operational hydrology and related geophysical sciences. Measurement of snow fall and

snow depth had also been started in few countries (USA, Switzerland, Finland) in late eighteenth century. The snow-met observations became widespread in snow covered mountains in late twentieth century (IPCC 2007). Snow-met observations include snow and meteorological variables defining the state of snow condition on ground and atmospheric conditions above the snow surface. General requrirement of a meteorological observation station may be found in WMO manual (2003a). The parameters recorded at a surface observation staion are present and past weather, wind direction and speed, amount and type of cloud, cloud-base height, visibility, temperature, relative humidity, atmospheric pressure, precipitation, snow depth, sun shine, solar radiation, soil/snow temperature and evaporation. Most of the parameters required for synoptic and climatological purposes may also be measured by automatic instrumentation (e.g., automatic weather stations (AWSs), micro meteorological towers etc.. The density of automatic instrumentation network is on the increase with enhanced capabilities of automatic systems (WMO 2008). At present, a number of automatic weather stations network are functioning for collection of meteorological data all over the globe and also in cryospheric regions for snow-met data collection. Some of the networks are Asian AWS network (AAN) deployed in meridional transect line in the monsoon Asia, Baseline Surface Radiation Network (BSRN) established to provide a worldwide network to continuously measure radiative fluxes at the Earth's surface, Portable Automated Mesonet (PAM) established in Colorado, USA, FLUXNET; a global network of mocrometeorological tower sites, Greenland Climate Network (GC-Net); a network of 18 AWS collecting climate information on Greenland's ice sheet, etc..

In Indian Western Himalaya, Snow and Avalanche Study Establishment (SASE) has set up manned observation stations and automatic weather stations network for collection of snow-met data in snow bound regions of Jammu & Kashmir, Himachal Pradesh and Uttarakhand state of India. SASE has also installed two automatic weather stations on Antarctic ice sheet close to Indian research station 'Maitri' in Antarctica.

Snow-met parameters have also been observed or estimated spatially at regional to glabal scale using meteorological satellite observations and general circulation models for various applications. Some of the satellite sensors are Earth Radiation Budget (ERB) sensors, Earth Radiation Budget Experiment (ERBE) sensors, Clouds and the Earth's Radiant Energy System (CERES), the Geostationary Earth Radiation Budget (GERB)

sensors etc. (Liang *et al.* 2010). In the following sections, a literature review on spatial estimation of some of the snow-met parameters (e.g., air temperature, surface temperature, relative humidity, snow depth and albedo) has been discussed.

2.2.1 Estimation of Air Temperature, Surface Temperature and Relative Humidity

Air temperature (T_a), relative humidity (*RH*) and surface temperature (T_s) are important parameters in the study of surface energy balance. T_a, T_s have been recorded at observation station manually using thermometers and *RH* has been recorded using hygrometers or psychrometers. T_a and *RH* have also been recorded automatically using AT/RH sensor whereas T_s has been recorded using IR (InfraRed) sensor mounted on a automatic weather station or micro-meteorological tower. Due to sparse observations on ground, typically spatial interpolation methods or modeling techniques have been used to estimate these parameters at spatial scale (Courault and Monestiez 1999, Negi *et al.* 2007, Dewali *et al.* 2009, Kumar *et al.* 2010, Xu *et al.* 2012, Lai *et al.* 2012).

Courault and Monestiez (1999) proposed a method for interpolation of daily maximum and minimum air temperature at the regional scale in southeast France using ordinary kriging with an error of 0.6°C to 2.0°C. Kumar *et al.* (2010) interpolated daily air temperature in Sutlej basin of western Himalaya using Gradient-plus-Inverse-Distance-Squared (GIDS) algorithm and observed an error of $\pm$ 5% to $\pm$ 20% of the ground observed values. GIDS algorithm combines the multiple regression and inverse distance squared approach. Xu *et al.* (2012) estimated near-surface air temperature from MODIS derived land surface temperature data by statistical regression algorithms in the Yangtze River Delta and reported an error ranging from 2.20°C to 2.34°C. Stahl *et al.* (2006) compared different approaches for spatial interpolation of daily air temperature in complex topography of British Columbia, Canada. They applied nearest neighbor technique with elevation adjustment, lapse rate by weighted regression with Gaussian filter approach, multiple linear regression (MLR) and GIDS model on different data sets and observed that all the models performed better for the data set having high density of stations. They also reported varied mean prediction errors during different months. For all the models, the mean absolute error (MAE) ranged from 1.22 to 1.99 °C whereas root mean square error (RMSE) varied from 1.83 to 2.83°C for all the models. GIDS performed best and showed

lowest MAEs of all the models. Eldrandaly and Abu-Zaid (2011) compared six spatial interpolation methods, namely, inverse Distance Weighted, Global Polynomial, Local Polynomial, Thin-Plate Spline, Ordinary Kriging and Universal Kriging for estimation of air temperature in western Saudi Arabia and observed that geostatistical methods (Ordinary Kriging and Universal Kriging) were superior to other methods having produced the lowest RMSE that ranged from 1.6°C to 1.9°C in different months. Chai *et al.*(2011) analysed and compared different spatial interpolation methods for monthly air temperature in Xinjiang Uygur region of China and reported that Multiple Linear Regression-Inverse Distance Weighted (MLR-IDW) performed better than other methods with least RMSE values ranging between 1.5°C and 4.0°C during different months.

Analysis of all the above results in different regions show that GIDS model has performed better in British Columbia, Canada (Stahl *et al.* 2006), Ordinary Kriging and Universal Kriging have performed superioir than other interpolation methods in Western Saudi Arabia (Eldrandaly and Abu-Zaid 2011), MLR-IDW has performed better in Xinjiang Uygur region of China (Chai *et al.* 2011). Thus, this reflects that the performance of a particular method for spatial estimation of temperature, highly depends on the region and the sample data set.

Surface temperature has been estimated for different land covers using various satellite sensors data (Wan and Dozier 1996, Key *et al.* 1997, Qin and Karnieli 1999, Wan 1999, Hall *et al.* 2004, Brogioni *et al.* 2011, Hall 2011). Generally, two types of methods are in vogue (i) single infrared channel method and (ii) the split-window method. Single-channel method requires radiative transfer model and vertical profiles of atmospheric data. The split-window method corrects for atmospheric effects based on differential absorption in adjacent infrared bands (Wan and Dozier 1996). Studies have been devoted to establish the methodology for retrieval of land surface temperature (LST) from thermal bands of Moderate Resolution Imaging Spectroradiometer (MODIS), Advanced Very High Resolution Radiometer (AVHRR), Advanced Spaceborne Thermal Emission and Reflection Radiometer (ASTER) and many other satellites sensor data. LST can be retrieved using thermal infrared remote sensing only in clear sky conditions while microwave techniques have all weather capabilities (Wan and Dozier 1996).

Split-window technique has been popularly used to develop the algorithms. The most popular form of the split-window technique is given as below,

$$T_s = T_i + A(T_i - T_j) + B \quad (2.1)$$

where, T_s is land surface temperature, T_i and T_j are brightness temperature of the i^{th} and j^{th} thermal bands of the multispectral satellite image (e.g., bands 4 and 5 for AVHRR, bands 31 and 32 for MODIS etc.) and can be estimated using Planck's radiation spectral equation (Wan and Dozier 1996), A and B are coefficients related to atmospheric effects, viewing angle and ground emissivity (Qin and Karnieli 1999). Coefficients A, and B can be determined in two ways;

(i) ground data measurements of surface temperature at sampled locations to be used in equation (2.1), and

(ii) through radiative transfer simulation using software e.g. LOWTRAN, MODTRAN etc. for a given location.

Radiative transfer simulation requires atmospheric data profiles at vertical levels (Qin and Karnieli 1999, Negi *et al.* 2007). Hall *et al.* (2004) produced daily surface temperature (IST) of sea ice at spatial resolution of 1-km and 4-km using Terra and Aqua MODIS images with RMSE of 1.2 K to 3.7 K. These products are available at the National Snow and Ice Data Centre (NSIDC) website (http://nsidc.org/NASA/MODIS). Key *et al.* (1997) estimated clear sky surface temperature of polar regions using thermal bands data of AVHRR and Along Track Scanning Radiometer (ATSR) and obtained accuracies in the range of 0.3 K to 2.1 K. Basist *et al.*(1998) demonstrated the capability of Special Sensor Microwave Imager (SSM/I) to observe the land surface temperature in United States and the globe and reported an absolute error of about 2.0°C with *in situ* measurements. Brogioni *et al.* (2011) estimated surface temperature of east Antarctic ice sheet using passive microwave remote sening data of Advanced Microwave Scanning Radiometer-Earth (AMSR-E) with RMSE of 2 K to 7 K. Negi *et al.* (2007) derived a regression relation for estimation of snow surface temperature of snow cover in Western Himalaya using MODIS thermal bands data and ground data. The equation has been validated from *in situ* recorded data in lower, middle and upper Himalaya and an RMSE of 2.5°C was reported. Surface temperature estimated from thermal bands data of different multi-spectral satellite sensors has advantage of higher spatial resolution as compared to that estimated from passive microwave data. Thus, the intensity of emissions captured by thermal bands of multi-spectral images are stronger as compared to the intensity of emissions captured by passive microwave images.

Analysis of these results show that various methods have been used to estimate land surface temperature from thermal bands of multispectral satellite images and passive microwave satellite images. However, the accuracy of surface temperature estimation varies for different satellite images in different regions of the globe. The accuracy can be achieved as low as 0.3 K to as high as 7 K from different satellite images. Generally, accuracies are high for multispectral optical satellite sensors images as compared to passive microwave satellite images. In the present thesis, thermal bands data of MODIS sensor have been used for estimation of surface temperature in the study area of Western Himalaya and Antarctica.

Kunkel (1989) has reported simple procedure for extrapolation of relative humidity by exponential function in mountainous Western United States. He has estimated lapse rate of dew point temperature from data collected at 47 locations and observed an RMSE of 3% - 5% in estimation of relative humidity. Sofan *et al.* (2007) estimated relative humidity based on MODIS derived precipitable water vapour in Java island, Thailand. They reported that precipitable water can be used to estimate relative humidity based on topography of certain region. They obtained correlation coefficient in the range of 0.84 - 0.92 between estimated relative humidity and recorded relative humidity by radiosonde experiments. Peng *et al.* (2006) estimated relative humidity from MODIS derived precipitable water vapour, specific humidity, DEM and air temperature values in Peninsular Malaysia and obtained mean absolute error of less than 5%. Dewali *et al.* (2009) generated relative humidity maps for Manali-Leh highway region in North-West Himalaya for snow avalanche application. They generated the maps using point observations of air temperature and relative humidity and DEM of the area. They obtained relative humidity in the range of 60%-92% of the study area and reported that regions with higher relative humidity values have higher threat of snow avalanches.

The above referred studies conclude that snow-meteorological parameters air temperature, surface temperature and relative humidity can be estimated spatially using various interpolation technique or can be derived from satellite images with varying accuracies for different regions. These parameters estimated at spatial level may be used for a variety of applications in snow/ice covered cryospheric rgions such as Western Himalaya and Antarctica, considered in the present work.

2.2.2 Snow Depth Estimation

Snow depth plays an important role in estimation of energy balance of a snow covered region. Quantity of heat conducted from snow surface to the ground or vice versa depends on the thickness and thermal conductivity of snow. Thermal conductivity of snow mainly depends on its density. Snow depth has been studied widely using ground observations as well as remote sensing observations in different cryospheric regions (Saraf *et al.* 1999, Shi and Dozier 2000, Brown *et al.* 2003, Kelly *et al.* 2003, Romanov and Tarpley 2007, Foppa *et al.* 2007, Das and Sarwade 2008, Jonas *et al.* 2009, Marofi *et al.* 2011, Dai *et al.* 2012). Various approaches have been adopted for mapping snow depth by researchers. These include interpolation of ground based measurements, algorithms for space-borne passive and active microwave observations, assimilation of space-borne observations with ground based measurements, LIDAR data processing before and after snowfall etc..

Foppa *et al.* (2007) mapped snow depth in Swiss Alps using *in situ* and space-borne observations at spatial resolution of 1-km. They used a spatial interpolation method based on the dependency of snow depth on altitude. An RMSE and MAE of 20-45 cm and 11-28 cm, respectively, has been reported during different days of the season 2005. Romanov and Tarpley (2007) used observations in the visible and infrared spectral bands from the Imager instrument onboard GOES to estimate snow depth. They used correlation between depth of snow pack and satellite-derived subpixel fractional snow cover to map snow depth over mid latitude areas of North America during winter seasons of 2003-04 and 2004-05 at 4 km spatial resolution. They compared snow depth maps with surface observations of snow depth and an error of 30% for snow depth below 30 cm, and 50% for snow depths ranging from 30 to 50 cm has been reported. Kelly *et al.* (2003) proposed an approach to estimate snow depth from spaceborne passive microwave data. The scattering signal observed in multifrequency passive microwave data was used to estimate snow depth. A four-year record of daily snow depth measurements at 71 meteorological stations, passive microwave data from the Special Sensor Microwave Imager (SSM/I), land cover data and digital elevation model were used to test the approach. An average error of 21 cm for the four year global data set has been reported. Che *et al.* (2008) reported on the spatial and temporal distribution of seasonal snow depth derived from Scanning Multichannel Microwave Radiometer (SMMR) and SSM/I passive microwave data in China. They first modified the Chang *et al.* (1987) algorithm of retrival of snow depth using passive

microwave data and then validated it using meteorological observation data, considering the influences from vegetation, wet snow, precipitation, cold desert and frozen ground. They assessed the accuracy of modified algorithm with measured snow depth at meteorological stations and reported standard deviations of 6.03 cm and 5.61 cm for SMMR and SSM/I derived snow depth respectively.

Dai *et al.* (2012) reported that static snow depth retrieval algorithms for passive microwave data i.e algorithms based on relationship of brightness temperature of different frequencies, brightness temperature difference of frequencies and snow depth, generally underestimate the snow depth at the beginning of the snow season, and overestimate it at the end of the snow season, as the snow characteristics vary with the age of the snow cover. They proposed a snow depth/SWE retrieval algorithm for passive microwave (AMSR/E) brightness temperature based on a priori snow characteristics, including grain size, density and temperature of the snowpack layers in Xinjiang, China. They concluded that understanding of *a priori* local snow characteristics can improve the snow depth and SWE estimation from passive microwave remote sensing data and reported an RMSE of 11.2 cm for deep snow stations having snow depth around 50 cm or more. Shi and Dozier (2000) used active microwave remote sensing to estimate snow depth. They estimated snow depth using SIR-C/X-SAR imagery from a physically based first order backscattering model with an RMSE of 34 cm.

Few studies have also been carried out to map snow depth in Indian Western Himalaya (Singh *et al.* 2007, Das and Sarwade 2008). Singh *et al.* (2007) developed a regression equation to estimate snow depth in Patseo region of Great Himalaya using passive microwave SSM/I data along with *in situ* recorded snow depth. They observed an RMSE of 37.5 cm in estimation of snow depth. However, the regression equation obtained is usually region specific and can be used for only Patseo region of H.P (Himachal Pradesh) Himalaya. Das and Sarwade (2008) used AMSR-E data to estimate snow depth in Indian Western Himalaya at a coarse spatial resolution of 5-km. They used Microwave Emission Model of Layered Snowpacks (MEMLS) along with AMSR-E to understand the difference in the snowpack emitted and sensor received signals and modified algorithm proposed by Chang *et al.* (1987) for mountainous terrain of Indian Western Himalaya. They found algorithm to be useful for estimation of snow depth from 5 to approximately 60 cm with absolute error of 20.34 cm. The main limitation of the algorithm was

estimation of snow depth only up to 1 m. However, a major part of the Indian Western Himalaya has snow depth more than 1 m during winter season. These limitations of models in Indian Western Himalaya provided an opportunity to explore for alternate techniques to map snow depth with larger acceptance.

Review of literature highlights that snow depth has been estimated spatially by various methods e.g. interpolation of *in situ* observations, space-borne observations of passive microwave remote sensing, assimilation of passive microwave with *in situ* observations etc. in different cryospheric regions. However, very few attempts have been made for spatial estimation of this parameter in Western Himalaya and there is a need to map this parameter at moderate to high spatial resolution for operational avalanche forecasting, snow melt run-off modeling, energy balance and other snow studies. In the present research work, spatial interpolation method proposed by Foppa *et al.* (2007) has been modified to estimate snow depth at spatial level in Indian Western Himalaya.

2.2.3 Estimation of Albedo

Albedo is a vital parameter in assessment of the surface energy balance. The albedo (α) of a surface is defined as the ratio of outgoing shortwave radiation flux ($SHW\uparrow$) to incoming shortwave radiation flux ($SHW\downarrow$) integrated over the upward and downward hemisphere respectively (Grenfell 2011). Albedo is typically measured using upward and downward looking pyranometers or albedometers. A number of ground measurement networks e.g. Surface Radiation Budget Network (SURFRAD), FLUXNET, BSRN, Atmospheric Radiation Measurement (ARM) etc. have been established to measure albedo (Liang *et al.* 2010). The albedo has also been estimated spatially from the data collected using multiangle (e.g. Multi-angle Imaging SpectroRadiometer (MISR), Polarization and Directionality of the Earth's Reflectances (POLDER)) and multispectral (e.g. MODIS, AVHRR, Visible Infrared Imaging Radiometer Suite (VIIRS)) sensors on polar orbiting platforms, geostationary satellites (e.g. Meteosat, Geostationary Meteorological Satellite (GMS), Geostationary Operational Environmental Satellite (GOES), Kalpana) as well as by using physical based numerical simulation in General Circulation Models (GCMs).

In cryospheric regions, variations in the surface albedo have large influence on snow/ice melt as it regulates absorption of shortwave radiation (Greuell and Oerlemans 2004). Researchers (e.g., Key *et al.* 2001, Stroeve and Nolin 2002a, 2002b, Greuell and

Oerlemans 2004, Liang *et al.* 2005, Stroeve *et al.* 2005, Moody *et al.* 2007, Painter *et al.* 2009, Wang and Zender 2010) have widely studied this parameter in cryopheric regions across the globe using remote sensing techniques.

Remote sensing offers a means to quantitatively estimate the surface reflectance in discrete spectral bands of large area. However, this spectral reflectance may not be directly used for energy balance estimation as it requires a integrated albedo in the reflective solar wavelength region. Therefore, an appropriate methodology to estimate broadband integrated albedo from narrow band spectral reflectance in discrete satellite bands is required. Generally two types of algorithms for estimating land surface broad band albedo, physically based and direct estimation have been used. A detail review of these algorithms may be found in Liang *et al.* (2010).

Liang *et al.* (1999) developed a direct retrieval algorithm that links top-of-atmosphere (TOA) narrowband albedo to land surface broadband albedo using a feed-forward neural network. The algorithm, although, has been designed for estimating albedo over any land cover types but appears to be particularly well designed for non-vegetated land cover. Liang (2000) has reported an extensive work on conversion of narrowband to broadband albedo (NBBA) for a number of satellite sensors including ASTER, AVHRR, MISR, POLDER, Enhanced Thematic Mapper Plus (ETM+), VEGETATION, MODIS etc.. They established a series of conversion formulae based on extensive radiative transfer simulations to estimate total shortwave albedo, total-, direct- and diffuse- visible albedos, total-, direct- and diffuse- near-infrared albedos. Liang *et al.* (2002) used extensive ground measurements in an area of diverse soils, crops and natural vegetation cover near northeast of Washington DC, USA to validate these broad band albedo formulae. They observed that average residual standard error of broadband albedo for various land covers was about 0.02. However, they could not validate the results for snow/ice covered regions. Stroeve (2001) assessed Greenland albedo variability from the AVHRR Polar Pathfinder data set from 1981 to 1998 and observed low albedo values (lower than mean albedo values from 1981 to 1998) during 1995 and 1998 due to considerable melt particularly near the western margin of the ice sheet. Stroeve and Nolin (2002a) retrieved snow albedo using data from MISR instrument over the Greenland ice sheet within 6% of the measured values. They used two different methods based on spectral and angular information from MISR

instrument. Key *et al.* (2001) estimated cloudy sky albedo of sea ice and snow using AVHRR with an uncertainty of approximately 7%.

Greuell and Oerlemans (2004) proposed equations for narrowband-to-broadband albedo conversion for glacier ice and snow for four different satellite sensors: Thematic Mapper (TM), AVHRR, MODIS and Multi-Angle Imaging Spectroradiometer (MISR). They proposed algorithm based on two-stream radiative-transfer models of ice and snow and atmosphere. They, however, could not validate on snow/ice surfaces using direct and simultaneous measurements for MODIS and MISR. They also believed that for TM and AVHRR data, the equations of Greuell *et al.* (2002) should be preferred as these were based on direct measurement rather than based on modeling. Schaaf *et al.* (2002) made MODIS derived 16-days average albedo products MOD43 (http://modis.gsfc.nasa.gov) at 1-km spatial resolution. These products include directional hemispherical albedo, bihemispherical albedo, Nadir BRDF (Bi-directional Reflectance Distribution Function)-Adjusted surface Rflectances, model describing the BRDF and quality assurance information. The accuracy of these albedo products had been assessed by Stroeve *et al.* (2005) on the Greenland ice sheet using ground-based albedo observations from 16 automatic weather stations. Results indicated that the MOD43 albedo product retrieved snow albedo with an RMSE of 0.07. Tasumi *et al.* (2008) proposed a rapid and operational method for estimating at-surface albedo from MODIS and Landsat TM/ETM+ sensors for cloud-free, low-haze conditions and sensor view angles less than 20° using SMARTS 2 (Simple Model of the Atmospheric Radiative Transfer of Sunshine 2) radiative transfer model. A standard error of 0.017 in albedo estimation had been reported. Wang and Zender (2010) studied the seasonal variability of snow albedo in Greenland using MODIS, MOD43 albedo products and reported that solar zenith angle explained up to 50% of seasonal albedo variability. The two other environmental factors considered, temperature and cloudiness, played insignificant roles in seasonal albedo variability. Negi and Kokhanovsky (2011) used ART (Atmospheric Radiative Transfer) theory to retrieve the spectral albedo for Himalayan snow using Hyperion sensor data and reported error in albedo estimation within $\pm$ 10%.

The studies reported reflect that land cover albedo has been studied widely at spatial level using various satellite sensors. Most of the techniques developed for estimation of albedo are based on radiative transfer simulation in atmosphere and surface,

and require deailed atmospheric data at vertical levels. Narrowband to broadband albedo algorithms are easy to implement as they only depend on spectral reflectance data of different bands. Although, the estimates of albeldo from a very few algorithms have been validated on snow/ice surface simultaneously with satellite observations, MODIS 16-days average albedo product MOD43 appear to be the best albedo products available at global scale for various applications. Bisht *et al.* (2005) and Bisht and Bras (2010a, 2010b) used these products to estimate net radiation flux on land covers other than snow/ice in Southern Great Plains, USA and reported mean errors of 14% with in situ recorded net radiation.

Albedo of snow also changes rapidly with time as compared to other land surfaces due to its metamorphic processes. So, for the study of surface energy fluxes of snow/ice, instant albedo at the time of satellite pass may be more useful as compared to 16-days average. In the present research work, narrowband to broadband algorithms have been derived using MODIS and AWiFS images and ground observations on snow/ice surfaces in Western Himalaya. The algorithms have been validated using *in situ* field measurements at the time of satellite passes. The algorithm developed for AWiFS image is first narroband to broadband albedo conversion algorithm.

2.3 Estimation of Surface Energy Fluxes Using *in situ* Observations

Many studies have been conducted all over the globe on estimation of surface energy fluxes of snow cover (Gustafsson *et al.* 2001, Fierz *et al.* 2003, Datt *et al.* 2008), glaciers (Wagnon *et al.* 2003, Giesen *et al.* 2008, Sicart *et al.* 2008, Azam *et al.* 2014), ice sheet (Reijmer and Oerlemans 2002, Van den Broeke *et al.* 2004a, Van As *et al.* 2005, Town and Walden 2009, Gusain *et al.* 2011), sea ice (Vihma *et al.* 2009) and lake ice (Doran *et al.* 1996) using *in situ* observations. Radiative energy fluxes, turbulent energy fluxes and sub surface conductive heat flux are the main components of the energy balance and differ in contribution to the net surface energy balance. The relative contribution of these energy fluxes strongly depends on the prevailing meteorological, topographical and surface conditions. Radiative energy fluxes are generally observed directly using pyranometers or pyrgeometers. A few parametrization schemes (Berliand 1960, Laevastu 1960, Zillman 1972, Maykut and Church 1973, Brutsaert 1975, Jacobs 1978, Moritz 1978, Marks and

Dozier 1979, Dozier 1980, Idso 1981, Bennett 1982, Iqbal 1983, Plüss and Ohmura 1996, Prata 1996, Dilley and O'Brien 1998, Niemelä 2001a, 2001b) are also in vogue to estimate different radiative energy fluxes using *in situ* meteorological observations. Turbulent energy fluxes can be measured directly using eddy covariance system or scintillometers. However, in most of the studies, these energy fluxes have been estimated using bulk transfer technique (Oke 1970, Moore 1983, Schneider 1999, Wagnon *et al.* 2003, Munneke *et al.* 2009, Azam *et al.* 2014). Bulk transfer equations use meteorological variables over the surface and at screen level height above the surface as input to estimate turbulent energy fluxes (Deardorff 1968, Oke 1970, Moore 1983). Contribution of sub surface heat flux in net energy balance is generally very low compared to radiative and turbulent energy fluxes and can be estimated using temperature measurements at different vertical levels inside the snowpack or ice. Sub surface heat flux can be measured directly using heat flux sensors placed inside snow/ice. In the following section, a review of various studies conducted to estimate surface energy fluxes using *in situ* measurements in cryospheric regions is presented.

Price and Dunne (1976) used a physically based energy balance model to predict daily snowmelt in the subarctic region. The estimated turbulent energy fluxes have been corrected for the effects of the stable and unstable stratification of the air over the snow surface. The predictions of the model have been compared with daily *in situ* observed melts and a high correlation coefficient (r = 0.85) between observed and estimated melt has been reported. Braithwaite *et al.* (1998) did reconnaissance study of glacier energy balance in North Greenland at two sites during 1993-94. They measured radiative energy fluxes and estimated turbulent energy fluxes using bulk aerodynamic method. The energy balance model has been tuned by choosing surface roughness and albedo to reduce the mean error between measured ablation and modelled daily melting. They observed that the net radiation was the main energy source for melting in North Greenland, although ablation was relatively low because the energy used by sublimation and conductive heat fluxes used energy that would otherwise be available for melting. Doran *et al.* (1996) studied the lake ice growth using energy balance approach of the perennially ice-covered lake in contact with Apfel Glacier, Bunger Hills oasis, east Antarctica. They observed that the extent of glacier ice contact became the controlling factor in maintaining an ice cover all year. This was due to the positive feedback for ice growth provided by the high albedo

of the adjacent glacier. Lewis *et al.* (1998) estimated surface energy balance on the surface and at the terminus of Canada Glacier, Taylor Valley, Antarctica during summer period of the year 1994-95 and 1995-96. They estimated melt on surface and terminus cliff using energy fluxes and compared with gauged flow in the glacial streams and observed that melt dominated ablation at terminus cliff of the glacier while sublimation dominated on glacier surface. Schneider (1999) estimated energy balance of a small glacier in Marguerite Bay on the west coast of the Antarctic Peninsula during austral summer of 1994/95 using automatic weather stations at three locations. Accumulation and ablation pattern were measured using stakes measurement and snow pit observations. They computed energy available for ablation from the AWS data and reported that estimated ablation correlated well (r=0.9) with the changes observed in snow pits. They observed that turbulent fluxes accounted for 55% of the summer-time energy budget at the surface and sensible heat was dominant energy source for ablation on the glacier. Bintanja (2000) presented spatial and temporal variability of heat budget of Antarctic snow and blue ice during summer using automatic weather station data collected at seven locations. He reported that blue ice areas absorbed about twice as much solar radiation as snow due to its low albedo (0.58). As a result, the blue ice areas are relatively warm. He also reported that latent heat fluxes over blue ice were considerably larger than those at snow cover. Reijmer and Oerlemans (2002) presented annual surface energy balance of ice sheet in Dronning Maud Land, East Antarctica using automatic weather station data. They reported that surface gained energy from the downward sensible heat flux that varied between ~ 3 W m^{-2} and ~ 25 W m^{-2}. The highest values of downward sensible heat flux were observed at the sites with largest surface inclination and high wind speeds. The net radiative flux was negative and balanced the sensible heat flux. They observed a strong correlation between heat budget and the katabatic wind flow. Wagnon *et al.* (2003) evaluated the surface energy balance of a cold, high-altitude tropical glacier, Illimani (Bolivia) during the dry season (mostly clear and cold atmosphere, strong westerly winds) of the years 1999, 2001 and 2002. They reported that daily net radiation was usually negative during dry winter because of high albedo of snow surface and low incoming longwave radiation due to low cloudiness. The latent heat flux was negative due to loss of mass through sublimation whereas sensible heat flux was positive during night but changed to negative during daytime unstable conditions. They reported that winter surface energy balance of

high-altitude cold tropical glacier was comparable to the summer surface energy balance over snow surfaces of the intermediate slopes of Antarctica. Van Den Broeke *et al.* (2004b) presented 4 years observations on near surface radiation balance in Antarctica from four automatic weather stations. They observed significant differences in the radiation balance of the three major climate regimes of East Antarctica i.e. coastal ice shelf, inland Antarctic plateau and katabatic wind zone. They reported that clouds not only limit atmospheric transmissivity for shortwave radiation but also strongly enhance the albedo for the shortwave radiation that reaches the surface. As a result, snow surface of the coastal ice shelves absorbed up to 65% less shortwave radiation in high summer than at the high plateau, where cloudy episodes and precipitation events are less frequent. They also reported that the katabatic wind zone showed the largest longwave and all-wave radiation loss in winter and over the year. This may be due to the fact that katabatic winds maintain a continuous transport of sensible heat toward the surface, which enhances outgoing longwave radiation. Klok *et al.* (2005) analysed meteorological data and surface energy balance of McCall glacier, Alaska, USA and studied the relationship between climate and ablation pattern at the ridge and at the ablation zone of the glacier. They reported that net radiation contributed 74% to the melt energy. Brock *et al.* (2006) studied the spatial and temporal variations in aerodynamic roughness length (z_0) on Haut Glacier d'Arolla, Switzerland during ablation season based on measurements of surface microtopography. They developed parameterization schemes to calculate z_0 variations for use in surface energy balance melt models using surface variables and meteorological measurements. The study shows that the accuracy of the bulk method depends on the accuracy with which z_0 can be specified and a variation of an order in z_0 value will change the values of turbulent energy fluxes by double. Van Den Broeke *et al.* (2006) presented summertime daily cycle of the Antarctic surface energy balance and its sensitivity to cloud cover and observed that spatial differences in the surface energy balance were largely controlled by differences in cloud cover. Giesen *et al.* (2008) presented surface energy balance in the ablation zone of Midtdalsbreen glacier in southern Norway. They reported that net solar radiation dominated the surface energy balance in summer, contributing on average 75% of the melt energy. The turbulent fluxes contributed to 35% of the net energy. Net longwave radiation and the subsurface heat flux were observed energy sinks and contributed in 8% and 2% of net energy ablation, respectively. Hoffman *et al.* (2008)

estimated surface energy balance of Taylor glacier, in the McMurdo Dry Valleys, Victoria Land, Antarctica using 11 years of daily meteorological data. They calculated ablation of the glacier from surface energy fluxes and observed a good correspondence between calculated (18.4 cm a^{-1} weq.) and measured (17.7 cm a^{-1} weq.) ablation. Sicart *et al.* (2008) studied the energy balance and glacier melt in different climates, The Bolivian Tropics, French Alps and northern Sweden. They computed the daily energy fluxes during melt seasons and investigated the correlations of energy fluxes with each other and with air temperature on three glaciers in contrasting climates. They observed that on the three glaciers, the turbulent fluxes were very poorly correlated to net radiation and sensible and latent heat fluxes were significantly correlated to each other. In Bolivian Tropics, variations of net radiations controlled the variations of surface energy balance (SEB) almost entirely as R^2 between net radiation and SEB was observed 0.9. SEB was very poorly correlated with turbulent fluxes and incoming longwave radiation with R^2 <0.2. The correlation between air temperature and SEB was small with R^2 <0.3. In French Alps the relative contribution of net radiation to the SEB was slightly smaller than Bolivian Tropics because of a higher value of sensible heat flux. The correlation between air temperature and SEB was moderate with $R^2 \sim 0.5$. In northern Sweden sensible heat flux accounted for approximately 70% variance of SEB followed by latent heat flux and net radiation. The correlation between air temperature and SEB was high with $R^2 \sim 0.65$. These results indicate distinct relationships between air temperature, different energy fluxes and surface energy balance in different climate.

Munneke *et al.* (2009) presented the summer surface energy balance of the snowpack at Summit, Greenland and observed net shortwave radiation flux was the largest energy source and net longwave radiation flux was the largest energy sink. On an average, sensible heat flux, latent heat flux and sub surface heat flux were small heat sinks to the snowpack. Vihma *et al.* (2009) estimated radiative and turbulent heat fluxes over snow covered sea ice in the western Weddel sea during early summer and observed positive net radiation flux and negative sensible and latent heat fluxes. They reported that larger portion of the absorbed solar radiation was returned to the atmosphere via turbulent heat fluxes. Bliss *et al.*(2011) estimated surface energy budget and sublimation of Taylor Glacier, Antarctica during 2003 to 2006 and observed a high sublimation rate of the glacier up to 40 cm a^{-1}. They reported that wind speed and vapour pressure gradient were

the governing variables on the glacier and observed that sublimation was about two times faster in summer than winter.

Approximately 2% of the Antarctic continent is in ice-free areas, also known as oases. The McMurdo Dry Valleys (ice free area ~ 4800 km^2) is the largest (Drewry *et al*. 1982) and Schirmacher Oasis (ice free area ~ 35km^2) is one of the smallest (Tyagi *et al*. 2011) oases in Antarctica. Surface energy balance of the McMurdo Dry Valley glaciers have been studied by many researchers (Lewis *et al*. 1998, Hoffman *et al*. 2008, Bliss *et al*. 2011), who have observed that sublimation dominates the surface mass balance of the ablation zone. Gusain *et al*. (2009b) reported surface energy and mass balance of the ice sheet close to Schirmacher Oasis during the summer of 2007–08 and reported a high ablation rate for the ice sheet.

Dakshin Gangotri Glacier, a part of the ice sheet close to the Schirmacher Oasis, is reported to be retreating with varying rates during different years in the past around the glacier tongue (Shrivastava *et al*. 2011). The surface energy fluxes of the ice sheet close to ice-free areas (oases) or dry valleys will be of interest in such cases of retreating ice sheet and growing oasis areas (Gusain *et al.* 2014a). A little is known about the surface energy fluxes near Schirmacher oasis in Dronning Maudland, Antarctica. Gusain *et al.* (2009b) studied the summer energy balance at the edge of the Antarctic ice sheet close to Schirmacher oasis and it will be of interest to know the temporal behavior of the energy fluxes during different seasons of the year. It is also of immense important to study the surface energy fluxes at the edge of the ice sheet as melting from these regions contribute to sea level rise.

From the literature discussed above, it is evident that estimation of surface energy fluxes depends on the location, surface characteristics and local weather conditions. Further, the contribution of each energy flux to net surface energy balance is different on snow/ice surfaces at different places. In Antarctica, these energy fluxes vary from ice shelf to coastal region and right up to high Antarctic Plateau. Antarctic coastal regions are characterized by mild temperatures and high katabatic winds while the Antarctic Plateau is characterized by cold temperatures and low wind speeds.

2.4 Estimation of Surface Energy Fluxes at Spatial Level

Components of the surface energy fluxes have been estiamated spatially using satellite sensor data or General Circulation Models (GCMs). Various algorithms or radiative transfer simulations have been used to estimate radiative energy fluxes from satellite data. The GCMs estimate radiative energy fluxes within atmosphere and at the surface. Review of methods using satellites sensor data to derive surface shortwave irradiance may be found in Pinker *et al.* (1995). Further, a detail review of estimation of radiative energy fluxes from remote sensing and model simulations may be found in Liang *et al.* (2010). In general, inputs required to estimate turbulent energy fluxes are surface wind, humidity, surface temperature, air temperature and surface roughness length. Over large heterogeneous areas, it may not be practical to obtain surface roughness lengths accurately, therefore physical models can not be directly applied to estimate turbulent energy fluxes. Generally, aerodynamic resistance energy balance method, also called as residual method, has been used to estimate turbulent energy fluxes over large areas (Kustas *et al.* 1989, Stewart *et al.* 1994, Jiang and Islam 2010). A few researchers (e.g., Price 1990, Kustas and Norman 1996, Jiang and Islam 2010) have also provided some alternative schemes to estimate turbulent energy fluxes using measured surface variables e.g. radiometric surface temperature, normalized difference vegetation index (NDVI), fractional vegetation cover (F_r) etc.. Following section provides a review on remote sensing based estimation of surface energy fluxes in different parts of the globe.

2.4.1 Radiative Energy Fluxes

Liu *et al.* (2005) compared surface downwelling shortwave and longwave radiative fluxes of the four satellite analysis and reanalysis projects data sets relevant to surface energy budget in the Arctic Ocean; (1) Cloud and Surface Parameter Retrieval (CASPR), (2) International Satellite Cloud Climatology Project (ISCCP-FD), (3) National Centres for Environmental Prediction Reanalysis II (NCEP-R2) and (4) European Centre for Medium-Range Weather Forecast 40-Year Reanalysis (ERA-40) with high quality *in situ* measurements from the Surface Heat Budget of the Arctic Ocean (SHEBA). They observed that CASPR and ISCCP-FD data sets have been more accurate than NCEP-R2

and ERA-40 data sets for the surface downward shortwave radiative flux. ERA-40 agreed well compared to other data sets with the SHEBA for the surface downward longwave radiative flux. They also examined the basin scale consistency of dominant spatial/temporal variability of the surface parameters across different data sets. Further, they observed that all data sets reproduce the patterns associated with the seasonal cycle, but vary in their ability to capture patterns linked to synoptic variability.

Bisht *et al.* (2005) proposed a simple scheme to estimate instantaneous net radiation over large heterogeneous area in Southern Great Plains, United States, for clear sky days using only remote sensing observations. They used various land data products e.g. land surface temperature, land surface emissivity, land surface albedo, and also atmospheric data products e.g. air temperature, dew temperature and aerosol depth of MODIS to estimate net radiation. They enumerated several sources of error e.g. error in estimation of land surface temperature, error in estimation of land surface emissivities, error in estimation of air and dew point temperature, error in estimation of land surface albedo etc., that affect operational estimation and implementation of net radiation algorithm from MODIS sensors. They observed that error in 16-day land surface albedo product was most significant in determining the accuracy of net radiation. Tang *et al.* (2006) estimated net shortwave radiation flux in plains of Huanghai and Huaihe river, China using MODIS data. They recalculated the parameterization coefficients of Masuda *et al.* (1995) based on more accurate radiative transfer model MODTRAN 4, for the estimation of the net surface shortwave radiation from TOA broadband albedo and observed an RMSE of less than 20 W m^{-2} for clear skies and 35 W m^{-2} for cloudy skies. However, these net shortwave radiation flux have yet not been evaluated in snow/ice covered regions.

Yang *et al.* (2006) developed an empirical model to estimate solar radiation from sunshine duration, air temperature and relative humidity. They used two radiative transmittances, one for clear sky based on local geographical and meteorological conditions and other cloud-related transmittance based on hourly, daily or monthly relative sunshine duration. They reported RMSE values of hourly radiation in the range of 40 – 70 W m^{-2} in USA, and Saudi Arabia and about 60 W m^{-2} in Japan, which were comparable to the errors of the Geostationary Meteorological Satellite radiation products. The model estimated solar radiation at coarse spatial resolution of more than 2°.

Samani *et al.* (2007) estimated daily net radiation over vegetation canopy using ASTER images and meteorological data. They used canopy temperature, albedo, shortwave radiation and air temperature to estimate net radiation through three different methods based on different parametrization schemes and observed an average error up to 30%.

Deneke *et al.* (2008) estimated incoming shortwave radiation flux during cloudy conditions using radiative transfer model and satellite derived cloud properties from METEOSAT SEVIRI. They observed an error of 56 W m^{-2}, 11 W m^{-2} and 4 W m^{-2} in hourly, daily and monthly mean incoming shortwave radiation flux.

Su *et al.* (2008) studied spatial and temporal scaling behavior of surface shortwave downward radiation based on MODIS and *in situ* measurements from Oklahoma MesoNet and the BSRN sites. They modified the University of Maryland (UMD) Surface Radiation Budget (SRB) model to estimate the surface shortwave downward radiation from MODIS. They observed that as the time scale of the site observations increased from 5 minutes to 55 minutes, the root mean square difference between the corresponding MODIS-derived and *in situ* surface shortwave downward radiation decreased steadly.

Tang and Li (2008) developed a statistical regression method to estimate the instantaneous downwelling longwave radiation for cloud free skies using top of the atmosphere radiance of the MODIS thermal infrared chanells. Regression has been established between downwelling longwave radiation (estimated using atmospheric radiative transfer model MODTRAN4) and top of the atmosphere radiance derived from MODIS thermal infrared chanells. They subsequently combined downwelling longwave radiation with MODIS land surface temperature/emissivity products (MOD11_L2) to estimate the instantaneous net longwave radiation. They reported that the proposed method was able to estimate downwelling longwave radiation and net longwave radiation with an RMSE of 30.1 W m^{-2} and 26.1 W m^{-2} respectively.

Wang and Pinker (2009) developed a forward inference scheme driven with satellite-based information to derive top of the atmosphere, surface and atmospheric spectral shortwave radiative fluxes at global sacle. The forward inference scheme was implemented with products from the MODIS sensor at 1° spatial resolution. They evaluated the derived surface fluxes with globally distributed Baseline Surface Radiation

Network (BSRN) measurements in the Antarctic, the Atlantic, North America, Europe and other continental sites and observed that daily radiative fluxes had a correlation coefficient greater than 0.96, and root-mean-square error (RMSE) less than 18%.

Niu *et al.* (2010) evaluated the radiative fluxes, estimated using MODIS products at high latitudes from Greenland and unique buoy measurements against land observations from the BSRN. They used the output of forward inference scheme of Wang and Pinker (2009). Their results showed that the MODIS products were in better agreement with observations than those from numerical models e.g. National Centers for Environmental Prediction (NCEP) and National Centers for Atmospheric Research (NCAR) reanalysis.

Chang *et al.* (2010) estimated net radiation in Chiayi plain of Taiwan using MODIS and images acquired by a high resolution airborne campaign in conjunction with meterological data and obtain a high correlation coefficient more than 0.8 between estimated and *in situ* observed net radiation.

Journée and Bertrand (2010) proposed to merge the *in situ* global solar radiation measurements with the operationally derived surface incoming global short-wave radiation products from Meteosat Second Generation satellites imageries to improve the spatio-temporal resolution of the surface global solar radiation data over Belgium. Average RMSE of these products has been reported ~ 96.5 W m^{-2} with in situ observations. They considered four approaches to merge ground-based and satellite-derived data, (1) mean bias correction (2) interpolated bias correction (3) ordinary kriging with satellite-based correction and (4) kriging with an external drift. They observed that kriging with an external drift and interpolated bias correction performed equlally well and better than the other two techniques. Merging ground-based and satellite-derived data using these two techniques reduced RMSE up to 9.2%.

Bisht and Bras (2010a) proposed a framework to estimate instantaneous and daily average net radiation under all sky conditions from the MODIS data in Southern Great Plains, United States. They utilized the MODIS cloud product (MOD06_L2) for cloud top temperature, cloud fraction, cloud emissivity, cloud optical thickness and land surface temperature for cloudy days. They reported an RMSE of 37 W m^{-2} and 38 W m^{-2} of instantaneous and daily average net radiation estimated under cloudy conditions respectively.

Review of literature on estimation of radiative energy fluxes reveals that various methods have been used to estimate radiative energy fluxes spatially. Many studies have been conducted to estimate incoming shortwave radiation flux, reflected shortwave radiation flux, incoming longwave radiation flux, outgoing longwave radiation flux and net radiation flux using remote sensing data e.g. MODIS, ASTER, AVHRR etc.. Most of these studies have been conducted over land cover other than snow/ice. Only few studies (Wang and Pinker 2009, Niu *et al.* 2010) have been reported for snow/ice surfaces at coarse spatial resolution of 1°. However, literature is silent on studies on the snow cover of Western Himalaya.

2.4.2 Turbulent Energy Fluxes

Jiang and Islam (2010) examined the theoretical background and implementation details of the aerodynamic resistance energy balance method or residual method with respect to remote sensing data applications. They observed that the residual method required estimation of aerodynamic resistance to heat transfer and need measurements of several ground based observations including land surface vegetation height and surface wind speed. Consequently, it became difficult to implement this method over large areas. They proposed a method for the distributed estimation of surface latent heat flux based on remotely sensed vegetation index and radiometric surface temperature. They presented performance of both the methods over the Southern Great Plains in the united states and reported that their proposed method performed well (correlation coefficient r=0.89 with *in situ* measurements) as compared to residual method (r=0.7) for distributed estimation of latent heat flux.

Chehbouni *et al.* (1997) presented a three-component model to estimate sensible heat flux over heterogeneous surfaces of arid and semi-arid regions in Nevada, USA. The three components of the surfaces were shrubs, soil under the shrubs and unshaded soil. The surface was represented with two adjacent compartments, first made up of two components, shrubs and shaded soil, and the second consisted of bare, unshaded soil. The sensible heat flux from each component was parameterized. Model performance was evaluated from data at two sites and an RMSE of 35 W m^{-2} for a range of values of sensible heat flux from -50 W m^{-2} to 400 W m^{-2} was observed at both the sites.

Mito *et al.* (2012) proposed a method to estimate sensible heat flux from MODIS data. They formulated a general method from bulk aerodynamic resistance equation to estimate sensible heat flux, which takes into account the surface emittance effect, water vapour column, canopy properties, air temperature and different atmospheric stabilities. The inputs to the proposed method were MODIS thermal bands (i.e. Band 31 and Band 32) data, MODIS calibrated radiance, emissivity product and water vapour product. The results showed an overall correlation coefficient of 0.9 with in situ observations of sensible heat flux.

Bastiaanssen (2000) estimated sensible and latent heat fluxes based on Surface Energy Balance Algorithm for Land (SEBAL) using Landsat Thematic Mapper images in Lower Gediz River Basin, Turkey during summer of 1998. The inputs to SEBAL were visible, near-infrared and thermal infrared data. They evaluated the temporal variability in heat fluxes between June and August months and their qualitative assessment showed that heat fluxes could be determined successfully from satellite data. However, no accuracy assessment of estimation of sensible and latent heat fluxes from satellite images was reported.

Review of literature on estimation of turbulent energy fluxes reflects that researchers have used various methods to estimate sensible and latent heat fluxes from satellite data e.g. residual method, three-component method, SEBAL etc. Some researchers have further modified the residual method and proposed algorithms to estimate turbulent energy fluxes using parameters like NDVI, radiant temperature, bowen ratio etc.. However, these studies have been conducted for land covers having vegetation, soil, shrubs and other than snow/ice.

2.5 Summary

In this chapter, a literature review on conventional snow-met observations, geo-spatial modeling of few snow-met parameters and estimation of surface energy fluxes using *in-situ* and remote sensing observations was presented. Manual meteorological observations started in seventeenth century. Wide spread automatic snow-met observations are on increase by the twenty first century. Many applications require snow-met observations to

be estimated at spatial level. Therefore, modeling techniques play an important role to estimate these parameters at spatial scale. Snow depth has been estimated spatially by interpolation of sparse *in situ* observations, algorithms for remote sensing observations, data assimilation of remote sensing and *in situ* observations etc. However, very few studies have been reported to estimate this parameter at spatial scale in Indian western Himalaya and developed algorithms are having limitations of being area specific, coarse spatial resolution and applicable for shallow snow cover.

Albedo has been measured by several ground measurement networks and estimated spatially using multi-angle and multi-sensor satellites, geostationary satellites and numerical simulation in climate models. Most of the methods are based on radiative transfer simulation and require detailed atmospheric data at vertical levels. Narrowband to broadband conversion methods appear useful as these methods are easy to implement and depend only on spectral reflectance of different bands. Albedo of snow cover at the time of satellite passes is required for estimation of surface energy fluxes using space-borne observations and there appears to be lack of appropriate albedo maps of the snowcover in Western Himalaya for better estimation of surface energy fluxes.

Studies have been conducted to estimate surface energy fluxes of snow cover, glaciers, ice sheet, sea ice, lake ice in cryospheric regions using *in situ* recorded snow-met parameters. These studies indicate that energy fluxes are dependent on the location, surface characteristics and local weather conditions, and contribution of various energy fluxes to net energy balance is different at different places.

Surface energy fluxes have also been estimated at spatial scale using satellite data or General Circulation Models (GCMs). Radiative enrgy fluxes have been estimated using parameterization schemes or using radiave transfer simulation. Aerodynamic resistance energy balance method or residual method has been used to estimate turbulent energy fluxes of large areas. However, only few studies have been reported for spatial estimation of surface energy fluxes of snow/ice surfaces and studies have been conducted at coarse spatial resolution. Literature is silent on such studies in the snow cover of Indian western Himalaya.

Thus, the literature review has resulted into several research gaps, which have formed the basis of defining the objectives of this research. To achieve the objectives of

the study, the required *in situ* and satellite data have been collected and analysed. The following chapter provides the detail of study area, data and data base generation for the study.

Chapter III

STUDY AREA, DATA AND DATA BASE GENERATION

3.1 Introduction

The aim of this chapter is to introduce the study areas, to provide details on *in situ* and remote sensing data used, to discuss pre-processing of remote sensing data and to explain creation of geospatial database. The physiography, topography and climate of study area have been described. *In situ* snow-met observations using automatic weather stations and manually at sampled locations have been elaborated. Spectroradiometer data collected in the field to extract hyperspectral signature of snow/ice media have also been analysed.

3.2 Study Area

In the present research, two study areas, namely, cryospheric regions of Antarctica and Indian Western Himalaya have been considered.

3.2.1 Study Area 1: Antarctica

Antarctica is the southern most continent of the Earth located south of 60˚S latitude. It includes the ice covered continent, isolated islands and a large part of the Southern ocean (King and Turner 1997). It is a pulsating continent that extends its mass during winter and reduced in summer. The continent itself makes up about 10% of the land surface of the Earth with the combined area of the ice sheets and the ice shelves being about 14 million square kilometer. The Antarctic ice sheet consists of three distinct morphological zones - East Antarctica, West Antarctica and the Antarctic Peninsula (King and Turner 1997). The Antarctic ice sheet varies in thickness across the continent and is at its greatest depth of 4776 m in East Antarctica. Although, Antarctica is best known for its uniform regions of ice and snow, there are many local topographic and morphologic features on the surface, such as ice-free areas also known as oases. Approximately 2% area of the Antarctic continent is in oases (Tyagi *et al.* 20011). Indian research station 'Maitri' is located in 'Schirmacher Oasis' in the coastal margin of the Dronning Maud Land, East Antarctica at 70˚45.94'S and 11˚44.13'E (Gusain *et al.* 2014a). The study area considered in the present work extends from 70.2°S to 72°S and 8.6°E to 14°E (Figure 3.1).

3.2.1.1 Physiography

The study area comprises ice shelves of Princess Astrid Coast, ice-free area of Schirmacher Oasis, continental ice sheet and Wohlthat mountains from north to south. Schirmacher Oasis (70°44’ - 70°46’ S, 11°24’ - 11°54’ E) is about 16 km long in an east-west direction with a maximum width of about 3 km, and about 70 km south from the Princess Astrid Coast in East Dronning MaudLand, Antarctica (Gusain *et al.* 2014a). It is a small maoraine covered rocky area having low lying hills. More than 80% area of the oasis is covered with snow during winter which melts off during summer. North of the Shirmacher Oasis is ice shelf spreading about 70 km up to Antarctic sea and south of the oasis is continental ice sheet which increases in thickness towards south. Wohlthat mountains are about 70 km south of the Shirmacher Oasis.

3.2.1.2 Climate

Antarctica is the coldest, driest and windiest continent on Earth. The elevated central

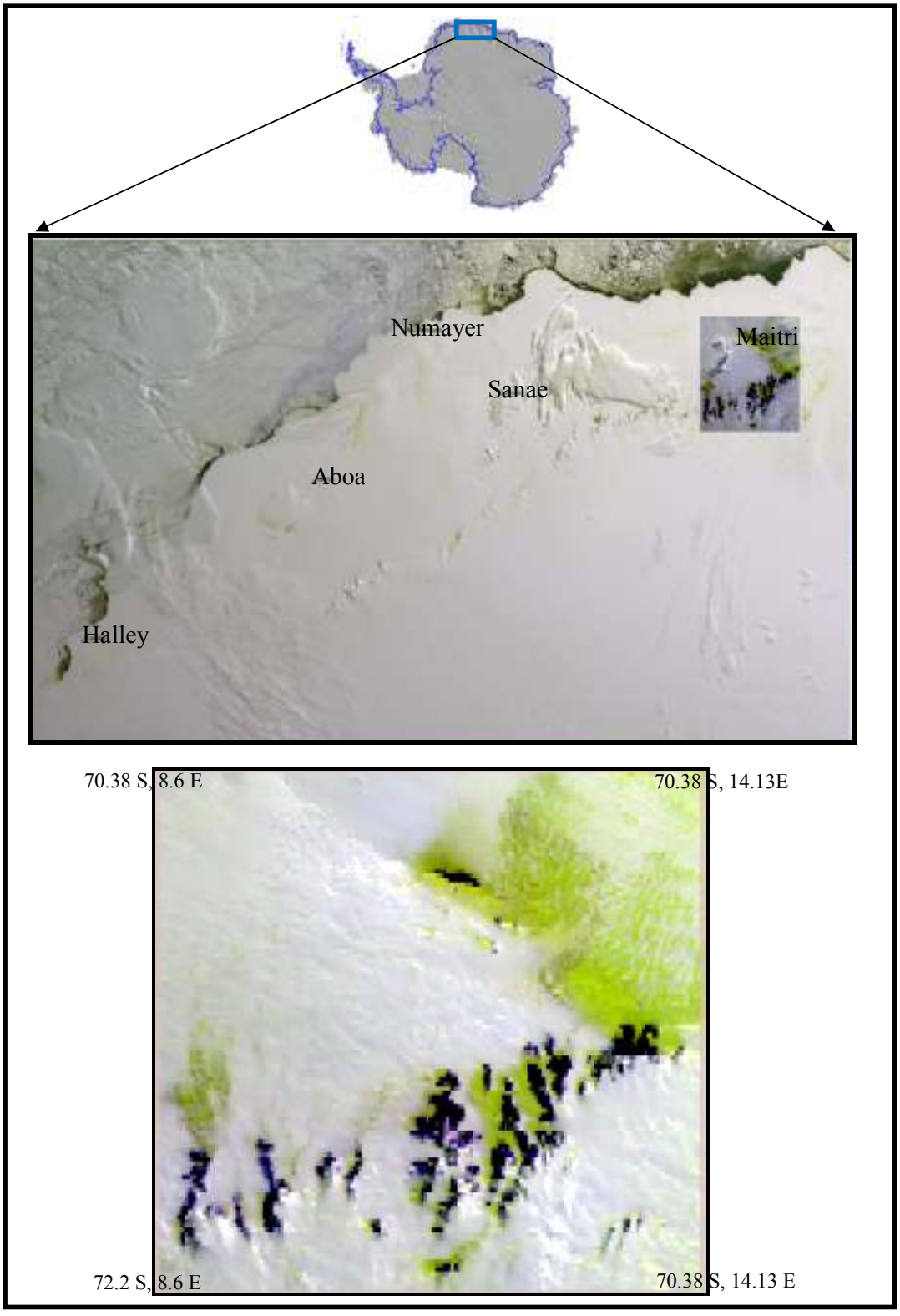

Figure 3.1 Geographical extent of Study Area 1: Antarctica region: An FCC (R:4, G:3, B:2) of MODIS image

plateau is a cold desert with annual mean temperatures between -50 ºC to -70 ºC and annual mean precipitation between 3 to 7 cm of water equivalent. The lower altitude coastal regions are much warmer (-10 ºC to -20 ºC annual mean) and receive more precipitation and have stronger winds than the higher regions. The annual mean of temperature, precipitation and wind at 'Maitri' in Schirmacher Oasis were observed around -9.6° C, 18 cm and 15.4 m s^{-1} respectively during past two decades (Taygi *et al.* 2011). The land mass is scoured by a regime of persistent and powerful katabatic, or gravity, winds which are the result of cold dense air rolling down the continental slope from the high Antarctic plateau. These gravity winds interact with the warmer air from the ocean to produce a narrow storm belt that rings the continent, producing clouds, fog and extremely severe blizzards.

3.2.1.3 Topography

Antarctica is the highest continent of the Earth in terms of average elevation as compared to other continents. The average elevation is 2200 m from the mean sea level. Most part of East Antarctica is above 3000 m in elevation. The average thickness of ice sheet is more than 2000 m in this part. In the study area considered, the elevation ranges from 22 m near Antarctic sea to 3003 m on high Antarctic plateau. Most part of the study area is flat ice sheet having slope less than 5°. A small terrain with slope angle between 20° - 30° also exists near Schirmacher Oasis and Wohlthat mountains.

3.2.2 Study Area 2: Western Himalaya

Indian Himalaya stretches about 2500 km from east to west (Sharma and Ganju 2000). It is extended in Jammu & Kashmir (J. & K.), Himachal Pradesh (H. P.), Uttarakhand, Sikkim, Arunanchal Pradesh (A. P.), Meghalaya, Nagaland, Manipur, Mizoram states of north India and is the major source of water for many rivers. Indian Western Himalaya mostly comprises of J. & K. and H. P. Himalaya. It stretches from Jammu region in south to Siachen glacier in the north and Naugam region (J. & K.) in west to Manali region (H. P.) in the east. Western Himalaya is composed of a series of many parallel ranges (except Shamshabari range) which rise progressively northwards. The southernmost series of hills

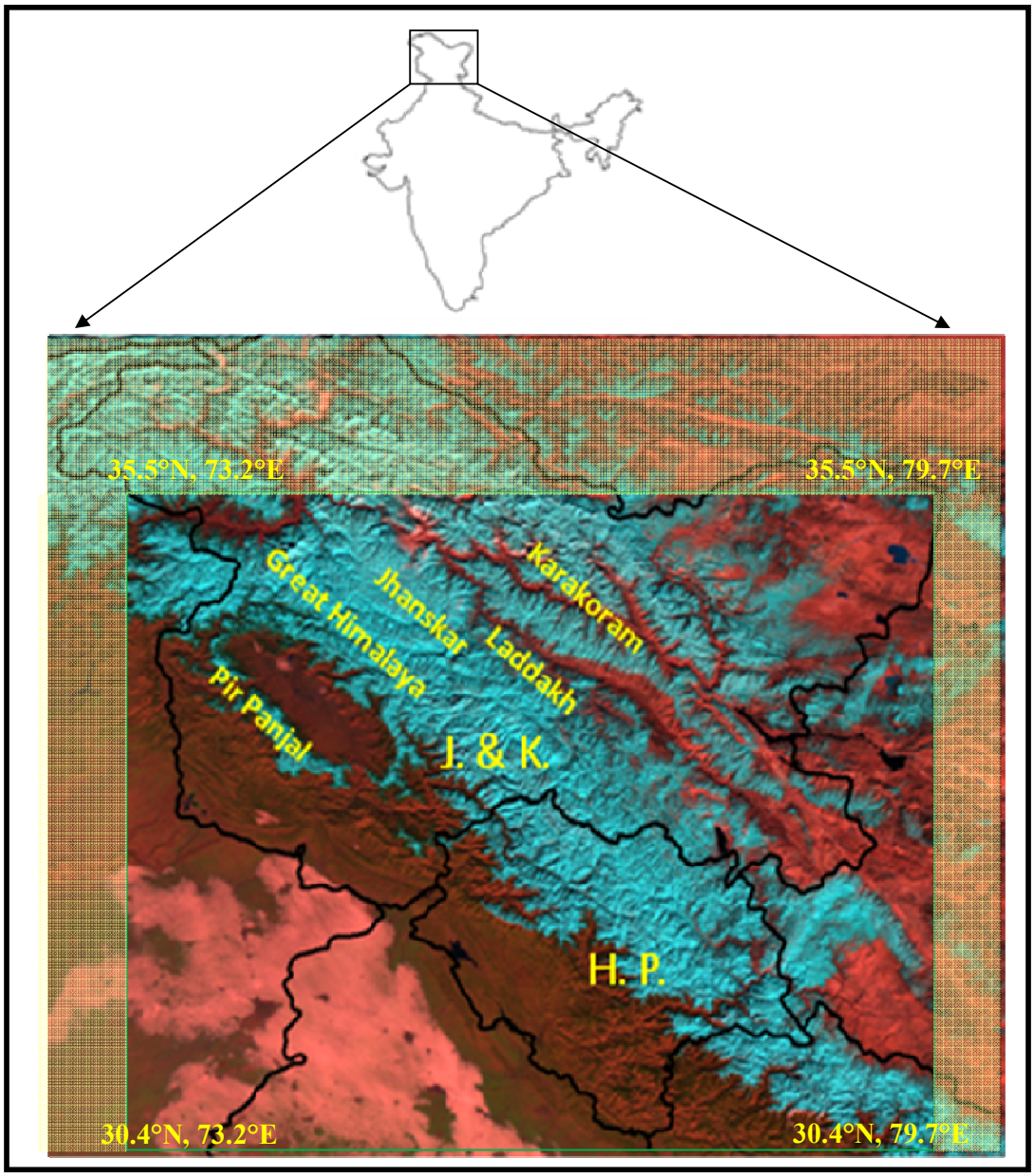

Figure 3.2 Geographical extent of study area 2: Western Himalaya: An FCC (R:4, G:3, B:2) of AWiFS image

are Shivalik and then encounters Dhauladhar, Pir Panjal, Shamshabari, Great Himalaya, Jhanskar, Laddakh and Karakoram while traversing towards the north. All the mountain ranges lie in the east-west direction except Shamshabari range which is in an arc shape in the north-south direction between Pir Panjal and Great Himalaya (Gusain *et al.* 2009a).

The entire region of the Indian Western Himalaya at elevation more than 1800 m receives snowfall during winter due to western disturbances. Figure 3.2 shows the geographical location of the study area in Western Himalaya.

3.2.2.1 Physiography

Pir Panjal, Great Himalaya, Shamshabari and Karakoram ranges are generally covered with seasonal snow during winter months January, February, March and April. In Karakoram range, snow cover exists throughout the year as this range also receives snowfall during summer months. In Pir Panjal range, most of the mountain slopes are forested and tree line exists up to an elevation of 3200 m. In Shamshabari range, the tree line exists up to 3300 m elevation and beyond that area is mainly barren/rocky with scanty trees and few patches of seasonal grasses (Gusain *et al.* 2009a). In Great Himalayan range, more than 95% slopes are barren/rocky and scanty trees at the lower elevation level or valley bottom may exist. Most of the Himalayan glaciers housed in the Great Himalayan range above elevation of 5000 m. Karakoram range is the northern most range of the Indian Himalaya and mountain slopes are rocky, glaciated and devoid of vegetation. Siachen glacier, which is one of the largest glacier in the world outside polar region falls in this range.

3.2.2.2 Climate

Climate of the Western Himalaya varies with seasons. November, December, January, February, March and April are winter months. Himalayan ranges receive snowfall due to western disturbances during these months. The maximum snowfall generally occurs in Pir Panjal and Shamshabari ranges (Gusain *et al.* 2004). Mean seasonal snowfall at Dhundi station (H. P.) falling in Pir Panjal range at an elevation of 3050 m has been recorded 817 cm in past two decades. Mean seasonal temperature varied from -1.5 °C to 2.8 °C at this staion with a mean of 0.4°C during past two decades.

In the Great Himalayan range, the temperature is generally low and snowfall is less as compared to the Pir Panjal and Shamshabari ranges. In this Himalayan range, the mean seasonal temperature at Patseo station (H. P.) at an elevation of 3800 m varied between -

5.9 °C to -10.7 °C with an average of -8.7 °C during past two decades. Seasonal snowfall varied between 134 cm to 410 cm with an average of 261 cm during last two decades.

Karakoram range is very cold during winters. The mean seasonal temperature varied from -14.3 °C to -23.7 °C with a past two decades average of -20.0 °C. Seasonal snowfall varied from 38 cm to 420 cm and average of past two decades were recorded as 197 cm at the observation station Kumar at an altitude of 5000 m from mean sea level (Gusain *et al.* 2009a).

3.2.2.3 Topography

Large topographic variation exists in the study area since it comprises of flat plane ground and high mountain peaks. Elevation in the study area rises while moving from south to north and varies from 158 m to 7665 m above mean sea level. Almost all aspect slopes from 0° to 359° may be observed with a slope angle as steep as more than 80° observed in the area. Permanent glaciated region above 5000 m elevation is common and most of the part of the Karakoram range is glaciated.

3.3 Data

In the present work snow meteorological data, spectroradiometer data and geo-spatial data have been used for development and validation of algorithms and estimation of surface energy fluxes. *In situ* recorded snow meteorological and spectroradiometer data for the study have been obtained from the data bank of Snow and Avalanche Study Establishment (SASE), a laboratory of Defence Research and Development Organisation (DRDO) in India. SASE has installed a number of automatic weather stations in Western Himalaya and Antarctica and has manned observation stations in Western Himalaya. Every year snow-met data are collected from all these stations by various field teams and stored as the data bank of SASE. Snow-met data are usually collected daily at 0830 hours and 1730 hours at manned field observation stations of SASE in Western Himalaya. Data from automatic weather stations installed in Western Himalaya are recieved directly at SASE data reception centre, Chandigarh through satellite communication. Data from automatic

weather stations installed in Antarctica are collected by scientific staff of SASE participating in Indian Scientific Expedition to Antarctica.

Geo-spatial data used in the present thesis are Survey of India (SOI) toposheets, Digital Elevation Models (DEM) generated from SRTM (Shuttle Radar Topograhic Mission) (http://srtm.csi.cgiar.org/) and ASTER (Advanced Space-borne Thermal Emission and Reflection Radiometer) (http://asterweb.jpl.nasa.gov/gdem.asp), satellite images from Terra and Aqua MODIS and IRS-P6 (or RESOURCESAT-1) AWiFS sensors. Details of these data for each study area are given in the following sections.

3.3.1 Study Area 1: Data Sources

3.3.1.1: *In situ* data

3.3.1.1.1 AWS Data

Two automatic weather stations have been used to collect the data for the study in Antarctica. AWS 1 has been installed on the ice sheet close to the Schirmacher oasis at about 1 km from 'Maitri' research station at 70˚46'05.1"S, 11˚42'12.2"E, 142 m coordinate. AWS 2 has been installed on ice sheet at about 8 km from 'Maitri' research station at 70˚47'40.9"S, 11˚41'43.1"E, 395 m coordinates. Both the AWS record air temperature, relative humidity, wind speed, wind direction, incoming solar radiation, reflected solar radiation, atmospheric pressure and surface temperature and have equipped with calibrated sensors with specifications given in Table 3.1 (Gusain *et al.* 2014a). AWS 1 was equipped with an additional ultrasonic snow depth sensor for few months during summer of 2007-2008 for monitoring variation on glacier surface due to accumulation / ablation processes. All the AWS sensors have been powered by a 100-ampere-hour battery mounted on AWS tower and kept inside a Nema-4 box. Hourly observations of cloud amount and cloud type are recorded conventionally at the Indian Research Station 'Maitri' by a team of scientists from IMD (India Meteorological Department) and SASE (Snow and Avalanche Study Establishment). AWS 1 data from March 2007 to February 2011 have been used for estimation of surface energy fluxes at the installation location in the present thesis. The location map showing Shirmacher Oasis, Maitri, Shelf Ice, Continental

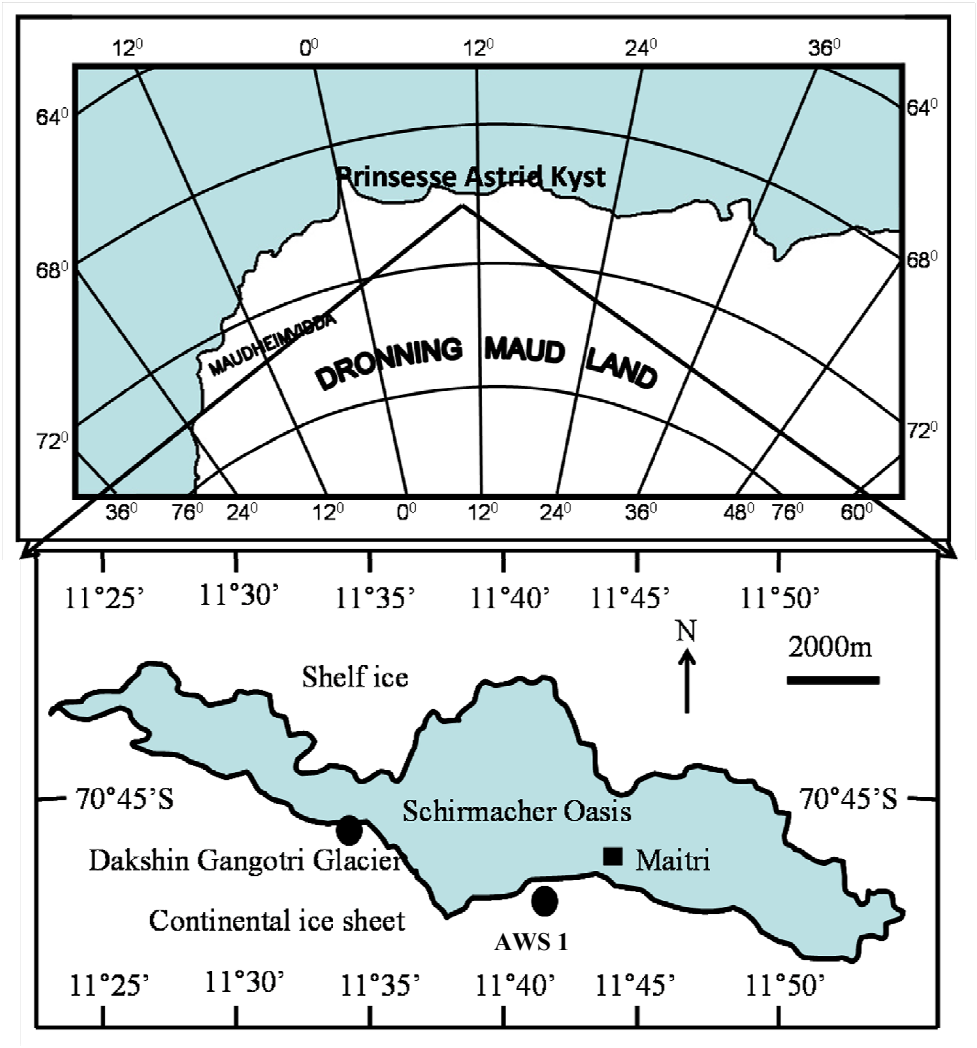

Figure 3.3: Location map of Schirmacher Oasis in Antarctica

Table 3.1: Specifications of AWS sensor

Sensor	Range	Accuracy	Type
Air Temperature	-50ºC to +50ºC	±0.3ºC	Campbell Scientific 41372V-90
Air Pressure	400 to 1100mBar	0.5mBar	Anika PTB210B2A1B
Relative Humidity	0-100%	±3% from 0-90% ±4% from 90-100%	Campbell Scientific 41372V-90
Wind speed	0-50m/sec	±0.3m/Sec	RM Young 05103
Wind direction	360 degree	±3 degree	RM Young 05103
Albedometer	305 to 2800nm	± 10%	Kipp & Zonen CM3

Snow Surface Temperature	-50ºC to +50ºC	±0.1ºC from -10ºC to +10ºC and ±0.3ºC else	Everest 4000
Snow depth	Up to 10m	± 1.0cm	Campbell Scientific SR50

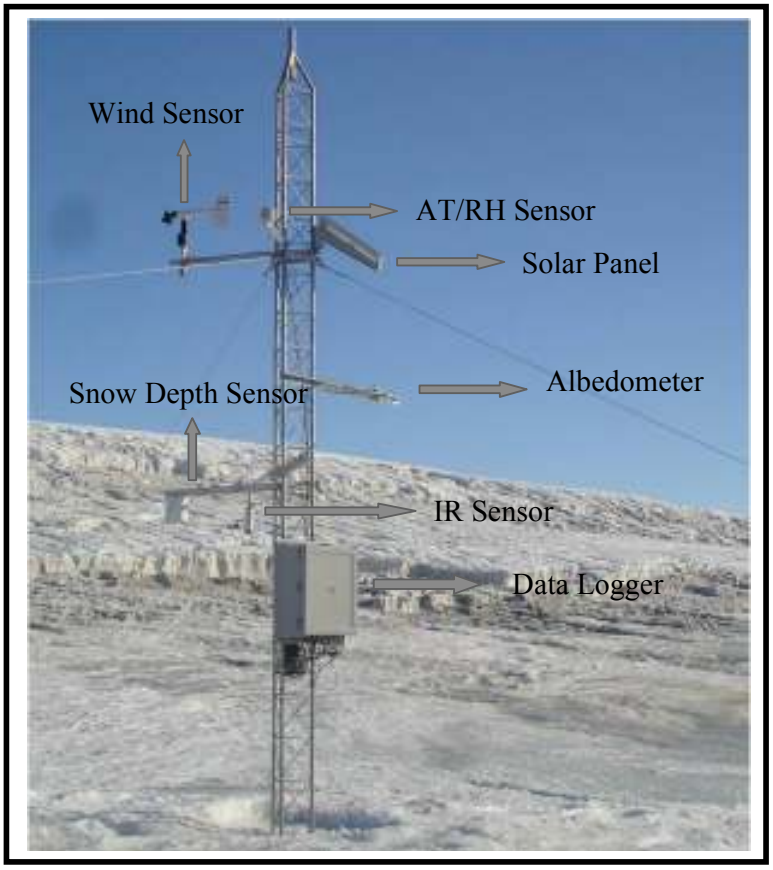

Figure 3.4: Photograph of AWS-1 in Antarctica

Ice Sheet and AWS1 is given in Figure 3.3.The photograph of AWS1 with sensors is shown in Figure 3.4. AWS 2 is installed on continental ice sheet about 7 km south of AWS1 location shown in Figure 3.3. AWS1 and AWS2 data have also been used in conjuction with MODIS images and SRTM DEM for spatial estimation of surface energy fluxes and validation on clear sky days. This has been discussed in Chapter 6 of the thesis.

3.3.1.1.2 Sub Surface Heat Flux Data

Data for the estimation of sub surface heat flux has been collected during 31st Indian Scientific Expedition to Antarctica by SASE using heat flux plate sensors. The data collected from 30-December-2011 to 4-January-2012 near AWS1 location have been used here for estimation of sub surface heat flux of the Antarctic ice sheet. The heat flux plates used in measurement of subsurface heat flux are shown in Figure 3.5. Two heat flux plates were used for the direct measurement of net subsurface heat flux inside the snow/ice media. These plates at a depth of 10 cm from top of the surface have measured the heat flux flowing through the media. Heat flux plate (consists of thermopiles) measured the differential temperature across the thin layer of ceramics plastic composite of known thermal properties. Details of heat flux sensor plate e.g. dimensions, sensitivity etc. are given in Table 3.2. The thermopiles of heat flux plate generated small voltage proportional to the local heat flux flow inside the snow/ice media. The heat flux plate measured the net subsurface heat flux across a cross section in a horizontal plane. Snow/ice temperature has been measured at the same depth along with the heat flux using two thermister based temperature sensors. A four channel data logger has been used to log the average data continuously at a time interval of 15 minutes. A twelve volt battery charged by the solar panel has been used to meet the power requirement of the experimental setup.

Table 3.2. Details of heat flux plate sensor

Diameter	80 mm
Thickness	5 mm
Nominal sensitivity	50 $\mu V/Wm^2$
Temperature range	-30^0C to $+70^0C$
Heat flux range	-2000 W/m^2 to +2000 W/m^2
Accuracy	5%

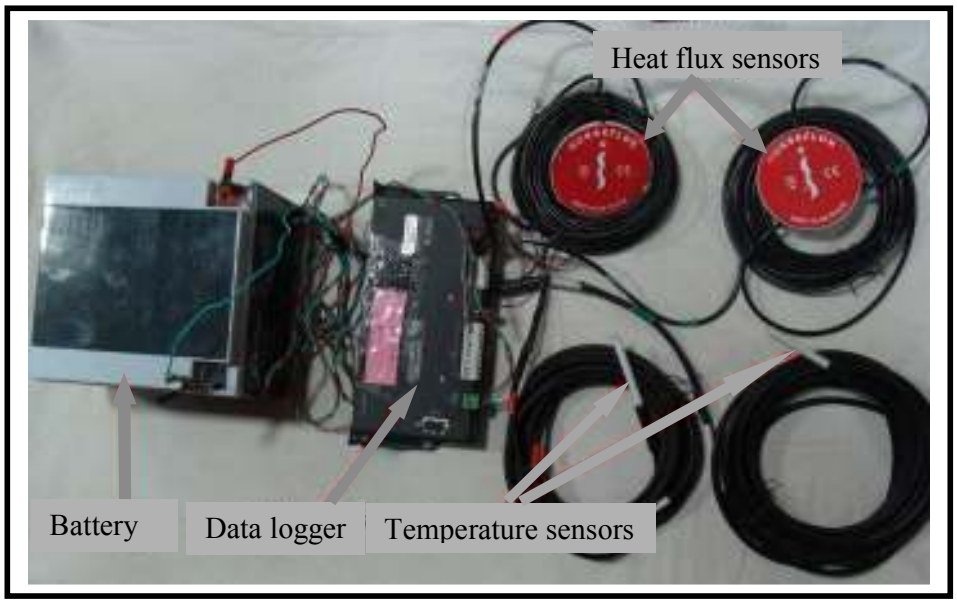

Figure 3.5 : Experimental setup for subsurface heat flux measurement

3.3.1.2: Geospatial Data

3.3.1.2.1: DEM

An SRTM DEM (generated in February, 2000) at spatial resolution of 90 m has been used in the study. SRTM DEM is freely available and can be downloaded from internet (http://srtm.csi.cgiar.org/). SRTM DEM has an error of approximately 16 m in elevation. DEM has been used to generate slope, aspect and elevation maps (Sanjeevi and Bhaskar, 2008). These maps have been used as input for the estimation of solar zenith angle and incoming shortwave radiation flux. The DEM has been shown in Figure 3.6 whereas the slope and aspect maps are given in Figure 3.7 and 3.8, respectively. In the study area, the elevation ranges from 22 m to 3003 m (m.s.l.), slope angle from 0° to 40° and aspect ranges from 0° to 359°.

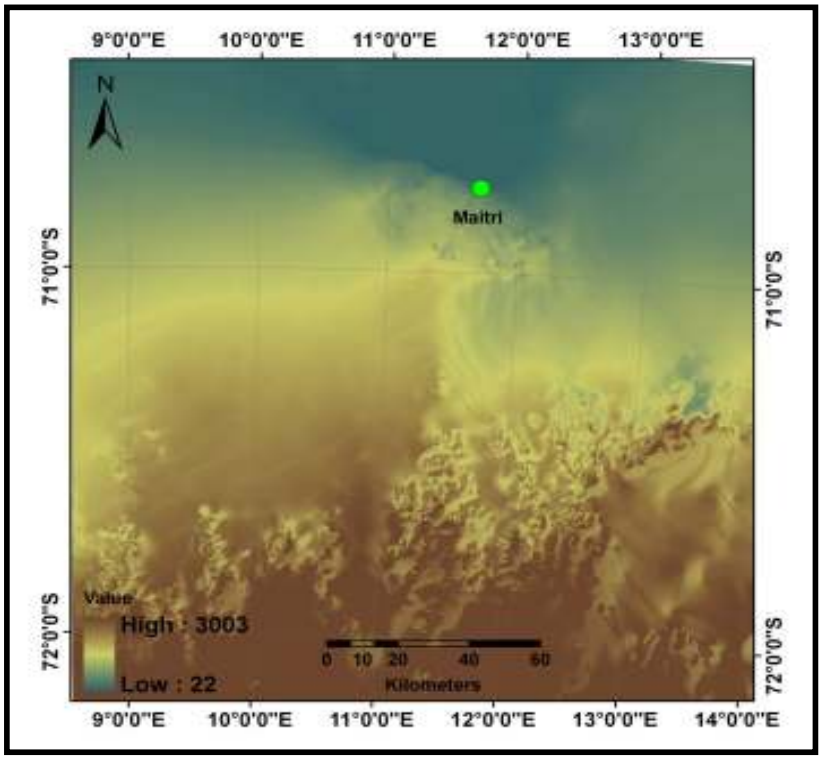

Figure 3.6: Digital Elevation Model of Study Area-1

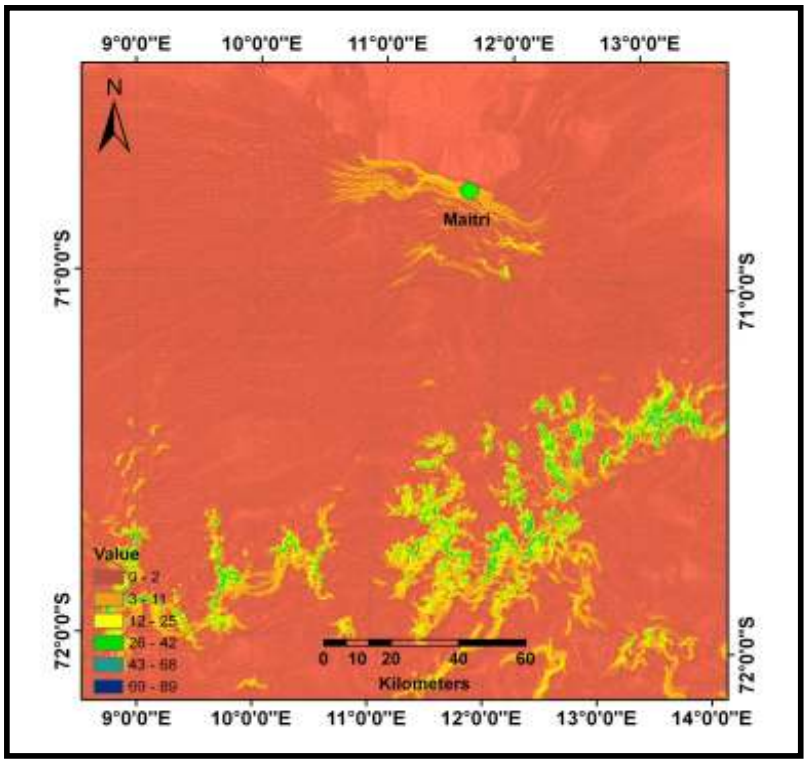

Figure 3.7: Slope map of Study Area-1

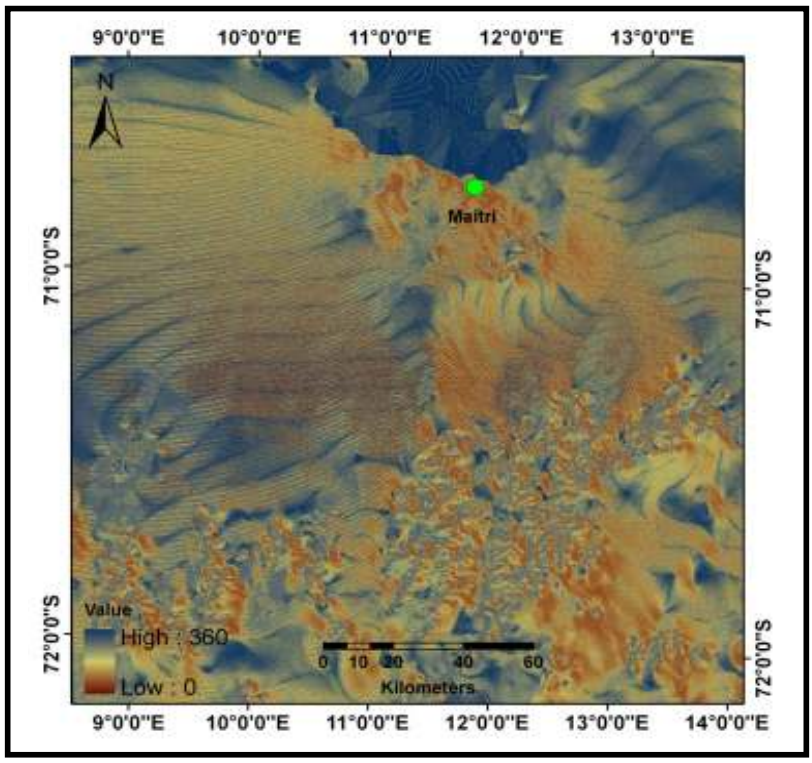

Figure 3.8: Aspect map of Study Area-1

3.3.1.2.2: MODIS Data

Images from Moderate Resolution Imaging Spectroradiometer (MODIS) sensor on-board Terra and Aqua satellite downloaded from http://ladsweb.nascom.nasa.gov have been used for estimation of albedo, surface temperature, net shortwave radiation flux, and net longwave radiation flux. MODIS images of clear sky days have been acquired for estimation of surface energy fluxes. MODIS is a key instrument aboard the Terra (EOS AM) and Aqua (EOS PM) satellites (Barnes *et al.* 1998). Terra and Aqua have a sun-synchronous, near polar, circular orbit. Aqua crosses the equator daily at 0800 UTC (1:30 p.m. IST) as it heads north (ascending mode) and Terra crosses the equator daily at 0530 UTC (11:00 a.m. IST) as it heads south (descending mode). Salient specifications of MODIS sensor (Salomonson *et al.* 1989) images are given in Table 3.3, which also includes characteristics of short wavelength and thermal bands. Dates of acquisition of MODIS images of Antarctica for the present thesis work are given in Table 3.4 and these

dates have been selected based on clear sky conditions in the study area. MODIS bands 1 to 7 have been used for estimation of albedo, as described subsequently in section 5.3 of chapter 5. MODIS bands 31 - 32 have been used for estimation of surface temperature (refer section 5.4 of chapter 5). Estimation of surface energy fluxes using MODIS images has been discussed in chapter 6.

Table 3.3: Salient Specifications of MODIS Sensor

MODIS Sensor				
Total number of bands			36	
Wavelength Range			0.4 μm – 14.4 μm	
Swath			2330 km	
Radiometric Resolution			12 bit	
Repeat Cycle			1-2 Days	
Orbit Elevation			705 km	
Band	**Spatial Resolution (m)**	**Spectral Resolution (μm)**	**Radiance_Scale ($mW/cm^2/sr/\mu m$)**	**Solar Exoatmospheric Spectral Irradiance ($mW/cm^2/\mu m$)**
Band 1	250 x 250	0.620 – 0.670	0.0026144000	160.327
Band 2	250 x 250	0.841 – 0.876	0.0009926000	98.700
Band 3	500 x 500	0.459 – 0.479	0.0027612000	209.071
Band 4	500 x 500	0.545 – 0.565	0.0021087000	186.400
Band 5	500 x 500	1.230 – 1.250	0.0005568000	47.600
Band 6	500 x 500	1.628 – 1.652	0.0002572000	23.800
Band 7	500 x 500	2.105 – 2.155	0.0000787000	8.700
Band 31	1000 x 1000	10.780 – 11.280	0.0000840022	-
Band 32	1000 x 1000	11.770 – 12.270	0.0000729698	-

Table 3.4: Dates of acquisition of MODIS images (Study Area-1)

S.No.	MODIS Images	S. No.	MODIS Images
1	02 October 2007	14	07 October 2008
2	11 October 2007	15	11 November 2008
3	20 October 2007	16	20 November 2008
4	27 October 2007	17	24 November 2008
5	01 January 2008	18	13 February 2009
6	03 January 2008	19	19 February 2009
7	05 January 2008	20	05 March 2009
8	07 January 2008	21	19 March 2009
9	02 February 2008	22	24 January 2010
10	13 February 2008	23	25 January 2010
11	17 February 2008	24	28 January 2010
12	21 February 2008	25	21 February 2010
13	02 October 2008		

3.3.2 Study Area 2: Data Sources

3.3.2.1: *In Situ* data

3.3.2.1.1: AWS Data

Data collected from twenty AWSs of similar specifications as given in Table 3.1 have been used in the present study. These AWSs have been installed at different elevations in different mountain ranges of Western Himalaya, as shown in Figure 3.9, and referred in Table 3.5. Air temperature and relative humidity data collected by AWS have been used for estimation of incoming shortwave radiation flux and incoming longwave radiation flux. Snow depth data collected by AWS has been used to validate the spatial interpolation algorithm for snow depth (refer section 5.2 of chapter 5). Albedo data has been used in validation of narrow band to broad band albedo algorithm of snow (refer section 5.3 of chapter 5). Incoming shortwave radiation flux, net shortwave radiation flux and net radiation flux data collected by AWS have been used in validation of spatially estimated incoming shrtwave radiation flux, net shortwave radiation flux and net radiation flux using

MODIS sensor images. The details of estimation of these energy fluxes and validation are provided in chapter 6.

3.3.2.1.2: Measurement of Snow Depth

Snow depth data recorded manually at 14 manned observation stations have been used for development of snow depth algorithm. Daily snow depth data has been recorded at manned observation stations of SASE using snow pole of height 5 m erected on a flat surface. The spatial locations of these 14 manned observation stations are shown in Figure 3.10 and given in Table 3.6.

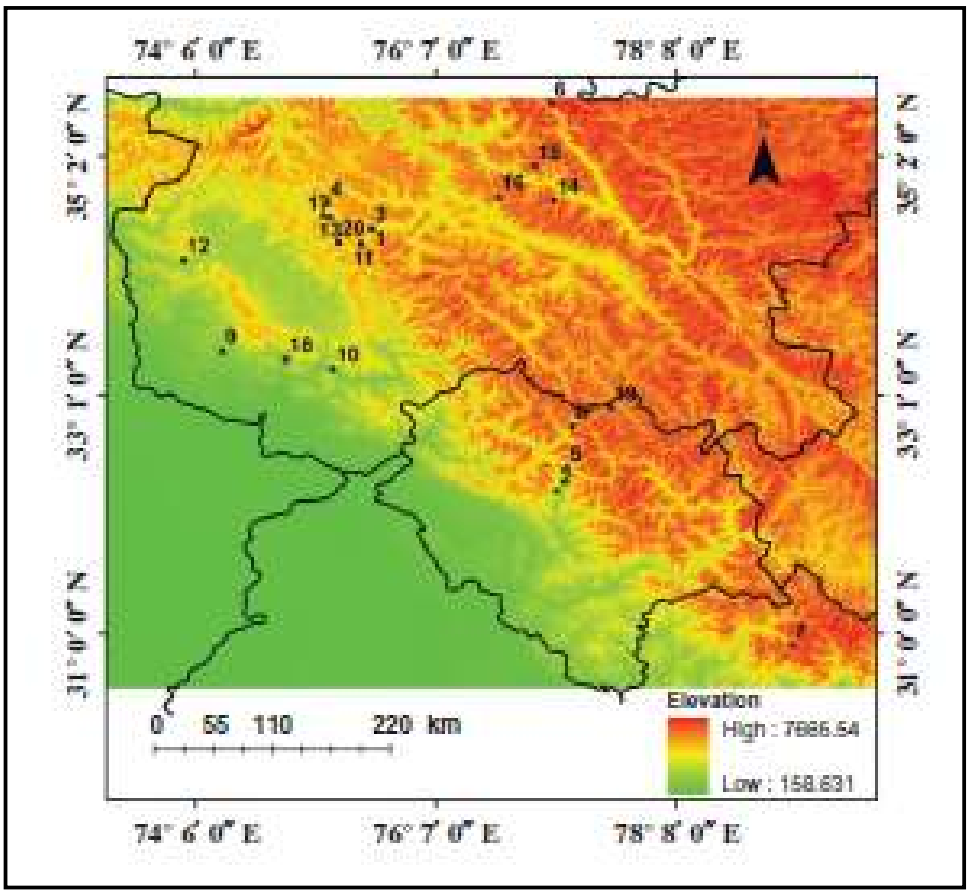

Figure 3.9: AWS locations in Western Himalaya

Table 3.5: AWS locations (Study Area-2) in Western Himalaya

AWS Number	Elevation (m)	Himalayan Range
1	3250	Great Himalayan range
2	4394	Pir Panjal Range
3	3092	Great Himalayan Range
4	2453	Great Himalayan Range
5	3093	Great Himalayan Range
6	4900	Karakoram Range
7	4461	Great Himalayan Range
8	3769	Great Himalayan Range
9	1143	Pir Panjal Range
10	780	Pir Panjal Range
11	3598	Great Himalayan Range
12	2951	Pir Panjal Range
13	2832	Great Himalayan Range
14	3108	Ladakh Range
15	4578	Karakoram Range
16	4014	Ladakh Range
17	3230	Great Himalayan Range
18	1602	Pir Panjal Range
19	4306	Great Himalayan Range
20	2745	Great Himalayan Range

Table 3.6: Manned observation locations (Study Area-2)

Number	Manned Observation Site	Elevation (m)	Himalayan Range
1	Banihal	3250	Pir Panjal
2	Srinagar	1664	Kashmir Valley

3	Gulmarg	2800	Pir Panjal
4	HaddanTaj	3080	Shamshabari
5	Stage-2	2650	Shamshabari
6	Ragini	3160	Shamshabari
7	Pharkian	2960	Shamshabari
8	Z-Gali	3192	Great Himalaya
9	Kanzalwan	2440	Great Himalaya
10	Dawar	2414	Great Himalaya
11	Sonamarg	2745	Great Himalaya
12	Drass	3250	Great Himalaya
13	Pathar	4250	Great Himalaya
14	Firmbase	4760	Great Himalaya

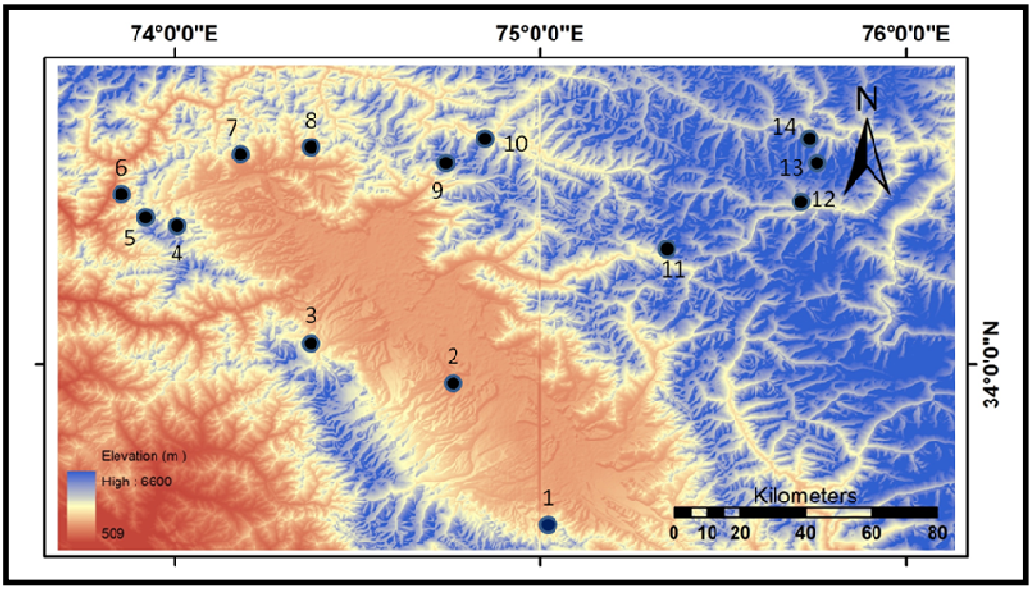

Figure 3.10 : Spatial locations of 14 manned observation stations

3.3.2.1.3: Spectroradiometer Data

The spectroradiometer data has been obtained from the existing spectral library of SASE. *In situ* measured data of spectral reflectance of snow and transmitted solar irradiance in the wavelength range from 350 to 2500 nm at the time of satellite passes are usually collected by various field scientists of SASE to create spectral library. The spectral data for winter season pertaining to Solang and Dhundi observatories in Pir Panjal range of HP Himalaya for the years 2005 to 2010 have been used here. Field Spec Pro ASD spectroradiometer, shown in Figure 3.11 was used to collect the spectral data of snow at 25^{o} field of view (FOV) under clear sky conditions on nearly flat surface. Simultaneously, solar transmitted spectral irradiances were also measured using a full sky remote cosine receptor having a 180^{o} FOV. These *in situ* measurements have been used for the development of narrowband to broadband albedo (NBBA) algorithm for AWiFS and MODIS data and its validation at Solang and Dhundi sites.

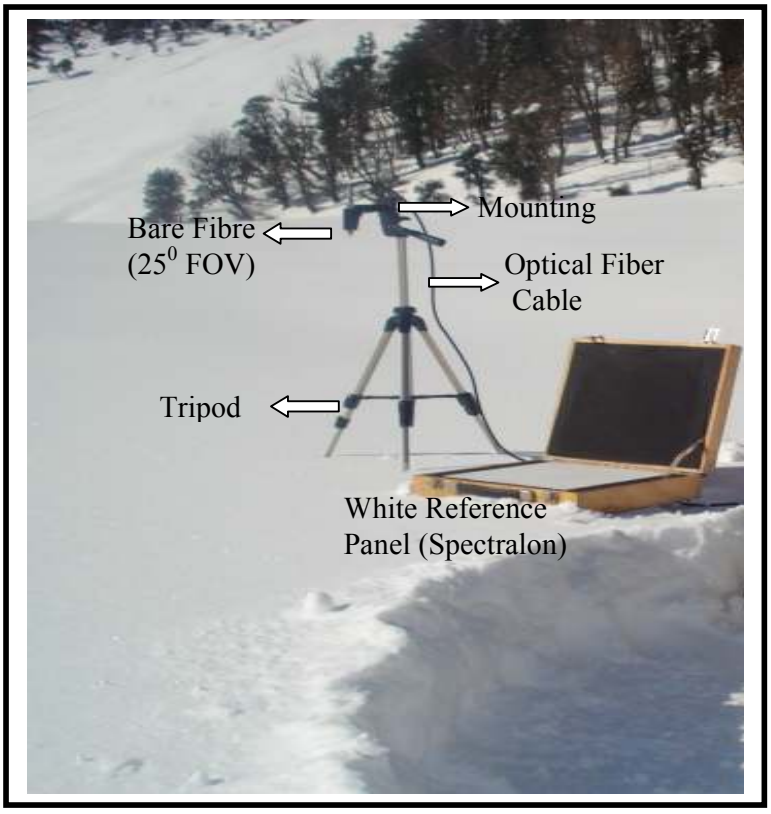

Figure 3.11: ASD Spectroradiometer

3.3.2.2: Geospatial data

3.3.2.2.1: DEM

SRTM DEM (freely available on internet and downloaded from http://srtm.csi.cgiar.org/) of Indian Western Himalaya has been used to generate slope, aspect and elevation maps of the study area. These maps have been used as input for estimation of solar zenith angle, snow depth and incoming shortwave radiation flux. Spatial estimation of snow depth has been discussed in section 5.2 of chapter 5 while spatial estimation of solar zenith angle and incoming shortwave radiation flux have been discussed in chapter 6 of this thesis. A variation in elevation from 158 m to 7665 m (Figure 3.9) has been observed in the study area of Western Himalaya. Figure 3.12 and 3.13 show slope and aspect maps of the study area retrieved from DEM. The slope angle in the region varies from 0° to 89° whereas aspect varies from 0° to 359°.

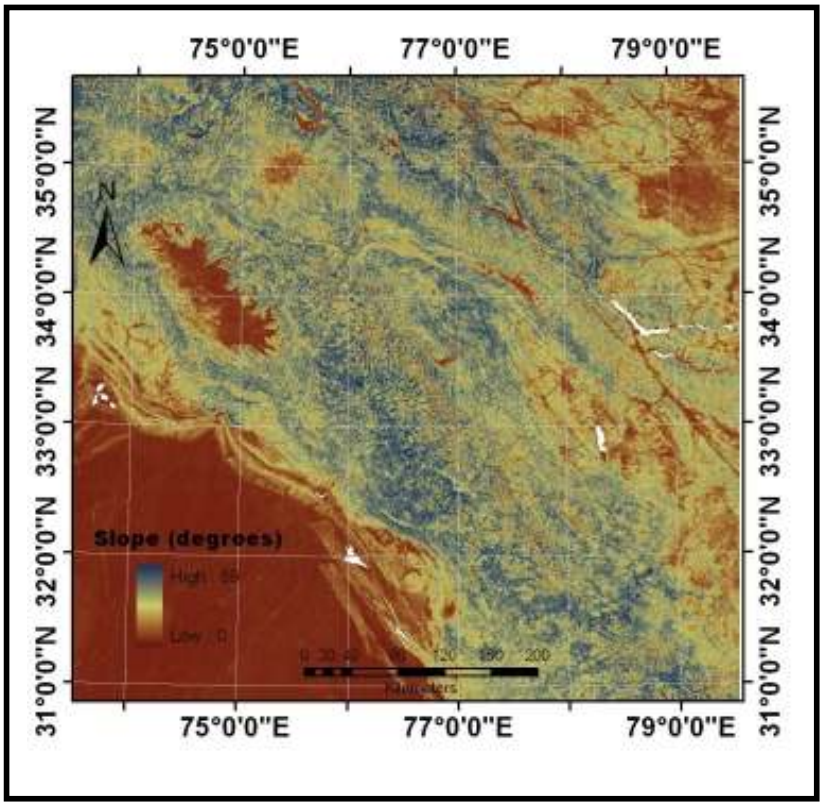

Figure 3.12: Variation in slope in Western Himalaya

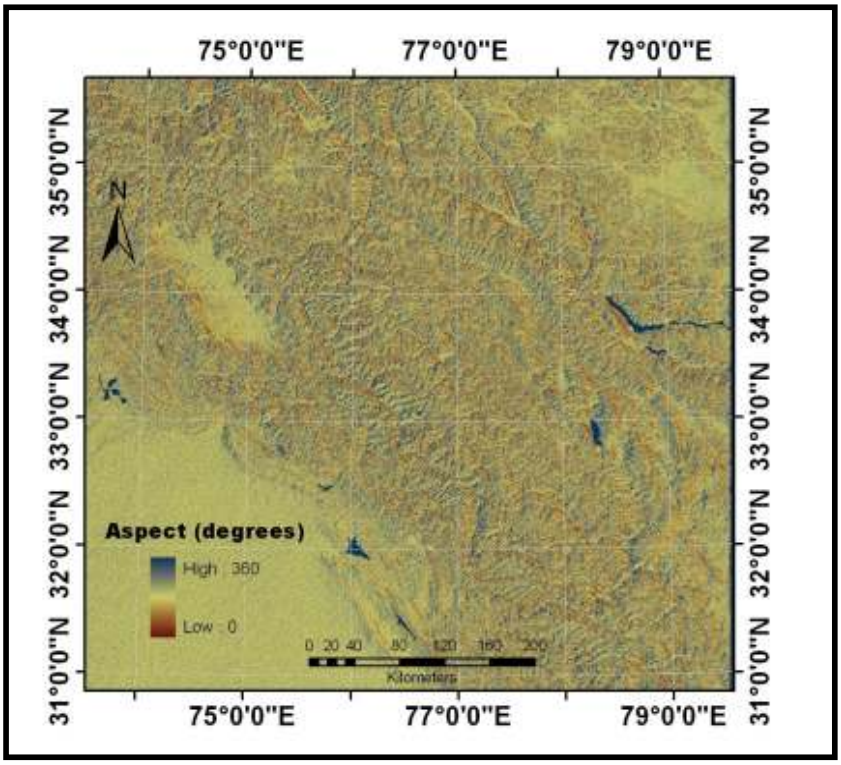

Figure 3.13: Variation in aspect in Western Himalaya

3.3.2.2.2: AWiFS Data

AWiFS images on-board RESOURCESAT-1 (also known as IRS P-6) satellite have been procured from National Remote Sensing Centre (NRSC), Hyderabad, India. The RESOURCESAT-1 satellite was launched in October 2003, by the Indian Space Research Organisatio (ISRO) and carried three sensors. AWiFS is one of those sensors. The salient specifications of AWiFS sensor are given in the Table 3.7. Twelve AWiFS images (Table 3.8) of different dates during clear sky have been used for narrow band to broad band albedo algorithm development (refer section 5.3 of chapter 5). These dates have been selected based on clear sky images. Further, the field spectroradiaometer data at these dates are also available.

Table 3.7 : Salient specifications of AWiFS sensor

AWiFS Sensor				
Total number of bands			4	
Wavelength Range			0.52 μm – 1.7 μm	
Swath			740 km	
Radiometric Resolution			10 bit	
Repeat Cycle			5 Days	
Orbit Elevation			817 km	
Band	**Spatial Resolution (m)**	**Spectral Resolution (μm)**	**Maximum Radiance ($mW/cm^2/sr/\mu m$)**	**Solar Exoatmospheric Spectral Irradiance ($mW/cm^2/\mu m$)**
Band 2	56 x 56	0.52 – 0.59	52.340	185.3281
Band 3	56 x 56	0.62 – 0.68	40.750	158.0420
Band 4	56 x 56	0.77 – 0.86	28.425	108.3570
Band 5	56 x 56	1.55 – 1.70	4.645	23.7860

3.3.2.2.3: MODIS Data

SASE is having Earth Receiving Station (ERS) of MODIS and its daily Terra and Aqua images have been received at SASE Chandigarh. MODIS images of Western Himalaya for the study has been collected from SASE data bank. These images have been used for dveleopment of NBBA algorithm and estimation of surface energy fluxes. Development of NBBA algorithm has been discussed in section 5.3 of chapter 5 and spatial estimation of surface energy fluxes have been discussed in chapter 6. Salient specification of MODIS sensor are given in Table 3.3. Dates of acquiring MODIS images of Western Himalaya used in the study are given in Table 3.8. The images have been acquired for clear sky days.

Table 3.8: Dates of acquisition of MODIS and AWiFS images (Study Area-2)

S.No.	AWiFS Images	MODIS Images
1	19 January 2005	10 November 2008
2	21 February 2005	26 December 2008
3	26 February 2005	31 December 2008
4	13 March 2005	20 January 2009
5	7 March 2007	28 January 2009
6	8 January 2009	30 January 2009
7	24 December 2008	26 February 2009
8	31 January 2009	16 March 2009
9	15 February 2009	13 April 2009
10	25 February 2009	17 April 2009
11	11 March 2009	22 April 2009
12	16March 2009	

3.3.3 Pre-processing of Remote Sensing Data

3.3.3.1 Geo-referencing of Images

Geo-referencing is the name given to the process of assigning geographic or map coordinates to features on a map or an image. Typically, for a first order polynomial transformation using least squares, a minimum of three ground control points (GCP) are required. Additional GCPs may be collected from features such as intersections of valleys, sharp river bends, road intersections, lake features that are easily identifiable in the images. Available geocoded IRS-LISS-III (Indian Remote Sensing, Linear Imaging Self Scanning-III) image has been used as the master image for geo-referencing of AWiFS images in ERDAS Imagine 9.3 software. The MODIS images were then georeferenced from AWiFS images. The geo-referencing of images has been performed using second order polynomial transformation (Mishra *et al.* 2012) at root mean square error between 0.1 to 0.7 of a pixel, using 18-20 ground control points (GCPs). Figure 3.14 shows the geo-referencing of MODIS image with AWiFS image. In this figure, the spatial distribution of GCPs used can also be seen. Nearest neighbor method was used for

resampling of pixels. Images were geo-referenced in Geographic (Lat/Lon) projection with WGS 84 Spheroid and Datum.

3.3.3.2 Conversion of Digital Numbers to Reflectance

Satellite sensors receive reflected signals from various target on Earth's surface in the form of Digital Numbers (DN) (Bowyer *et al.* 2003). First, the digital numbers of pixels in AWiFS images have been converted to spectral radiance, $L_{sat\lambda}$ ($mWcm^{-2}Sr^{-1}\mu m^{-1}$) using the following relationship (Markham and Barker 1986, Negi *et al.* 2009),

$$L_{sat\lambda}(AWiFS) = \frac{L_{max\lambda} - L_{min\lambda}}{DN_{max\lambda}} DN_{sat\lambda} + L_{min} \quad (3.1)$$

where, $DN_{max\lambda}$ and $DN_{sat\lambda}$ are maximum and at-satellite DN values respectively in different AWiFS spectral bands. $L_{max\lambda}$ and $L_{min\lambda}$ are the maximum and minimum values of spectral radiance in different bands, as obtained from sensor's header information (Table 3.6). For, AWiFS, $L_{min\lambda}$ = 0 and $DN_{max\lambda}$= 1023.

At satellite spectral radiance, $L_{sat\lambda}$, for each pixel of MODIS images in different bands are calculated using equation (3.2) given as (Qu *et al.* 2006),

$$L_{sat\lambda}(MODIS) = radiance\_scales_{\lambda} \times (DN - radiance\_offset_{\lambda}) \quad (3.2)$$

Where, $radiance\_scales_{\lambda}$ and $radiance\_offset_{\lambda}$ are the scale and offset parameters respectively for MODIS sepectral bands, $radiance\_scales_{\lambda}$ for MODIS bands are given in Table 3.3. $radiance\_offset_{\lambda}$ for bands 1-7 of MODIS are zero and for bands 31 and 32 are 1577.34 and 1658.22 respectively. The estimated value of radiance at each pixel has been corrected using combination of dark object subtraction (DOS1 and DOS3) model (Song *et al.* 2001) for atmospheric correction. It is a simple and efficient model for operational use in the absence of *in situ* data of various atmospheric parameters such as aerosol, water vapor content etc., at the time of image acquisition (Kim and Lee 2005, Mishra *et al.* 2009).

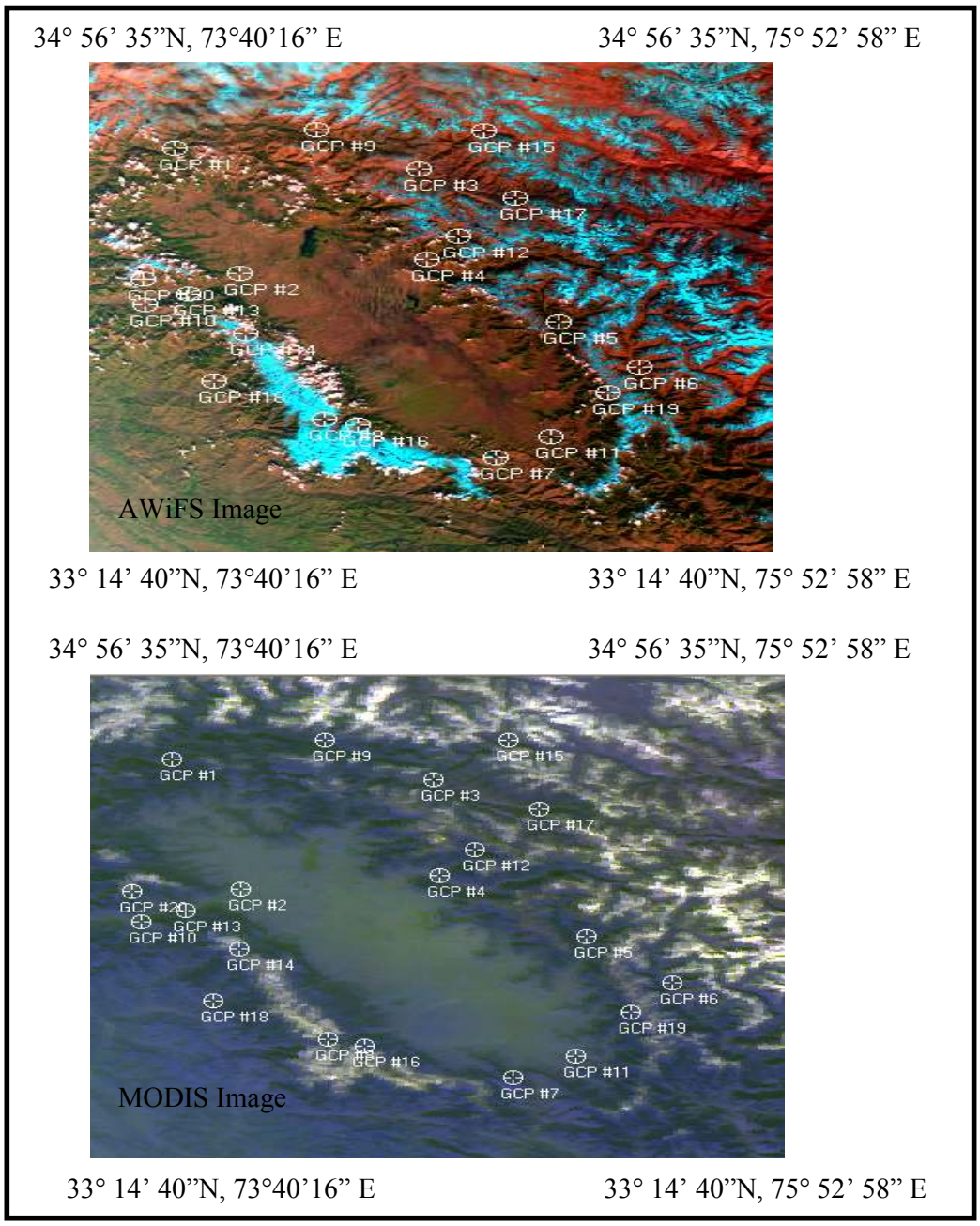

Figure 3.14 : Geo-referencing of MODIS image with AWiFS image

The DOS1 model assumes no atmospheric transmittance loss and no diffused downward radiation at the surface (Chavez 1989). DOS3 computes upwelling and downwelling radiation transmittances of the atmosphere to correct the image for path

radiance resulting from the interaction of the electromagnetic radiation with molecules and aerosols. It assumes Rayleigh scattering only. The optical thickness for Rayleigh scattering has been obtained from the equation proposed by Russell *et al.* (1993). The value of transmittance using Rayleigh scattering has been estimated for AWiFS and MODIS spectral bands and are given in Table 3.9. The dark objects (e.g. shadow, deep clean water) are not absolutely dark (Chavez 1988) due to atmospheric scattering effects. Assuming 1% surface reflectance for the dark objects, the path radiance has been estimated using the model proposed by Chavez (1989, 1996) and Moran *et al.* (1992). In this model, the path radiance depends on sensors gain and bias, DN values, atmospheric transmittances in the viewing and illumination directions, exo-atmospheric solar irradiance and solar zenith angle.

Table 3.9. Upwelling and downwelling Transmissivity due to rayleigh scattering for AWiFS and MODIS spectral bands.

Transmissivity	**Band1**	**Band2**	**Band3**	**Band4**	**Band5**	**Band6**	**Band7**
AWiFS-'t_v'	-	0.935	0.965	0.986	0.999	-	-
AWiFS-'t_z'	-	0.911	0.952	0.980	0.998	-	-
MODIS-'t_v'	0.965	0.989	0.877	0.936	0.997	0.999	1.0
MODIS-'t_z'	0.941	0.981	0.801	0.895	0.996	0.999	1.0

The spectral reflectance corrected for path radiance, under lambertian assumption, of each pixel in AWiFS and MODIS images is then computed using the following equation (3.3) (Song *et al.* 2001, Pandya *et al.* 2002),

$$R_\lambda = \frac{\pi\left(L_{sat\lambda} - L_p\right) d^2}{t_v \left(E_0 \cos\theta t_z + E_d\right)} \qquad (3.3)$$

where, t_v and t_z are atmospheric transmittance along the path from the ground surface to sensor and from sun to ground respectively. t_v and t_z have been estimated by the method proposed by Russell (1993) and Song *et al.*(2001) (Table 3.9). E_0 is the exo-atmospheric spectral irradiances and are given in Tables 3.3 and 3.7. θ is the solar zenith angle at

each pixel and has been estimated using method given by Kasten (1962). d is the earth – sun distance in astronomical units and obtained from the approach given by Van Der Meer (1996). E_d is the downwelling diffused radiation and has been assumed as zero according to Chavez (1996). L_p is the path radiance and has been obtained from the approach given by Chavez (1989, 1996).

3.3.3.3 Topographic Corrections

A number of image based topographic correction methods (e.g. Cosine correction, C-correction, Minneart correction, statistical etc.) have been proposed by Civco (1989), and Colby (1991). An extensive study on the feasibility of different topographic correction methods for the Himalayan region has been reported by Mishra *et al.* (2009, 2010) who have recommended slope matching method more appropriate for the mountainous region. Slope matching method, as represented by equation (3.4) has been used for topographic correction in the present study.

$$R_\lambda^t = R_\lambda + (R_{\lambda max} - R_{\lambda min}) \left(\frac{\langle cosi \rangle s \quad cosi}{\langle cosi \rangle s} \right) C_\lambda \qquad (3.4)$$

where, R_λ^t is topographically corrected spectral reflectance, R_λ is obtained from equation (3.3), $R_{\lambda max}$ and $R_{\lambda min}$ are the maximum and minimum spectral reflectance values as obtained from R_λ image, $\langle cosi \rangle s$ is average value of illumination on south aspect, $cosi$ is illumination obtained from the equation proposed by Civco (1989) (equation 3.5). C_λ is the normalization coefficient for different bands and is estimated using equation proposed by Nichol *et al.* (2006) (equation 3.6). Value of cos*i* has been estimated as,

$$\cos i = \cos \Phi \cos\theta + \sin \Phi \sin\theta \cos(\alpha_s - \alpha_a) \qquad (3.5)$$

where, *i* is the local incidence angle and can be defined as the angle between the direct solar rays and normal to the surface, Φ is slope of the surface, θ is solar zenith angle, α_s and α_a are aspect of the surface and solar azimuth angle respectively. Value of C_λ has been estimated as,

$$C_\lambda = \frac{S_\lambda' - N_\lambda}{N_\lambda' - N_\lambda} \quad (3.6)$$

where S_λ' is mean reflectance value on sunlit slopes after first stage normalization, N_λ is mean reflectance value on shady slopes in uncorrected image, N_λ' is mean reflectance value on shady slope after first stage normalization. The first stage of the two stage normalization by slope matching technique is given as,

$$R_{n\lambda ij} = R_{\lambda ij} + (R_{max} - R_{min}) \times \left(\frac{\langle \cos i \rangle_s - \cos_{ij} i}{\langle \cos i \rangle_s}\right) \quad (3.7)$$

where, $R_{n\lambda ij}$ is the normalized reflectance values for image pixel ij in wave band λ, $R_{\lambda ij}$ is the uncorrected original reflectance on the tilted surface for image pixel ij in wave band λ, $\langle \cos i \rangle_s$ is the mean value of illumination on south aspect and $\cos_{ij} i$ is illumination for each pixel ij of the study area.

3.3.3.4 Derivation of Normalised Difference Snow Index (*NDSI*) Image

The MODIS images have been used to derive *NDSI* images for the study area to descriminate between snow/ice and other land covers in the region. The *NDSI* image has been derived from the spectral reflectance of the pixels using the following formulation (Hall *et al.* 1995),

$$NDSI = \frac{Green - SWIR}{Green + SWIR} \quad (3.8)$$

where, *Green* denotes the spectral reflectance of pixels in the green band and *SWIR* denotes the spectral reflectance of pixels in the shortwave infrared band. Figure 3.15 shows the *NDSI* image in the study area. This image has been used to generate the binary image of snow covered and non-snow covered area.

3.3.3.5 Retrieval of Binary Snow Cover Image

Binary snow cover maps of the study area has been generated using *NDSI* image. Several studies have been conducted to map snow cover based on *NDSI* values (Arora *et al.* 2011) and majority of the researchers (e.g., Hall *et al.* 2002, Kulkarni *et al.* 2006, Negi *et al.* 2009, Mishra *et al.* 2009 etc.) have used criterion $NDSI \geq 0.40$ for discrimination of snow from other land covers. In this study also, $NDSI \geq 0.40$ has been used to map snowcover. Water body pixels merging with snow have been masked using reflectance in NIR band by setting a threshold of NIR>11% for discrimination between snow and water bodies, as used in many studies (e.g., Hall *et al.* 2002, Negi *et al.* 2009, Sharma *et al.* 2012 etc.). Figure 3.16 shows the binary snow cover map of Western Himalaya on 26-December-2008. It can be seen that there is a large variation in snowcover as the topography changes. In Pir Panjal and Shamshabari ranges of Lower Himalayan region, snowcover exists above 2000 m elevation from mean sea level while in Karakoram range of Upper Himalayan region, valleys are snow free even at an elevation of 4100 m m.s.l..

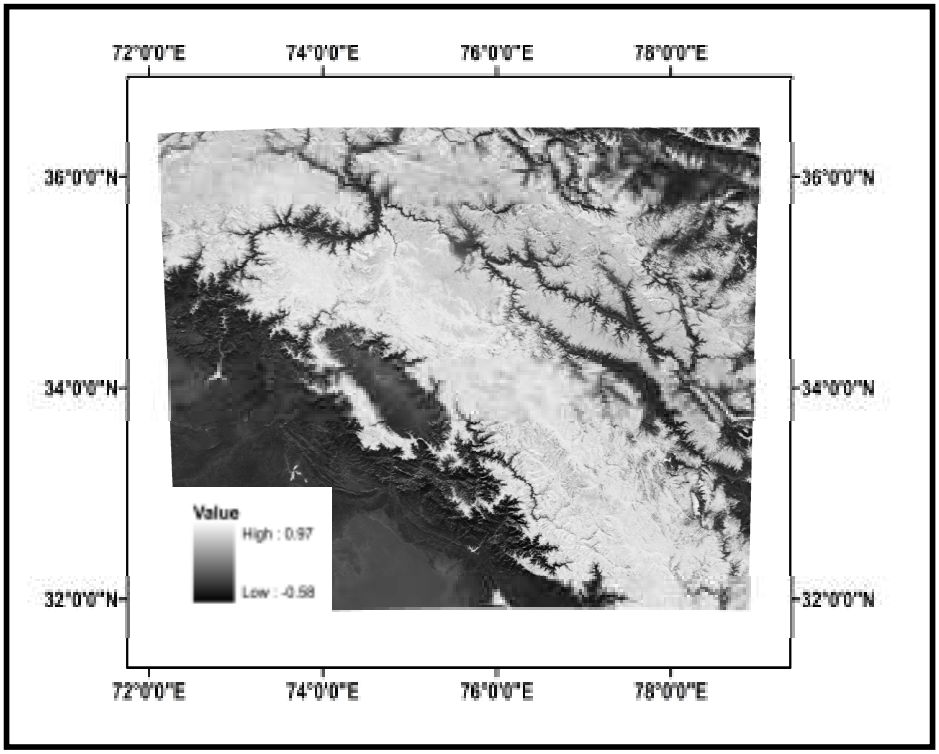

Figure 3.15: NDSI image of the Study Area-2 for 26 December 2008.

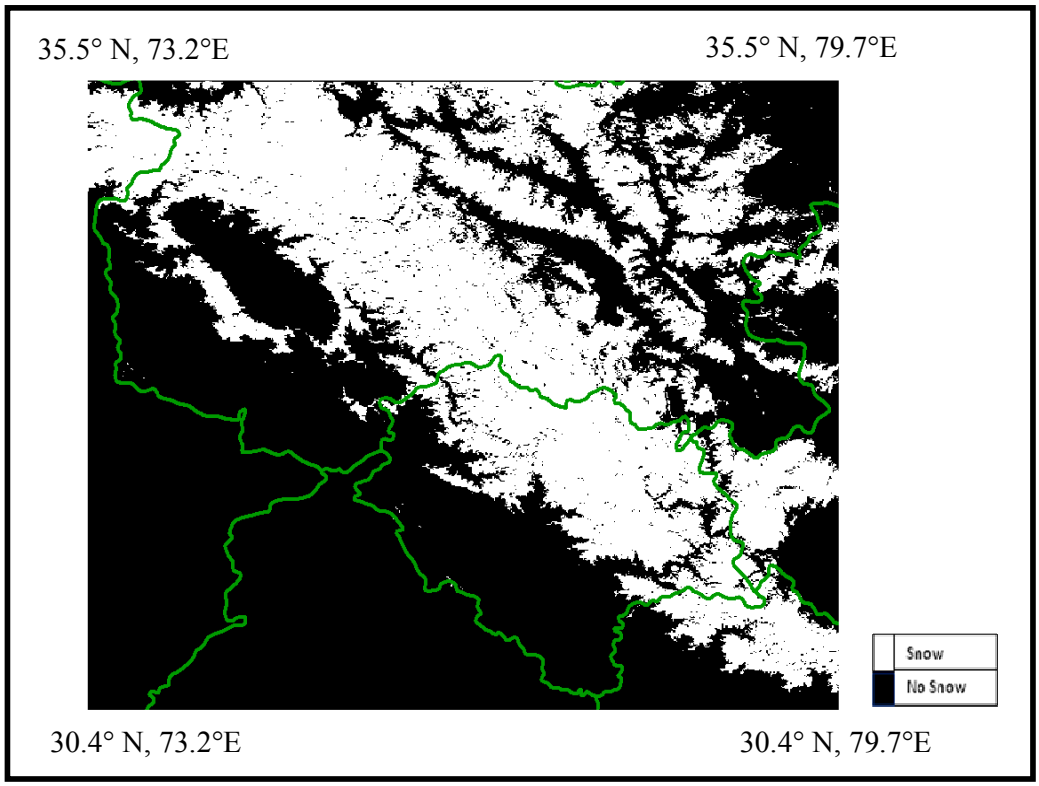

Figure 3.16 : Binary snow cover map of the Study Area-2 for 26 December 2008

The binary snowcover map will be used in extraction of snowline image and masking of snow/non-snow area in surface energy flux maps of the study area.

3.3.3.6 Retrieval of Brightness Temperature from MODIS Thermal Bands

MODIS Thermal bands 31 (10.780 µm - 11.280 µm) and 32 (11.770 µm - 12.270 µm) have been used to estimate brightness temperature in the study area. According to the black body radiation principle, the spectral radiance emitted from surface as a black body can be described by Planck's spectral radiation equation (Ulaby *et al.* 1990), given as,

$$L_\lambda (T) = 2\, h\, c^2\, \lambda^{-5}\, (e^{\,hc/\lambda kT} - 1)^{-1} \qquad (3.9)$$

where, L_λ is spectral radiance of black body, h is Planck's constant (6.626×10^{-34} J s), c is velocity of light (3×10^8 m s^{-1}), λ is wavelength, k is Boltzmann's constant (1.381×10^{-23} J K^{-1}) and T is Brightness Temperature.

Using equation (3.9), the brightness temperature can be estimated as (Qin and Karnieli, 1999),

$$T = hc\lambda^{-1}k^{-1}\,[\log(1+2\,h\,c^{2}\,\lambda^{-5}\,L_{\lambda}^{-1})]^{-1} \qquad (3.10)$$

In equation (3.10), mean wavelength 11.03 μm and 12.02 μm for the MODIS bands 31 and 32 have been used respectively for the estimation of brightness temperature.

Spectral radiance (L_{λ}) values for MODIS bands 31 and 32 have been estimated using equation (3.2) given by Qu *et al.* (2006). Figure 3.17 shows the estimated brightness temperature from MODIS band 31 for the study area of Indian Western Himalaya. It can be seen from this figure that the brightness temperature varies from 248 K to 305 K. Brightness temperature above 290 K generally exists in low altitude snow free areas. Brightness temperature images of band 31 and band 32 of MODIS sensor have been used to estimate surface temperature map in the study area of Western Himalayas and Antarctica.

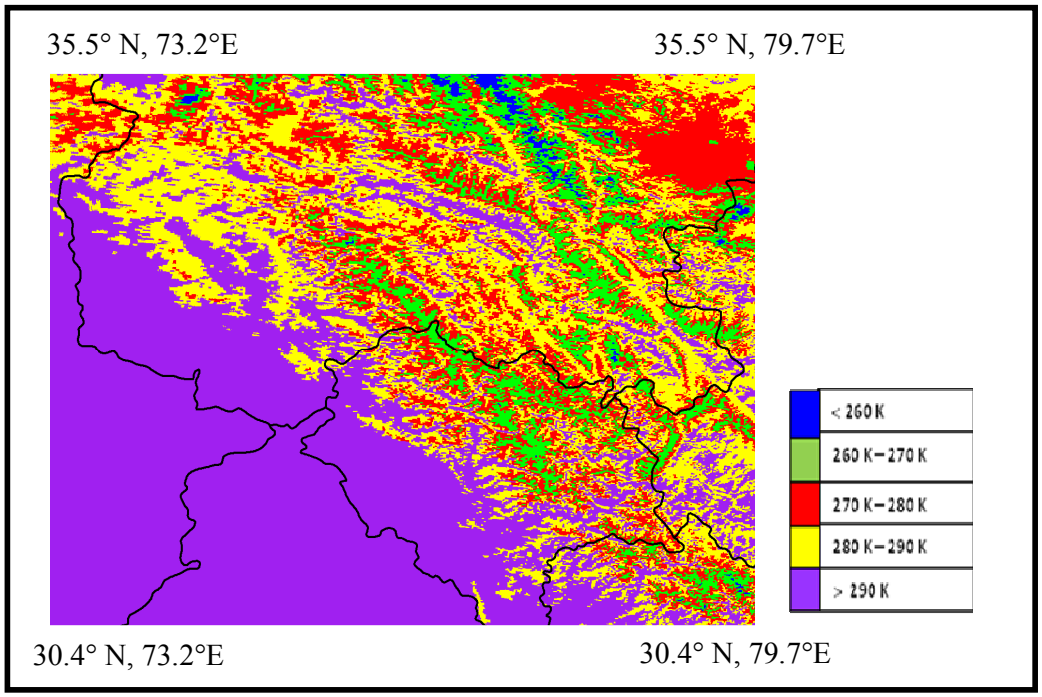

Figure 3.17 : Brightness temperature image retrieved from MODIS band 31

3.4 Summary

In this chapter, the details of the study area, data and data base generation has been provided. Physiography, topography and climate of the two study areas, namely, Antarctica and Indian Western Himalaya have been discussed. Details on *in situ* data using automatic weather station, spectroradiometer and manual observation have been provided. A description of geo-spatial data alongwith their technical specifications have also been given. Pre-processing of satellite data e.g. geo-referencing of images, atmospheric corrections, topographic corrections has been explained. Retrieval of NDSI image, binary snow cover map and brightness temperature image have been presented.

In this thesis *in situ* data in conjunction with geo-spatial data presented in the chapter will be used in estimation of surface energy fluxes at spatial scale. Surface energy fluxes have also been estimated using only *in situ* data. The next chapter presents the details on the estimation of surface energy fluxes using *in situ* data in Antarctica.

Chapter IV

ESTIMATION OF SURFACE ENERGY FLUXES USING *IN SITU* MEASUREMENTS IN ANTARCTICA

4.1 Introduction

The estimation of surface energy fluxes of snow/ice media using *in situ* measured snow meteorological parameters may be regarded as well established, as can be seen from the review of literature on estimation of surface energy fluxes of snow cover, glaciers, ice sheet, shelf ice, lake ice etc. in chapter 2. It has been observed that surface energy fluxes depend on the location, surface characteristics of the snow/ice media and prevailing local weather conditions. In Antarctica, these energy fluxes vary from coastal Antarctic region to high Antarctic Plateau. However, little is known about the temporal variation of energy fluxes at the edge of the ice sheet in proximity of oases (ice free areas). In this chapter, surface energy fluxes have been estimated at the edge of the Antarctic ice sheet close to Schirmacher oasis using AWS data. Temporal and diurnal variation of snow-met parameters and energy fluxes have been presented during different seasons.

4.2 Estimation of Surface Energy Fluxes

Surface energy fluxes at the edge of the Antarctic ice sheet close to Schirmacher Oasis have been estimated using AWS1 data, as discussed in chapter 3. Air temperature, surface

temperature, relative humidity, wind speed, incoming shortwave radiation, outgoing shortwave radiation, atmospheric pressure, cloud amount, cloud type data of four years from March 2007 to February 2011 have been used to estimate energy fluxes. The energy fluxes have been analysed for summer season (November, December, January, February), winter season (May, June, July, August), transition period from summer to winter (March, April; here after referred as transition1) and transition period from winter to summer (September, October; here after referred as transition2).

4.2.1 Methodology

The three principal fluxes of energy at the Earth's surface are the radiative energy fluxes, turbulent energy fluxes and subsurface heat flux. The net energy exchange between the earth and the atmosphere is the residual of these energy fluxes (King and Turner 1997). Net change in energy storage of a glacier or ice sheet ΔQ is expressed as,

$$\Delta Q = SHW\downarrow - SHW\uparrow + LW\downarrow - LW\uparrow + SHF + LHF + G \quad (4.1)$$

Equation (4.1) can be reframed as,

$$\Delta Q = SHW_{net} + LW_{net} + SHF + LHF + G \quad (4.2)$$

$$\Delta Q = R_{net} + SHF + LHF + G \quad (4.3)$$

where,

$SHW\downarrow$ - Incoming shortwave radiation flux

$SHW\uparrow$ - Outgoing shortwave radiation flux

SHW_{net} - Net shortwave radiation flux

$LW\downarrow$ - Incoming longwave radiation flux

$LW\uparrow$ - Outgoing longwave radiation flux

LW_{net} - Net longwave radiation flux

R_{net} - Net radiation flux

SHF - Sensible heat flux

LHF - Latent heat flux

G - Sub surface heat flux

All the above terms are estimated at the surface and are defined positive when directed towards the surface.

4.2.1.1 Shortwave Radiation Flux

Shortwave or solar radiation drives the general circulation of the atmosphere and the weather systems that are observed on a day-to-day basis. Most of this energy is absorbed in the tropics and mid-latitude areas, with the polar regions receiving much less as a result of the low sun angle at these latitudes. The high albedo (reflectivity) of the snow and ice surface also results in much of the incoming solar radiation being returned to space so that the fraction absorbed is much less than that absorbed in the extra polar regions. Even after higher surface reflectivity, radiation is extremely important in determining the surface energy budget of the Antarctica, as it affects many aspects of the Antarctic climate.

Incoming or global solar radiation ($SHW\downarrow$) consists of two components: a direct element which arrives from the solid angle subtended by the sun's disk and a diffuse component, which arrives from the remainder of the sky. The outgoing solar radiation ($SHW\uparrow$) is the upward shortwave radiation that has been reflected by the surface and diffused by atmospheric particles in the layer between the surface and the observation point. When the outgoing solar radiation measured close to the surface, the diffused part is very small. The ratio of the reflected short wave radiation to the global solar radiation is called the albedo (α) of the surface. The albedo of the glacier surface varies considerably across the Antarctic as well as according to season. The amount of solar radiation absorbed by the surface is called the net shortwave radiation (SHW_{net}) and is defined as the global radiation less the reflected short wave radiation. The expression for the net shortwave radiation (Paterson 1994, Lewis *et al.* 1998) can be written as,

$$SHW_{net} = SHW\downarrow - SHW\uparrow = SHW\downarrow (1- \alpha) \quad (4.4)$$

4.2.1.2 Longwave Radiation Flux

The net longwave radiation (LW_{net}) at snow/ice surface is sum of the outgoing component $LW\uparrow$ (negative) and incoming component $LW\downarrow$ (positive). $LW\uparrow$ is due to longwave radiation emission of snow/ice surface and $LW\downarrow$ is due to longwave radiation emitted by the clouds and atmospheric gases. The outgoing component is usually greater than the incoming component, so net longwave flux is generally negative and expresses the loss of energy from the snow/ice surface in longwave part of the electromagnetic spectrum (4μm – 40μm). Incoming longwave radiation depends on the temperature and composition of the atmosphere and estimated using a model developed by Prata (1996), which computes emissivity of the atmosphere (ϵ_m) depending on precipitable water content (w_p) and given as,

$$LW\downarrow = \epsilon_m \sigma T_a^4 \quad (4.5)$$

where,

$$\epsilon_m = 1 - (1+w_p) \exp\{-(1.2+3.0w_p)^{1/2}\} \quad (4.6)$$

and $$w_p = 46.5 (e_a/T_a) \quad (4.7)$$

e_a is vapour pressure (Pa) and T_a is air temperature measured at about 2-3 m above snow/ice surface.

$LW\uparrow$ has been estimated using Stefan-Boltzmann law and given as,

$$LW\uparrow = \epsilon_s \sigma T_s^4 \quad (4.8)$$

where, σ is the Stephan Boltzmann constant (5.67×10^{-8} W m^{-2} K^{-4}), T_s is surface temperature in kelvins and ϵ_s is the surface emissivity. The surface emissivity of the snow/ice surface is assumed to be unity (Bintanja and Van den Broeke 1994).

On a cloud free day, the net longwave radiation absorbed by the glacier surface is given as,

$$LW_{net} = LW\downarrow - LW\uparrow \quad = \epsilon_m \sigma T_a^4 - \epsilon_s \sigma T_s^4 \tag{4.9}$$

Clouds affect net longwave radiation flux significantly (Ackerman and Knox 2003). Clouds absorb longwave radiations emitted by earth surface and re-emit longwave radiation. As a result, the incoming longwave radiation on glacier surface increases in the presence of clouds. In overcast sky conditions, the net longwave radiation is given by,

$$LW_{net} = (\epsilon_m \sigma T_a^4 - \epsilon_s \sigma T_s^4)(1-K_c N) \tag{4.10}$$

where, the coefficient K_c depends on the type and height of clouds, and N is the amount of cloudiness in terms of fraction of sky covered. Experimental values of K_c reported by the US Army Corps of Engineers (1956) are (Upadhyay 1995): $K_c = 0.76$ for low clouds, $K_c = 0.52$ for medium clouds, and $K_c = 0.26$ for high clouds.

4.2.1.3 Turbulent Energy Fluxes

Turbulent eddies over a glacier surface mix the air vertically (Cuffey and Paterson 2010). The temperature of the air adjacent to the glacier surface equals the temperature of the ice or snow. If the temperature of the air in the lower atmospheric boundary layer is different from the air adjacent to glacier surface, then turbulent eddies transfer heat to equalize the temperature. The transfer of heat due to temperature difference in the air layers is governed by sensible heat flux. Similarly, if the moisture content in the air layer adjacent to glacier surface is different from the moisture content in the air above, then turbulent eddies also transfer moisture to equalize. This moisture transfer between the air layers is governed by latent heat flux. Estimation of sensible and latent heat flux using snow-met parameters is given in the following sections.

4.2.1.3.1 Sensible Heat Flux

Sensible heating represents the combined processes of conduction and convection (Ackerman and Knox 2003). Generally, the snow/ice surface is colder than the air above and the heat transfers from warm air to the colder surface by the process of sensible heating and the glacier surface gains energy. In case of temperature inversion, the heat

transfer takes place in opposite direction and glacier surface ablates energy. The vertical turbulent-sensible heat flux (*SHF*) is expressed in flux-gradient form (Braithwaite 1998) as,

$$SHF = \rho\, C_p\, K_H\, (\partial T/\partial z - \Gamma) \quad (4.11)$$

Where ρ is the density of air, C_p is the specific heat of air (1005J $Kg^{-1}K^{-1}$), K_H is the coefficient of turbulent diffusivity, $\partial T/\partial z$ is the vertical temperature gradient and Γ is the adiabatic lapse rate. In the air layer close to the glacier surface, equation (4.11) can be reformulated in terms of snow-met data as following (Ambach and Kirchlechner 1986, Paterson 1994),

$$SHF = (C_p\, \rho_0 / P_0)\, K_n\, P\, w\, (T_a - T_s) \quad (4.12)$$

$$K_n = k_v^2 / [\log(z_a/z_0)]^2 \quad (4.13)$$

where ρ_0 is the density of air (~1.29 Kg m^{-3}) at the standard atmospheric pressure P_0 (~1.013x10^5 Pa), K_n is a dimensionless transfer coefficient, P is the mean atmospheric pressure at the measuring site, w and T_a are measured wind speed and air temperature, k_v is von Karman's constant (~0.41), z_a is air temperature sensor height above ground and z_0 is aerodynamic roughness length. In the present study, the value of z_0 has been taken as 1 mm based on the literature (Van de Wal and Russell 1994, Bintanja 1995, Konzelmann and Braithwaite 1995, Gusain *et al.* 2009b).

4.2.1.3.2 Latent Heat Flux

Latent heat flux is an important component of the surface energy budget and is carried by turbulent transport in the atmospheric boundary layer. The moisture content of the air at the surface is determined by the saturation vapour pressure. If the vapour pressure of dry overlying air is less than saturation vapour pressure at surface, then moisture transfers from the surface to the air above and vice versa. The surface evaporates or sublimates to maintain saturation of the air adjacent to it (Cuffey and Paterson 2010) and this process consumes latent heat. Latent heat flux can be either positive or negative. Latent heat per unit area (latent heat flux) is given (Paterson 1994) by,

$$LHF = L_v\,(0.623\rho_0/P_0)K_n\,w\,(e_a\text{-}e_s) \tag{4.14}$$

Where, L_v is the latent heat of vaporization, e_a is the vapour pressure at height z above glacier surface and e_s is the saturation vapour pressure at the glacier surface. e_s is a function of the surface temperature and is 611 Pa for a melting surface (Paterson 1994). For distinguishing sublimation and condensation, guidelines given by Ambach and Kirchlechner (1986), and Greuell and Konzelmann (1994) have been followed,

i) When $(e_a\text{-}e_s)$ is positive and $T_s = 0^{\circ}C$, water vapour condenses as liquid water on the melting glacier surface with $Lv = 2.514$ MJ kg^{-1}

ii) When $(e_a\text{-}e_s)$ is negative, there is sublimation with $Lv = 2.849$ MJ kg^{-1}.

iii) When $(e_a\text{-}e_s)$ is positive and $T_s < 0^{\circ}C$, there is deposition from vapour to solid ice with $Lv = 2.849$ MJ kg^{-1}.

Because of the daily cycle of radiative heating and cooling, there is a daily cycle of static stability in the atmospheric boundry layer (ABL) (Roland Stull 2000). The atmospheric stability conditions in the boundry layer are (1) Unstable atmospheric conditions (2) Stable atmospheric conditions and (3) Neutral atmospheric conditions. The equations of sensible and latent heat fluxes given in equations (4.12), (4.13), (4.14) are applicable for neutral atmospheric conditions. Corrections for stable and unstable atmospheric conditions have been applied using the transfer coefficient K_n in terms of bulk Richardson number (R_i), given as (Price and Dunne, 1976),

$$R_i = gz_a(T_a\text{-}T_s)/(T_a\,w^2) \tag{4.15}$$

where, g is acceleration due to gravity, z_a is air temperature sensor height above ground, T_a is air temperature, T_s is the surface temperature and w is the wind speed.

For unstable conditions (i.e., $Ri<0$), the effective transfer coefficient is computed as $K_n.(1\text{-}10R_i)$, for neutral conditions (i.e., $Ri = 0$), the effective transfer coefficient is taken as K_n, and for stable conditions (i.e., $Ri>0$), the effective transfer coefficient is computed as $K_n/(1+10R_i)$ (Price and Dunne 1976).

4.2.1.4 Sub Surface Heat Flux

Heat transfer takes place between glacier surface and ice underneath mainly using conduction process. If the glacier surface is at higher temperature than the ice below, the transfer of heat takes place from the surface towards down. If the glacier surface is at lower temperature than the ice below, the transfer of heat takes place towards surface from the ice underneath. In the present work, subsurface heat flux has been measured directly using heat flux plate sensors, as described in section 3.3.1.1.2 of chapter 3. The experimental set up for measuring sub surface heat flux has also been shown in Figure 3.5.

4.2.2 Results and Discussion

4.2.2.1 Meteorological Parameters

Daily averages of surface temperature (T_s) and air temperature (T_a) at the study location of AWS 1 in Antarctica (Figure 3.3) from 1-March 2007 to 28-Feb 2011 are shown in Figure 4.1 (a, b). Table 4.1 shows the averages of meteorological parameters during different seasons. Large short-term variability and a strong annual cycle have been observed in the T_a and T_s for all the four years (Gusain *et al.* 2014a). Over the entire period, averages of T_a and T_s are -10.2˚C $\pm$ 7˚C (mean $\pm$ standard deviation) and -11.4˚C $\pm$ 7.4˚C respectively. Radiative heating during summer causes T_a to reach its maximum daily average value above 4.0˚C at the study location. Absence of shortwave radiation and continuous longwave cooling of the surface cause T_a to dip down below -20˚C during winter. August and September are the coldest months during all the four years. It is because the energy loss by net longwave radiation dominates over the energy gained by net shortwave radiation till the month of September. October onwards, net radiation becomes heat source to the glacier, as the energy gained by net shortwave radiation flux dominates the energy loss due to net longwave radiation flux. Diurnal variation in the T_a and T_s are shown in Figure 4.2a during the different seasons. The amplitude of diurnal variation of T_a and T_s have been observed as highest during the transition2 period (2.0˚C and 1.4˚C) followed by summer (1.6˚C and 1.3˚C) and transition1 (0.9˚C and 1.0˚C) periods. The lowest amplitude has been observed during the winter (0.35˚C and 0.3˚C) period. The high amplitude of diurnal variation during summer and transitions periods may be due to the

high diurnal variation in solar heating. The maximum temperature has occurred in the diurnal cycle around local solar noon. The average values of T_a are higher as compared to the average values of T_s in the diurnal cycle for all the seasons at the observation location, which contributes to the downward sensible heat flux. High correlation (R^2 between 0.89 to 0.98) has been observed between daily-averaged T_a (T_{ad}) and daily-averaged T_s (T_{sd}) for different seasons. The highest correlation (R^2 = 0.98) has been observed for winter and transition1 period. Figure 4.4 shows the correlation for winter season. Regression equation for each season is given in Table 4.2. These regression equations may be useful in estimation of surface temperature when only air temperature is measured or vice versa.

Daily mean relative humidity (*RH*) varies from 26% to 97% (Figure 4.1c) during the study period and exhibits large short-term variability and seasonal cycle. Monthly average *RH* varies from 35% to 62%. Relative humidity is high during summer months when there is warm air advection and low during winter and transition periods. Events with more than 80% daily average relative humidity at the location corresponds to passage of cyclonic storms. Cyclonic events are generally more frequent in coastal stations as compared to interior part of Antarctica. The dominant wind direction is from the east during cyclonic events at the observation location. In general, the air close to the oasis is dry with four year mean *RH* of 50%. Relative humidity has been observed as higher during summer than in other seasons (Table 4.1). Figure 4.2b shows the mean diurnal variation in *RH* during different seasons. The amplitudes of the diurnal cycle for summer, winter, transition1 and transition2 seasons are 4%, 0.5%, 1.5% and 2%, respectively. High diurnal variation during summer corresponds to the high diurnal variation in radiation and low katabatic winds. Low diurnal variation during winter may be due to high katabatic winds causing air moisture to be well mixed in the boundary layer.

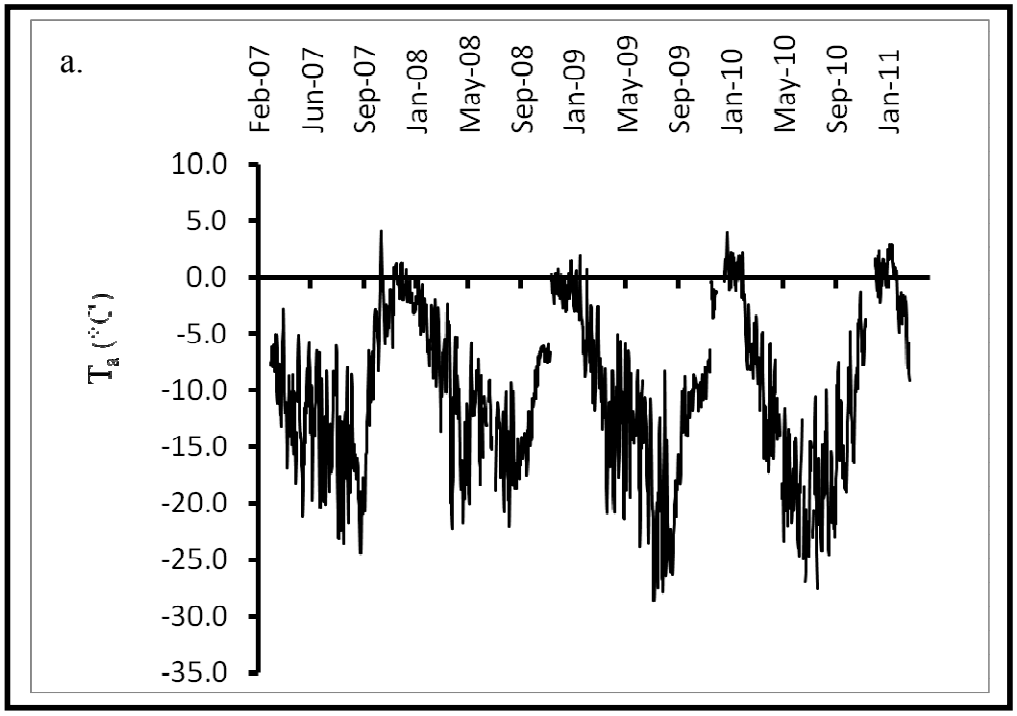
a.
Feb-07
Jun-07
Sep-07
Jan-08
May-08
Sep-08
Jan-09
May-09
Sep-09
Jan-10
May-10
Sep-10
Jan-11
10.0
5.0
0.0
-5.0
-10.0
-15.0
-20.0
-25.0
-30.0
-35.0
T_a (°C)

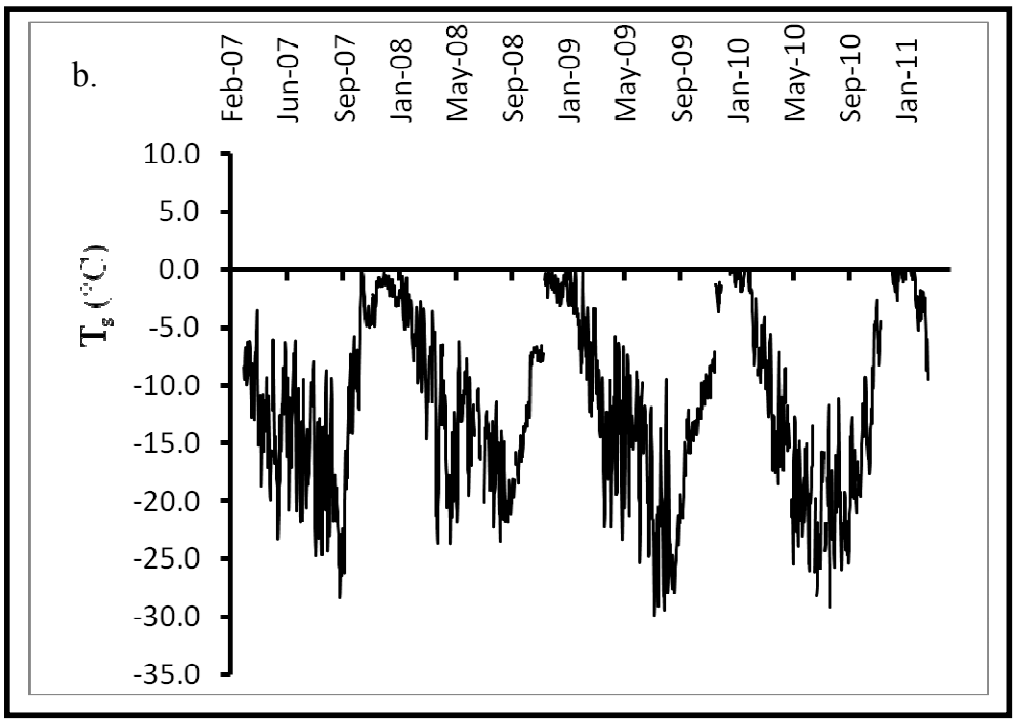
b.
Feb-07
Jun-07
Sep-07
Jan-08
May-08
Sep-08
Jan-09
May-09
Sep-09
Jan-10
May-10
Sep-10
Jan-11
10.0
5.0
0.0
-5.0
-10.0
-15.0
-20.0
-25.0
-30.0
-35.0
T_g (°C)

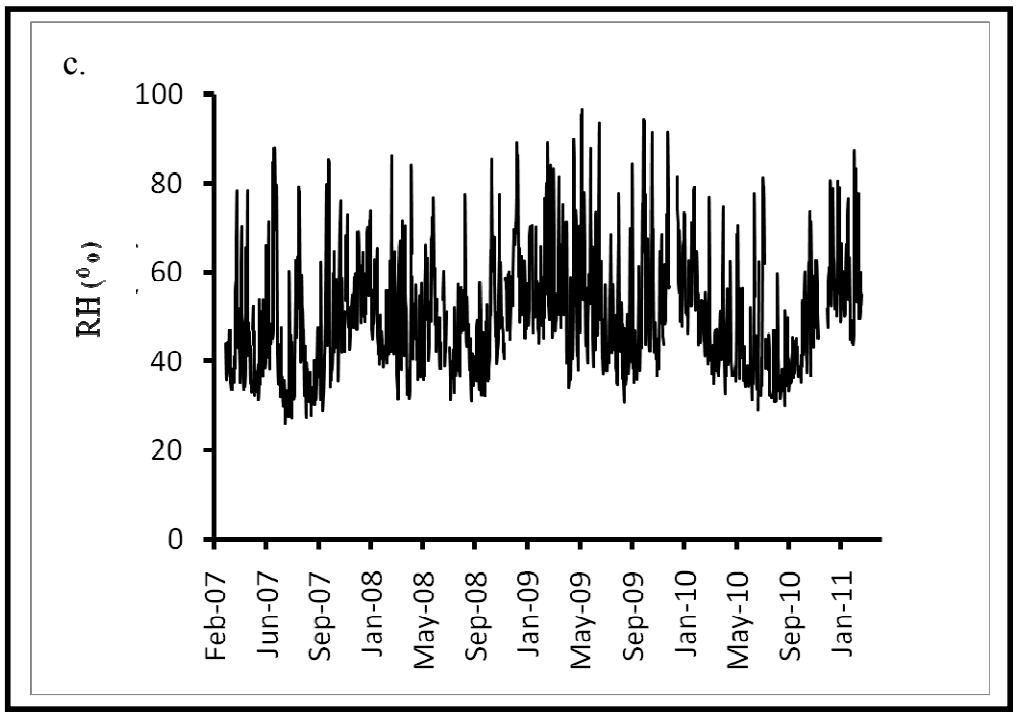
c.
RH (%)
100
80
60
40
20
0
Feb-07
Jun-07
Sep-07
Jan-08
May-08
Sep-08
Jan-09
May-09
Sep-09
Jan-10
May-10
Sep-10
Jan-11

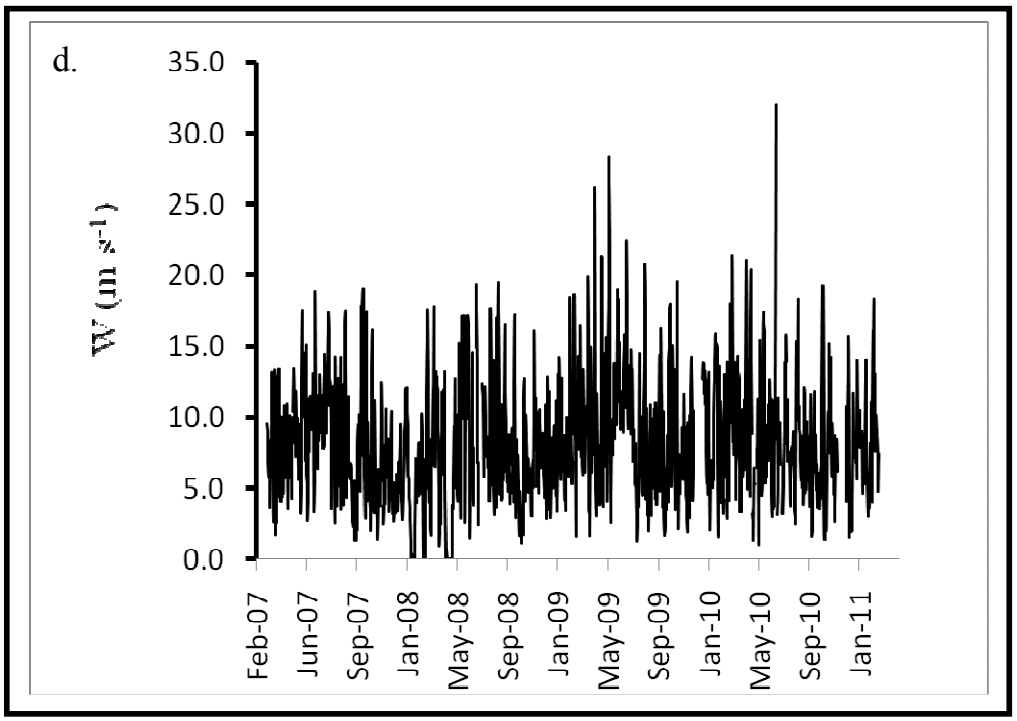
d.
W (m s-1)
35.0
30.0
25.0
20.0
15.0
10.0
5.0
0.0
Feb-07
Jun-07
Sep-07
Jan-08
May-08
Sep-08
Jan-09
May-09
Sep-09
Jan-10
May-10
Sep-10
Jan-11

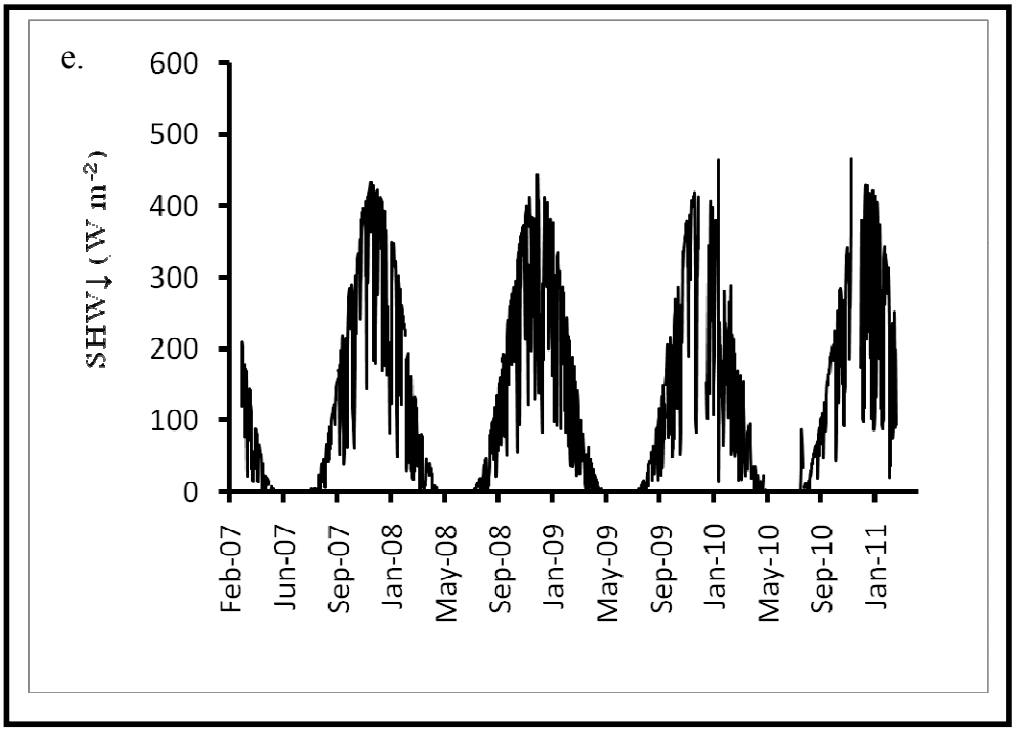
e.
SHW↓ (W m-2)
600
500
400
300
200
100
0
Feb-07
Jun-07
Sep-07
Jan-08
May-08
Sep-08
Jan-09
May-09
Sep-09
Jan-10
May-10
Sep-10
Jan-11

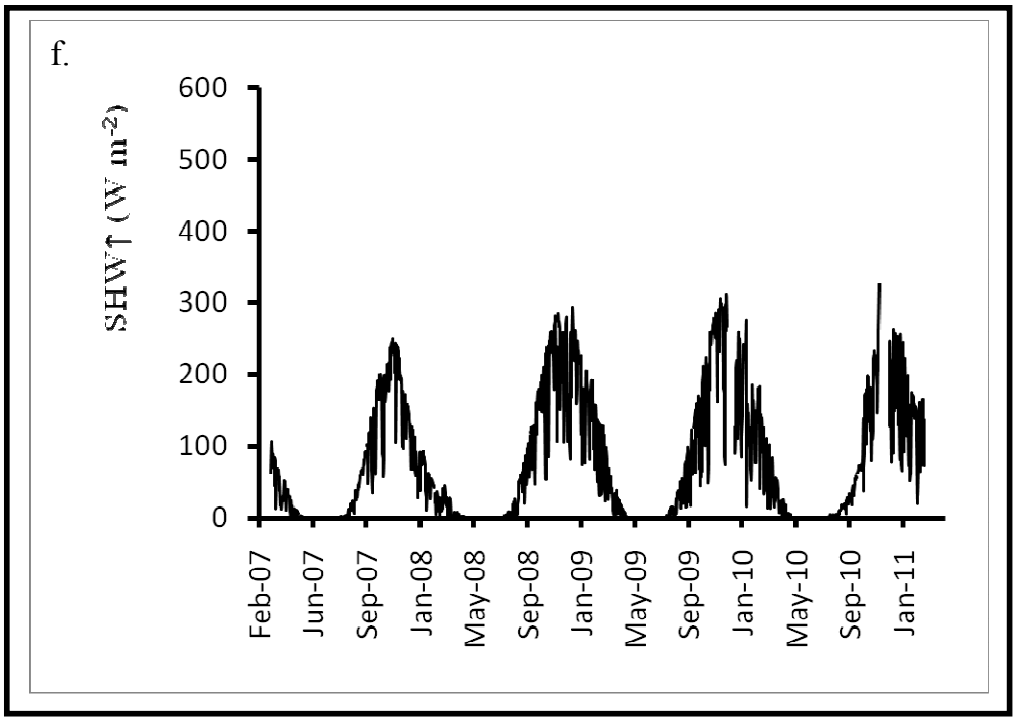
f.
SHW↑ (W m-2)
600
500
400
300
200
100
0
Feb-07
Jun-07
Sep-07
Jan-08
May-08
Sep-08
Jan-09
May-09
Sep-09
Jan-10
May-10
Sep-10
Jan-11

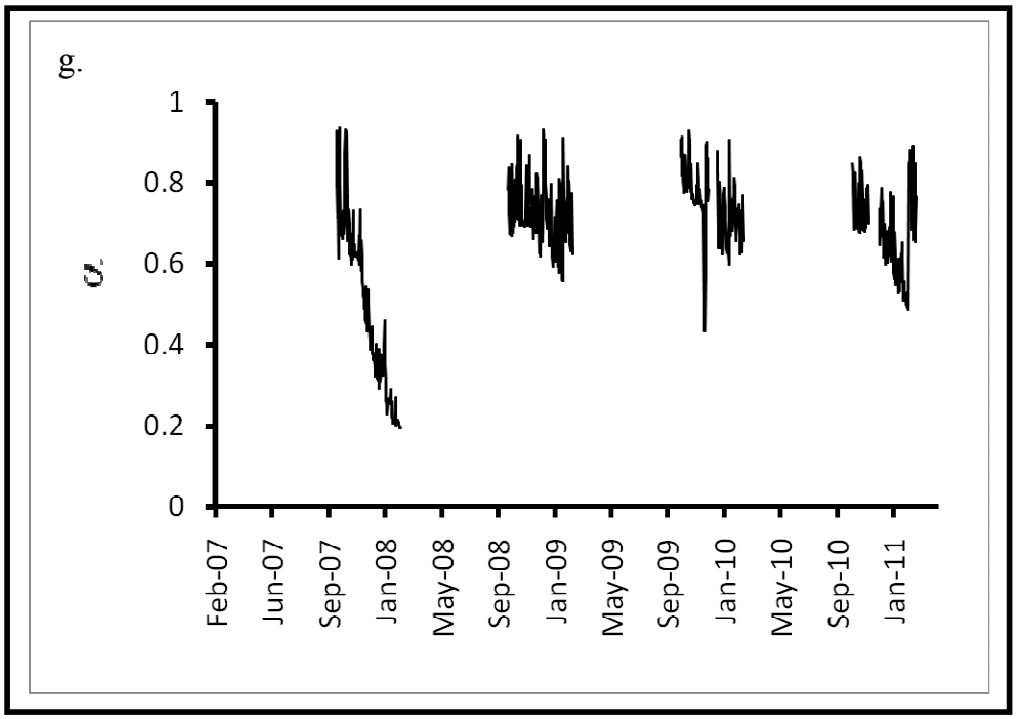

Figure 4.1 : Daily averages of (a) T_a (b) T_s (c) RH (d) w (e) $SHW\downarrow$ (f) $SHW\uparrow$ and (g) α

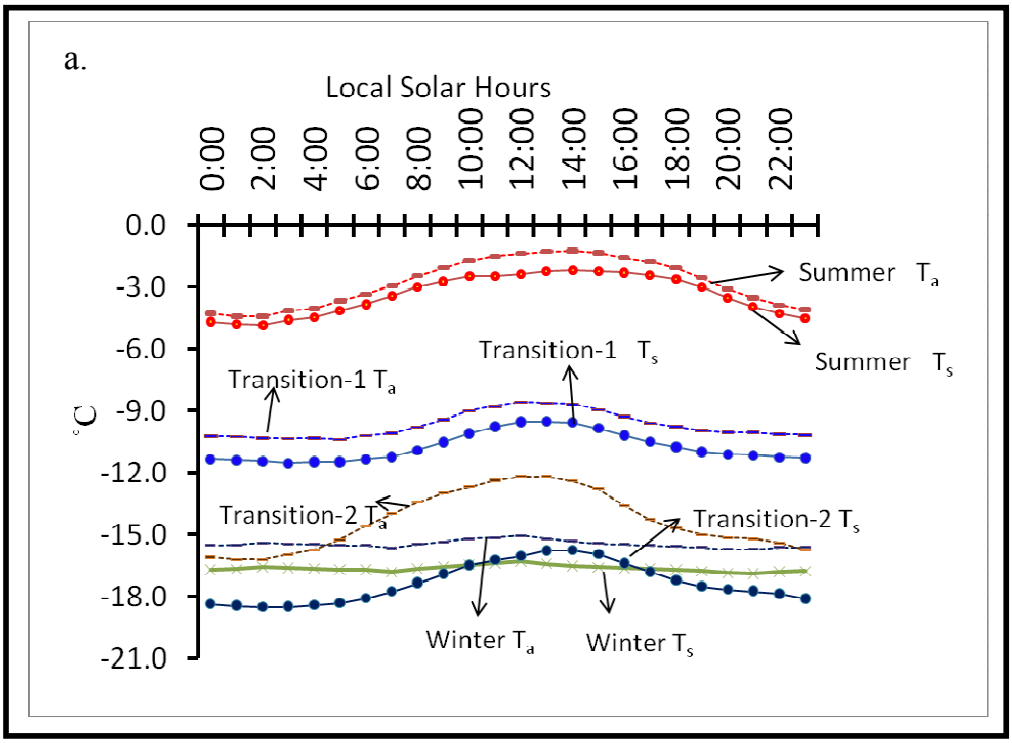
a.
Local Solar Hours
0:00
2:00
4:00
6:00
8:00
10:00
12:00
14:00
16:00
18:00
20:00
22:00
0.0
-3.0
-6.0
-9.0
-12.0
-15.0
-18.0
-21.0
°C
Summer T_a
Summer T_s
Transition-1 T_s
Transition-1 T_a
Transition-2 T_a
Transition-2 T_s
Winter T_a
Winter T_s

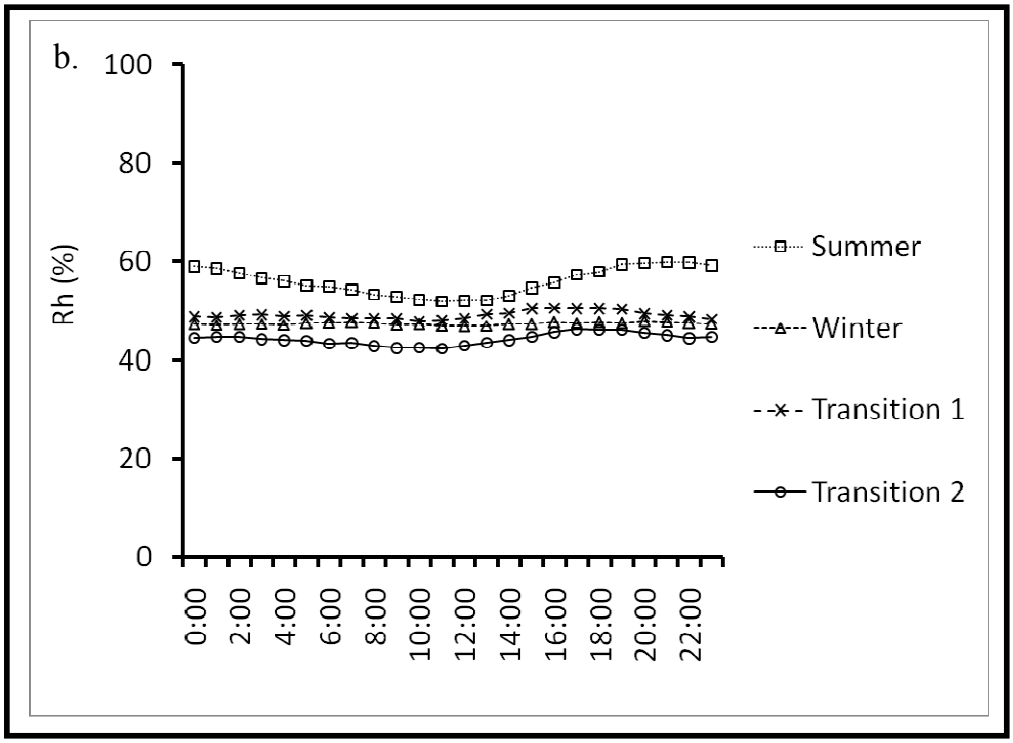
b.
100
80
60
40
20
0
Rh (%)
0:00
2:00
4:00
6:00
8:00
10:00
12:00
14:00
16:00
18:00
20:00
22:00
Summer
Winter
Transition 1
Transition 2

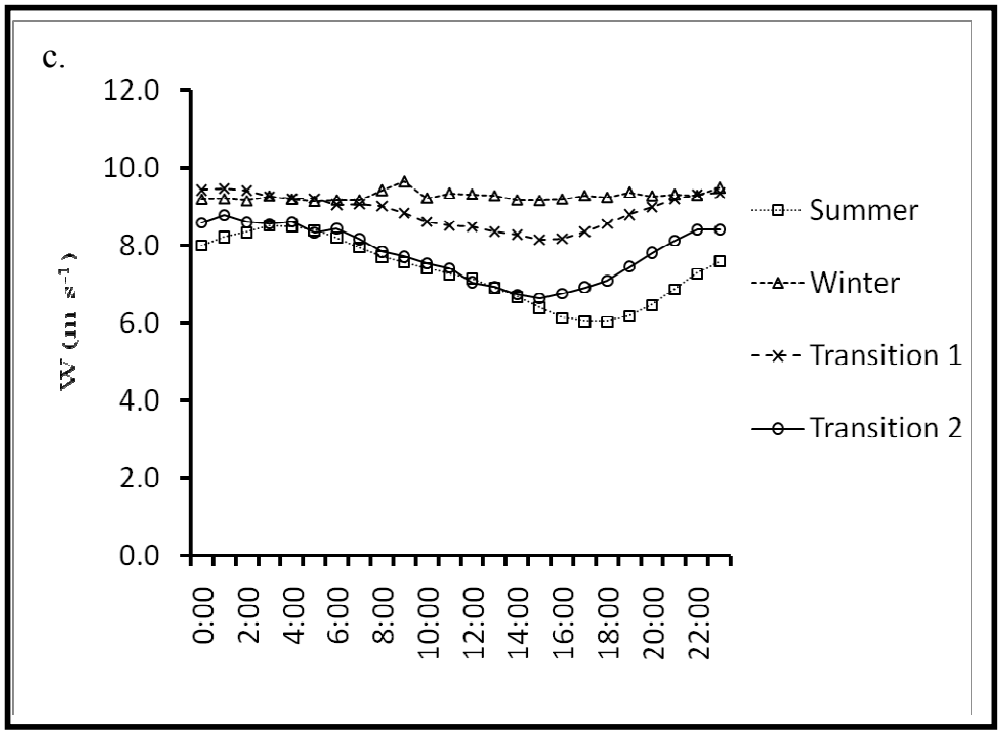
c.
12.0
10.0
8.0
6.0
4.0
2.0
0.0
W (m s-1)
0:00
2:00
4:00
6:00
8:00
10:00
12:00
14:00
16:00
18:00
20:00
22:00
Summer
Winter
Transition 1
Transition 2

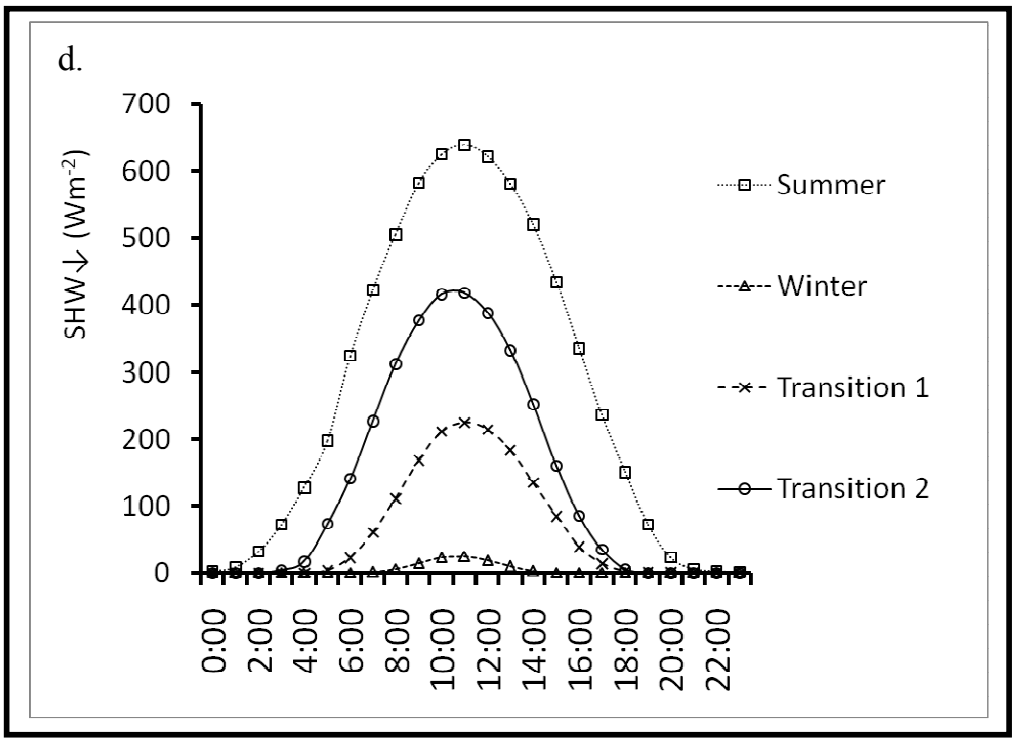
d.
700
600
500
400
300
200
100
0
SHW↓ (Wm-2)
0:00
2:00
4:00
6:00
8:00
10:00
12:00
14:00
16:00
18:00
20:00
22:00
Summer
Winter
Transition 1
Transition 2

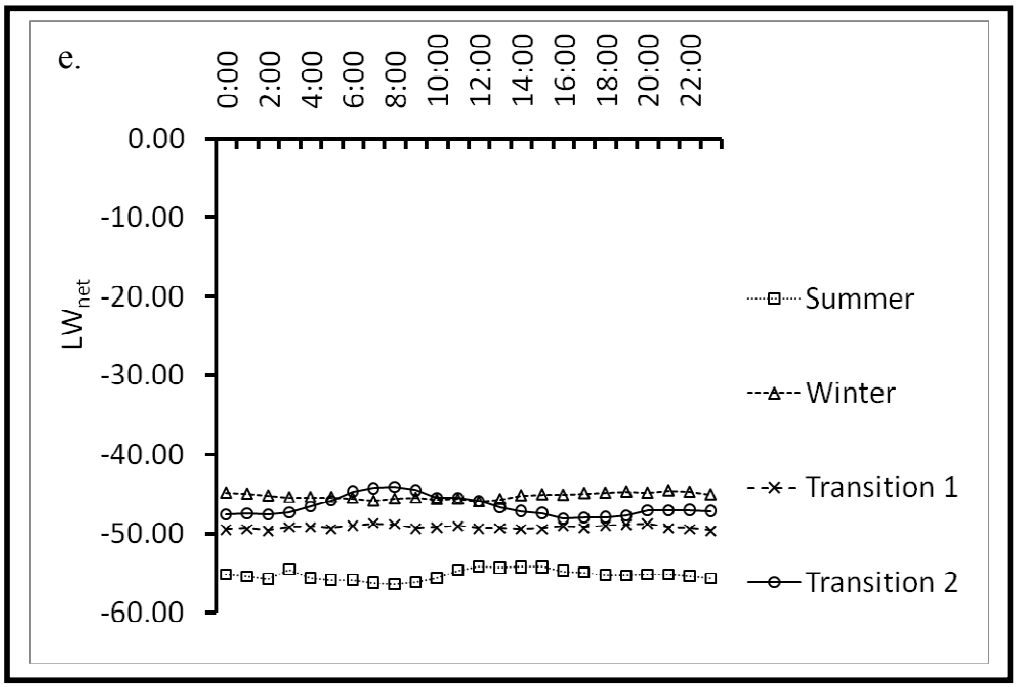
e.
0:00
2:00
4:00
6:00
8:00
10:00
12:00
14:00
16:00
18:00
20:00
22:00
0.00
-10.00
-20.00
-30.00
-40.00
-50.00
-60.00
LW$_{net}$
Summer
Winter
Transition 1
Transition 2

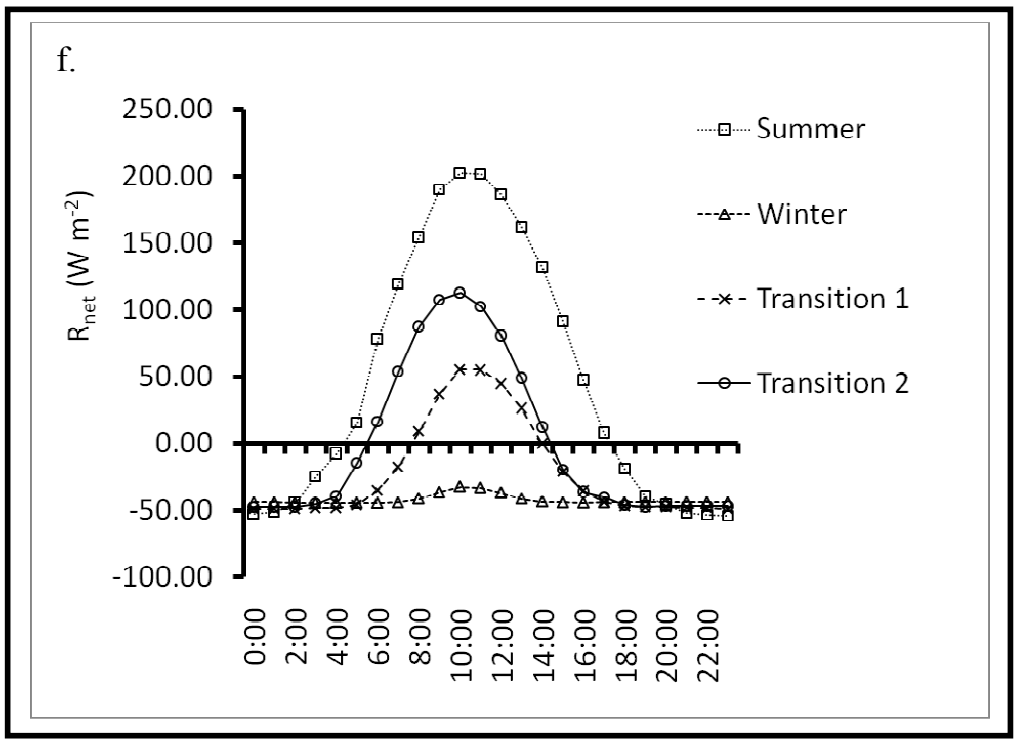
f.
250.00
200.00
150.00
100.00
50.00
0.00
-50.00
-100.00
R$_{net}$ (W m^{-2})
0:00
2:00
4:00
6:00
8:00
10:00
12:00
14:00
16:00
18:00
20:00
22:00
Summer
Winter
Transition 1
Transition 2

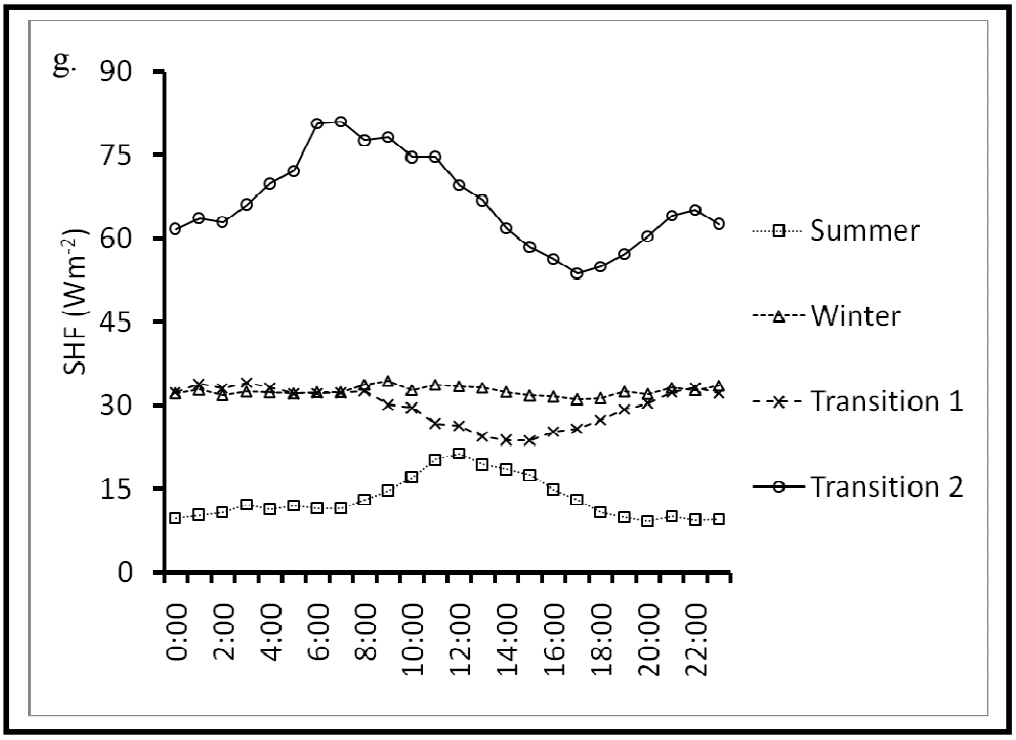
g.
SHF (Wm-2)
90
75
60
45
30
15
0
0:00
2:00
4:00
6:00
8:00
10:00
12:00
14:00
16:00
18:00
20:00
22:00
Summer
Winter
Transition 1
Transition 2

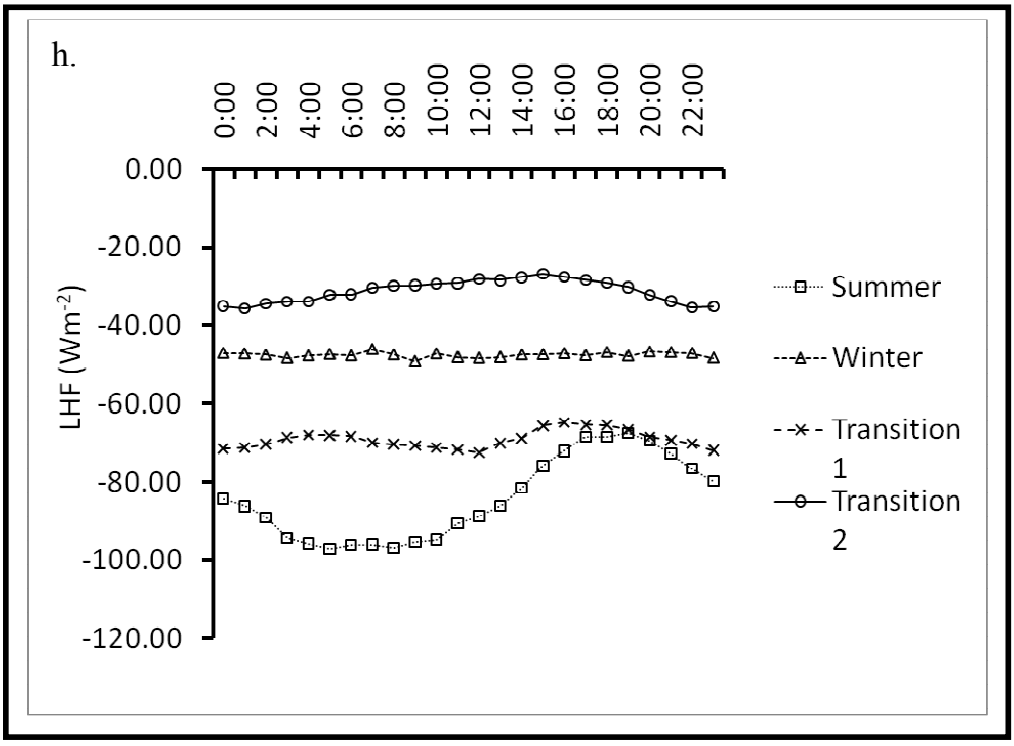
h.
LHF (Wm-2)
0.00
-20.00
-40.00
-60.00
-80.00
-100.00
-120.00
0:00
2:00
4:00
6:00
8:00
10:00
12:00
14:00
16:00
18:00
20:00
22:00
Summer
Winter
Transition 1
Transition 2

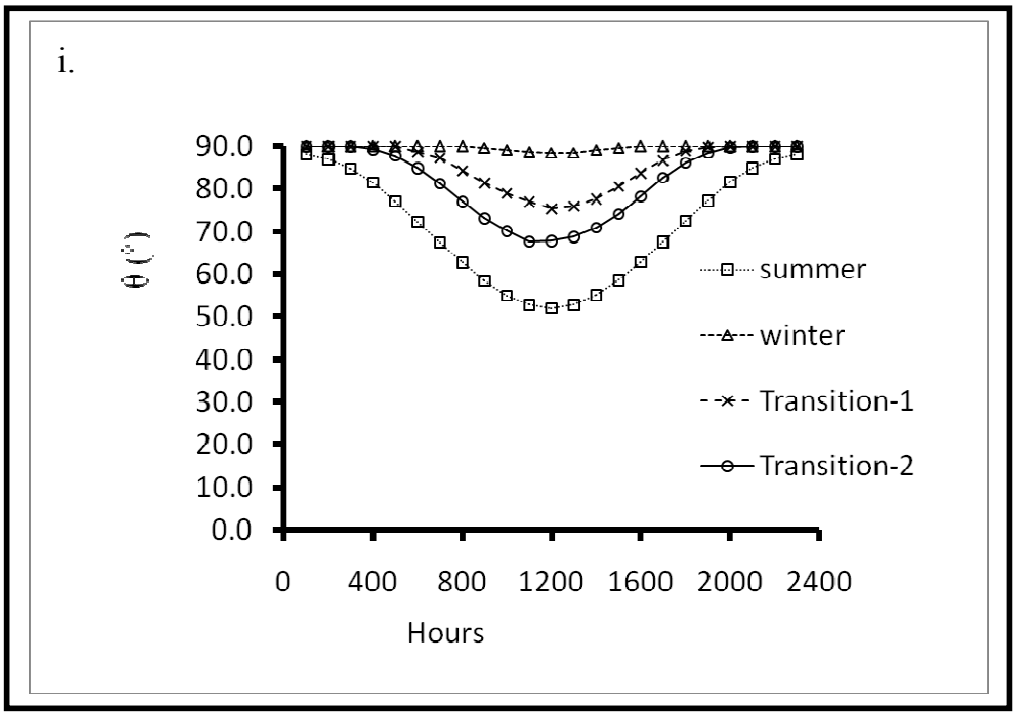

Figure 4.2 : Diurnal variation during different seasons in (a) T_a , T_s (b) RH (c) w (d) $SHW\downarrow$ (e) LW_{net} (f) R_{net} (g) SHF (h) LHF and (i) Solar Zenith Angle (θ)

Table 4.1 : Seasonal and annual mean of meteorological parameters and energy fluxes over 4 years.

Parameter	**Summer mean**	**Winter mean**	**Transition1 mean**	**Transition2 mean**	**Annual mean**
T_s (˚C)	-3.3	-16.6	-10.7	-17.3	-11.4
T_a (˚C)	- 2.8	-15.4	-9.7	-14.3	-10.2
RH (%)	56	47	49	44	50
w (ms^{-1})	7.3	9.3	8.9	7.8	8.3
Cloud Amount (Octa)	5.0	6.3	5.5	5.3	5.5
*α	0.64	-	-	0.75	0.66
SHW↓ (Wm^{-2})	272	5	62	136	122
SHW↑ (Wm^{-2})	170	2	34	89	76
SHW_{net} (Wm^{-2})	102	3	28	47	46
LW_{net} (Wm^{-2})	-55.2	-45.2	-49.2	-46.6	-49
R_{net} (Wm^{-2})	46.8	-42.2	-21.2	0.4	-3
SHF (Wm^{-2})	13.2	32.6	29.8	66.4	32
LHF (Wm^{-2})	-84.3	-47.5	-69.1	-31.2	-61

REF (Wm^{-2})	-24.3	-57.1	-60.5	35.6	-32

* Mean albedo for the days of the season when mean daily solar zenith angle is < 80˚.

Table 4.2 : Regression equations between T_{sd} and T_{ad} for different seasons.

Season	**Regression Equation**	R^2
Winter	$T_{sd} = 1.041 * T_{ad} - 0.431$	0.98
Transition1	$T_{sd} = 1.04 * T_{ad} - 0.52$	0.98
Transition2	$T_{sd} = 0.964 * T_{ad} - 3.01$	0.89
Summer	$T_{sd} = 0.901 * T_{ad} - 0.837$	0.94

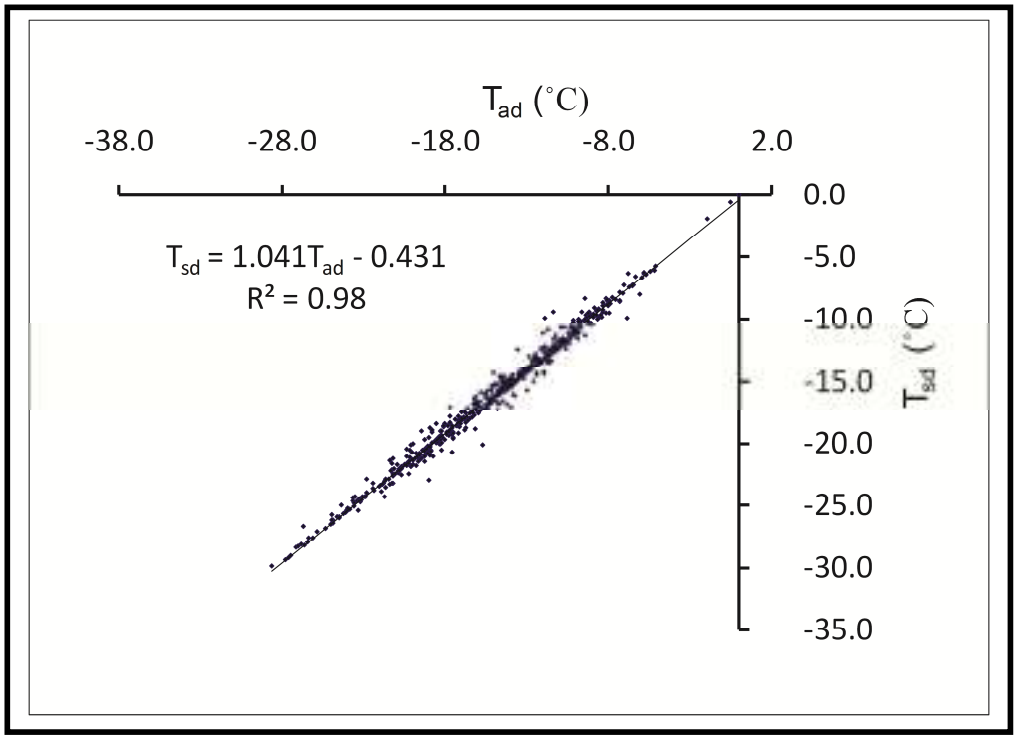

Figure 4.3 : Correlation between T_{ad} and T_{sd} during winter season

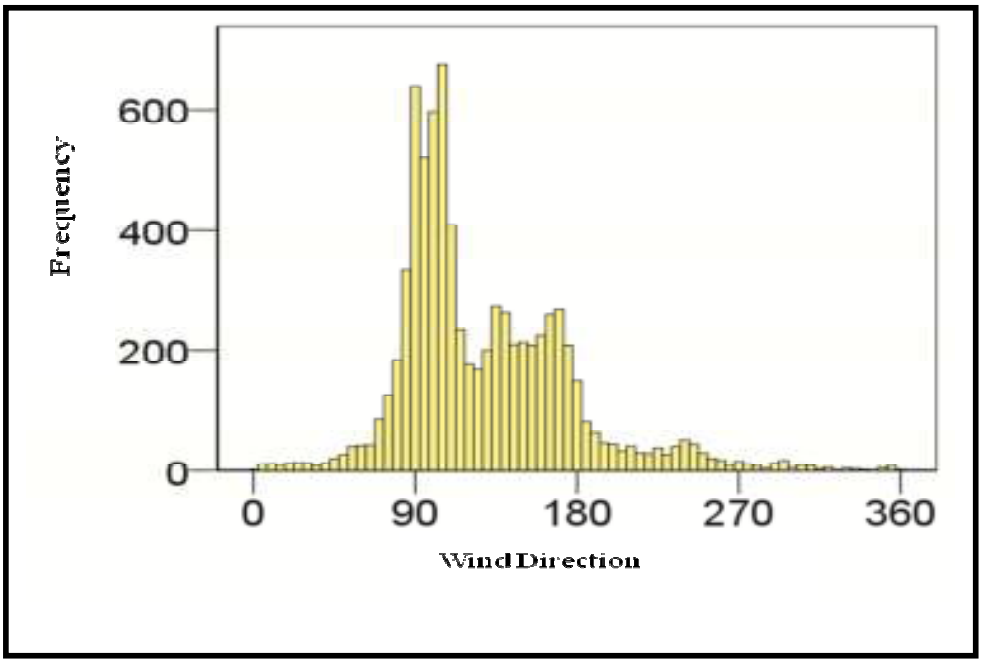

Figure 4.4 : Wind directions at the study site in Antarctica

Strong katabatic winds are observed at the study location due to its topographic setting down a steep slope from the Antarctic Plateau. Daily mean speed has been recorded up to 32 m s^{-1} (Figure 4.1d) and major wind directions are East, South-East and South (Figure 4.4). The wind is characterized by short period of calm and light wind followed by a period of high wind. Generally, high wind events correspond to passage of low pressure systems (Tyagi *et al*. 2011) at the observation site. Monthly mean speed varies from 3.2 m s^{-1} to 11.7 m s^{-1} with a four-year average of 8.3 m s^{-1}. A strong seasonal cycle has been observed in the wind speed. During winter season, wind speed is high as compared to other seasons (Table 4.1). Diurnal variation may be observed in the wind speed (Figure 4.2c). The amplitudes of the diurnal cycle are 1.25 m s^{-1} for summer, 0.25 m s^{-1} for winter, 0.65 m s^{-1} for transition1 and 1.1 m $s^{-1}$for transition2 seasons. High diurnal variation during summer and transition periods corresponds to high diurnal variation in insolation. Insolation heats the glacier surface and destroys the surface temperature inversion which results in weakening of the katabatic forcing. Low wind speed in the afternoon during summer and transition periods corresponds to weakening of katabatic forcing, which may be due to break up of surface inversion (Zhou *et al.* 2009).

High seasonal and short term variability may be observed in the incoming and outgoing shortwave radiation fluxes (*SHW*↓ and *SHW*↑) at the study site (Figures 4.1e & f). Seasonal variability is mainly associated with annual variation in mean solar zenith angle. Short term variation is due to frequent passage of frontal systems and clouds (Van den Broeke *et al.* 2004b). Hourly mean *SHW*↓, not shown in the figure, have been observed up to 1100 Wm^{-2}, while daily averages are up to 499 Wm^{-2} (Figure 4.1e) with a four-year mean of 123 Wm^{-2}. As expected, *SHW*↓ is the highest during summer season, followed by transition2 and transition1 period, and is almost zero for the winter months. Mean top of the atmosphere insolation has been calculated at the location using mean Earth-Sun distance, solar constant and solar zenith angle values during the seasons. An overall transmissivity of 0.65, 0.6 and 0.72 have been observed during summer, transition1 and transition2 periods, respectively. The mean annual atmospheric transmissivity at the observation location has been observed as 0.659 which is comparable to those reported by Van den Broeke *et al.* (2004b) as 0.666 at AWS 5 and 0.632 at AWS 4 location in coastal

Antarctica. Mean atmospheric transmissivity for clear sky days has been observed as 0.8 at the observation site.

Outgoing shortwave radiation flux (*SHW*↑) mainly depends on *SHW*↓ and surface characteristics. Hourly and daily mean *SHW*↑ measured at the observed site varies between 732 Wm^{-2} and 385 Wm^{-2} respectively with four yearly average of 76.7 Wm^{-2}, which is low as compared to other coastal sites reported in Antarctica. Daily mean albedo of the glacier surface is shown in Figure 4.1g for the days with mean daily solar zenith angle < 80°. Albedo varies from 0.19 to 0.93 with mean annual albedo of 0.65 during 4 years. Summer months of the 2007-08 season has exceptionally low albedo values. This may be due to high melting at the glacier surface during this year (Gusain *et al.* 2009b). High inter-annual variation may be observed in the albedo values and summer 2007-08 was lowest with mean albedo of 0.44. Mean albedo values during the summer of 2008-09, 2009-10 and 2010-11 have been observed as 0.72, 0.73 and 0.67 respectively. The albedo at the present study location is low as compared ($\alpha \sim 0.84$) to reported by Van den Broeke *et al.* (2004b), and is comparable with the albedo ($\alpha \sim 0.63$) at Taylor glacier, McMurdo dry valleys, reported by Bliss *et al.* (2011). The present location is very close to the ice free area of the Shirmacher Oasis, therefore, the windblown dust or debris events contributes to melting of the glacier surface, which results into low albedo values (Gusain *et al.* 2009b).

In terms of cloud amount, most of the days have been observed partly cloudy to cloudy at the observation location and only 188 days have been observed cloud free in the 4 years. Mean seasonal cloud amount has been observed as 5.5 octa, 5.3 octa, 6.3 octa and 5.0 octa during transition1, transition2, winter and summer seasons, respectively (Table 4.1). The variation in cloud amount has an impact on the variation in incoming shortwave radiation flux during different seasons.

Figure 4.2d shows the diurnal variation of *SHW*↓ during different seasons. In the diurnal cycle, *SHW*↓ has been observed as more than 120 Wm^{-2} for 15 hours during summer, and 10 and 7 hours during transition2 and transition1 seasons respectively. These values can be generalised as average sunshine hours for these seasons, as per the WMO norms, which state that the incoming radiation more than 120 Wm^{-2} can be considered as sunshine. The amplitudes of the diurnal cycle during summer, winter, transition1 and

transition2 periods are 318 Wm^{-2}, 12.5 Wm^{-2}, 112 Wm^{-2} and 209.5 Wm^{-2}, respectively. The diurnal variations in incoming shortwave radiation flux during the seasons are in correspondence with the diurnal variation in solar zenith angle shown in Figure 4.2i. High amplitude of incoming shortwave radiation flux during summer and transition2 period may be due to high amplitude of solar zenith angle during these periods.

4.2.2.2 Radiative Energy Fluxes

Figure 4.5a shows the temporal variation of monthly mean values of net shortwave radiation flux (SHW_{net}), net longwave radiation flux (LW_{net}) and net radiation flux (R_{net}) from March-2007 to February-2011. The hourly and daily mean SHW_{net} varies up to 765 Wm^{-2} and 272 Wm^{-2} respectively (not shown in the figure) with a four-year average of 46 Wm^{-2}. As can be seen (Figure 4.5a), net shortwave radiation flux for the summer months of 2007-08 is high as compared to other years, since during this particular season, albedo values were exceptionally low. A rise in T_a up to 6.5˚C in the first week of November 2007 might have started early melting of the ice sheet and triggered a positive feedback loop of albedo causing excessive melting during the season (Gusain *et al.* 2009b). Annual mean $SHW\downarrow$ at the site has been observed as 122 Wm^{-2}, which matches with those reported by Van den Broeke *et al.* (2004b) as 121.3 Wm^{-2} and 127.2 Wm^{-2} at the coastal locations. Outgoing shortwave radiation flux at the study location has been observed as low, with annual mean of 76 Wm^{-2} as compared to the values of 105.9 Wm^{-2} and 106.5 Wm^{-2} reported by Van den Broeke *et al.* (2004b). Annual mean net shortwave radiation flux of 46 Wm^{-2} has been observed at the location, which is high as compared to other coastal locations reported by Van den Broeke *et al.* (2004b). This may be attributed to low albedo values due to melting and wind blown dust events, as discussed earlier.

Seasonal variability in the LW_{net} has also been observed. Hourly LW_{net} varies from -12 Wm^{-2} to -94.4 Wm^{-2} whereas the daily mean LW_{net} varies from -14 Wm^{-2} to -81 Wm^{-2} with a four-year average of -49 Wm^{-2}. Net longwave radiation flux is high during summer period due to high surface temperature of the glacier. Figure 4.2e shows diurnal variation of LW_{net} during different seasons. The amplitudes of the diurnal cycle of LW_{net} are 1.1 Wm^{-2} , 0.7 Wm^{-2} , 0.5 Wm^{-2} and 2 Wm^{-2} for the summer, winter, transition1 and transition2

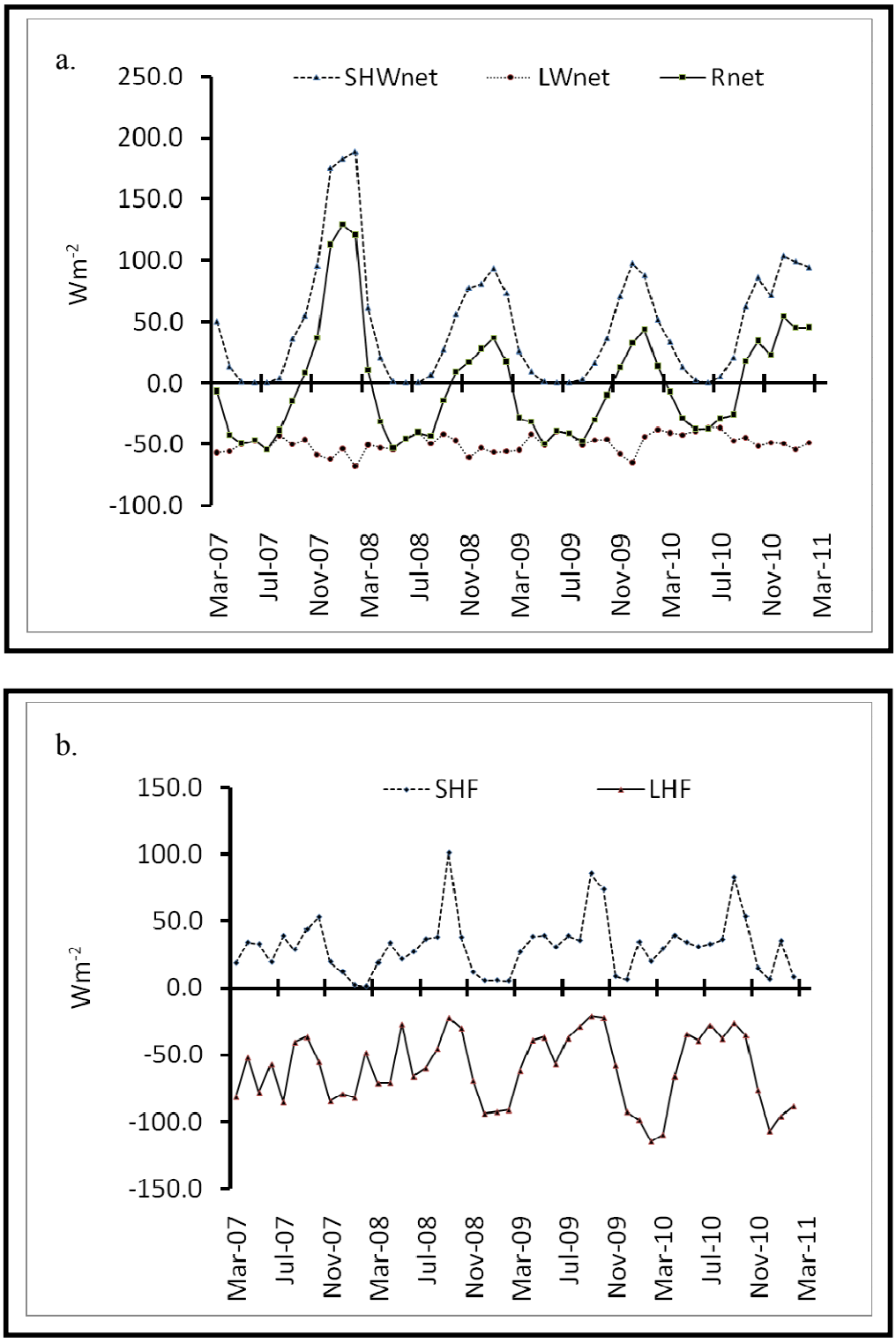

Figure 4.5 : Monthly mean (a) Radiative and (b) Turbulent energy fluxes

periods, respectively. High diurnal variation during transition2 and summer may be due to high diurnal variations in the T_a and T_s during this period.

Net radiation flux line (figure 4.5a) changes from positive to negative twice a year during all four years. At these points, R_{net} is zero and SHW_{net} balances the LW_{net}. Above these points, SHW_{net} dominates LW_{net} and glacier surface absorbs radiation, which increases the glacier surface temperature with melting starting at 0˚C. Below these points, LW_{net} dominates the SHW_{net} and the glacier surface loses energy, tending to decrease the surface temperature. The time when R_{net} varies from negative to positive in a year, is different for all the four years. Generally, during October, November, December, January, February and March months R_{net} has been observed as positive at the site. In the diurnal cycle (Figure 4.2f), net radiation is positive for about 15 hours during summer season. The amplitudes of the diurnal cycle are 128.2 Wm^{-2}, 6.1 Wm^{-2}, 52 Wm^{-2} and 80.3 Wm^{-2} for summer, winter, transition1 and transition2 seasons, respectively. High diurnal variations during the transition periods and summer may be due to high diurnal variations in SHW_{net} during these periods.

4.2.2.3 Turbulent Energy Fluxes

Sensible and latent heat fluxes have been estimated using equation (4.12) and (4.14). High temporal variability in the sensible (*SHF*) and latent heat (*LHF*) fluxes has been observed (Figure 4.5b). A strong seasonal cycle has been observed in the *SHF* during all the four years. Sensible heat flux has been observed as the lowest during the summer period, which gradually increases during the transition1 and winter periods, reaching maximum values during transition2 periods. Monthly average value of sensible heat flux varies from 1.3 Wm^{-2} to 101 Wm^{-2} with a 4-year average of 31.1 Wm^{-2}. A higher difference between T_s and T_a during transition2 period has caused higher values of *SHF* during this period. Figure 4.2g shows the diurnal variation of *SHF* during different seasons. The amplitudes during summer, winter, transition1 and transition2 period are 6 W m^{-2} , 1.6 W m^{-2} , 5.1 W m^{-2} and 13.6 W m^{-2} respectively. High diurnal variation during transition periods and the summer season may be due to high diurnal variation in T_s and T_a during these periods. Monthly average *LHF* varies from -21.2 Wm^{-2} to -115.4 Wm^{-2} with 4 yearly mean of -61.3

Wm^{-2}. Latent heat flux has been observed high during the summer period (seasonal mean -84.3 Wm^{-2}) followed by transition1 (seasonal mean -69.1 Wm^{-2}), winter (seasonal mean -47.5 Wm^{-2}) and transition2 (seasonal mean -31.2 Wm^{-2}) period. Comparatively low values of *LHF* during transition2 period and winter season may be due to low values of T_s during this period. Figure 4.2h shows diurnal variation of *LHF* during different period. The amplitudes of diurnal cycle are 14.8 Wm^{-2} , 1.5 Wm^{-2} , 3.8 Wm^{-2} and 4.4 Wm^{-2} for the summer, winter, transition1 and transition2 periods, respectively. High diurnal variation during summer may be due to high diurnal variation in surface temperature and wind speed.

4.2.2.4 Subsurface Heat Flux

Hourly subsurface heat flux have been measured for few summer days at the study location using heat flux plates, as described in chapter 3. Figure 4.6 shows the hourly variation of sub surface heat flux, which varies from – 21 Wm^{-2} to + 21 Wm^{-2} during 30-December 2011 to 4-January-2012. Mean subsurface heat flux of - 0.9 W m^{-2} has been observed during observation period which is less than 1% of the net radiation flux and net energy balance of that period. Contribution of subsurface heat flux to the net energy balance has been observed as very low in comparision to radiative and turbulent energy fluxes at the site during observations period.

4.2.2.5 Comparison with other Antarctic locations

Values of meteorological parameters and surface energy fluxes estimated in the present study have been assessed with those obtained at other coastal locations and locations close to oases or dry valleys. Van Den Broeke *et al.* (2004b, 2005) presented results from four AWSs installed in Dronning Maud Land, Antarctica. The *in situ* observations at AWS 5 has been compared with those observed at the study site at Schirmacher Oasis as it is located just inland of the grounding line in the coastal katabatic wind zone of the ice sheet in Dronning Maud Land. A comparison of the annual meteorological parameters and surface energy fluxes is shown in Table 4.3. The present study site has comparatively low

temperatures, low relative humidity and high wind speed, which will result in higher latent heat flux. High net shortwave radiation flux at the present study location is because of low albedo values. As the study location is close to ice free area of Schirmacher Oasis, wind blown dust events and high melting rate may be the reason for low albedo values.

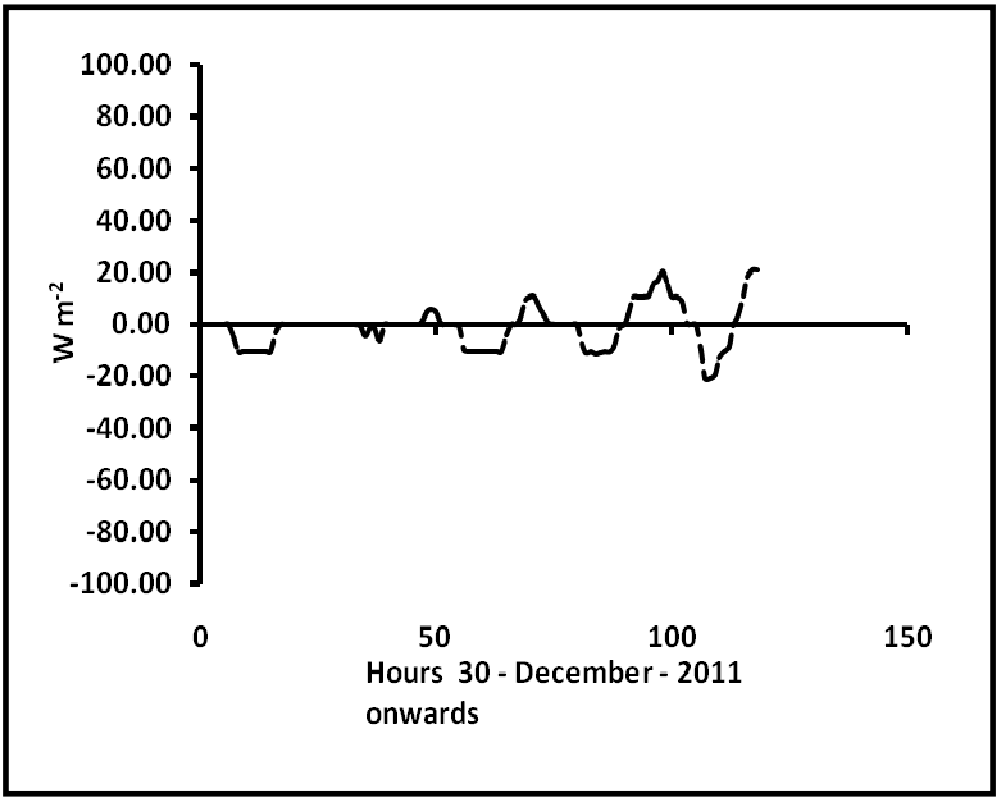

Figure 4.6 : Hourly subsurface heat flux (30 - December - 2011 onwards)

Annual mean net longwave radiation flux at AWS5 is reported -36.3 Wm^{-2} (Van den Broeke *et al.* 2004b), while at the present study site, it is -49 Wm^{-2}. The difference of 12.7 Wm^{-2} in the net longwave radiation flux at both the sites may be due to a combination of factors (e.g., differences in surface temperature, air temperature, atmospheric emissivities, cloud amount and cloud type etc.) at both the locations. In the present study, the parameterization scheme has been used to estimate net longwave radiation flux whereas Van den Broeke *et al.* (2004b) have measured net longwave radiation flux directly. Parameterization schemes used for estimation of longwave radiation fluxes may also have

various sources of error. Niemelä *et al.* (2001a) presented a comparison of the results of several incoming longwave radiative flux parameterization schemes with *in situ* recorded data. They have reported a bias -5 Wm^{-2}, standard deviation 8.4 Wm^{-2}, and RMS difference of 9.8 Wm^{-2} to Prata's scheme, which has been used to estimate incoming longwave radiation flux in the present study. For cloudy sky conditions, the uncertainty in the estimated longwave flux will be higher. So, all these factors may have contributed in difference of the net longwave radiation flux at the present study location and at the site reported by Van den Broeke *et al.* (2004b).

The meteorological parameters, mean annual air temperature, wind speed, relative humidity and incoming shortwave radiation flux have also been compared with those reported by Doran *et al.* (1996) at the Bunger Hills oasis, a large ice-free expanse on the coast of East Antarctica and are shown in Table 4.3. Mean annual air temperature and incoming shortwave radiation flux observed in the present study are comparable to those at Bunger Hills oasis while relatively lower relative humidity and high katabatic winds have been observed at the present study location. Parameters air temperature, relative humidity, wind speed, net shortwave radiation flux, net longwave radiation flux, net radiation flux, sensible heat flux and latent heat flux have also been compared for summer and winter seasons with those estimated in Bliss *et al.* (2011) at the Taylor Glacier, McMurdo Dry Valleys and are shown in Table 4.4. The present study location has comparatively high wind and low relative humidity during the summer and winter seasons. Both locations have high positive net radiation during summer and negative net radiation during winter. Sensible heat flux is positive for both the location during summer as well winter indicating flow of heat from air to surface for most of the time. Higher sensible heat flux has been observed at Taylor Glacier during winter indicating comparatively higher differences of surface and air temperature. Negative latent heat flux at both locations shows sublimation of ice and higher latent heat flux at present study location indicates higher rate of sublimation which may be as a result of higher wind speed and higher surface temperature.

Table 4.3 : Mean annual comparison of the meteorological parameters and surface energy fluxes at Study Area-1 site with coastal site location in WDML and Bunger Hills Oasis.

Parameter	**AWS 5 (Coastal WDML) Van Broeke et al (2004b)**	**Dozer point (Present study)**	**Bunger Hills Oasis East Antarctica (Doran et al, 1996)**
T_a (˚C)	-16.5	-10.2	-11.2
RH (%)	83	50	68.8
u (ms^{-1})	7.8 (10 m height)	8.3	4.6
SHW↓(Wm^{-2})	127.2	122.0	115
SHW↑(Wm^{-2})	-106.5	-76.0	-
SHW_{net} (Wm^{-2})	20.7	46.0	-
LW_{net} (Wm^{-2})	-36.3	-49.0	-
R_{net} (Wm^{-2})	-15.6	-3.0	-
Mean albedo	0.83	0.66	-
Mean annual atmospheric transmissivity	0.666	0.659	-

Table 4.4 : Mean seasonal comparison of the meteorological parameters and surface energy fluxes at Study Area-1 site with Taylor Glacier in McMurdo Dry valley

Parameter	**Summer Weather station (Wx T) Taylor Glacier, Bliss *et al.* 2011**	**Summer Dozer Point (Present study site)**	**Winter Weather station (Wx T) Taylor Glacier, Bliss *et al.* 2011**	**Winter Dozer Point (Present study site)**
T_a (˚C)	-4.6	-2.8	-26.8	-15.4

RH (%)	62.2	56	63	47
u (ms^{-1})	4.4	7.3	5.9	9.3
SHW_{net} (Wm^{-2})	125	102	0	3
LW_{net} (Wm^{-2})	-85	-55.2	-56	-45.2
R_{net} (Wm^{-2})	40	46.8	-56	-42.2
SHF (Wm^{-2})	6	13.2	55	32.6
LHF (Wm^{-2})	-33	-84.3	-5	-47.5

4.2.2.6 Energy Budget Closure

Net energy balance at the glacier surface is sum of R_{net}, *SHF*, *LHF* and sub surface heat flux (*G*) and is termed as residual energy flux (*REF*) (monthly mean of 4 years data are shown in Figure 4.7). Positive *REF* is the energy available for melt if glacier surface temperature is at 0˚C (Gusain *et al.* 2014a). Hourly melt has been estimated from the *REF* (Ambach and Kirchlechner 1986, Greuell and Konzelmann 1994) at the glacier surface for 4 years. Sublimation has been estimated from LHF. Monthly estimated sublimation and melt are shown in Figure 4.8. Melt has been observed during summer season only with December and January months having the highest melt rate. Highest sublimation has been observed during summer season and the lowest during transition2 period. Generally, this trend has been observed for all the four years. Estimated ablation (sum of sublimation and melt) at the glacier surface has been compared with recorded ablation from the ultra-sonic sensor for a limited period (Figure 4.9) at the study location. A high correlation coefficient (r^2 = 0.97) has been observed between estimated and recorded ablation (Figure 4.9). The ablation from the energy balance method has been obtained as 1.51 m w.eq. from 10 November 2007 to 7th February 2008 against recorded ablation of 1.53 m w.eq., which indicates that energy balance method estimated ablation is close to the actual ablation of the ice sheet.

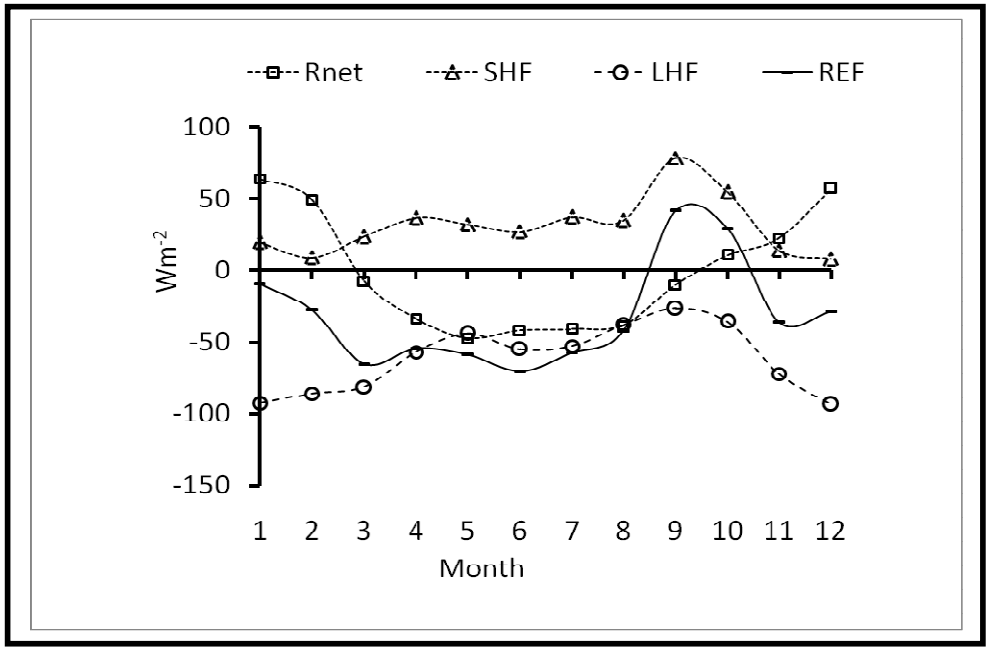

Figure 4.7: Monthly mean energy fluxes (based on 4 years data)

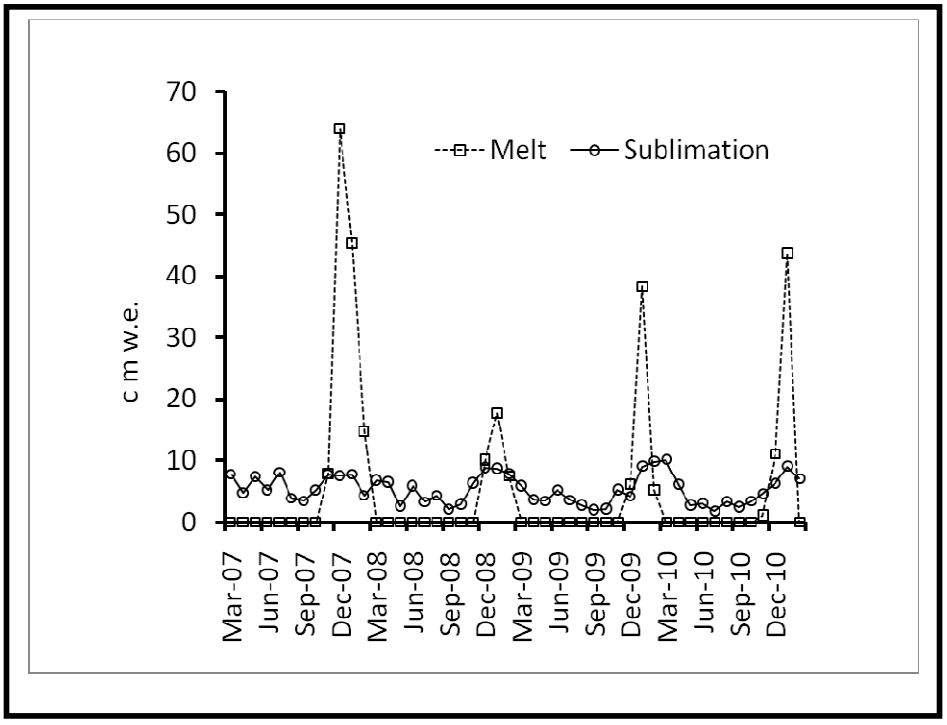

Figure 4.8: Monthly estimated sublimation and melt

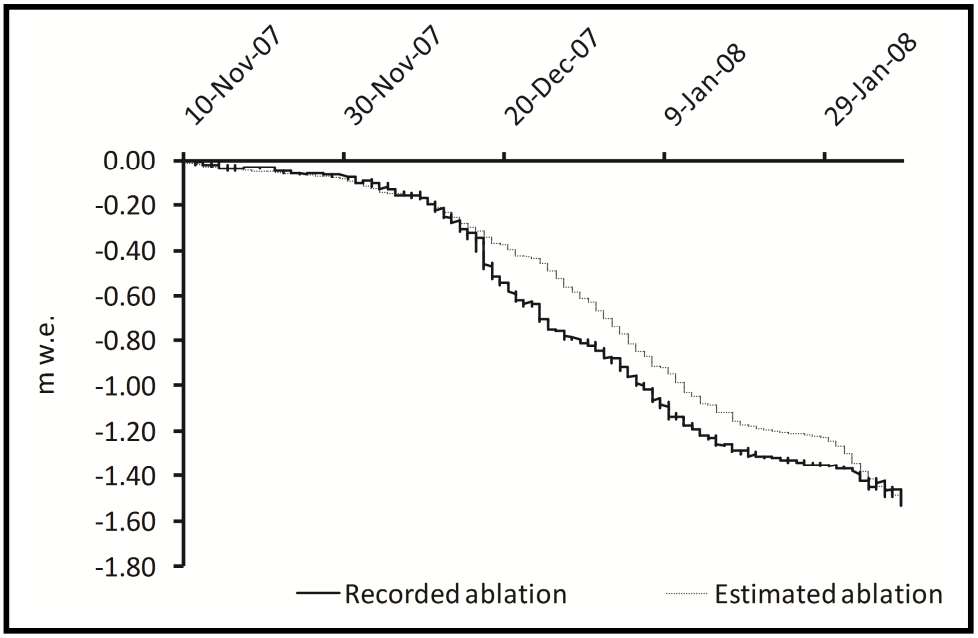

Figure 4.9: Recorded and estimated ablation

4.3 Summary

In this chapter, a four-years analysis of the meteorological parameters, radiative and turbulent energy fluxes of the ice sheet has been presented. Meteorological parameters have been recorded using *in situ* AWS measurements on ice sheet close to the Schirmacher Oasis in East Dronning Maud Land, Antarctica. The energy fluxes have been analysed for summer season, winter season and transition periods. The meteorological conditions at the observation site were characterised by mild air temperature (annual mean -10.2 ˚C), low relative humidity (annual mean 50%) and high katabatic winds (annual mean 8.3 m s^{-1}). Net shortwave radiation flux was high as compared to other coastal site of Dronning Maud Land and was comparable to those observed at Taylor Glacier, Mc Murdo Dry valleys, Antarctica. The mean annual atmospheric transmissivity was 0.659 for all weather days and 0.8 for clear sky days. Net longwave radiation flux was observed high as compared to the other coastal site of Dronning Maud Land and low as compared to the Taylor glacier site. Sensible heat flux was positive throughout the year and was the highest

(66.4 W m^{-2}) during transition2 period and the lowest (13.2 W m^{-2}) during summer season. Latent heat flux was the highest during summer (-84.3 W m^{-2}) and lowest (-31.2 W m^{-2}) during transition2 period. Latent heat flux was observed high as compared to the Taylor Glacier for both summer and winter seasons. Mild temperature, low relative humidity and high katabatic wind as compared to other Antarctic coastal locations cause high latent heat flux of the ice sheet close to Schirmacher Oasis equivalent to monthly sublimation rate of 5.29 cm w.eq.

All the *in situ* snow-met parameters and cloud data required for the study of the energy balance of the glacier/snow cover have not been collected in Western Himalaya. However, the method presented for energy balance may also be applicable to snow cover/glaciers of Western Himalaya.

In situ snow-met observations in cryospheric regions are difficult to obtain due to harsh climatic and topographic conditions. Cryospheric regions have limitations of poor monitoring using sparse *in situ* snow-met observations all over the globe. Surface energy fluxes estimated from sparse snow-met observations may therefore not characterize spatial variation of energy fluxes over a large snow/ice covered regions. Researchers have been making efforts to estimate surface energy fluxes of large areas using satellite remote sensing in conjuction with *in situ* observations. Next two chapters of this thesis present geo-spatial modeling of snow-met parameters and estimation of surface energy fluxes at spatial level.

Chapter V

MODELING OF SNOW-MET PARAMETERS

5.1 Introduction

Spatial variation in snow-met parameters over a large snow covered area may not be adequately characterized by sparse *in situ* measurements. In this chapter, a study on spatial modeling of three important snow-met parameters, namely, snow depth, snow albedo and snow/ice surface temperature has been presented.

The literature shows that snow depth has been estimated spatially using active and passive microwave satellite (Shi and Dozier 2000, Das and Sarwade 2008, Takala *et al.* 2011, Dai *et al.* 2012) data, through interpolation of *in situ* measurements (Foppa *et al.* 2007, Moreno and Bravo 2006), LIDAR and GPR surveys etc.. This parameter has also been estimated using passive microwave data in Western Himalaya snow cover from the regression model (Singh *et al.* 2007) and MEMLS model (Das and Sarwade 2008). These models have their own limitations as discussed in chapter 2. Here, an interpolation method proposed by Foppa *et al.* (2007) has been modified to estimate snow depth at spatial level in Western Himalaya.

Snow cover albedo has been studied over large snow covered regions using various satellite images e.g. MODIS, ASTER, AVHRR, AWiFS, LANDSAT, ETM+ etc. by a number of researchers (e.g., Liang *et al.* 1999, 2002, 2010, Greuell and Oerlemans 2004, Greuell *et al.* 2002, Schaaf *et al.* 2002). In most of the studies, the albedo estimation has

been based on radiative transfer simulation and required detailed atmospheric data at vertical levels. Narrowband to broadband albedo algorithms have also been developed (Song and Gao 1999, Liang 2000) and are easy to implement and provide albedo values at the time of satellite pass. The information on instant albedo at the time of satellite pass is very important for the estimation of net shortwave radiation flux. In this chapter, an algorithm for estimation of instantaneous albedo of snow/ice covered regions at the time of satellite pass using narrowband to broadband conversion method has been proposed.

The surface temperature has also been retrieved for different regions of the globe using thermal bands data obtained from sensors e.g. MODIS, AVHRR, ASTER etc. (Wan and Dozier 1996, Key *et al.* 1997, Hall *et al.* 2004, Brogioni *et al.* 2011, Hall 2011). Split-window algorithm and its variations has popularly been used to estimate surface temperature from thermal bands data. Here also, the same algorithm has been implemented to estimate surface temperature of the study area of Antarctica using thermal bands 31 and 32 of MODIS sensor.

5.2 Modeling Snow Depth

Snow depth has been modeled in Western Himalaya using interpolation of *in situ* measurements. Data from 14 manned observation locations of SASE have been used in modeling. A concept on generating virtual snow depth data to increase the density of input points (Foppa *et al.* 2007) has been included by defining snow line from remote sensing images. Estimated snow depth during different days of the winter season 2012-13 has been validated at 9 remote places using AWS recorded snow depth data in the study area. Figure 5.1 shows the manned observation locations and AWS locations. Detail methodology for estimation of snow depth and their validation, and analysis of results has been given in the following sections.

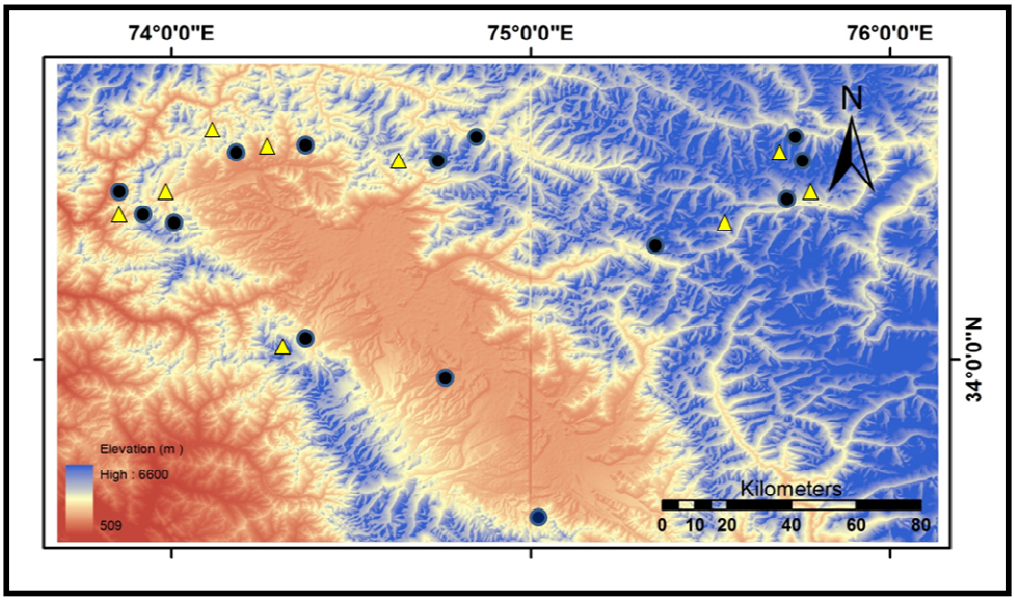

Figure 5.1 : Manned and AWS observation locations for snow depth (Circles in the map show manned snow depth observation locations and triangles show AWS snow depth observations).

5.2.1 Methodology

5.2.1.1 Generation of virtual snow depth data

Snow cover of Indian Western Himalaya has been mapped widely using remote sensing data obtained from a variety of sensors e.g. AWiFS, MODIS, LISS-3, LISS-4 etc. (Negi *et al.* 2008, Negi *et al.* 2009, Kulkarni *et al.* 2006, Sharma *et al.* 2014 etc.). SASE has also been involved in producing near real time binary snow cover maps of the Western Himalaya using MODIS data (Negi *et al.* 2008). An Earth Receiving Station (ERS) of MODIS has been established at SASE, Chandigarh, which receives daily real time images of Terra and Aqua MODIS at 0530 GMT and 0900 GMT. These images have been processed in near real time for generation of binary snow cover maps. These binary snow cover maps have been generated by the method described in section 3.3.3.5 of chapter 3. Lines differenciating between snow and no-snow in snow cover maps are termed as snowlines. Snowlines in different parts of the study area have been extracted from these maps using raster to vector conversion in Erdas Imagine 9.3 software.

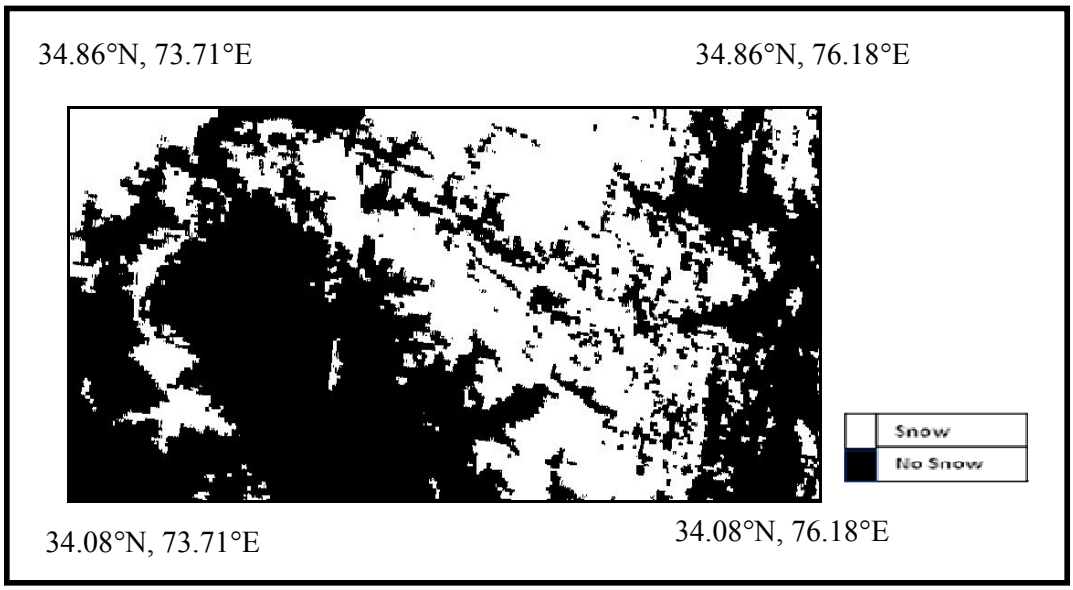

Figure 5.2 : Binary snow cover image retrieved from MODIS image

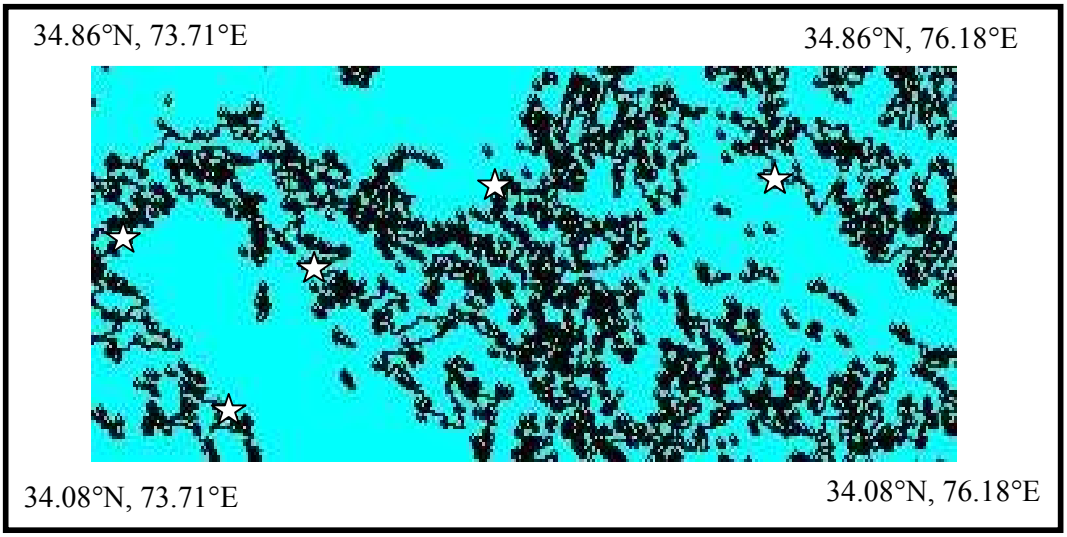

Figure 5.3 : Vector snow line map retrieved from binary snow cover image. Stars in the map show input data points with zero snow depth.

Figure 5.2 shows a binary snow cover map in the study area and Figure 5.3 shows the retrieved snow line image from the binary snow cover map. Snow depth at the edge of these snowlines has been considered as zero. Three to five such points with zero snow

depth have been selected manually from snowline of different parts of the study area (shown with star symbol in Figure 5.3) to include in the input data. Thus, the density of input data points for interpolation has been increased. The input data including three virtual snow depth data points for 03-03-2013 are given in Table 5.1.

Table 5.1 : Input data for interpolation model for 03-March-2013

Number	**Location**	**Elevation (m)**	**Snow Depth (cm)**
1	Banihal	3250	157
2	Srinagar	1664	0
3	Gulmarg	2800	145
4	HaddanTaj	3080	265
5	Stage-2	2650	215
6	Ragini	3160	300
7	Pharkian	2960	240
8	Z-Gali	3192	208
9	Kanzalwan	2440	143
10	Dawar	2414	212
11	Sonamarg	2745	130
12	Drass	3250	75
13	Pathar	4250	281
14	Firmbase	4760	191
15	Z_1	1643	0
16	Z_2	1943	0
17	Z_3	1751	0

5.2.1.2 Algorithm to estimate snow depth

Spatial interpolation method proposed by Foppa *et al.* (2007) uses snow depth data at discrete points to create a model of snow depth, from which a value for any location can

be estimated. The method is based on the dependency of snow depth on elevation above mean sea level. This general dependency is later adjusted through the *in situ* snow depth observations to represent the local and regional characteristics of the snow distribution. Snow depth at a particular pixel in the study area will have higher influence of the snow depth values at the nearest *in situ* observation location. The algorithm incorporates two steps.

Step 1: First, the base value, which describes the correlation between the snow depth and the elevation of a location *via* a power function, is determined. The general formulation is given as,

$$HS_j = G\,(he_j) + A_j \tag{5.1}$$

where, HS_j is the snow depth (cm) at grid cell (location) j, G is the base value (cm) obtained *via* a mathematical function, A_j is the compensation factor (cm), he_j the elevation or altitude or height of location j above mean sea level.

As the general description is an approximation that explains 50–70% of the total variance of the snow depth with elevation, the base value is adjusted with a local to regional compensation factor in a second step. The compensation factor value is added to the base value to adjust the snow depth value for each 500 m pixel (i.e., MODIS pixel).

Step 2: In this step, the base value is adjusted with a compensation factor. The compensation factor is calculated as the average of the difference of the base value of snow depth and the measured values of snow depth for the three locations nearest to the location where the snow depth has to be estimated. The formula for the compensation factor applied to three locations is given as,

$$A_j = \sum_{i=1}^{3} \frac{HS_i - G_i}{3} \tag{5.2}$$

here, HS_i is the snow depth (cm), G_i is the base value (cm), j is the location or pixel at which the snow depth has to be estimated, i is the three nearest locations where base value of snow depth has been estimated. It is important to note that the three nearest locations

are not just planimetric distance-wise but also elevation wise. The distance equation thus used is,

$$ds_{ji} = [(X_j - X_i)^2 + (Y_j - Y_i)^2 + p * (he_j - he_i)^2]^{1/2} \quad (5.3)$$

where, (X_j, Y_j, he_j) are the coordinates of the point where the snow depth has to be estimated and (X_i, Y_i, he_i) are coordinates of nearest three locations where base values have been estimated. The elevation of the neighboring points to the estimated value has been included to favor neighboring stations that lie in larger distance on the same elevation level over those neighboring stations that lie in smaller distance on a different elevation level. p is a weighting factor applied to favour horizontal distance over vertical distance as the snow depth varies with elevation and have similar values at same elevation level in a region. Foppa *et al.* (2007) assigned the value of p=5000 and obtained this value empirically through a sensitivity analysis of the compensation value for various p values.

The Foppa *et al.* (2007) method has some limitations, as stated below,

(1) Only one mathematical function (i.e., power function) has been used to describe the dependency of snow depth on elevation above mean sea level.

(2) Equal weightage has been given to the three locations nearest to the location where the snow depth has to be determined in estimation of compensation factor.

(3) The value of weighting factor p has been kept constant for all the days for which snow depth has been estimated.

The proposed spatial interpolation method has been suitably modified to get over these limitations and appear to be more flexible than the Foppa *et al.* (2007) model.

In the Step 1 of base value estimation, instead of using only a power function as the mathematical function, other mathematical functions such as linear, exponential, quadratic, etc. have been investigated. Snow depth changes daily due to metamorphic processes and ablation. Spatial and temporal variation in snow depth may not be represented well by only one mathematical function, so other mathematical functions have also been investigated. Each of these functions has been applied to estimate the snow depth. The RMSE between the estimated and observed snow depth for each function has been calculated. The mathematical function that gives the least RMSE has been selected and used as the function to estimate the base value of the snow depth. Thus, the type of base equation is not fixed rather dynamic as per the nature of the input data. In Foppa *et al*

(2007) model the base equation was fixed as power function while in the modified model the base equation is dynamic and may change daily as per the variation in input data.

In Step 2, modification has been done in estimation of compensation factor. The compensation factor has been computed as the weighted average of the difference of the base value of the snow depth and the observed values of snow depth at three stations that are nearest to the location at which the snow depth has to be estimated. The weights have been introduced to reduce the errors in estimation of snow depth. After determining the three nearest known snow depth locations, the weight to each location is given on the basis of its distance from the location where snow depth has to be estimated. Higher weight will be assigned to the known snow depth location which has least distance to the location where snow depth has to be estimated. The weight assigned to each location is given by,

$$we_i = \frac{(\sum_{i=1}^{3} ds_i)}{ds_i} \tag{5.4}$$

where, ds_i is the distance given in Equation (5.3). The normalised weight for each station is then calculated as,

$$nwe_i = \frac{we_i}{(\sum_{i=1}^{3} we_i)} \tag{5.5}$$

The formula for the compensation factor has thus been modified as,

$$A_i - \sum_{i=1}^{n} n\, we_i u_i \tag{5.6}$$

where, u_i is the difference between the observed snow depth and estimated snow depth at three known snow depth locations.

Once the appropriate mathematical function, weights, values of p etc. have been optimized, the equation 5.1 has been applied to the complete dataset acquired for the study area shown in Figure 5.1. At each pixel of the DEM, the base value of the snow depth ($G\ (he_j)$) and compensation factor (A_j) has been estimated. Given the elevation at each pixel through DEM, base value of the snow depth has been estimated using appropriate mathematical function. For instance, in Table 5.2 lists various mathematical functions,

which have been investigated. From these functions, appropriate mathematical function has been selected based on the least RMSE value obtained in determining base value of snow depth on 03.03.2013. The coefficients a, b, c of the mathematical functions have been estimated using the best fit between elevation and snow depth observations at known data points. The least RMSE between observed snow depth and estimated snow depth has been obtained for the quadratic mathematical function ($ahe^2+bhe+c$). So, this mathematical function has been selected for the estimation of base value of snow depth at each pixel. Given the input value *he* (elevation) from DEM at each pixel, base value of snow depth has been estimated for the complete dataset.

Table 5.2 : Mathematical functions investigated for selection of base value equation.

Mathematical Function	**Coefficient a**	**Coefficient b**	**Coefficient c**	**RMSE**
Linear ($ahe+b$)	0.0807900	-65.2000000	-	80.0649000
Quadratic ($ahe^2+bhe+c$)	-5.2040000e-005	0.4053000	-529.6000000	61.3708000
Power 1° (ahe^b)	0.0229000	1.1180000	-	81.9011000
Power 2° ($ahe^b + c$)	-3.6770000e+011	-2.8350000	259.9000000	62.5485000
Exponential 1° ($a.exp(bhe)$)	66.9600000	0.0003075	-	88.3790000

Adjustment factor at each pixel of the study area has been estimated using equation 5.6. For estimating adjustment factor at a pixel, first u_i at three nearest known snow depth locations have been estimated. Three nearest locations of a pixel has been selected by calculating distance of known snow depth locations using equation 5.3. Optimum value of '*p*' parameter in equation 5.3 has been obtained through a sensitivity analysis by studying

the RMSE between the observed snow depth and estimated snow depth. Estimated snow depth has been obtained by adding the base value of the snow depth to the adjustment parameter with different *p* values. The value of *p* has been varied from 100 to 5000 at an interval of 100. Then nearest stations of a pixel have been selected using distances calculated from equation 5.3. The snow depth has been estimated for the stations and the RMSE have been calculated for each value of *p*. A scatter plot showing RMSE values for different values of *p* for 03.03.2013 data is shown in Figure 5.4. From this plot, the value of *p* that produced minimum RMSE has been used for further calculations. For 03.03.2013 data, the value of *p* has been obtained as 1700.

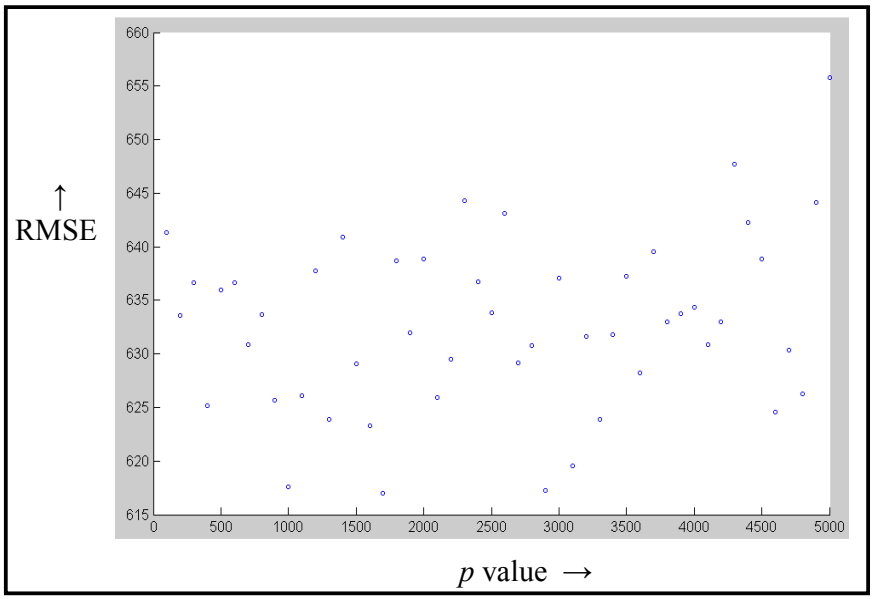

Figure 5.4 : RMSE values for different values of *p* for 03.03.2013 data

In the model proposed by Foppa *et al.* (2007), a fixed value of *p* was used for the data set of all days. In the present modified method, the value of *p* is dynamic and changes for every day data set. This *p* value has been fixed based on the least RMSE value between observed and estimated snow depth. Once *p* value has been selected, distances of the three nearest stations of a pixel has been computed. Using equation 5.5 and 5.6, normalised weights and compensation factor has been estimated. Using the estimated base value of snow depth $G\left(he_j\right)$ and compensation factor (A_j), snow depth has been estimated for each pixel of the study area.

Snow depth on 03 March 2013 has been estimated by both the methods i.e original model proposed by Foppa *et al.* (2007) and modified method proposed in the present research work. Results of the methods have been compared and discussed in the next section.

5.2.2 Results and Discussion

Snow depth estimated by modified algorithm has been compared with the snow depth obtained from the original algorithm proposed by Foppa *et al.* (2007). Table 5.3 shows the estimated show depth over calibration points for 03 March 2013 data using original and modified algorithm. It can be seen that the modified algorithm shows higher correlation coefficient (r = 0.86 vs r = 0.71) and better RMSE (37 cm vs 56 cm) as compared to that produced by the original algorithm. Table 5.4 shows the estimated snow depth over validation points using both the algorithms. It has been observed that for validation points also, modified algorithm shows higher correlation coefficient (r = 0.66 vs r =0.46) and better RMSE (65 cm vs 82 cm) as compared to that obtained from the original algorithm. After validating the snow depth estimated from the modified algorithm on the field data it has been applied on each pixel to ultimately generate snow depth maps for the different days of the winter season 2012-13. Maps have been generated for 02 January 2013, 04 January 2013, 07 January 2013, 21 January 2013, 03 March 2013, 25 March 2013 and 05 April 2013. Snow depth maps for four days e.g. 21 January 2013, 03 March 2013, 25 March 2013 and 5 April 2013 are shown in Figure 5.5. These snow depth maps have been also validated at 9 pixel locations using the data recorded by AWS (locations shown in Figure 5.1). Correlation coefficient between estimated and observed snow depth at validation locations have varies from 0.52 (on 21 January 2013) to 0.92 (on 02 January 2013) and RMSE varies from 24 cm (on 04 January 2013) to 65 cm (on 03 March 2013) on these dates. Figure 5.6 shows the estimated vs observed snow depth on these dates. A correlation coefficient of 0.71 and RMSE of 42 cm have been observed during different days of the season in the study area of Western Himalaya.

Table 5.5 shows the minimum, maximum and average snow depth as extracted from the snow depth maps of different dates. It can bee seen from the table that average snow depth in the study area increases from 21-January-2013 to 03-March-2013 and then

decreases till 05-April-2013. During January and February months, the air temperature in the study area are generally below 0°C. The snow depth accumulates after each snow fall in the region, which leads to higher average snow depth up to 03-March-2013. During the month of March, temperature in lower Himalaya rises above 0°C and hence the ablation of the snow cover starts in most of the part of lower Himalaya. Due to ablation of the snow cover, average snow depth decreases from 03-March-2013 to 05-April-2013. It has also been noticed from Table 5.5 that there is a continuous increase in the maximum snow depth in the study area from 21-January-2013 to 05-April-2013 and the difference between average snow depth and maximum snow depth on each date is high. On these dates, the maximum snow depth has been recorded from different parts of the study area and depends on the total snowfall, wind activity and temperature of that part of the study area. On 05-April-2013, maximum snow depth appears near Pathar location of study area. The meteorological data indincate that air temperature is below °C at this location. Thus, ablation of the snow cover has not started near this location. The reason for the high difference between average snow depth and maximum snow depth may be high wind deposition of snow at certain locations in the study area.

Snow depth maps have not been generated for the Study Area-1 i.e. Antarctica, as snow depth data for input in the algorithm are not available. However, if input data points are available, the algorithm will work for the Study Area-1 also.

Table 5.3 : Estimated snow depth using original and modified algorithm at calibration points for 03 March 2013

Number	**Location**	**Snow depth (cm)**	**Snow depth estimated by original algorithm (cm)**	**Snowdepth estimated by modified algorithm (cm)**
1	Banihal	157	95	156
2	Srinagar	0	0	0
3	Gulmarg	145	85	138
4	HaddanTaj	265	251	245

5	Stage-2	215	223	186
6	Ragini	300	285	298
7	Pharkian	240	180	182
8	Z-Gali	208	248	239
9	Kanzalwan	143	171	166
10	Dawar	212	176	171
11	Sonamarg	130	89	133
12	Drass	75	220	191
13	Pathar	281	176	251
14	Firmbase	191	235	199

Table 5.4 : Estimated snow depth using original and modified algorithm at validation points for 03 March 2013

Validation location Number	**Observed Snow Depth (cm)**	**Estimated by old model**	**Estimated by modified model**
1	62	240	192
2	72	145	134
3	130	205	169
4	103	83	136
5	214	233	228
6	212	230	219
7	75	170	172
8	111	79	123
9	208	223	186

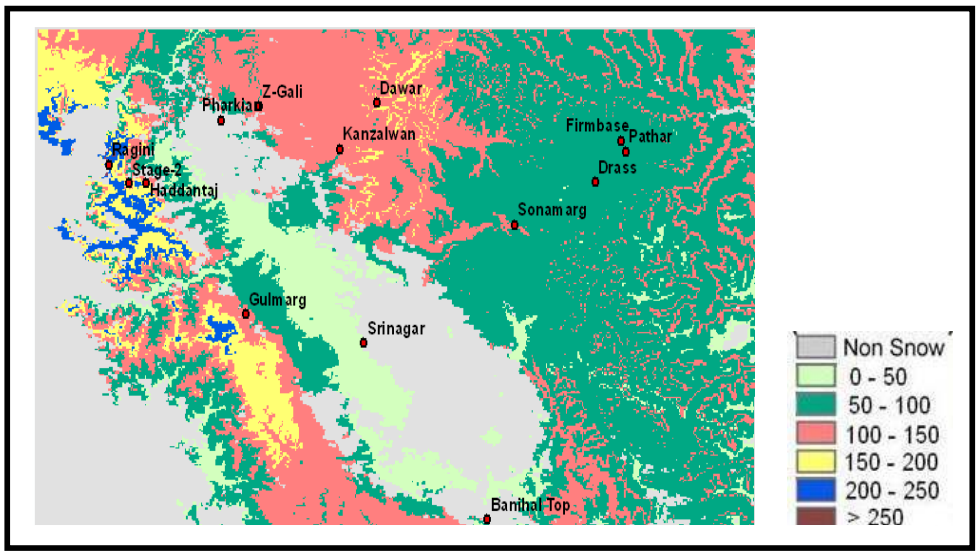

Figure 5.5a : Snow depth (cm) map for 21-January-2013

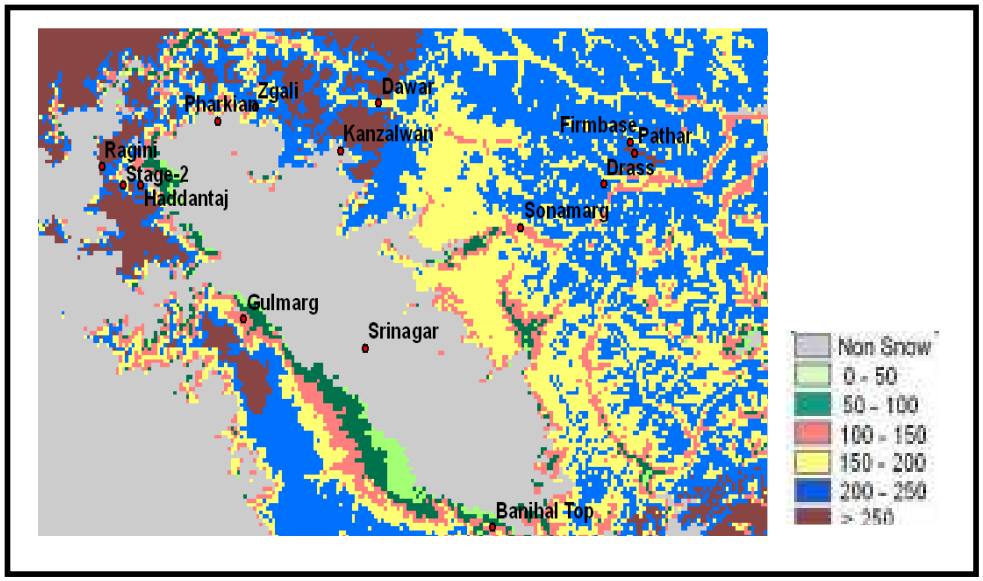

Figure 5.5b : Snow depth (cm) map for 3-March-2013

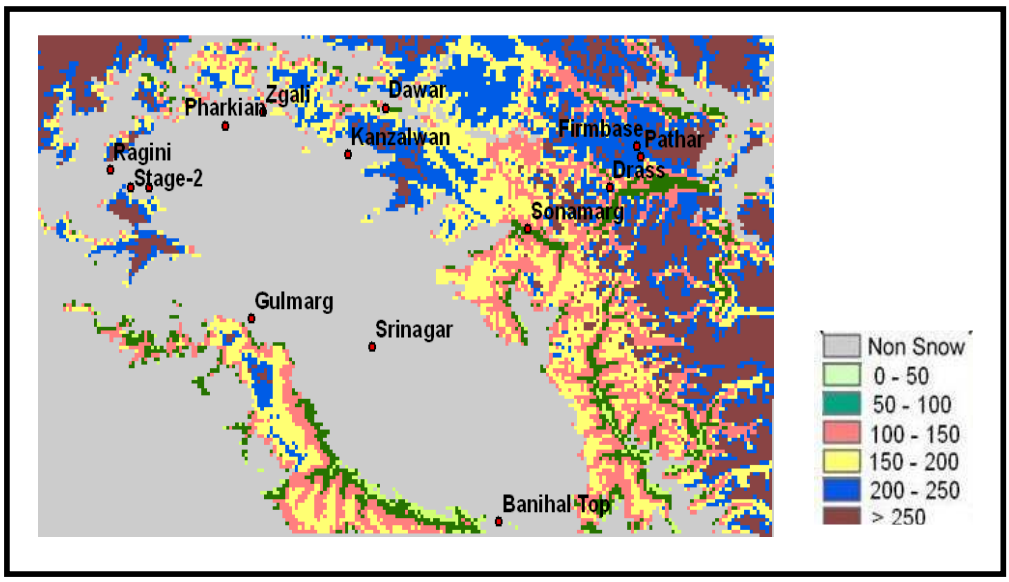

Figure 5.5c : Snow depth (cm) map for 25-March-2013

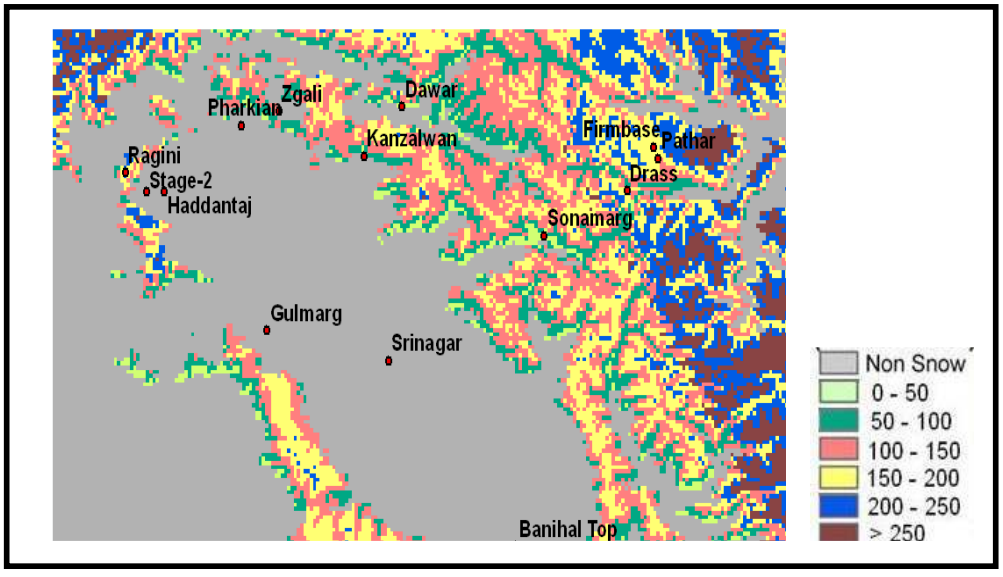

Figure 5.5d : Snow depth (cm) map for 5-April-2013

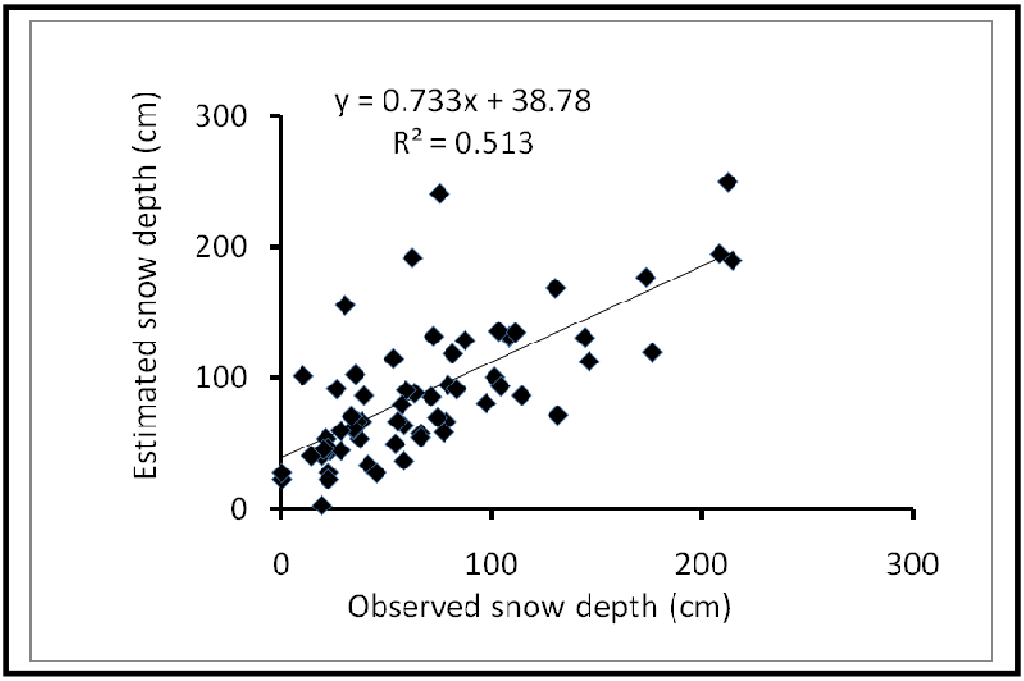

Figure 5.6: Estimated vs Observed snow depth for different dates during the season 2012-13

Table 5.5 : Minimum, maximum and average snow depth for different dates

Date	**Minimum Snow Depth (cm)**	**Maximum Snow Depth (cm)**	**Average Snow Depth (cm)**
21.01.2013	0	285.0	70.1
03.03.2013	0	307.0	128.3
25.03.2013	0	389.0	90.5
05.04.2013	0	465.0	72.7

5.3 Modeling Albedo

Broad band albedo of the snow cover has been modeled using snow cover reflectances in the narrow bands. Hyper spectral signatures of the snow cover have been collected in field using spctroradiometer experiments. These experiments have been conducted at Solang and Dhundi experimental site, shown in Figure 5.7. Collected hyperspectral signatures have reflectance of snow cover and solar irradiance in the wavelength band 350 nm to 2500 nm and are shown in Figure 5.8. Spectral reflectance for snow in the wavelength range 350 nm to 900 nm is high and is observed as greater than 0.6 for all the days. During peak winter period (January and February months), spectral reflectance of snow in visible region (400 nm – 700 nm) is more than 0.8. From 900 nm to 1500 nm, the spectral reflectance of the snow decreases and in the shortwave infrared region (SWIR) beyond 1500 nm reflectance of snow is low observed to be less than 0.2. Solar irradiance is high in the visible region between 400 nm to 700 nm and is more than 1 $W/cm^2/\mu m$. Beyond visible region solar irradiance decreases gradually and observed less than 0.2 $W/cm^2/\mu m$ in the SWIR region. These hyperspectral signatures have been used to develop the algorithm for estimation of broadband albedo of snow from AWiFS and MODIS images. Algorithm has been developed for the wavelength bands which are available in AWiFS and MODIS sensors and the input for the algorithm is reflectance in different wavelength bands of AWiFS and MODIS sensors. The algorithms have been validated using the *in situ* albedo data collected at three sites i.e. Solang, Dhundi and Patseo and these sites are shown in Figure 5.7. The detail methodology of the model development and results are given in the following sections.

5.3.1 Methodology

Snow covered surfaces are usually characterized by very high spectral reflectance in the visible wavelength region, which rapidly decreases in NIR and SWIR regions (Mishra *et al.* 2012). Figure 5.8 shows the average spectral reflectance characteristics of snow cover and spectral distribution of transmitted solar irradiance at different sampling locations

surrounding Solang and Dhundi stations in the study area during six different passes of satellite carrying AWiFS sensor. It can be inferred from these figures that snow is characterized by high spectral reflectance in the visible part of an electromagnetic spectrum. It tends to decline in the near infrared region until 1050 nm wavelength, where marginal increase in reflectance occurs. A minor peak in reflectance can be seen at approximately 1090 to 1100 nm wavelength. The minor peaks can also be seen at around 1800 nm and 2250 nm wavelength with a sharp dip in reflectance at about 1950 nm to 2050 nm. This is due to the presence of water absorption bands at these wavelengths. The transmitted solar irradiance (Figure 5.8) has been found to be maximum in visible wavelength region with a gradual decrease with increase in wavelength. The irradiance contribute 46.2 % in 400-700 nm, 26.8% between 700-1000 nm, 16.7% in 1000-1500 nm and 10.2% in 1500-2500 nm wavelength regions. The *in situ* observations have been used to,

i) establish a relationship between existing narrow AWiFS and MODIS wave bands and corresponding broadband for estimation of values of the conversion factors in development of algorithm.

ii) estimate broad band albedo (BBA) and its validation with AWiFS satellite sensor retrieved albedo.

Narrowband reflectance in VIS and SWIR regions of AWiFS and MODIS sensors are very important in characterizing snow surface conditions. Data from three bands of AWiFS (Bands 2, 4 and 5) and seven bands of MODIS (Band1- Band7) have been used to develop the algorithm for narrow band to broad band albedo (NBBA) of snow. The flow chart of detailed methodology for NBBA is given in the Figure 5.9.

Song and Gao (1999) proposed an approach to convert narrow band reflectance (NBR) to broad band albedo (BBA) from Advance Very High Resolution Radiometer (AVHRR) image acquired in two bands. The same approach has been adopted here to derive a new algorithm considering three spectral bands (Band 2, Band 4 and Band 5) of AWiFS image (Table 3.6 given in chapter 3) and seven spectral bands (Band 1 – Band 7) of MODIS image (Table 3.4 given in chapter 3).

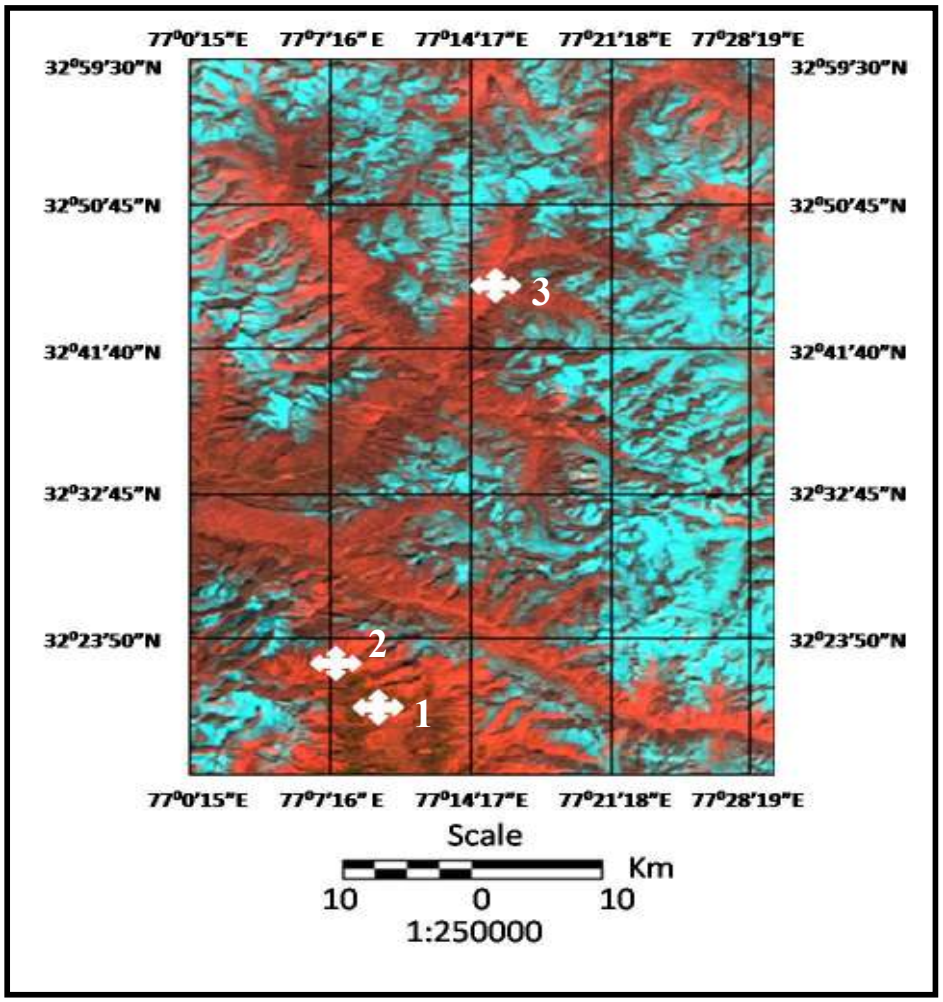

Figure 5.7 : Experimental sites for collection of *in situ* data used for model development and validation. Site 1 : Solang, Site 2: Dhundi and Site 3: Patsio.

The surface integrated albedo, α, in any wavelength interval, $\Delta\lambda$, is defined as the ratio of the integrated reflected energy , $\sum E_{s\Delta\lambda}\,\rho_{\Delta\lambda}$, to the integrated downward irradiance, $\sum E_{s\Delta\lambda}$, at the solar zenith angle, θ and can be expressed as (Liang 2003),

$$\alpha = \frac{\sum_{\Delta\lambda} E_{s\Delta\lambda}\,\rho_{\Delta\lambda}}{\sum_{\Delta\lambda} E_{s\Delta\lambda}} \tag{5.7}$$

where, $E_{s\Delta\lambda}$ is the incoming solar energy and $\rho_{\Delta\lambda}$ is the surface reflectance in wavelength interval,$\Delta\lambda$. Precise estimation of BBA from narrow band reflectance (NBR) from a remote sensing image can be obtained when following three factors are accounted for:

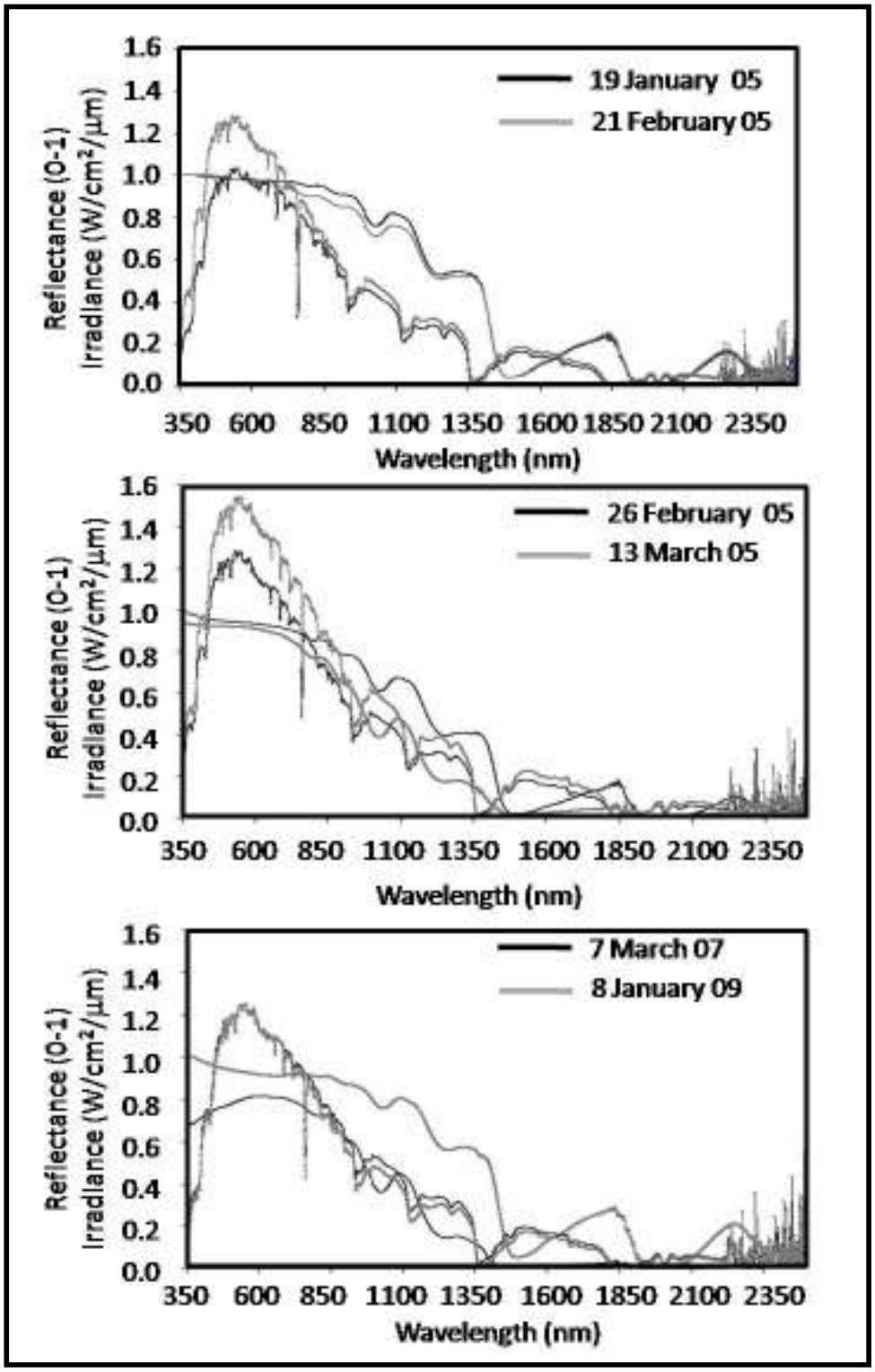

Figure 5.8: Field observations of spectral reflectance (0-1) and irradiance during different dates corresponding to the time of AWiFS acquisition.

(i) the spectral reflectance characteristics of the surface of interest, (ii) the spectral distribution of the irradiance, and (iii) the wavelength region of the discrete spectral bands.

The AWiFS image has four narrow spectral bands in VIS (λ = 520-590 nm and 620-680 nm), NIR (770-860 nm) and SWIR (1550-1700 nm). The reflectance in these narrow bands can be converted to the total BBA in the spectrum (400 - 2500 nm). Similarly, seven narrow spectral bands of MODIS image in VIS (459-479 nm, 545-565 nm and 620-670 nm), NIR (841-876 nm and 1230-1250 nm) and SWIR (1628-1652 nm and 2105 - 2155 nm) can be used for NBR to BBA conversion. To convert from NBR to BBA, however, an improved understanding of the relationship between the reflectance characteristics of the narrow bands with that of broad band for snow surfaces is required. In the present work, the spectrum has been divided into different sub-regions as, for AWiFS image; the VIS sub region (400-700 nm), NIR sub region (700-1500nm) and SWIR sub region (1500-2500 nm). In case of MODIS image, different sub regions are VIS (400-500 nm, 500-600 nm and 600-700 nm), NIR (700-1000 nm and 1000-1500 nm), and SWIR(1500-2000 nm and 2000 - 2500 nm). The selection of the sub regions depends primarily on (i) consistency of data in AWiFS and MODIS narrow spectral bands in these regions (ii) independence in spectral reflectance characteristics of snow surface in these regions.

The total BBA for AWiFS image considering solar irradiance in the three sub-regions (i.e. VIS, NIR, and SWIR) can be represented as,

$$\alpha_{AWiFS} = \frac{\sum_{\Delta\lambda 1} E_{s\Delta\lambda 1}\ \rho_{\Delta\lambda 1} + \sum_{\Delta\lambda 2} E_{s\Delta\lambda 2}\ \rho_{\Delta\lambda 2} + \sum_{\Delta\lambda 3} E_{s\Delta\lambda 3}\ \rho_{\Delta\lambda 3}}{\sum_{\Delta\lambda} E_{s\Delta\lambda}} \tag{5.8}$$

where, the wavelength interval $\Delta\lambda$ represents spectral region (400-2500 nm); $\Delta\lambda 1$, $\Delta\lambda 2$ and $\Delta\lambda 3$ correspond to three sub regions of the spectrum (i.e., $\Delta\lambda 1$: 400-700 nm; $\Delta\lambda 2$: 700-1500 nm and $\Delta\lambda 3$: 1500-2500 nm). E_s and ρ are solar irradiance and reflectance in different bands, respectively.

Similar to equation (5.8), the BBA for MODIS can be represented as,

$$\alpha_{MODIS} = \frac{\sum_{\Delta\lambda m1}^{\Delta\lambda m7} E_{s\Delta\lambda m}\ \rho_{\Delta\lambda m}}{\sum_{\Delta\lambda} E_{s\Delta\lambda}} \tag{5.9}$$

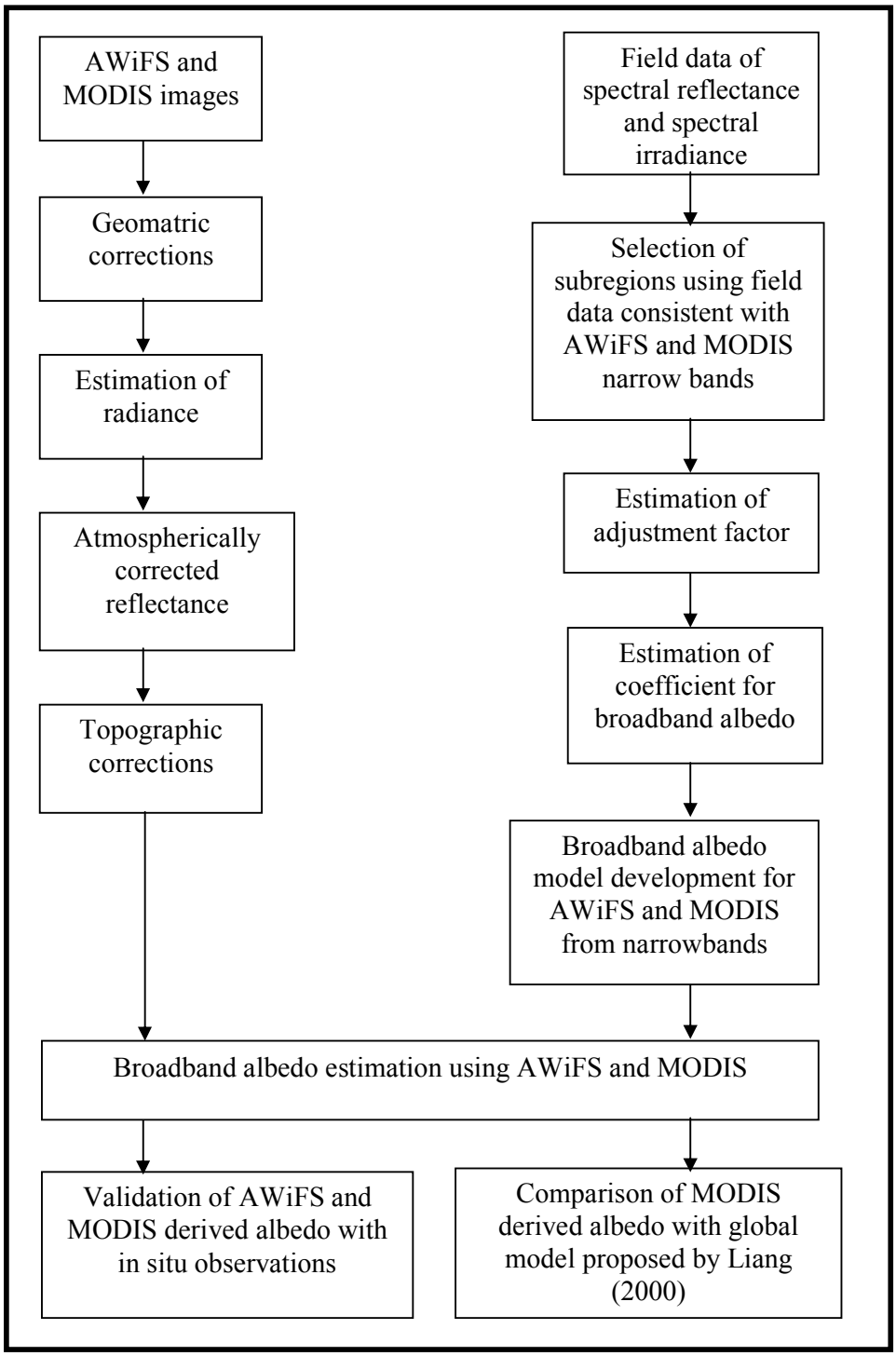

Figure 5.9: Flow chart showing methodology for model development of broad band albedo and validation.

where, $\Delta\lambda_{m1-m7}$(m suffix for MODIS) represents seven sub regions of solar spectrum in VIS, NIR and SWIR. $E_{s\Delta\lambda m}$ and $\rho_{\Delta\lambda m1-m7}$ are the solar irradiance and reflectance corresponding to broadband sub regions in different wavelength bands, $\Delta\lambda_{m1-m7}$ $(\Delta\lambda_{m1}, \Delta\lambda_{m2}, \ldots, \Delta\lambda_{m7})$ respectively.

The estimated values of broadband reflectance obtained from equations (5.8) and (5.9) may be different than the narrow band reflectances in corresponding AWiFS and MODIS spectral bands respectively. Therefore, an adjustment factor that defines the relation between broad band and narrow band reflectance may be derived (Song and Gao 1999). The adjustment factor quantifies the ratio of the reflected radiations within the narrow spectral bands to the reflected radiations of the corresponding broad band in VIS, NIR and SWIR regions.

Let f_1 to f_3 and f_{1m} to f_{7m} be the adjustment factors for AWiFS and MODIS images respectively. Equation (5.8) for AWiFS can then be rewritten as,

$$a = \frac{f_1^{-1} E_{s\Delta\lambda v} \rho_{\Delta\lambda v} + f_2^{-1} E_{s\Delta\lambda n} \rho_{\Delta\lambda n} + f_3^{-1} E_{s\Delta\lambda s} \rho_{\Delta\lambda s}}{\sum_{\Delta\lambda} E_{s\Delta\lambda}} \tag{5.10}$$

where, subscripts v, n and s refer to narrow VIS, NIR and SWIR bands of AWiFS sensor respectively. By comparing (5.8) with (5.10), f_1, f_2 and f_3 can be estimated for AWiFS as,

$$f_1 = \frac{\rho_{\Delta v} E_{s\Delta\lambda v}}{\sum E_{s\Delta\lambda_1} \rho_{\Delta\lambda_1}} \tag{5.11a}$$

$$f_2 = \frac{\rho_{\Delta n} E_{s\Delta\lambda n}}{\sum E_{s\Delta\lambda_2} \rho_{\Delta\lambda_2}} \tag{5.11b}$$

$$f_3 = \frac{\rho_{\Delta s} E_{s\Delta\lambda s}}{\sum E_{s\Delta\lambda_3} \rho_{\Delta\lambda_3}} \tag{5.11c}$$

Similarly, the adjustment factors, f_{1m}, f_{2m}, -----,f_{7m}, may be estimated for MODIS as,

$$f_{1m} - \frac{\rho_{\Delta v_1} E_{s\Delta\lambda v_1}}{\sum E_{s\Delta\lambda m_1} \rho_{\Delta\lambda m_1}} \tag{5.12a}$$

$$f_{2m} = \frac{\rho_{\Delta n_2} E_{s\Delta\lambda n_2}}{\sum E_{s\Delta\lambda m_2} \rho_{\Delta\lambda m_2}} \tag{5.12b}$$

$$f_{3m} = \frac{\rho_{\Delta v_3} E_{s\Delta\lambda v_3}}{\sum E_{s\Delta\lambda m_3} \rho_{\Delta\lambda m_3}} \tag{5.12c}$$

$$f_{4m} = \frac{\rho_{\Delta v4}\, E_{s\Delta\lambda v4}}{\sum E_{s\Delta\lambda m4}\, \rho_{\Delta\lambda m4}} \tag{5.12d}$$

$$f_{5m} = \frac{\rho_{\Delta n5}\, E_{s\Delta\lambda n5}}{\sum E_{s\Delta\lambda m5}\, \rho_{\Delta\lambda m5}} \tag{5.12e}$$

$$f_{6m} = \frac{\rho_{\Delta s6}\, E_{s\Delta\lambda s6}}{\sum E_{s\Delta\lambda m6}\, \rho_{\Delta\lambda m6}} \tag{5.12f}$$

$$f_{7m} = \frac{\rho_{\Delta s7}\, E_{s\Delta\lambda s7}}{\sum E_{s\Delta\lambda m7}\, \rho_{\Delta\lambda m7}} \tag{5.12g}$$

where, subscripts v, n and s refer to narrow VIS, NIR and SWIR bands of MODIS sensor. $\Delta\lambda_{m1}, \Delta\lambda_{m2}$ ….., $\Delta\lambda_{m7}$ represent broadband sub-regions consistent with MODIS the spectral bands.

Assuming a linear relationship between the narrowband and the broadband albedo (Stroeve and Nolin 2002a, 2002b), the surface albedo from data of AWiFS and MODIS sensors can be estimated as,

$$\alpha_{AWiFS} = c_1 \rho_2 + c_2 \rho_4 + c_3 \rho_5 + d \tag{5.13}$$

$$\alpha_{MODIS} = c_{1m}\, \rho_{1m} + c_{2m}\, \rho_{2m} + c_{3m}\, \rho_{3m} + c_{4m}\, \rho_{4m} + c_{5m}\, \rho_{5m} + c_{6m}\, \rho_{6m} + c_{7m}\, \rho_{7m} + d_m \tag{5.14}$$

where, c's are coefficients, ρ's are narrow band reflectance in AWiFS and MODIS bands, and d is an offset, which is typically determined by comparing estimated values of albedo from the model with those obtained from *in-situ* observations. On combining equations (5.10), (5.11) and (5.13), the values of coefficients may be estimated as:

$$c_i = w_i\, f_i^{-1} \tag{5.15}$$

Where, w_i is the percentage of solar irradiance within the i^{th} wavelength bands of AWiFS or MODIS sensors to that of irradiance received in the wavelength range 350 nm to 2500 nm. This is estimated using *in situ* observations of solar spectral irradiance (Figure 5.8). The values of f_i are calculated using the *in situ* observations of spectral reflectance and spectral irradiance in equations (5.11) and (5.12) recorded at the time of satellite pass.

5.3.2 Results and Discussion

5.3.2.1 Algorithms for AWiFS and MODIS Sensor Images

The values of empirical coefficient, c_i, for AWiFS and MODIS sensors have been estimated using equation (5.15) and are given in the Table 5.6. Higher values of AWiFS coefficients C_1 and C_2 indicate higher contribution of AWiFS band 2 and band 4 reflectance in the broadband albedo of snowcover. Higher values of MODIS coefficients $C_{1m} - C_{5m}$ indicate higher contribution of MODIS bands 1-5 reflectnace in the broadband albedo. Using coefficients $C_1 - C_3$ and $C_{1m} - C_{7m}$, given in Table 5.6, equation 5.13 and 5.14 can be re-written as,

$$\alpha_{AWiFS} = 0.463\rho_2 + 0.360\rho_4 + 0.094\rho_5 + 0.026 \quad (5.16)$$

$$\alpha_{MODIS} = 0.145\rho_{1m} + 0.275\rho_{2m} + 0.138\rho_{3m} + 0.165\rho_{4m} + 0.214\rho_{5m} + 0.06\rho_{6m} + 0.06\rho_{7m} - 0.11 \quad (5.17)$$

Using equations (5.16) and (5.17), broadband albeo of snowcover can be estimated from AWiFS and MODIS sensor images, respectively.

Table 5.6 Model coefficients for AWiFS and MODIS to convert narrowband to broad band albedo

AWiFS Coefficients		MODIS Coefficients	
C_1	0.463	C_{1m}	0.145
C_2	0.360	C_{2m}	0.275
C_3	0.094	C_{3m}	0.138
D	0.026	C_{4m}	0.165
		C_{5m}	0.214
		C_{6m}	0.06
		C_{7m}	0.06
		d_m	-0.011

5.3.2.2 Validation of Broadband Albedo (BBA) Algorithms

In this section, results of satellite sensor estimated snow BBA and their validation with *in situ* observations at Solang, Dhundi and Patsio sites have been presented. At Solang and Dhundi sites, BBA maps have been validated using *in situ* data of spectroradiometer. At Patsio site, BBA maps have been validated using *in situ* data of albedometer mounted on AWS. Albedo maps using MODIS images have also been validated in Study Area-1 i.e. Antarctica. Detail discussion of validation of BBA maps are given as following,

5.3.2.2.1 Validation at Solang and Dhundi sites using AWiFS image

The BBA maps obtained using equation (5.16) for snow covered regions of Solang-Dhundi and surrounding area are shown in the Figure 5.10. Solang and Dhundi sites lie in the Pir Panjal range of Western Himalaya. The snow BBA measured from ASD spectroradiometer has been used for validation at these sites. The value of broadband albedo of snow in these maps varies from 0.2 to 0.9. In majority of the area, higher values (0.7 - 0.9) can be seen for the data acquired during January and February months than those obtained for the month of March, where the albedo in most of the snow area ranges from 0.5 - 0.7. This decrease may be attributed to the melting of snow during March. Figure 5.11 shows the comparison of AWiFS retrieved BBA and *in situ* recorded BBA at Solang and Dhundi sites during different days. In first plot of the Figure 5.11, x-axis shows the *in situ* recorded (observed) albedo values while y-axis shows the AWiFS retrieved (estimated) albedo values. The R^2 between observed and estimated values has been obtained more than 0.94 during different days. Second plot of the Figure 5.11 shows the comparison of *in situ* recorded and AWiFS retrieved albedo on 19 January 2005, 21 February 2005, 26 February 2005, 13 March 2005, 7 March 2007 and 8 January 2009 respectively. These dates correspond to the dates of AWiFS image acquisition. The RMSE between observed and estimated albedo has been obtained as 0.03.

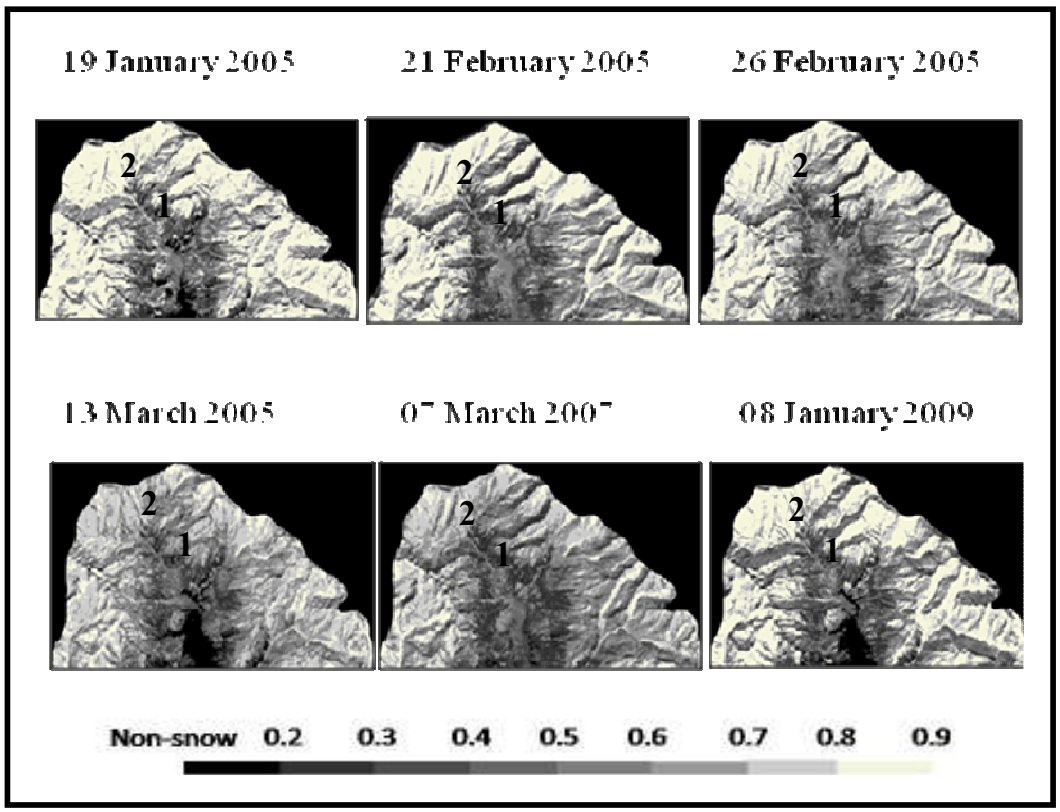

Figure 5.10 : Broadband albedo using AWiFS images for dates of *in situ* observations at validation sites 1 and 2 (Geographic extent of the maps are from 32°14' 55" N - 32°23'50"N and 77°01'30" E - 77°16'10"E).

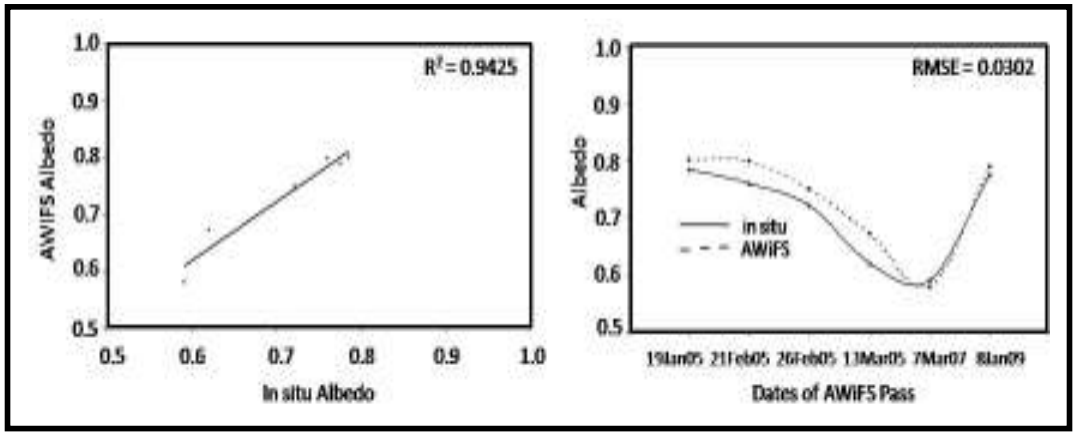

Figure 5.11: Comparison of the retrieved snow broadband albedo with the *in situ* measurements at sites Solang and Dhundi.

5.3.2.2.2 Validation at Patsio site using AWiFS and MODIS Images

Patsio site lies in the Great Himalaya range of Western Himalaya. The snow BBA measured from albedometer mounted on AWS has been used for validation at this site. Figure 5.12 shows the maps of snow BBA using AWiFS images. These maps have been validated with *in situ* albedo measurements. Figure 5.13 shows the relationship between AWiFS retrieved snow broadband albedo and *in situ* measured albedo at Patsio site. In first plot of the Figure 5.13, x-axis shows the *in situ* recorded (observed) albedo values while y-axis shows the AWiFS retrieved (estimated) albedo values. The R^2 between observed and estimated values has been obtained 0.94 during different days. Second plot of the Figure 5.13 shows the comparison of *in situ* recorded and AWiFS retrieved albedo on 24 December 2008, 08 January 2009, 31 January 2009, 15 February 2009, 25 February 2009, 11 March 2009 and 16 March 2009 respectively. These dates correspond to the dates of of AWiFS image acquisition. The RMSE between observed and estimated albedo has been obtained as 0.0274. The R^2 value and RMSE show that the AWiFS estimated BBA are in close agreement with the *in situ* measurements at the Patsio site also.

The snow BBA estimated from MODIS images have been validated with *in situ* observations at Patsio site. The proposed model for MODIS has also been compared with global albedo model proposed by Liang (2000). Figure 5.14a shows the correlation between MODIS estimated BBA of snow using proposed model with *in situ* observed albedo at Patsio site. A high correlation (R^2=0.88) has been observed between model estimated and measured albedo at the site. Figure 5.14b shows the correlation between MODIS estimated BBA of snow using Liang (2000) model and *in situ* observed albedo at the same site. A high correlation (R^2=0.84) has also been observed for the Liang (2000) model. Figure 5.14c shows the RMSE between the *in situ* measured albedo with proposed model, as well as with Liang (2000) model. A low RMSE (0.026 for proposed model and 0.031 for Liang model) have been observed between estimated albedo and *in situ* measured albedo for both the models. The global albedo model developed by Liang (2000) has not been validated for snow and ice, although the model is validated for other land covers. These results show that both the models can estimate broadband albedo of snowcover using MODIS images efficiently. However, model proposed in the present work performed slightly better, which indicates that the proposed model may produce

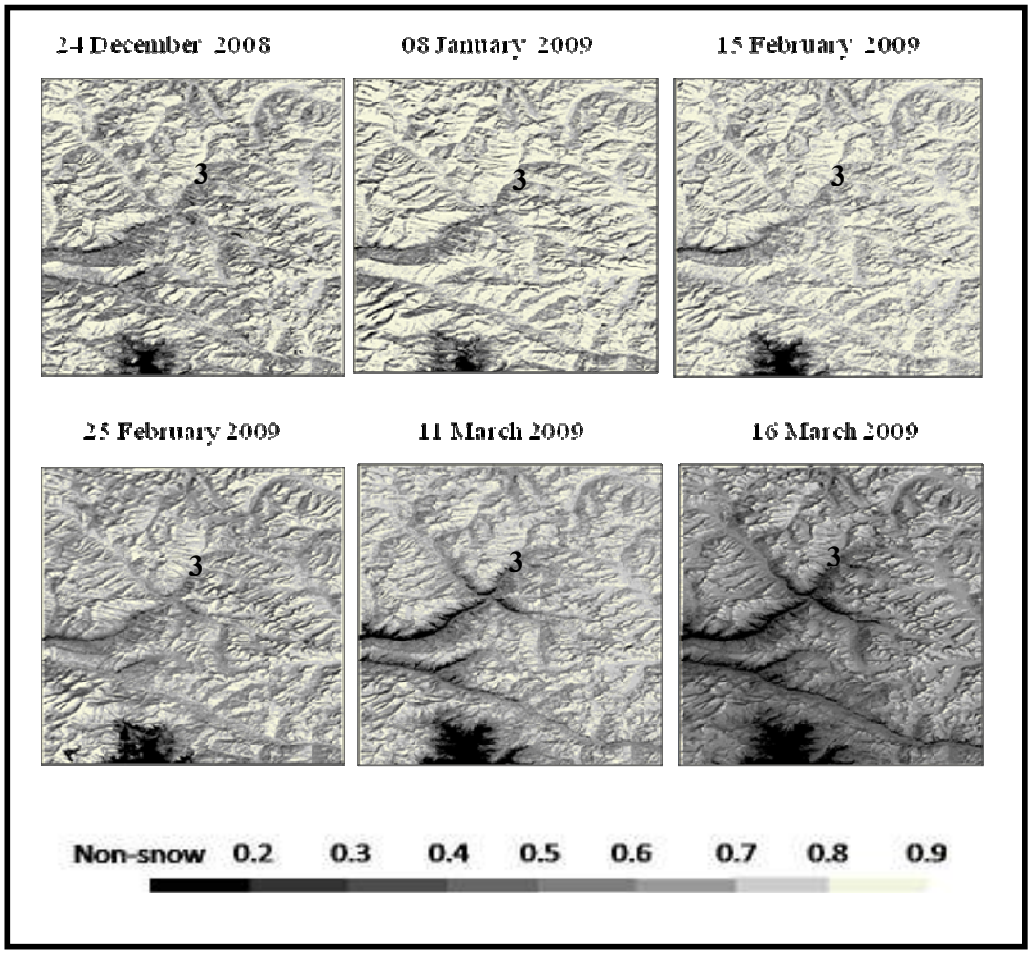

Figure 5.12 : Broadband albedo using AWiFS images for dates of *in situ* observations at validation site 3 (Geographic extent of the maps are from 32°14' 55" N - 32°59'30"N and 77°0'15" E - 77°28'19"E).

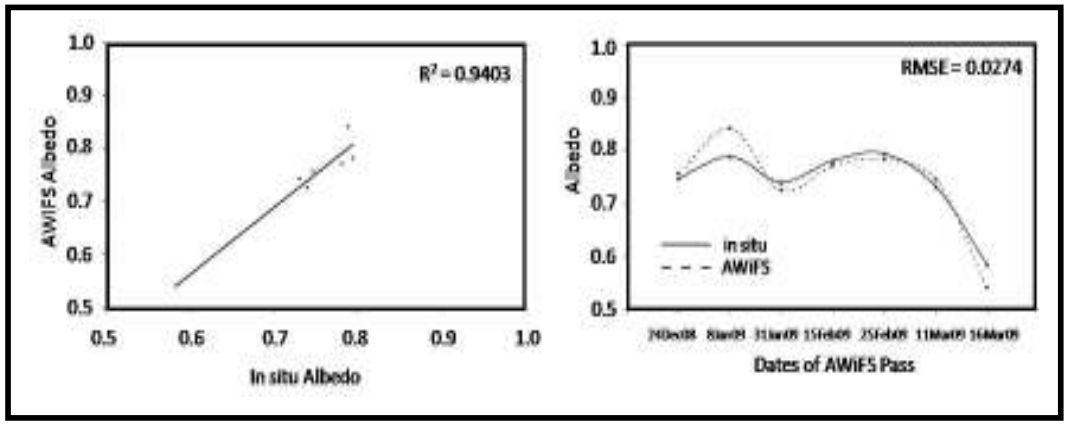

Figure 5.13: Comparison of the AWiFS retrieved snow broadband albedo with the *in situ* measurements at Patsio site

better BBA maps for the study area. Figure 5.15 shows the thematic maps produced from proposed BBA model using MODIS images in the study area during different dates.

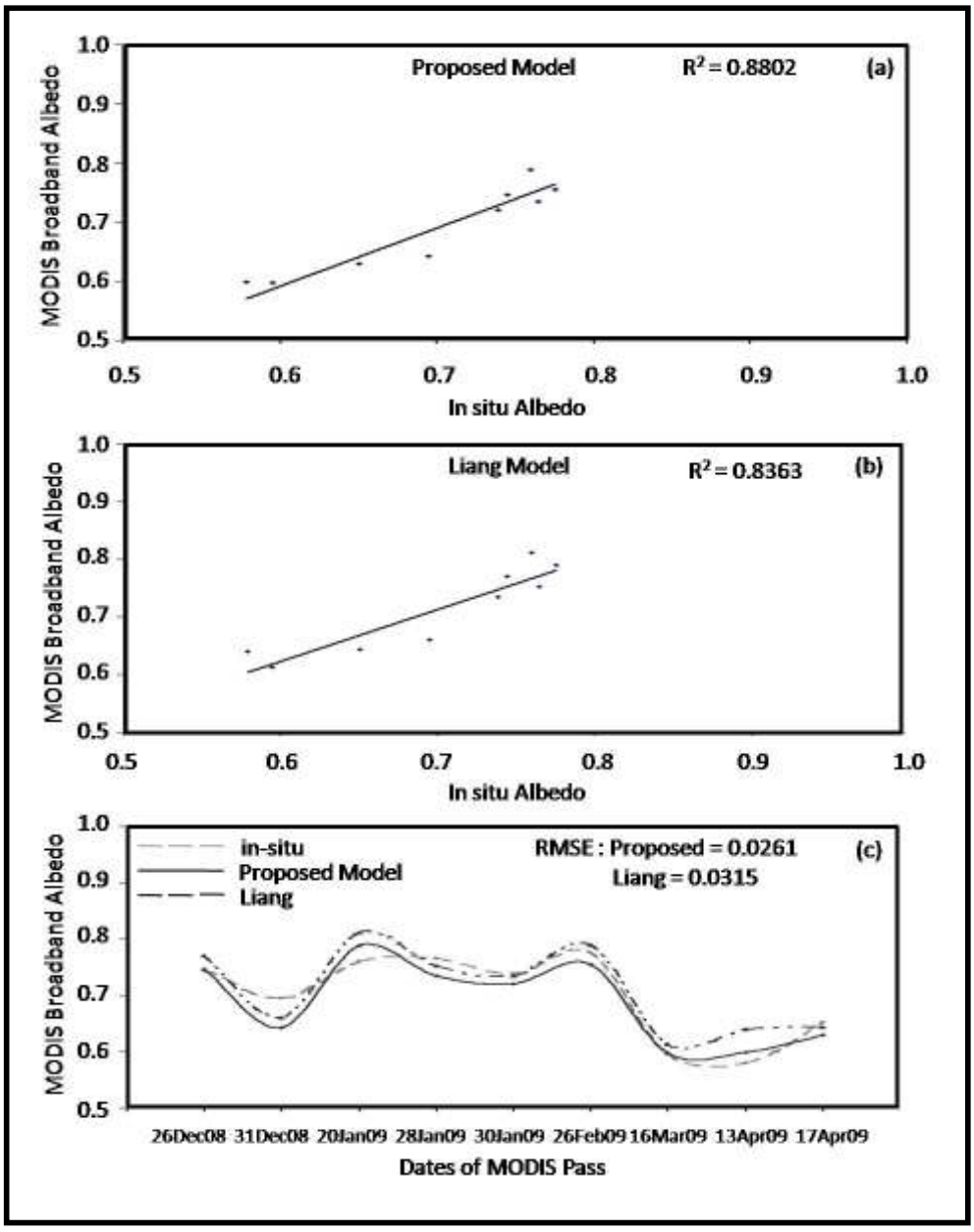

Figure 5.14 Validation of the satellite (MODIS) retrieved snow broadband albedo with the *in situ* measurements at site 3 (Patsio) for (a) Proposed Model (b) Liang Model (c) RMSE of proposed and Liang model

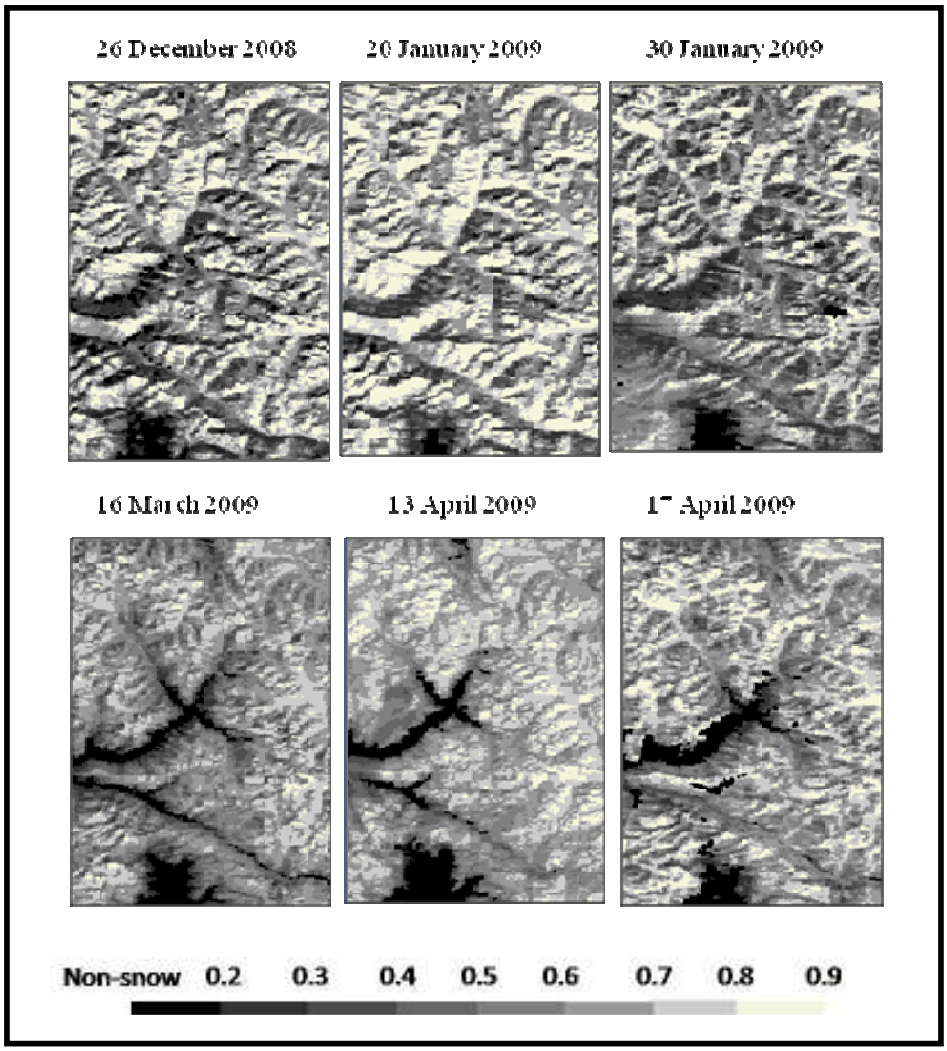

Figure 5.15: Thematic maps of broadband albedo of snow generated from MODIS images (Geographic extent of the maps are from 32°14' 55" N - 32°59'30"N and 77°0'15" E - 77°28'19"E)

5.3.2.2.3 Validation in Study Area-1 (i.e. Antarctica) using MODIS Images

Broad band albedo maps have also been estimated for the Study Area-1 i.e Antarctica using MODIS images. These BBA maps have been validated using AWS 1 and AWS 2 data of Antarctica. BBA maps on 27 October 2007, 17 February 2008, 24 November 2008, 24 January 2010, 28 January 2010 and 21 February 2010 have been validated using *in situ* recorded albedo values. Figure 5.16 shows the BBA map on 17 February 2008. Albedo of the most of the part of the ice sheet in the study area ranges between 0.4 to 0.8. Albedo

near exposed mountain rocks in the study area are less than 0.4. Figure 5.17 shows the correlation between estimated and observed albedo values on these dates. In this figure, x-axis shows the *in situ* recorded (observed) albedo values while y-axis shows the MODIS retrieved (estimated) albedo values. The correlation coefficient between observed and estimated values has been obtained 0.75 and RMSE has been obtained 0.07 during above mentioned dates. Values of correlation coefficient and RMSE show that the algorithm developed for MODIS data is also performing well in Antarctica region.

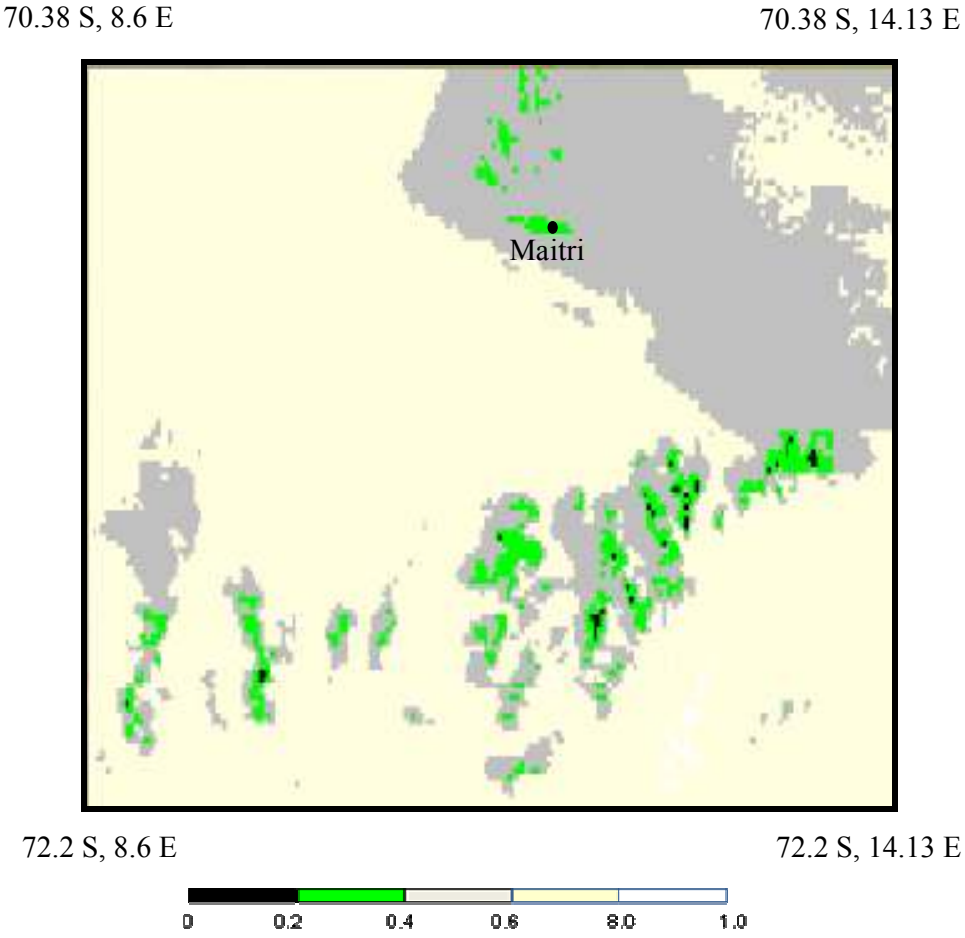

Figure 5.16 : Broad Band Albedo map using MODIS for 17-February-2008 (Study Area-1)

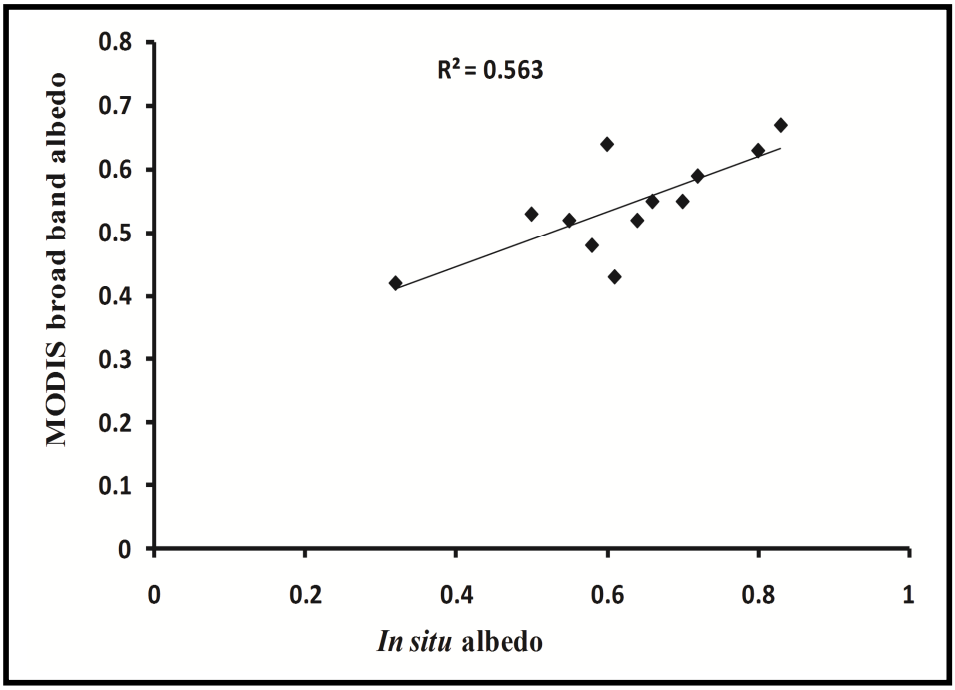

Figure 5.17 : Validation of MODIS retrieved BBA with *in situ* albedo measurements (Study Area-1).

5.4 Modeling Surface Temperature in Antarctica

Surface temperature has been modeled using MODIS thermal bands data and AWS data in the Study Area-1 i.e. Antarctica. Split window algorithm has been used to model surface temperature. Data of IR sensor mounted on AWS at the time of satellite pass has been used to develop algorithm in conjuction with MODIS derived brightness temperature. Developed algorithm has been validated at AWS locations. Detailed methodology of algorithm development is given in the following section.

5.4.1 Methodology

The following form equation within the framework of the split window algorithm (Qin and Karnieli 1999) has been used for estimation of surface temperature in Antarctica.

$$T_s = a + b.T_{31} + c.(T_{31} - T_{32}) \quad (5.18)$$

where, T_s is surface temperature, T_{31} is brightness temperature of MODIS band 31, T_{32} is brightness temperature of MODIS band 32, and a, b, c, are regression coefficients. Emissivity of the snow/ice surface has been assumed to be unity (Bintanja and Van den Broeke 1994).

Brightness temperature of MODIS band 31 and band 32 has been estimated from Planck's spectral radiation equation (3.9) and (3.10) as described in chapter 3. T_s at the time of MODIS pass has been taken from data of IR sensor mounted on AWS in Antarctica. Surface temperature and brightness temperature data of 20 clear sky days of the years 2007, 2008, 2009 (Table 3.3 in chapter 3) has been used in equation (5.18) to obtain regression coefficients using least square method. The coefficients obtained are given as following,

a = -260.0967412, b = 0.959826974, and c = -1.034104696

Values of the coefficients a, b, and c have been used in equation (5.18) to estimate surface temperature of the Study Area-1 using MODIS images. Surface temperature has been estimated at each pixel of the MODIS image. The algorithm has been validated at the AWS 1 and AWS 2 locations using data of different days of the year 2010 (Table 3.3 in chapter 3).

5.4.2 Results and Discussion

Figure 5.19 shows the MODIS derived surface temperature map of the study area on 12-January-2010 at 0900 hours. As can be seen, the surface temperature varies from -19.2°C to 6.9°C with mean value of -7.8°C $\pm$ 4.7°C. Surface temperature has also been estimated for different days of the years 2007, 2008, 2009 and 2010 mentioned in Table 3.3. Validation of the estimated surface temperature at the locations of AWSs has been carried out. The resulting regression plot between estimated and observed surface temperature is shown in Figure 5.19 and high coefficient of determination ($R^2 = 0.99$) has been obtained. Mean absolute error between observed and estimated surface temperature has varied from 0.1°C to 1.5°C during different days with mean absolute error of 0.6°C and RMSE of 0.8°C.

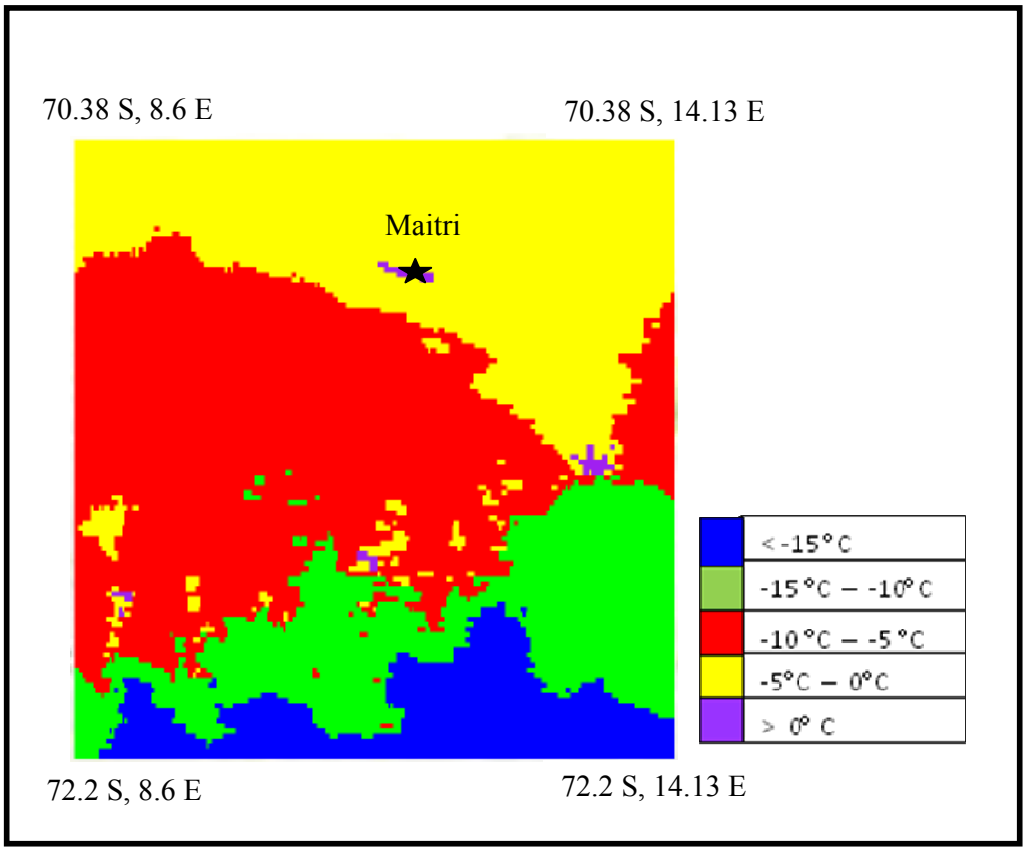

Figure 5.18: Surface temperature map for 12-January-2010: 0900hours (Study Area-1)

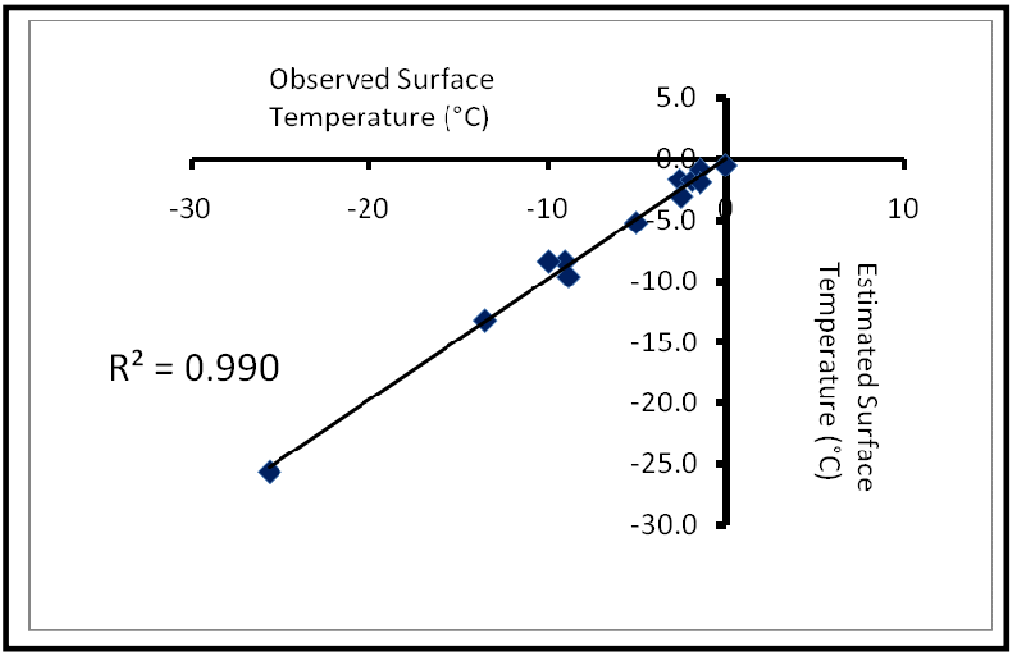

Figure 5.19: Observed vs estimated surface temperature for different days

Surface temperature has also been estimated in the Study Area-2 i.e Western Himalaya using MODIS images. Algorithm developed by Negi *et al.* (2007) has been used to estimate surface temperature using equation 5.18. The values of a, b, c estimated by Negi *et al.* (2007) for Western Himalaya are given as,

a = 22.20189692, b = 0.9272294273, and c = - 3.3071281612.

Figure 5.20 shows the surface temperature map of the snow covered region of Western Himalaya at 0530 UTC on 26-December-2008, produced by the algorithm of Negi *et al.* (2007). Surface temperature varies from 242 K to 281 K and mean surface temperature of the region has been obtained as 264±7 K. Pixels showing surface temperature below 265 K represent dry snow (Negi *et al.* 2007). Pixels showing surface temperature above 270 K are mostly concentrated in the lower Himalayan region and some pixels showing surface temperature above 273 K may be having snow cover mixed with other land covers.

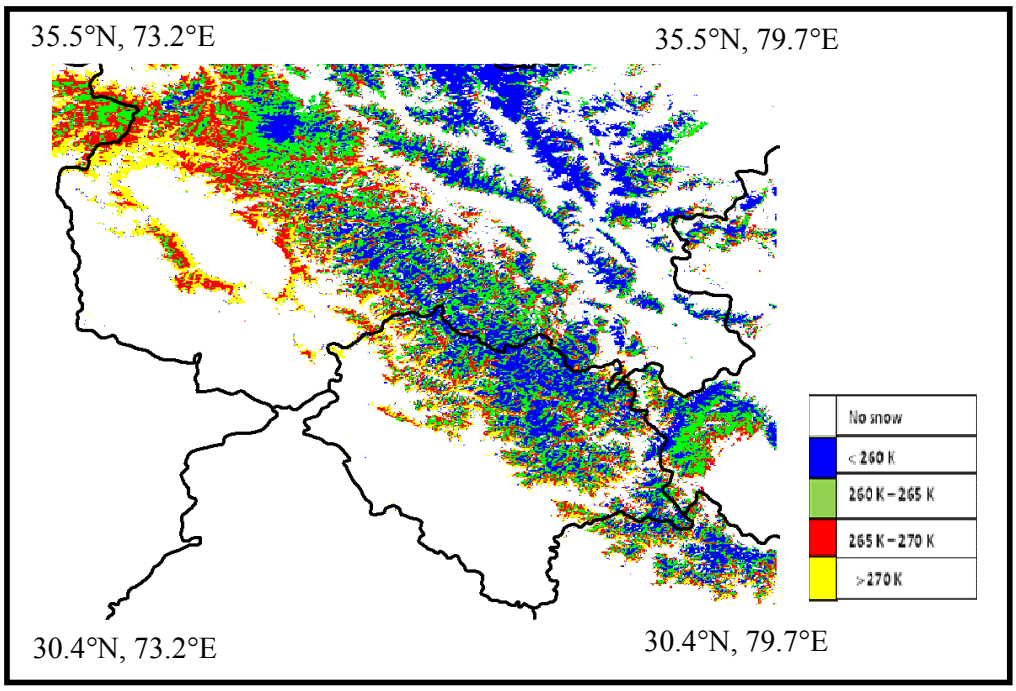

Figure 5.20: Surface temperature map of Western Himalaya

These surface temperature maps of the Study Area-1 and Study Area-2 have been used to estimate outgoing longwave radiation flux in these study areas.

5.5 Summary

In this chapter, methods for spatial estimation of snow depth, snow cover albedo and surface temperature have been presented. Spatial interpolation method proposed by Foppa *et al.* (2007) has been modified to generate maps of snow depth in western Himalaya. The snow depth maps have been generated at spatial resolution of 0.5 km. Proposed method has advantages over the previously estimated snow depth in western Himalaya by having higher spatial resolution and may be applicable for all snow thicknesses. These maps can be very useful in spatial estimation of sub surface heat flux, avalanche forecasting, hydrological and other snow studies.

Snow surface broadband albedo is a fundamental component in estimation of net shortwave radiation flux. Algorithms for direct retrieval of snow broadband albedo using AWiFS and MODIS data have been developed and presented. Algorithm for AWiFS is the first algorithm reported to estimate braodband albedo of snow from narrow band reflectances. *In situ* measurements of spectral reflectance and transmitted solar irradiance have been used for estimation of conversion factors and coefficients required for development of snow broadband albedo using AWiFS and MODIS data. The retrieved albedo from AWiFS and MODIS has been validated with *in situ* measurements at Solang, Dhundi and Patsio sites in Study Area-2 . The algorithm for MODIS has been also validated at AWS 1 and AWS 2 locations in Study Area-1. The overall high correlation coefficient and low RMSE values between AWiFS and MODIS derived BBA and *in situ* albedo have been observed. These algorithms may be usefull to estimate net shortwave radiation flux of snow covered region at spatial level.

The surface temperature in the Study Area-1 has been estimated from MODIS data based on split window algorithm and has been validated at AWS locations. The coefficient of determination (R^2) and RMSE of 0.99 and 0.8°C respectively have been obtained between observed and estimated surface temperature. The algorithm will be usefull to estimate outgoing and net long wave radiation flux in the Study Area-1. Next chapter presents spatial estimation of surface energy fluxes using remote sensing and *in situ* measured data in the Study Area-2 (Western Himalaya) and Study Area-1 (Antarctica).

Chapter VI

SPATIAL ESTIMATION OF SURFACE ENERGY FLUXES

6.1 Introduction

Incoming shortwave radiation flux, net shortwave radiation flux, net longwave radiation flux and net radiation flux have been estimated at spatial level for the study area of Indian Western Himalaya and Antarctica using remote sensing data. These energy fluxes have been evaluated with *in situ* observed radiation fluxes from AWS data. Spatial and temporal variation of energy fluxes have also been analysed on north and south aspect slopes of mountain topography in Western Himalaya.

6.2 Methodology

Surface energy fluxes have been estimated at spatial level in Western Himalaya and Antarctica using MODIS sensor images and *in situ* recorded AWS data. In Western Himalaya, energy fluxes on north and south aspect slopes have been extracted from maps of energy fluxes using aspect image of the study area. Mountain slopes having aspect between 0° to 22.5° and 337.5° to 360° have been selected as north aspect slopes. Slopes having aspect between 157.5° to 202.5° have been selected as south aspect slopes. Detail methodology of estimation of energy fluxes is given as following.

6.2.1. Estimation of Net Shortwave Radiation Flux

Zillman (1972) parameterization scheme, as reported in Niemela *et al.* (2001b) and Bisht *et al.* (2005) has been used to estimate incoming shortwave radiation flux ($SWF\downarrow$), given as,

$$SWF\downarrow = S_0 \cos^2\theta/[1.085\cos\theta + e_a(2.7 + \cos\theta)0.001 + 0.1] \quad (6.1)$$

where, S_0 is solar constant (1367 W m^{-2}), θ is solar zenith angle and e_a is water vapour pressure. Water vapour pressure has been estimated using the parameterization scheme given by Niemela *et al.* (2001b),

$$e_a = RH \exp(26.23 - 5416/T_a) \quad (6.2)$$

where, RH is the relative humidity and T_a is the air temperature. In case of mountainous topography, to include the effect of slope and aspect in equation (6.1), solar zenith angle θ is replaced with angle of incidence i, which is the angle between the incident sun rays and normal to the surface, given as, (Gates 1980).

$$\cos i = \sin\varphi \cos a \cos(\alpha_a - \alpha_s) + \cos\varphi \sin a \quad (6.3)$$

where, φ is the slope angle, a is the elevation angle of the sun, α_a is azimuth angle of the sun and α_s is the aspect of the surface. Slope, aspect, elevation and azimuth angles have been obtained from the respective maps generated from the SRTM DEM of the study area (refer sections 3.3.1.2 and 3.3.2.2).

Air temperature and relative humidity maps for both the study area have been generated using DEM and AWS data using method, as given in the following.

The spatial modeler in ERDAS IMAGINE 9.3 has been used. AWS recorded air temperature data, elevation value of AWS, DEM of the study area and environmental lapse rate (ELR) of 6.5˚C km^{-1} have been used to produce air temperature maps. Flow chart of producing air temperature maps in spatial modeler is shown in Figure 6.1. The saturation vapour pressure (e_s) has been calculated at each AWS location, according to the following equation (Buck 1981),

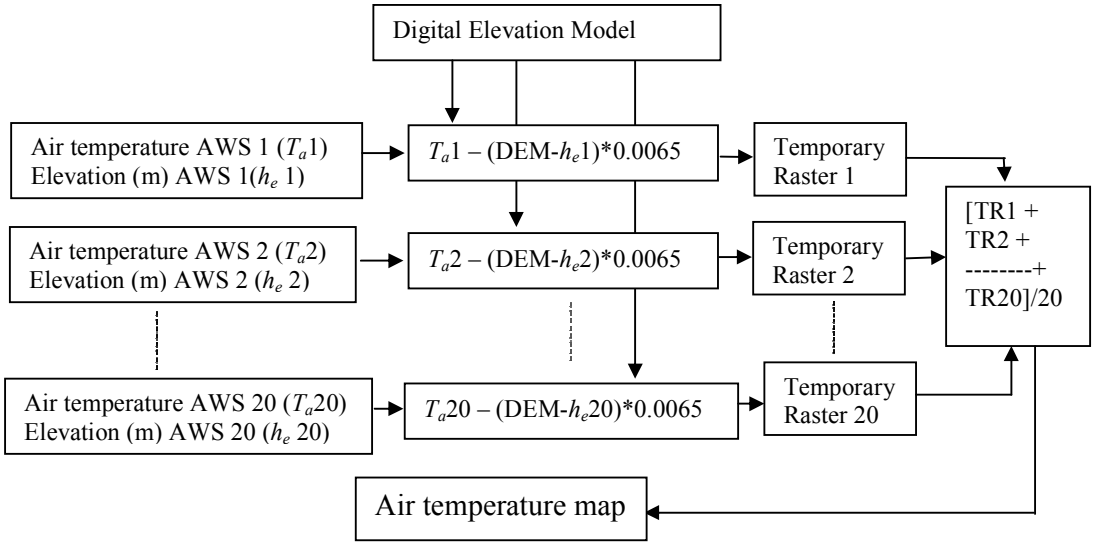

Figure 6.1: Flow chart of producing air temperature map in spatial modeler

$$e_s = a \exp [bT_a/(c + T_a)] \quad (6.4)$$

where, T_a is air temperature.

For water, a = 611.21 Pa, b =17.502, and c = 240.97°C, and

For ice, a = 611.15 Pa, b =22.452, and c = 272.55°C.

Relative humidity (RH) and saturation vapour pressure (e_s) at AWS locations have been used to calculate vapour pressure (e_a) at these locations and given as,

$$RH = 100 (e_a / e_s) \quad (6.5)$$

Finally, dew point temperature value at an AWS location has been obtained from the following equation,

$$T_d = [c \ln (e_a /a) / (b- \ln (e_a/a))] \quad (6.6)$$

where, a, b and c are the constants given above and e_a is the vapour pressure.

Dew point temperature maps have been produced using spatial modeler in ERDAS IMAGINE 9.3. Map has been generated using dew point temperature values at the AWS locations and applying lapse rate in DEM. Relative humidity map has been generated from the air temperature and dew point temperature map (Dewali *et al.* 2009) using spatial

modeler. Relative humidity and air temperature maps have been used to estimate vapour pressure map and finally, from equation (6.1), incoming shortwave radiation flux map has been generated. Figures 6.2, 6.3 and 6.4 show air temperature map, relative humidity map and incoming shortwave radiation flux map respectively, generated using the method explained above for the data collected at 0530 UTC on 26 December 2008.

Reflectance in band 1 to band 7 of MODIS images have been used to estimate broadband albedo of the snow/ice covered region. Derivation of reflectance in MODIS spectral bands has been discussed in chapter 3. Since albedo of snow changes rapidly with time as compared to other land surfaces due to its metamorphic processes, the instant albedo of the snow surface has been used to estimate net shortwave radiation flux. Algorithm for estimation of broadband albedo using MODIS images has been discussed in chapter 5 and given in equation 6.7 as following,

$$\alpha = 0.145\,\rho_1 + 0.275\,\rho_2 + 0.138\,\rho_3 + 0.165\,\rho_4 + 0.214\,\rho_5 + 0.06\,\rho_6 + 0.06\,\rho_7 - 0.011 \quad (6.7)$$

where, ρ_1, ρ_2, ρ_3, ρ_4, ρ_5, ρ_6 and ρ_7 are narrow band reflectance in MODIS spectral band 1, 2, 3, 4, 5, 6 and 7 respectively. This equation has been used to estimate snow surface albedo (α) at the time of satellite pass. Albedo map of snow/ice covered region at 0530 UTC on 26 December 2008 generated from MODIS image using equation (6.7) is shown in Figure 6.5.

Net shortwave radiation flux (SWF_{net}) has been estimated using incoming shortwave radiation flux (equation 6.1) and snow albedo (equation 6.7) and is given as,

$$SWF_{net} = SWF\downarrow(1 - \alpha) \quad (6.8)$$

Net shortwave radiation flux map generated using this equation for 26 December 2008 is given in Figure 6.6 and analysis of the map is given in results and discussion section.

6.2.2 Estimation of Net Longwave Radiation Flux and Net Radiation Flux

Incoming longwave radiation flux has been estimated using model proposed by Prata (1996) and is given as,

$$LW\downarrow = \epsilon_m \sigma T_a^4 \quad (6.9)$$

where, ϵ_m is emissivity of the atmosphere, σ is Stephan Boltzmann constant (5.67 x 10^{-8} W m^{-2} K^{-4}) and T_a is air temperature in kelvin. ϵ_m is estimated as,

$$\epsilon_m = 1 - (1+w_p) \exp\{-(1.2+3.0w_p)^{1/2}\} \quad (6.10)$$

and $$w_p = 46.5 \, (e_a/T_a) \quad (6.11)$$

where, w_p is precipitable water content and e_a is vapour pressure (Pa).

Outgoing longwave radiation flux has been estimated using Stephan Boltzmann equation and is given as,

$$LW\uparrow = \epsilon_s \sigma T_s^4 \quad (6.12)$$

where, σ is Stephan Boltzmann constant, T_s is surface temperature in kelvin and ϵ_s is surface emissivity. Surface temperature maps for both the study areas have been generated using MODIS data. Thermal bands 31 and 32 of MODIS images have been used to estimate surface temperature using split window algorithm, as discussed in section 5.4.1.

Net longwave radiation flux has been estimated as,

$$LW_{net} = LW\downarrow - LW\uparrow = (\epsilon_m \sigma T_a^4 - \epsilon_s \sigma T_s^4) \quad (6.15)$$

and net radiation flux for clear sky days has been estimated as,

$$R_{net} = SWF_{net} + LW_{net} = SWF\downarrow(1-\alpha) + (\epsilon_m \sigma T_a^4 - \epsilon_s \sigma T_s^4) \quad (6.16)$$

Figures 6.7 and 6.8 show the net longwave radiation flux and net radiation flux maps on 26 December 2008, generated using equation 6.15 and 6.16 respectively.

Surface energy flux maps of the study area of Western Himalaya have been generated on 10-November-2008, 26-December-2008, 26-February-2009 and 22-April-2009 of the winter season 2008-09. These days have been selected on the basis of availability of cloud free images of MODIS, availability of AWS data from maximum locations out of 20 AWS locations in the study area, and to account for the temporal variation in different energy fluxes during the season. These maps have also been generated for the study area of Antarctica on clear sky days of the years 2008, 2009 and 2010 mentioned in Table 3.4.

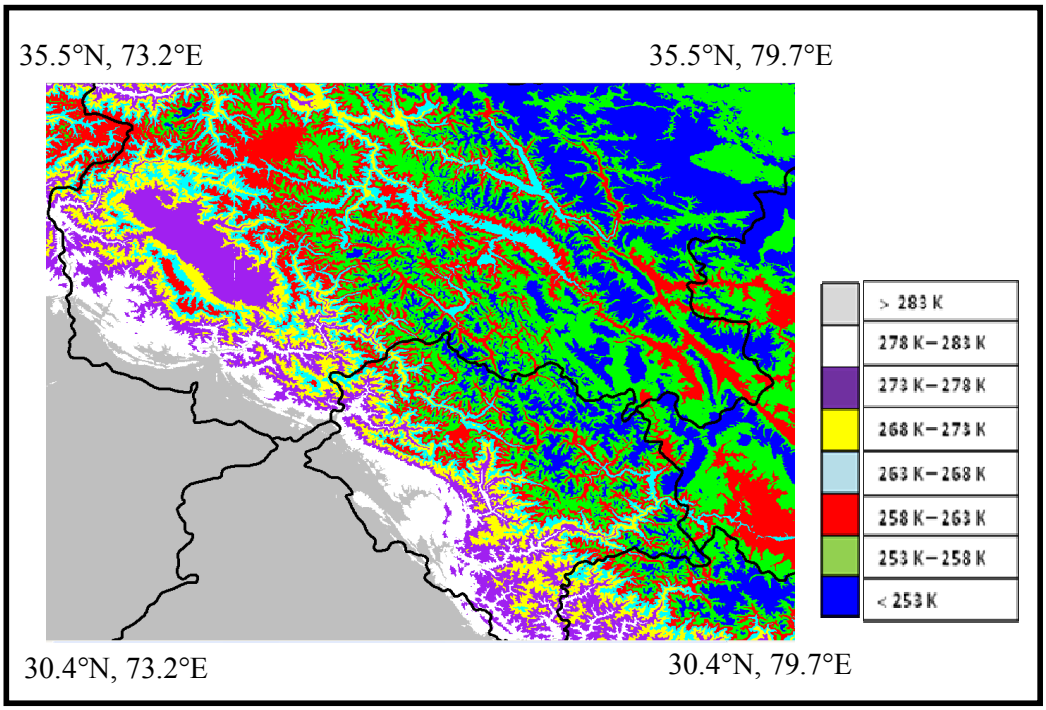

Figure 6.2: Air temperature map

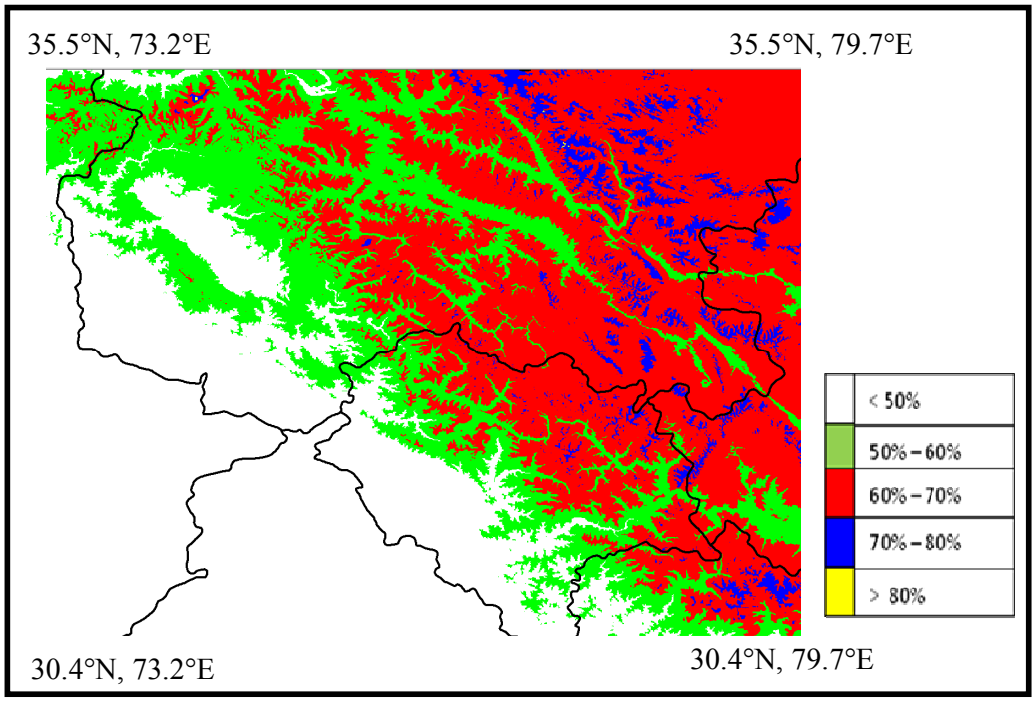

Figure 6.3: Relative humidity map

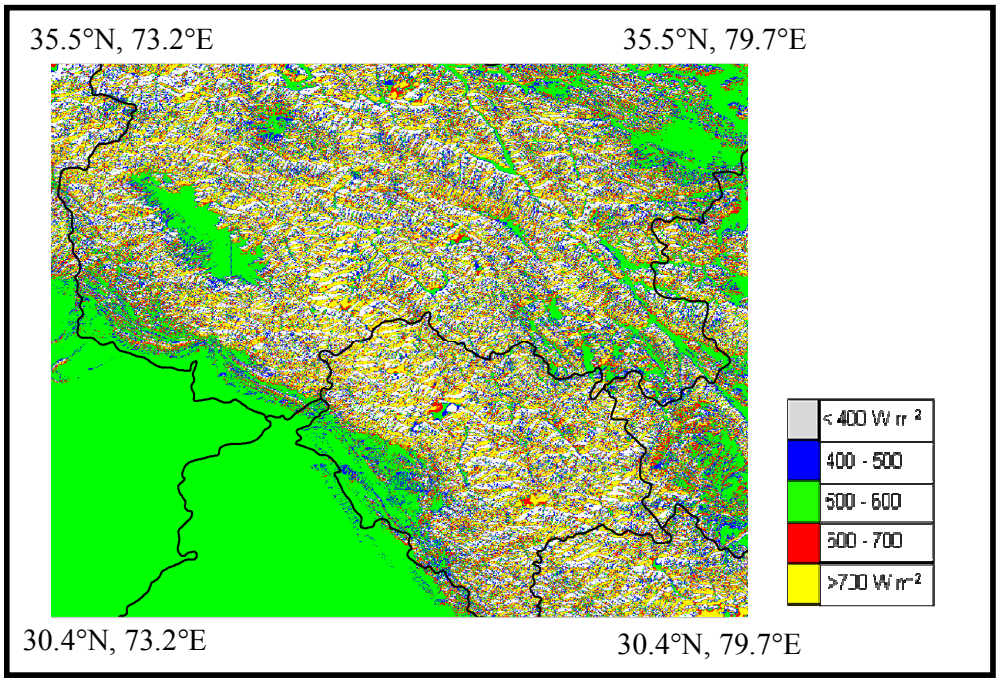

Figure 6.4: Incoming shortwave radiation flux map

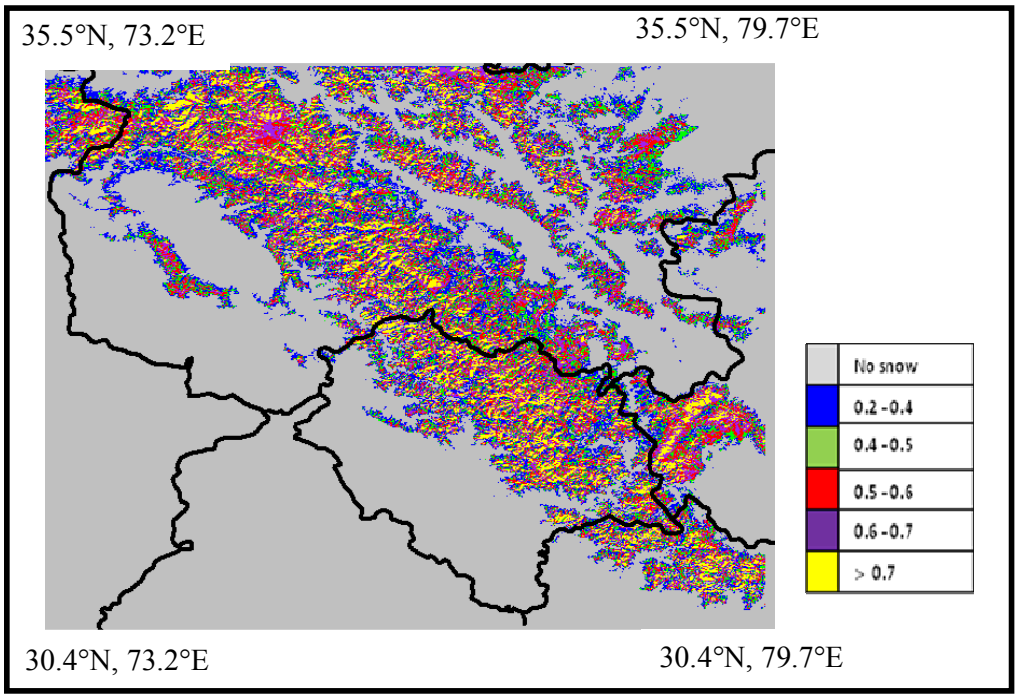

Figure 6.5: Albedo map

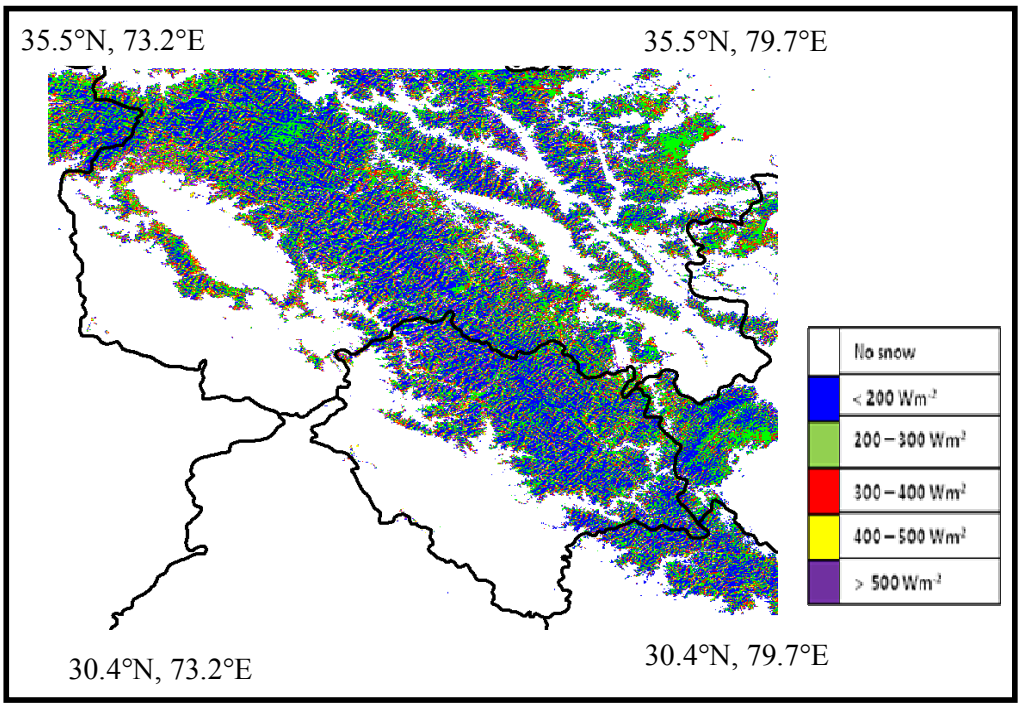

Figure 6.6: Net shortwave radiation flux map

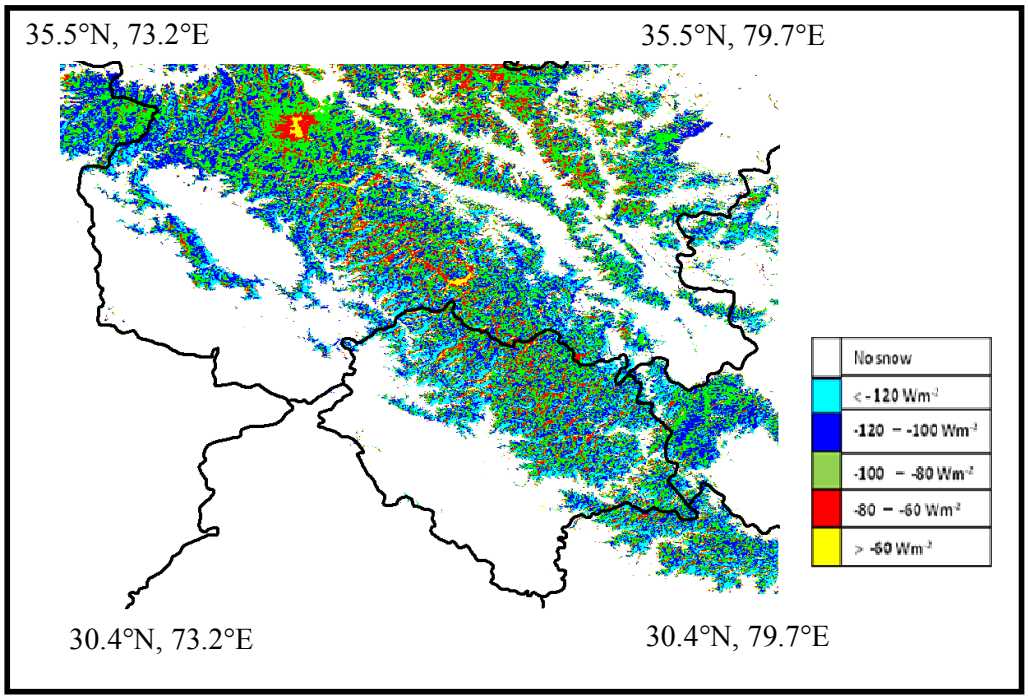

Figure 6.7: Net longwave radiation flux map

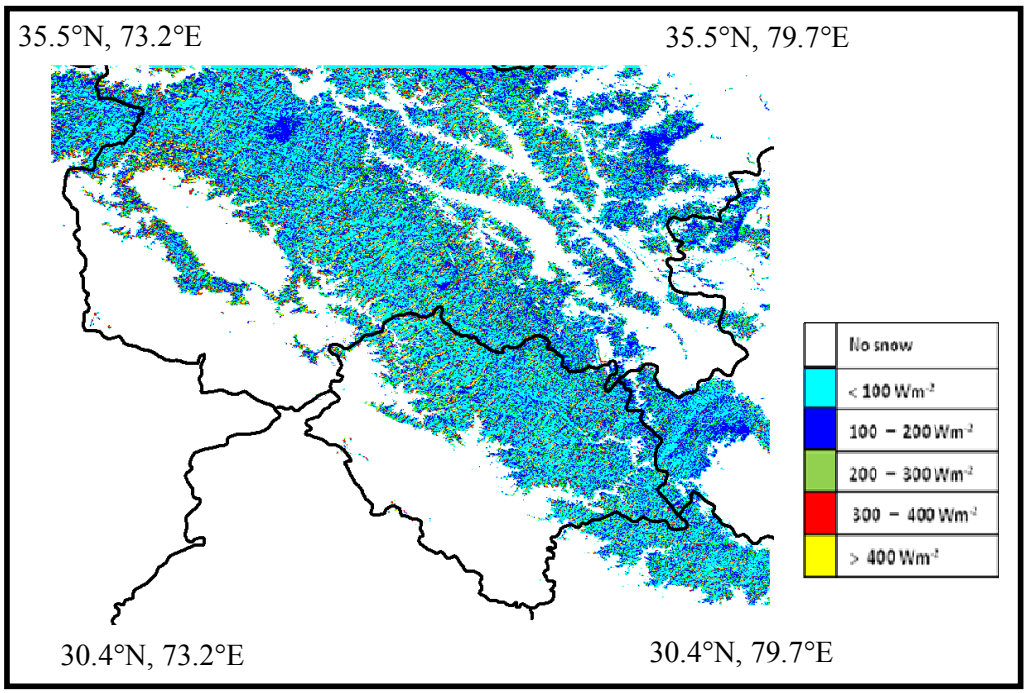

Figure 6.8: Net radiation flux map

6.3 Results and Discussion

6.3.1 Surface Energy Fluxes in Indian Western Himalaya

Air temperature and relative humidity maps generated for Indian western Himalaya on 26-December 2008 using AWS data and DEM are shown in Figure 6.2 and 6.3. Table 6.1 shows the AWS recorded air temperature and estimated air temperature. The absolute error between AWS recorded air temperature and estimated air temperature varies from 0.5 K to 7.5 K and an overall RMSE of 4.9 K has been obtained. The parameterization scheme to estimate incoming shortwave radiation flux (equation 6.1) is heavily influenced by the air temperature, since an error of $\pm$ 1 K in estimation of air temperature can produce an error of approximately $\pm$ 17 W m^{-2} in incoming shortwave radiation flux (Gusain *et al.* 2014b). This error has been estimated by varying air temperature values in equation 6.2 and placing corresponding values of vapour pressure in equation 6.1.

Table 6.1 shows the AWS recorded relative humidity and estimated relative humidity. The absolute error between AWS recorded relative humidity and estimated

relative humidity varies from 2% to 21% and an overall RMSE of 10.6 % has been obtained. An error of $\pm$ 1 % in estimation of relative humidity can produce an error of approximately $\pm$ 5 W m^{-2} in incoming shortwave radiation flux. This error has been estimated by varying the *RH* values in equation 6.2 and placing corresponding values of vapour pressure in equation 6.1.

Incoming shortwave radiation flux has been estimated from air temperature and relative humidity map using Zillman (1972) parameterization scheme given in equation (6.1). Niemela *et al.* (2001b) evaluated the results of Zillman parameterization scheme with hourly averaged point surface radiation observations at Jokioinen and Sodankylä, Finland in 1997. The bias, the standard deviation (SD) and the RMSE were observed as 11.7 W m^{-2}, 37.0 W m^{-2}, 38.8 W m^{-2} respectively at Jokioinen, and the corresponding RMSE of -15.4 W m^{-2}, 27.5 W m^{-2}, and 31.5 W m^{-2} respectively were observed at Sodankylä. It is therefore expected that these reported errors inherent in the scheme may have impact on estimation of radiation fluxes in present study.

Figure 6.4 shows the estimated incoming shortwave radiation flux map on 26 December 2008 at the time of MODIS satellite pass in the study area. Incoming shortwave radiation flux varies from 296 W m^{-2} to 803 W m^{-2} in the region with a mean of 538 W m^{-2}. Incoming shortwave radiation flux shows large spatial variation due to large variation in the slope angle and aspect of the mountain slopes in the study area. Local incidence angle of the solar radiation varies with slope angle and aspect of the mountain slope, which results in variation of incoming shortwave radiation flux. From Table 6.2, a variation in incoming shortwave radiation flux on north and south aspect slopes in the study area can be clearly seen.

Table 6.1: Recorded and estimated air temperature and relative humidity values

AWS Number	**Recorded air temperature (K)**	**Estimated air temperature (K)**	**Recorded relative humidity (%)**	**Estimated relative humidity (%)**
1	275.7	270.3	46	52
2	269.6	268.3	DNR	-
3	256.1	259.2	72	63

4	264.9	260.9	65	61
5	267.3	262.0	DNR	-
6	257.0	255.2	62	64
7	264.5	259.5	60	63
8	265.4	262.2	38	59
9	287.9	281.6	44	46
10	289.2	282.2	39	47
11	257.1	264.6	72	59
12	272.9	269.4	67	52
13	263.8	268.0	61	53
14	269.7	276.7	50	61
15	260.8	258.5	51	65
16	264.6	259.4	DNR	-
17	269.2	262.2	43	54
18	271.0	271.5	DNR	-
19	262.8	264.8	49	60
20	271.2	267.9	51	55

(DNR shows data not recorded at the particular location)

Figure 6.9 shows a comparison of the estimated and AWS recorded values of incoming shortwave radiation flux at 20 observation locations of Indian western Himalaya. Absolute errors of 22 W m^{-2} to 126 W m^{-2} with mean absolute error of 69 W m^{-2} and RMSE of 75 W m^{-2} between AWS recorded and estimated incoming shortwave radiation flux have been observed. RMSE obtained is about $\pm$14% of the mean incoming shortwave radiation flux and is in correspondence with the errors published in literature.

The incoming shortwave radiation flux has also been estimated on 10-November-2008, 26-February-2009 and 22-April-2009, as discussed in previous section and the mean values with standard deviation (S.D.) for each date are shown in Table 6.2. Wang and Pinker (2009) estimated daily averaged incoming shortwave radiation flux using forward inference scheme at spatial resolution of 1° (approximately 100 km) in Arctic, Antarctic, Pacific, Atlantic, North America and Europe region and reported an RMSE of 25-47 W m^{-2}, about $\pm$14-25% of the mean values in these regions. Niu *et al.* (2010) also evaluated

daily averaged incoming shortwave radiation flux at high latitudes of north and South Polar Region, estimated from MODIS by the model proposed by Wang and Pinker (2009). They reported an RMSE of 22.8 – 38.1 W m^{-2}, about $\pm$14-21% of the mean value. In the present study also, the radiation flux has been obtained at about $\pm$14-27% of the mean values in Himalaya, which also matches with those published in the literature. Additionally, incoming shortwave radiation flux maps in this study have been produced at much higher spatial resolution (i.e., 0.5 km) than produced in earlier studies (i.e., 100 km) around the globe.

Further, the variation in the incoming shortwave radiation flux computed on north and south aspect slopes on different dates are shown in Table 6.2. It can be seen that the mean incoming shortwave radiation flux in the study area decreases from 10-Novemeber-2008 to 26-December-2008 and then increases on 26-February-2009 and 22-April-2009. This may be attributed to the increase in the mean solar zenith angle from 10-November 2008 to 26-December-2008 and then its decrease till 22-April-2009 in the study region. The mean solar zenith angle at 0530UTC on the dates mentioned were 51.2°, 58.9°, 46.9° and 24.4° respectively. Moreover, the incoming shortwave radiation flux on south aspect slopes has been observed higher than those observed on north aspect slopes for all dates. This may be due to low incidence angle (i) of solar radiation on south aspect slopes as compared to that on the north aspect slopes (Table 6.3). The variation in 1° incidence angle may result in variation of 7-9 W m^{-2} in the incoming shortwave radiation flux on different slopes in the study area (Gusain *et al.* 2014b).

Figure 6.5 shows the albedo map, as an output of the narrowband to broadband albedo of the snow estimated using equation (6.7). The detail discussion of the validation of estimated albedo values using MODIS sensor images has been given in section 5.3.2.2.2. The no-snow region in the image has been masked using binary snow cover maps, as described in section 3.3.3.5. The albedo values of the snow covered region have been found to be 0.47 $\pm$ 0.15, 0.50 $\pm$ 0.20, 0.70 $\pm$ 0.17 and 0.72 $\pm$ 0.16 on 10-november-2008, 26-December-2008, 26-February-2009 and 22-April-2009, respectively. These albedo values have been used for estimation of net shortwave radiation flux of the snow cover as mentioned in equation (6.8). The net shortwave radiation flux map at the time of Terra MODIS satellite pass on 26-December-2008 is shown in Figure 6.6. The estimated

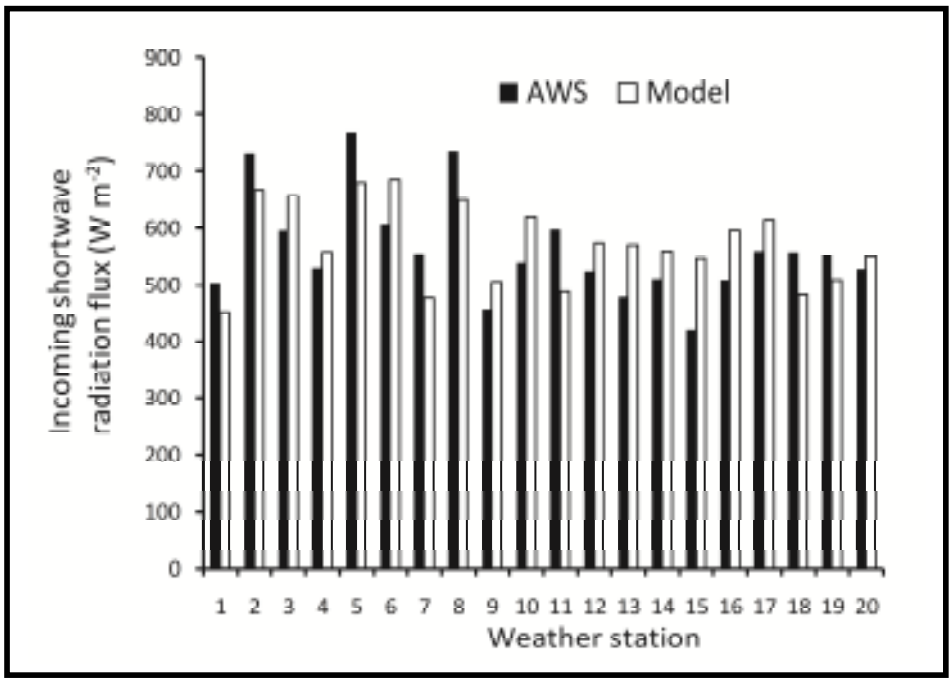

Figure 6.9: Comparison of estimated and *in situ* recorded incoming shortwave radiation flux

Table 6.2: Values of estimated incoming shortwave radiation flux in Study Area-2, on north aspect slopes and on south aspect slopes for different dates.

Date	**Incoming shortwave radiation flux in the study region (mean ± SD)**	**Incoming shortwave radiation flux on north aspect slopes (mean ± SD)**	**Incoming shortwave radiation flux on south aspect slopes (mean ± SD)**
10-Nov-2008	636 ± 192 W m^{-2}	417 ± 204 W m^{-2}	810 ± 146 W m^{-2}
26-Dec-2008	538 ± 143 W m^{-2}	392 ± 97 W m^{-2}	679 ± 111 W m^{-2}
26-Feb-2009	716 ± 185 W m^{-2}	523 ± 202 W m^{-2}	871 ± 119 W m^{-2}
22-Apr-2009	960 ± 129 W m^{-2}	852 ± 150 W m^{-2}	1038 ± 58 W m^{-2}

Table 6.3: Mean incidence angle on north aspect slopes and south aspect slopes for different dates.

Date	**Mean incidence angle on north aspect slopes**	**Mean incidence angle on south aspect slopes**
10-Nov-2008	65.9°	39.7°
26-Dec-2008	67.4°	50.3°
26-Feb-2009	61.1°	36.9°
22-Apr-2009	40.1°	20.8°

values of net shortwave radiation flux varies from 24 W m^{-2} to 779 W m^{-2} in the region with mean value of 262 $\pm$ 135 W m^{-2}. Net shortwave radiation flux has also been estimated on above mentioned dates and values are given in Table 6.4. According to estimated incoming shortwave radiation flux in the study area, the net shortwave radiation flux should have been the highest on 22-April-2009 with a decrease on 26-February-2009, 10-November-2008 and the least on 26-December-2008, respectively. However, the results in this study do not reflect that. On analysis of the meteorological data recorded at various observation stations, a wide spread snowfall in the Pir panjal, Great Himalaya and Karakoram ranges of the study area has been observed that on 20-21 April-2009, and on 23-25 February 2009. This has resulted in high albedo and low net shortwave radiation flux on 22-April-2009 and 26-February-2009. Further, as no fresh snow fall has been observed in the region before 10-November-2008 and the snow was also more than 20 days old, it has resulted in low albedo of the snow cover and high net shortwave radiation flux on 10-November-2008. Figure 6.10 shows the estimated and AWS recorded net shortwave radiation flux for the stated period. Total 36 data points of net shortwave radiation flux have been obtained from the AWSs in the snow covered region for its comparison with estimated values for stated period. A significantly high coefficient of determination (R^2) of 0.81 and RMSE of 84.9 W m^{-2} (about $\pm$19.2% of the mean value) has been observed between estimated and the AWS recorded net shortwave radiation flux.

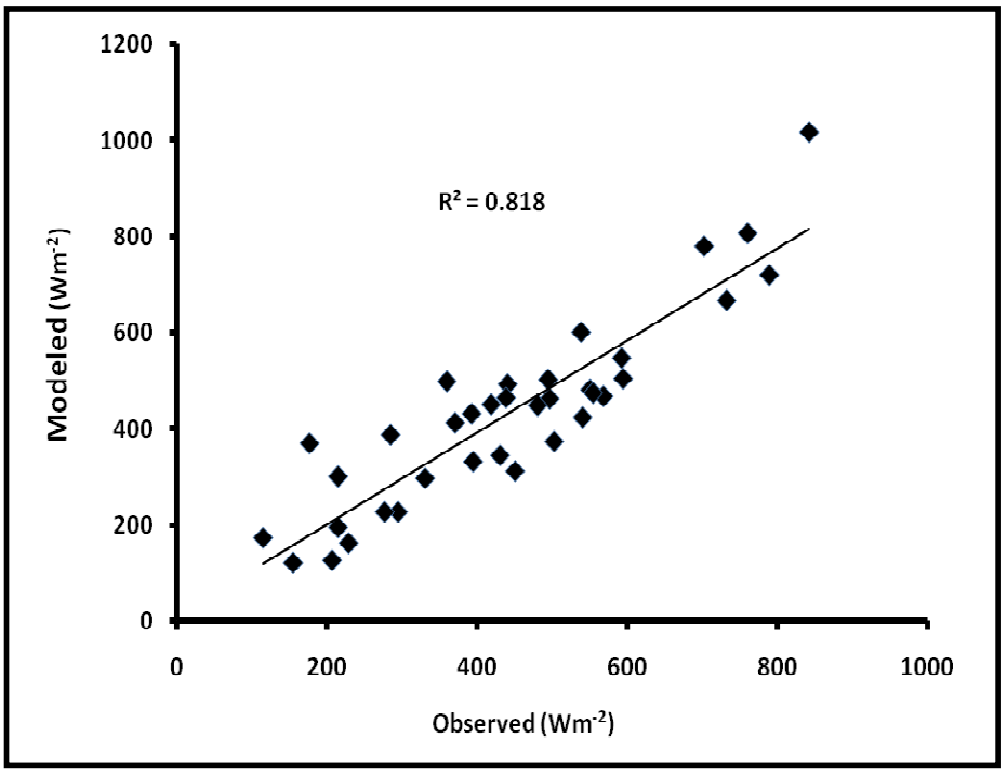

Figure 6.10: Model estimated vs *in situ* observed net shortwave radiation flux

Table 6.4: Values of estimated net shortwave radiation flux in Study Area-2, on north aspect slopes and on south aspect slopes for different dates.

Date	**Net shortwave radiation flux of snow covered region (mean ± SD)**	**Net shortwave radiation flux on north aspect snow covered slopes (mean ± SD)**	**Net shortwave radiation flux on south aspect snow covered slopes (mean ± SD)**
10-Nov-2008	302 ± 128 W m^{-2}	219 ± 109 W m^{-2}	392 ± 145 W m^{-2}
26-Dec-2008	262 ± 135 W m^{-2}	191 ± 78 W m^{-2}	340 ± 155 W m^{-2}
26-Feb-2009	193 ± 120 W m^{-2}	163 ± 98 W m^{-2}	218 ± 145 W m^{-2}
22-Apr-2009	260 ± 148 W m^{-2}	229 ± 123 W m^{-2}	287 ± 163 W m^{-2}

As there is no data of estimated net shortwave radiation flux map for snow covered region is available from any other source, the results of this study cannot be compared. The net shortwave radiation flux has also been estimated on the north and south aspect slopes and is given in Table 6.4. Mean net shortwave radiation flux on south aspect slopes has been observed to be comparatively higher than those observed on the north aspect slopes for all the above mentioned dates. This may be due to high mean incoming shortwave radiation flux on south aspect slopes as compared to that on north aspect slopes. High variation in net shortwave radiation flux on different aspect snow covered slopes may be attributed to the variation in latitude (from 30.5°N to 35.6°N) as well as variation in slope (from 0° - 87°) in the elevation range up to 7666 m in the study area.

Incoming longwave radiation flux and outgoing longwave radiation flux have been estimated using equations (6.9) and (6.12) respectively. Net longwave radiation flux has been estimated using equation (6.15). The map for snow covered region at 0530 UTC on 26 December 2008 is shown in Figure 6.7. Estimated values of net longwave radiation flux vary from -231 W m^{-2} to -28 W m^{-2} in the region with mean value of -103 $\pm$ 21 W m^{-2}. Net longwave radiation flux has also been estimated on 10-November-2008 and 26-February-2009 and given in Table 6.5. It has been observed that south aspect slopes lose more energy in the form of longwave radiation as compared to north aspect slopes for all the above mentioned dates. This may be due to higher surface temperature on south aspect slopes than that on north aspect slopes.

Net radiation flux in the study area has been estimated using equation (6.16) and Figure 6.8 shows net radiation flux map at 0530 UTC on 26-December-2008. Net radiation in the study region varies from -204 W m^{-2} to 779 W m^{-2} with mean value of 156 $\pm$ 140 W m^{-2}. Net radiation flux has also been estimated on 10-November-2008 and 26-February-2009 and shown in Table 6.6. It has been observed that net radiation flux on south aspect slopes is comparatively higher than that observed on north aspect slopes. This may be due to higher values of net shortwave radiation flux on south aspect slopes as compared to north aspect slopes. Figure 6.11 shows the estimated and AWS recorded net radiation flux for the stated period. Total 22 data points of net radiation flux have been obtained from the AWSs in the snow covered region for its comparison with estimated values for stated period. A coefficient of determination (R^2) of 0.651, MAE of 71 W m^{-2} and RMSE of 90 W m^{-2} has been observed between estimated and the AWS recorded net

radiation flux. RMSE obtained is about ±42% of the mean values of AWS recorded net radiation flux and is higher compared to RMSE values obtained in estimation of incoming shortwave radiation flux, net shortwave radiation flux and net longwave radiation flux. These three radiation fluxes are component of the net radiation flux and RMSE involved in estimation of each component contribute to higher values of RMSE in estimation of net radiation flux. There is no data of estimated net radiation flux map for snow covered region available from any other source to compare the results of this study.

Table 6.5: Estimated net longwave radiation flux in Study Area-2, on north aspect slopes and on south aspect slopes for different dates.

Date	**Net longwave radiation flux of snow covered region (mean ± SD)**	**Net longwave radiation flux on north aspect slopes of snow covered region (mean ± SD)**	**Net longwave radiation flux on south aspect slopes of snow covered region (mean ± SD)**
10-Nov-2008	-104 ± 26 W m^{-2}	-99 ± 25 W m^{-2}	-111 ± 28 W m^{-2}
26-Dec-2008	-103 ± 21 W m^{-2}	-99 ± 21 W m^{-2}	-109 ± 23 W m^{-2}
26-Feb-2009	-96 ± 23 W m^{-2}	-92 ± 21 W m^{-2}	-99 ± 25 W m^{-2}

Table 6.6: Estimated net radiation flux in Study Area-2, on north aspect slopes and on south aspect slopes for different dates.

Date	**Net radiation flux of snow covered region (mean ± SD)**	**Net radiation flux on north aspect slopes of snow covered region (mean ± SD)**	**Net radiation flux on south aspect slopes of snow covered region (mean ± SD)**
10-Nov-2008	192 ± 129 W m^{-2}	116 ± 111 W m^{-2}	278 ± 140 W m^{-2}
26-Dec-2008	156 ± 140 W m^{-2}	92 ± 86 W m^{-2}	230 ± 161 W m^{-2}
26-Feb-2009	94 ± 119 W m^{-2}	70 ± 95 W m^{-2}	116 ± 141 W m^{-2}

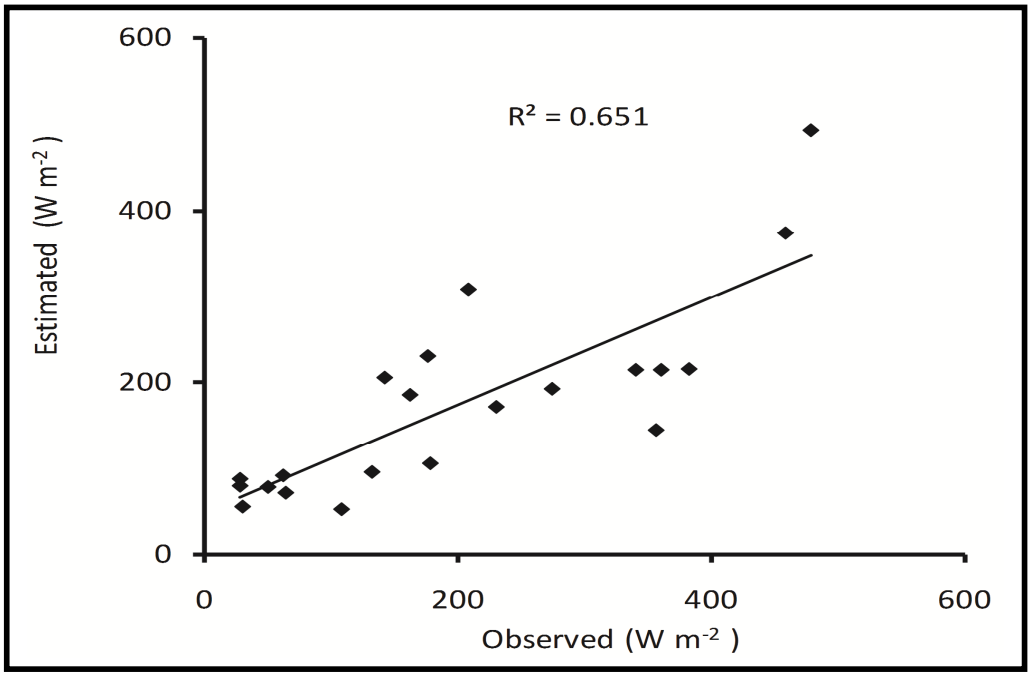

Figure 6.11: Model estimated vs *in situ* observed net radiation flux

6.3.2 Surface Energy Fluxes in Antarctica

Incoming shortwave radiation flux, net shortwave radiation flux, net longwave radiation flux and net radiation flux have also been estimated at spatial level for the study area in Antarctica. Air temperature and relative humidity maps for the study area have been generated using AWS data and SRTM DEM based on the method described in section 6.2.1. Incoming shortwave radiation flux has been estimated using equation (6.1) and flux map at 0900 UTC on 12-January-2010 is shown in Figure 6.12. Incoming shortwave radiation flux varies from 64 W m^{-2} to 1139 W m^{-2} with mean values of 632 $\pm$ 51W m^{-2} in the study region. Large spatial variation has been observed in mountainous region of the study area as compared to flat ice sheet, as shown in Figure 6.12. This may be due to large variation in incidence angle of solar radiation on mountain slopes. Incoming shortwave radiation flux has also been estimated for other clear sky days, as mentioned in Table 3.3. Figure 6.13 shows a comparison of the estimated and AWS recorded values of incoming shortwave radiation flux during different days. Absolute errors of 1 W m^{-2} to 179 W m^{-2} with mean absolute error of 92 W m^{-2} and RMSE of 105 W m^{-2} between AWS recorded

and estimated incoming shortwave radiation flux have been observed. RMSE obtained is about $\pm$20% of the mean values of the incoming shortwave radiation flux and is in correspondence with the RMSE values of 14-25% reported by Wang and Pinker (2009) and 14-21% reported by Niu *et al.* (2010) in different cryospheric regions.

Albedo of the ice sheet has been estimated from MODIS data using equation (6.7). Input to the equation is only reflectance in first seven bands of the MODIS image. Figure 6.14 shows the estimated albedo map at 0900 hour on 12-January-2010. The detail discussion of the validation of albedo maps in Antarctica using MODIS sensor images has been given in section 5.3.2.2.3 of chapter 5. Albedo varies from 0.1 to 0.8 in the study area with mean values of 0.68 $\pm$ 0.09. Low albedo values have been observed around ice-free areas. Net shortwave radiation flux has been estimated using equation (6.8). Figure 6.15 shows net shortwave radiation flux map at 0900 hours on 12-January-2010. Net shortwave radiation flux varies from 17 W m^{-2} to 895 W m^{-2} in the study area with mean values of 204 $\pm$ 60 W m^{-2}. Figure 6.16 shows a comparison of the estimated and AWS recorded values of net shortwave radiation flux during different days. Absolute errors of 2 W m^{-2} to 129 W m^{-2} with mean absolute error of 65 W m^{-2} and RMSE of 75 W m^{-2} between AWS recorded and estimated net shortwave radiation flux have been observed. RMSE obtained is about $\pm$28% of the mean values of the net shortwave radiation flux. As there is no data available from any other source on estimation of net shortwave radiation flux for snow/ice covered region, the results of this study cannot be compared.

Net longwave radiation flux has been estimated using equation (6.15). Figure 6.17 shows net longwave radiation flux map at 0900 hours on 12-January-2010. Net longwave radiation flux varies from -173 W m^{-2} to -60 W m^{-2} in the study area with mean values of -85 $\pm$ 14 W m^{-2}. Mean absolute error of 15 W m^{-2} and RMSE of 18 W m^{-2} have been obtained in estimation of net longwave radiation flux at AWS locations. RMSE obtained is about $\pm$25% of the mean values of the net longwave radiation flux. Net radiation flux has been estimated using equation (6.16). Figure 6.18 shows net radiation flux map at 0900 hours on 12-January-2010. Net radiation flux varied from -141 W m^{-2} to 814 W m^{-2} in the study area with mean values of 128 $\pm$ 57 W m^{-2}. Figure 6.19 shows a comparison of the estimated and AWS observed values of net radiation flux during different days. Absolute errors of 4 W m^{-2} to 136 W m^{-2} with mean absolute error of 70 W m^{-2} and RMSE of 81 W m^{-2} between AWS recorded and estimated net radiation flux have been observed. RMSE

obtained is about ±47% of the mean values of net radiation flux. RMSE obtained in estimation of net shortwave radiation and net longwave radiation fluxes contribute to higher value of RMSE in estimation of net radiation flux.

In Anatrctica, November, December, January and February are the summer months and melting of ice sheet has been observed during these months (Figure 4.8, chapter 4). Table 6.7 shows mean values of solar zenith angle, surface temperature, albedo, incoming shortwave radiation flux, net shortwave radiation flux, net longwave radiation flux and net radiation flux in the study area of Antarctica on 12-January-2010, 28-January-2010 and 21-February-2010. Incoming shortwave radiation flux in the study area has been found to decrease from 12-January-2010 to 21-February 2010 and this may be attributed to increasing solar zenith angle during this period. Decrease in albedo values from 12-January-2010 to 21-February-2010 may be due to melting of ice sheet during this period. Net shortwave radiation flux decreases from 12-January-2010 to 21-February 2010 and has been observed in correspondence with the values of incoming shortwave radiation flux and albedo on these dates. A decrease in the net longwave radiation flux from 12-January-2010 to 21-February-2010 has been observed and may be attributed to decrease in surface temperature during this period. It has also been observed from AWS data that net longwave radiation flux values are higher during summer period compared to winter period (discussed in section 4.2.2.2). Net radiation flux decreases from 12-January-2010 to 21-February-2010 due to decrease in net shortwave radiation flux and net longwave radiation flux. The decrease in net radiation flux indicates the decrease in amount of energy available for melting of the ice sheet during the stated period.

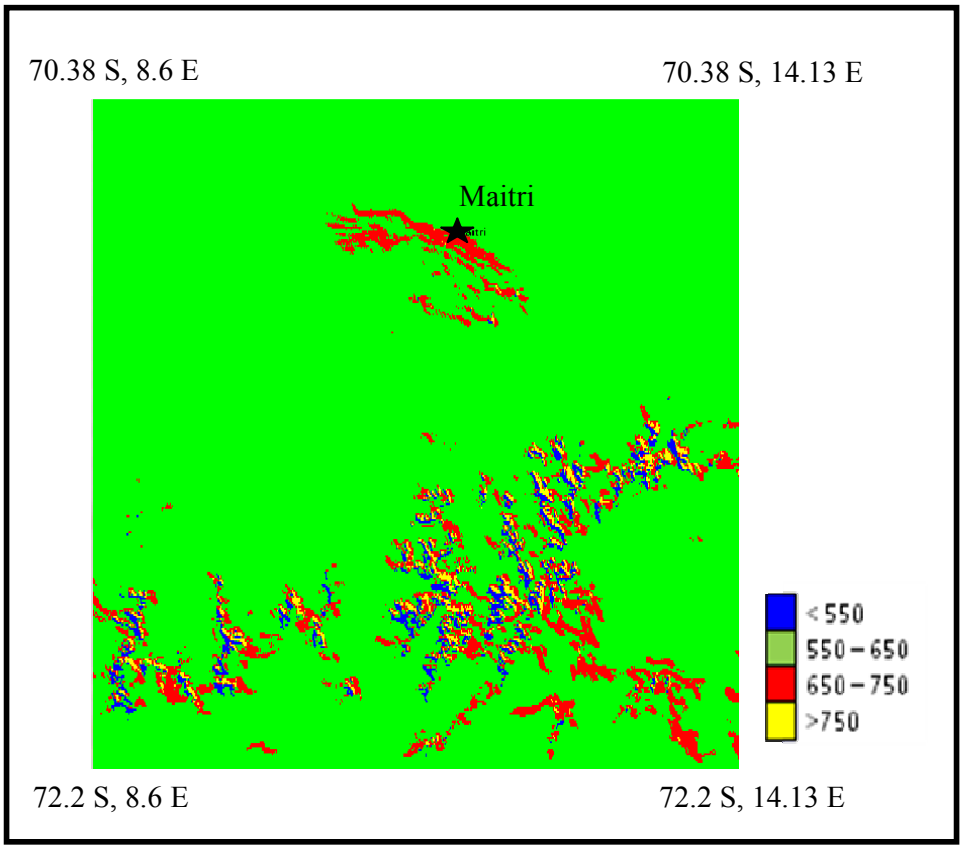

Figure 6.12: Incoming shortwave radiation flux (W m^{-2}) in Antarctica

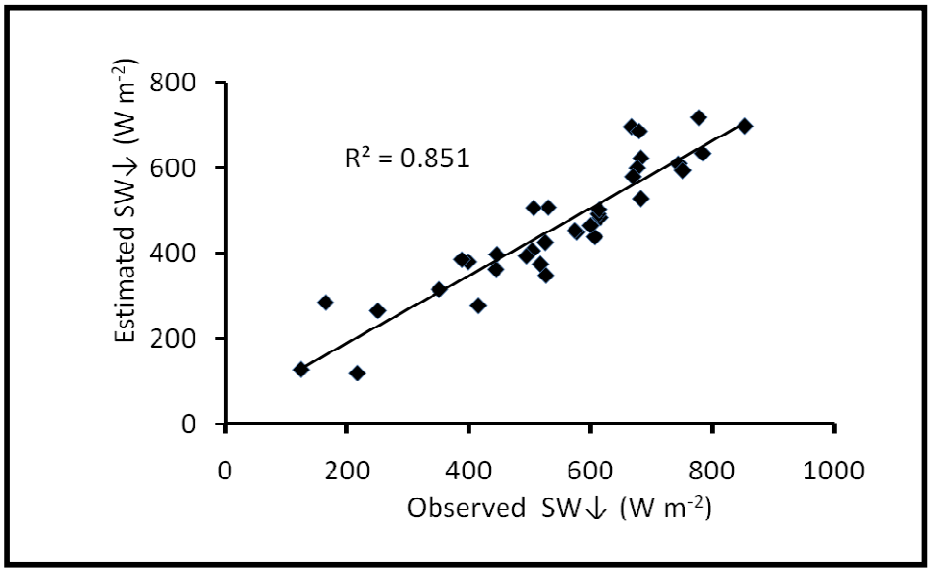

Figure 6.13: Model estimated vs *in situ* observed incoming shortwave radiation flux in Antarctica

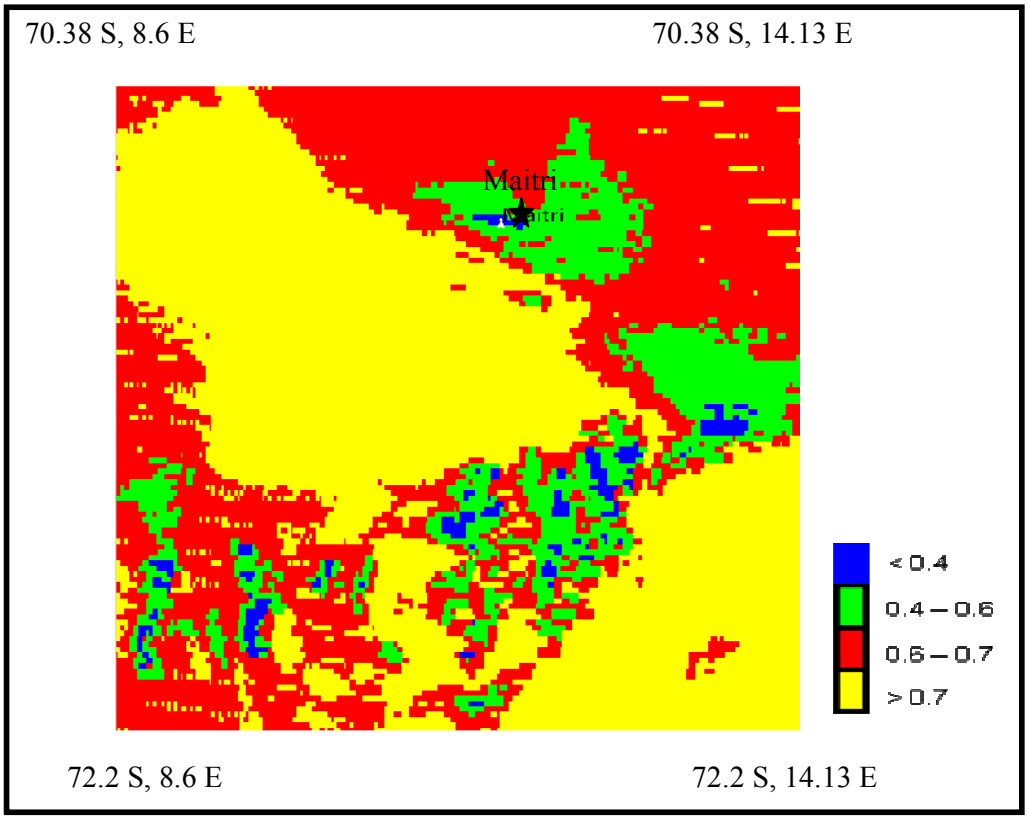

Figure 6.14: Albedo map of Antarctica study area

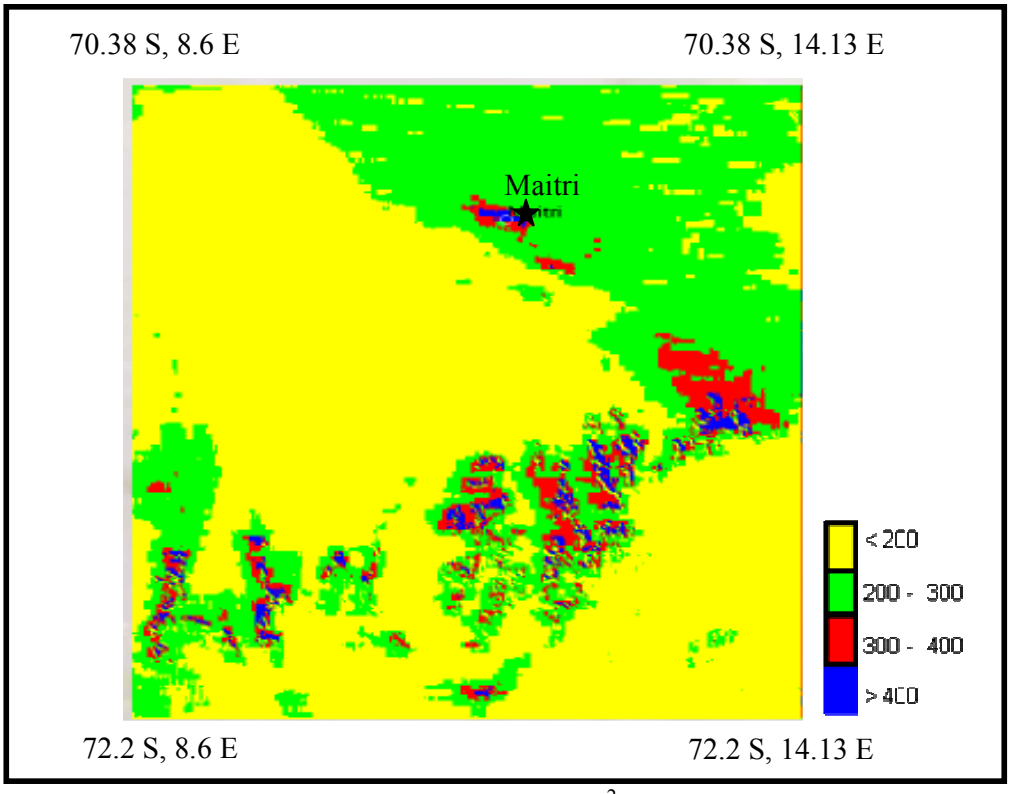

Figure 6.15: Net shortwave radiation flux (W m^{-2}) in Antarctica

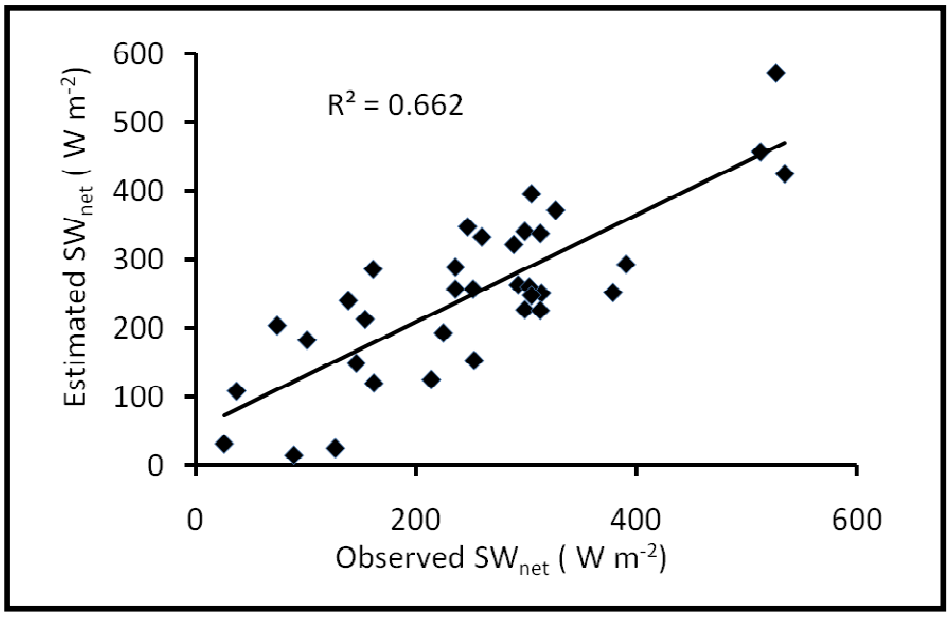

Figure 6.16: Model estimated vs *in situ* observed net shortwave radiation flux in Antarctica

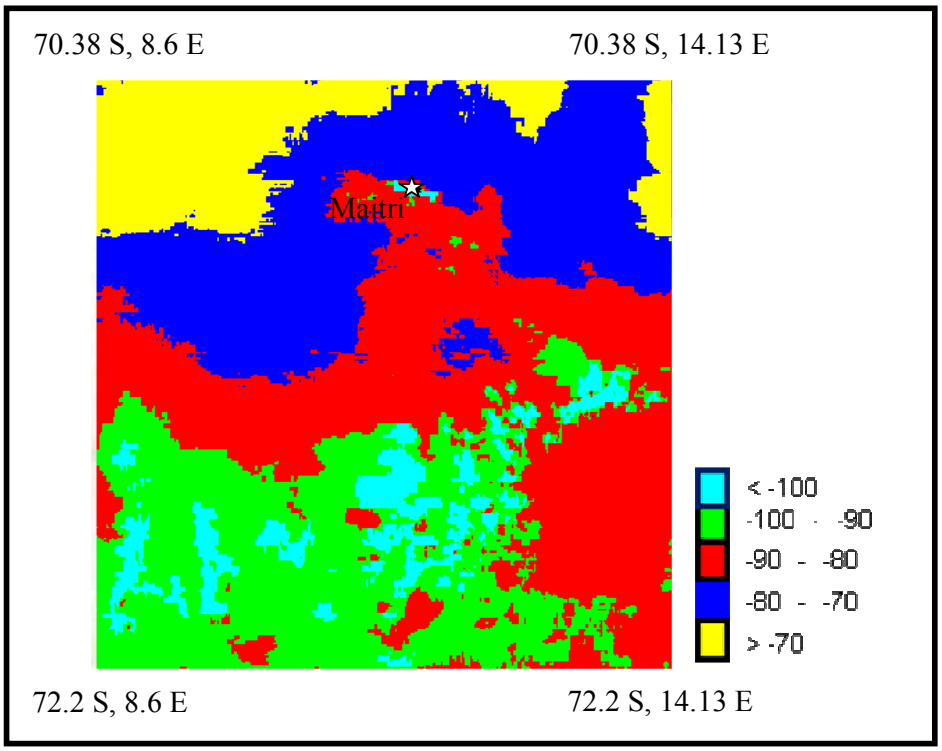

Figure 6.17: Net longwave radiation flux (W m^{-2}) in Antarctica

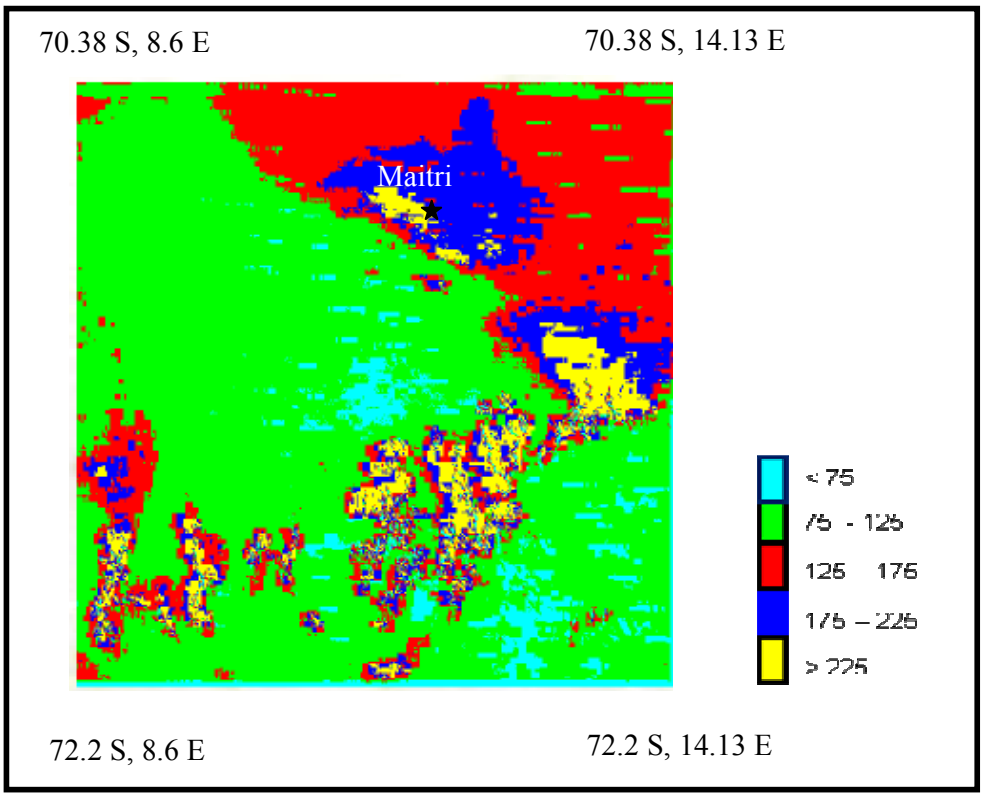

Figure 6.18: Net radiation flux (W m^{-2}) in Antarctica

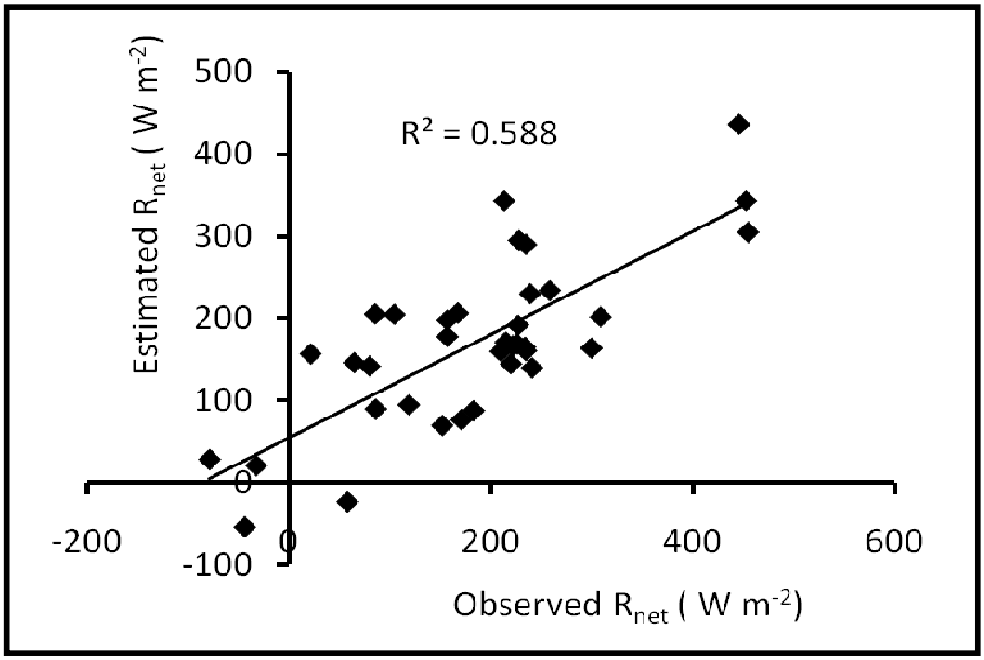

Figure 6.19: Model estimated vs *in situ* observed net radiation flux in Antarctica

Table 6.7: Mean values of different parameters in the Study Area-1

Date	**Solar Zenith Angle (°) (mean ± SD)**	**Surface temperature (°C) (mean ± SD)**	**Albedo (mean ± SD)**	**Incoming shortwave radiation flux ($W\ m^{-2}$) (mean ± SD)**	**Net shortwave radiation flux ($W\ m^{-2}$) (mean ± SD)**	**Net longwave radiation flux ($W\ m^{-2}$) (mean ± SD)**	**Net Radiation flux ($W\ m^{-2}$) (mean ± SD)**
12-Jan-2010	54.7 ± 0.35	-7.8 ± 4.7	0.68 ± 0.09	632 ± 51	204 ± 60	-85 ± 14	128 ± 57
28-Jan-2010	57.8 ± 0.36	-9.5 ± 4.6	0.67 ± 0.08	603 ± 55	202 ± 56	-82 ± 11.6	120.5 ± 54
21-Feb-2010	68.7 ± 0.26	-18.6 ± 4.9	0.65 ± 0.08	409 ± 57	143 ± 48	-64.5 ± 13.5	76.6 ± 42.5

6.4 Summary

The chapter described the estimation of incoming shortwave radiation flux, net shortwave radiation flux, net longwave radiation flux and net radiation flux at spatial level using MODIS images. Estimated energy fluxes have been evaluated using *in situ* recorded energy fluxes at AWS locations. Only few studies (Wang and Pinker 2009, Niu *et al.* 2010) on estimation of incoming shortwave radiation flux for snow/ice surfaces have been reported at coarse spatial resolution of 1°. A summary of the results obtained from the present study is produced in the following,

I. Incoming shortwave radiation flux has been estimated at spatial resolution of 0.5 km with an accuracy of $\pm$14-27% of the mean values. The accuracy is comparable to that reported by Wang and Pinker (2009) and Niu *et al.* (2010).

II. Net shortwave radiation flux has been estimated with RMSE of $\pm$19-28% in both the study areas. Net longwave radiation and net radiation fluxes have been estimated up to RMSE of $\pm$25 % and $\pm$47% of the mean values, respectively. As there is no data from any other source on spatial estimation of these radiation fluxes for snow/ice covered region, the results of this study cannot be compared. RMSE obtained in estimation of net shortwave radiation and net longwave radiation fluxes contribute to higher value of RMSE obtained in estimation of net radiation flux.

III. The spatial and temporal variation of energy fluxes on north and south aspect slopes of mountain topography in western Himalaya have also been discussed. Incoming shortwave radiation flux on south aspect slopes has been observed high compared to north aspect slopes in Western Himalaya because of low mean incidence angle of solar radiation on south aspect slopes compared to north aspect slopes. Variation in amount of incoming shortwave radiation flux on north and south aspect slopes leads to variation in net shortwave radiation flux, net longwave radiation flux and net radiation flux on these aspect slopes. These variations in energy fluxes may be responsible for different metamorphic processes in the snowcover of north and south aspect slopes, which ultimately will result in variation of snowcover properties e.g snow grain type and size, density, shear strength, hardness etc. on these slopes.

After rigorous experiments, maps of radiation fluxes of snow/ice covered regions have been produced. These geospatial maps may be quite useful in many snow and hydrological studies in the Himalayan region and Antarctica, particularly in absence of large *in situ* data. Nevertheless, the accuracy of estimation of these energy fluxes may further be improved by increasing the density of *in situ* observations .

In the next chapter, conclusion derived from the research, major research contributions and the scope of further research have been presented.

Chapter VII

CONCLUSION AND FUTURE SCOPE

7.1 Introduction

Surface energy fluxes of cryospheric regions have many applications in glaciology, hydrology, climatology, snow avalanche forecasting and other snow/ice related studies. Energy balance of these regions are goverened by the interaction of cryosphere and atmosphere through exchange of heat, mass and momentum at the cryosphere-atmosphere interface. Various physical processes e.g. sublimation, evaporation, condensation, deposition, melt, freezing etc. are associated with these exchanges at the interface. Snow/ice covered regions gain or lose mass and energy by these physical processes. The exchange of heat and mass can be quantified through quantification of surface energy fluxes. The principal components of the surface energy fluxes are shortwave and longwave radiative energy fluxes, sensible and latent heat turbulent energy fluxes and sub surface heat flux. These energy fluxes can be measured directly using instruments or can be estimated quantitatively using the meteorological parameters over the snow/ice surface and in the air above. In this research, focus has been placed on estimation of some of the snow-met parameters to characterize various energy fluxes. The snow-met parameters used in

estimation of energy fluxes are air temperature (T_a), surface temperature (T_s), relative humidity (*RH*), wind speed (*w*), atmospheric pressure (*P*), albedo (α), snow depth, cloud amount, cloud type etc.

Radiative energy fluxes are generally observed directly using pyranometers or pyrgeometers. A few parametrization schemes are also in vogue to estimate different radiative energy fluxes using *in situ* meteorological observations. Turbulent energy fluxes can be measured directly using eddy covariance system or scintillometers. However, in most of the studies, these energy fluxes have been estimated using bulk transfer technique. Bulk transfer equations use meteorological parameters over the surface and at screen level height above the surface as input to estimate turbulent energy fluxes. The relative contribution of different energy fluxes to net energy balance differ spatially and strongly depends on the prevailing meteorological, topographical and surface conditions.

Geospatial science encompassing remote sensing and GIS provides an opportunity to study surface energy fluxes at spatial and temporal scales. Estimation of surface energy fluxes of a large study area using remote sensing requires estimation of snow meteorological data at each pixel of the image. Snow-met parameters at each pixel can be estimated from *in situ* observations using appropriate interpolation techniques or modeling of the parameters using physical/statistical or other methods. The main aim of the present research was therefore on geo-spatial modeling of a few snow-met parameters and estimation of surface energy fluxes using *in situ* as well as remote sensing observations for the snow/ice covered cryospheric regions. The specific objectives were:

i) Development of an approach for geo-spatial interpolation of snow depth.

ii) Development of an approach for broad band albedo of snow cover from narrow bands reflectances using moderate and high resolution satellite data.

iii) Estimation of surface energy fluxes at the edge of the Antarctic ice sheet using *in situ* observations and studying their temporal variability.

iv) Estimation and evaluation of incoming shortwave radiation flux, net shortwave radiation flux, net longwave radiation flux and net radiation flux of snow/ice covered regions using remote sensing technique.

v) Study of spatial variability of surface energy fluxes on different aspects of mountain topography.

7.2 Summary of the Research

Different approaches have been employed to accomplish the objectives of this research. Two study areas, namely, cryospheric regions of Antarctica and Western Himalaya have been considered for the study. Snow depth has been mapped in Western Himalaya using spatial interpolation of *in situ* measurements. The interpolation method is based on the dependency of snow depth and elevation above sea level. This general dependency is later adjusted through the *in situ* snow depth observations to represent the local and regional characteristics of the snow distribution. Regression relations between snow depth and elevation have been determined via mathematical functions e.g. linear, exponential, quadratic, logarithmic, power etc. Each of these functions has been applied and investigated. The mathematical function with the least RMSE has been used as the function to estimate the base value of the snow depth. The base value of snow depth at a particular location has been adjusted through a compensation factor. The compensation factor has been computed as the weighted average of the difference of the base value of the snow depth and the observed values of snow depth at three stations that are nearest to the location at which the snow depth has to be estimated. This method has been used to produce snow depth map at spatial resolution of 0.5km. The snow depth maps have been validated at few remote locations of the study area.

Algorithms for direct retrieval of snow broadband albedo using AWiFS and MODIS data have been developed and presented. *In situ* measurements of spectral reflectance and transmitted solar irradiance have been used for estimation of conversion factors and coefficients required for development of snow broadband albedo using AWiFS and MODIS data. The retrieved albedo from AWiFS and MODIS data have been validated with *in situ* measurements at the time of satellite pass in the study area.

Split-window algorithm has been employed to develop an algorithm for estimation of surface temperature in the study area of Antarctica. MODIS thermal bands data and AWS recorded surface temperature data at the time of MODIS pass have been used to develop the regression equation.

Surface energy fluxes have been estimated at the edge of the Antarctic ice sheet using *in situ* snow-met observations. Bulk aerodynamic method has been used to estimate turbulent energy fluxes. Four-years analysis of the meteorological parameters, radiative

and turbulent energy fluxes at the edge of the ice sheet close to the Schirmacher Oasis in East Dronning Maud Land have been presented. Surface energy fluxes have been analysed for summer season, winter season and transition periods, and their temporal variability have been presented.

Spatial variation in surface energy fluxes over a large snow/ice covered area cannot be adequately characterized by energy fluxes estimated using *in situ* measurements. Incoming shortwave radiation flux, net shortwave radiation flux, net longwave radiation flux and net radiation flux have been estimated spatially in western Himalaya and Antarctica using MODIS data in conjuction with *in situ* observed snow-met parameters. Estimated energy fluxes have been evaluated using AWS recorded data. Spatial and temporal variation of energy fluxes on north and south aspect slopes of mountain topography in western Himalaya have also been discussed.

The studies conducted in this research have led to a number of significant conclusions.

7.3 Conclusion

The broad and specific conclusions derived on the basis of the results obtained are stated below,

7.3.1 Broad Conclusions

i. A novel algorithm for geospatial interpolation of snow depth in Western Himalaya has been developed. The algorithm improves upon the limitations of earlier published snow depth interpolation algorithm. The proposed algorithm has advantages over the previous models for estimation of snow depth in Western Himalaya, as it is obtained at higher spatial resolution than those by other models and is applicable for all snow thicknesses. The algorithm will be useful in spatial estimation of sub-surface heat flux, avalanche forecasting, hydrological and other snow studies in Western Himalaya.

ii. An algorithm has been developed for broad band albedo of snow cover from narrow bands reflectance of MODIS and AWiFS data. The algorithm can be used in various snow studies for estimating net shortwave radiation flux and snow melt run off.

iii. Surface energy fluxes have been estimated at the edge of the ice sheet using *in situ* observations. Sublimation and melt have been calculated for 4-years from energy fluxes. The study will be useful in understanding the temporal variability in surface energy fluxes and ablation pattern at the edge of the Antarctic ice sheet.

iv. Incoming shortwave radiation flux, net shortwave radiation flux, net longwave radiation flux, and net radiation flux of snow/ice covered regions have been estimated using remote sensing technique and validated. The findings shall be very valuable in various applications of glaciology, hydrology and other snow studies.

7.3.2 Specific Conclusions

i. An algorithm has been proposed to generate snow depth maps in Western Himalaya at spatial resolution of 0.5 km. The algorithm improved upon the limitations of earlier published algorithm by,

   a. providing the base snow depth equation a dynamic mathematical function, which may vary daily as per the variation in input data.

   b. computing the compensation factor using weighted average of the difference of the base value of the snow depth and the observed values of snow depth at three stations that are nearest to the location at which the snow depth has to be estimated.

   c. keeping weighting factor '*p*' as variable and computed based on least RMSE between observed snow depth and estimated snow depth.

ii. From the proposed snow depth algorithm, an overall correlation coefficient of 0.71 and RMSE of 42 cm between estimated and *in situ* collected snow depth have been obtained.

iii. An algorithm has been proposed for estimation of broad band albedo of snow cover using AWiFS and MODIS sensors images. The retrieved albedo from these images have been validated with *in situ* measurements at Solang, Dhundi and Patsio sites

in the study area. The overall R^2 and RMSE values for AWiFS were observed 0.94 and 0.03, and for MODIS were 0.88 and 0.026 respectively. The albedo maps produced by the algorithm can be used in estimation of net shortwave radiation flux, melt run-off studies and other hydrological studies of snow/ice covered regions.

iv. An algorithm for estimation of surface temperature in the study area of Antarctica has been developed using split-window technique. The coefficient of determination (R^2) and RMSE of 0.99 and 0.8°C, respectively have been obtained between estimated and AWS recorded surface temperature. The algorithm will be useful to estimate outgoing and net long wave radiation flux in the study area of Antarctica.

v. Four-years analysis of the meteorological parameters, radiative and turbulent energy fluxes at the edge of the Antarctic ice sheet has been presented. It has been observed that the meteorological conditions at the observation site have generally been characterised by mild air temperature (annual mean -10.2 ˚C), low relative humidity (annual mean 50%) and high katabatic winds (annual mean 8.3 m s^{-1}). The mean annual atmospheric transmissivity has been observed 0.659 for all weather days and 0.8 for clear sky days at the location.

vi. The energy fluxes have been analysed for summer season, winter season and transition periods. Net radiative flux has been the main heat source to the glacier during summer (summer mean 46.8 Wm^{-2}) and heat sink during winter (winter mean -42.2 Wm^{-2}). Sensible heat flux (annual mean 32 Wm^{-2}) has been the heat source whereas latent heat flux (annual mean -61 Wm^{-2}) has been the heat sink to the glacier surface, throughout the year. Temporal variation of these energy fluxes explain the variation in physical properties of the ice sheet e.g. ice surface temperature, amount of ice melt and sublimation during different months.

vii. Mild temperature, low relative humidity and high katabatic wind as compared to other Antarctic coastal locations cause high latent heat flux at the edge of the ice sheet close to Schirmacher Oasis. This latent heat flux is equivalent to monthly sublimation rate of 5.29 cm w.eq.. This high sublimation rate contribute to higher rate of ablation of the ice sheet at the location.

viii. Incoming shortwave radiation flux and net shortwave radiation flux have been estimated at spatial resolution of 0.5 km and net longwave radiation flux and net

radiation flux have been estimated at spatial resolution of 1.0 km in Western Himalaya and Antarctica using *in situ* observed snow-met parameters and MODIS sensor images. Thus, in the present study the incoming shortwave radiation flux has been estimated at higher spatial resolution as compared to previously reported studies with comparable accuracy of $\pm$14-27% of the mean values. RMSE in estimation of incoming shortwave radiation flux, net shortwave radiation flux and net radiation flux has been found to be 75 W m^{-2}, 84.9 W m^{-2}, 90 W m^{-2} respectively in Western Himalaya and 105 W m^{-2}, 75 W m^{-2}, 81 W m^{-2} respectively in Antarctica. As there is no data from any other source on estimation of net shortwave radiation and net radiation fluxes for snow/ice covered region, the results of this study cannot be compared.

ix. Spatial and temporal variation of energy fluxes on north and south aspect slopes of mountain topography in Western Himalaya has been assessed. Incoming shortwave radiation flux on south aspect slopes has been observed higher than those observed on north aspect slopes for the study period. This may be due to low incidence angle (i) of solar radiation on south aspect slopes as compared to that on the north aspect slopes. Temporal variation in the incoming shortwave radiation flux has been found to be in accordance with the variation of solar zenith angle. However, the temporal variation of net shortwave radiation flux has been found to depend on incoming shortwave radiation flux and the albedo of the snow cover.

7.4 Major Research Contributions

The major research contributions from this research are,

i. A novel geo-spatial interpolation algorithm for snow depth developed here has the potential to be used at operational level in snow avalanche forecasting.

ii. It is believed that algorithm developed for estimation of broad band albedo of snow from narrow band reflectance is the first attempt for AWiFS satellite data.

iii. Four-years sublimation and melt of Antarctic ice sheet have been estimated using energy fluxes. The study highlights the high ablation rate of ice sheet at the study location as compared to other parts of east Antarctica.

iv. This is perhaps the first study reported on spatial estimation of radiation fluxes in Western Himalayan snowcover and on spatial variation of energy fluxes in north and south aspect slopes.

7.5 Future Scope

The work presented in the thesis may be envisaged as a contribution to the geo-spatial modeling of snow-met parameters, estimation of surface energy fluxes at spatial scale and evaluation using *in situ* recorded energy fluxes, generation of information on temporal variation of energy fluxes, sublimation and melt at the edge of the Antarctic ice sheet, and spatial variation of radiation fluxes on different aspect slopes in mountain topography. However, more work may be carried out in future to strengthen the present work. Some of the pointers for future work may be enumerated as,

i. Air temperature has been modeled at spatial scale using temperature lapse rate (TLR) method. Other spatial interpolation technique may be explored as air temperature has impact on accuracy of incoming shortwave radiation flux and consequently on other energy fluxes.

ii. Turbulent energy fluxes i.e. sensible and latent heat fluxes may be estimated at spatial level using remote sensing data in conjuction with *in situ* recorded snow-met parameters for wide applications. Estimation of sub surface heat flux at spatial level may also be attempted using snow depth maps, surface temperature maps and snow cover density obtained from *in situ* observations.

iii. Surface energy fluxes of the snow/ice covered region have been estimated at the time of satellite pass. These fluxes may be modeled for daily averages and diurnal variation for variety of applications.

iv. Accuracy of the estimated fluxes may be increased by increasing the density of *in situ* observations in the study area and increasing the accuracy of estimated snow-met parameters at spatial level.

REFERENCES

Ackerman, S. A., and Knox, J. A., 2003, *Meteorology – Understanding the Atmosphere*, Thomson Brooks/Cole, USA, pp. 486.

Alam, A., Romshoo, S. A., and Bhat, M. S., 2011, Estimation of snowmelt runoff using Snowmelt Runoff Model (SRM) in A Himalayan watershed, *World Journal of Science and Technology,* 1(9), pp. 37 – 42.

Ambach, W. and Kirchlechner, P., 1986, Nomographs for the determination of meltwater from ice and snow surfaces by sensible and latent heat. *Wetter Leben*, 38, pp. 181–189.

Anderson, E. A., 1976, A point energy and mass balance model of a snow cover, *NOAA Technical Report NWS 19*, US National Weather Service, pp. 150.

Armstrong, R. L. and Brun, E., 2008, *Snow and Climate (Physical Processes, Surface Energy Exchange and Modeling)*, Cambridge University Press, UK, pp. 254.

Arora, M. K., Shukla, A. and Gupta, R. P., 2011, Digital image information extraction techniques for snow cover mapping from remote sensing data, *Encyclopaedia of Snow, Ice and Glaciers (edited by Vijay P. Singh, Pratap Singh and Umesh K. Haritashya)*, Springer, pp. 213- 231.

Azam, M. F., Wagnon, P., Vincent, C., Ramanathan, A. L., Mandal, A. and Pottakkal, J. G., 2014, Processes governing the mass balance of Chhota Shigri Glacier (Western Himalaya, India) assessed by point-scale surface energy balance measurements, *The Cryosphere Discussion*, 8, pp. 2867-2922.

Barnes, W. L., Pagano, T. S. and Salomonson, V. V., 1998, Prelaunch characteristics of the Moderate Resolution Imaging Spectroradiometer (MODIS) on EOS-AM1, *IEEE Transactions on Geoscience and Remote Sensing*, 36, pp. 1088–1100.

Bastiaanssen, W.G.M., 2000, SEBAL-based sensible and latent heat fluxes in the irrigated Gediz Basin, Turkey, *Journal of Hydrology,* 229, pp. 87–100.

Basist, A., Grody, N. C., Peterson, T. C. and Williams, C. N., 1998, Using the Special Sensor Microwave/Imager to monitor land surface temperatures, wetness and snowcover, *Journal of Applied Meteorology*, 37, pp. 888-911.

Bennett, T. J., 1982, A coupled atmosphere–sea ice model study of the role of sea ice in climatic predictability, *Journal of Atmospheric Science*, 39, pp. 1456–1465.

Berliand, T. C., 1960, Method of climatological estimation of global radiation, *Meteorologiya i Gidrologiya,* 6, pp. 9–12.

Bintanja, R., 1995, The local surface energy balance of the Ecology Glacier, King George Island, Antarctica: measurements and modelling. *Antarctic Science*, 7, pp. 315–325.

Bintanja, R., 1999, On the glaciological, meteorological, and climatological significance of Antarctic blue ice areas, *Reviews of Geophysics*, 37, pp. 337-359.

Bintanja, R., 2000, Surface heat budget of Antarctic snow and blue ice: Interpretation of spatial and temporal variability, *Journal of Geophysical Research*, 105, pp. 24387-24407.

Bintanja, R. and Reijmer, C. H., 2001, Meteorological conditions over Antarctic blue-ice areas and their influence on the local surface mass balance, *Journal of Glaciology*, 17, 37–50.

Bintanja, R., Jonsson, S. and Knap, W. H., 1997, The annual cycle of the surface energy balance of Antarctic blue ice, *Journal of Geophysical Research*, 102(D2), pp. 1867–1881.

Bintanja, R. and Van Den Broeke, M. R., 1995b. The surface energy balance of Antarctic snow and blue ice, *Journal of Applied Meteorology*, 34(4), pp. 902 – 926.

Bintanja, R. and Van Den Broeke, M. R., 1994, Local climate, circulation and surface-energy balance of an Antarctic blue-ice area. *Annals of Glaciology*, 20, pp. 160–168.

Bisht, G., Venturini, V., Islam, S. and Jiang, L., 2005, Estimation of the net radiation using MODIS (Moderate Resolution Imaging Spectroradiometer) data for clear sky days, *Remote Sensing of Environment*, 97, pp. 52-67.

Bisht, G., and Bras, R. L., 2010a, Estimation of the net radiation from MODIS data under all sky conditions: Southern Great Plains case study, *Remote Sensing of Environment*, 114, pp. 1522-1534.

Bisht, G. and Bras, R. L., 2010b, Estimation of net radiation from the Moderate Resolution Imaging Spectroradiometer over the continental United States, *IEEE Transactions on Geoscience and Remote Sensing*, 49 (6), pp. 2448-2462.

Bliss, A. K., Cuffey, K. M. and Kavanaugh, J. L., 2011, Sublimation and surface energy budget of Taylor Glacier, Antarctica, *Journal of Glaciology*, 57, pp 684-696.

Bolch, T., Kulkarni, A., Kääb, A., Huggel, C., Paul, F., Cogley, J. G., Frey, H., Kargel, J. S., Fujita, K., Scheel, M., Bajracharya, S., Stoffel, M., 2012, The state and fate of Himalayan glaciers, *Science*, 336, pp. 310-314.

Bowyer, P., Danson, F. M., Trodd, N., 2003, Methods of sensitivity analysis in remote sensing: implications for canopy reflectance model inversion, *IEEE International Geoscience and Remote Sensing Symposium(IGARSS)*, 21-25 July 2003, 6, pp. 3839 – 3841.

Braithwaite, R. J., Konzelmann, T., Marty, C. and Olesen, O. B., 1998, Reconnaissance study of glacier energy balance in North Greenland, 1993-94. *Journal of Glaciology*, 44, 147, pp.239-247.

Brock, B.W., Willis, I. C., Sharp, M. J. and Arnold, N. S., 2000, Modelling seasonal and spatial variations in the surface energy balance of Haut Glacier d'Arolla, Switzerland, *Annals of Glaciology*, 31, 53–62.

Brock, B. W., Willis, I. C. and Sharp, M. J., 2006, Measurement and parameterization of aerodynamic roughness length variations at Haut Glacier d'Arolla, Switzerland, *Journal of Glaciology,* 52, pp. 281-297.

Brogioni, M., Macelloni, G., Pettinato, S., Montomoli, F., 2011, Estimation of air and surface temperature evolution of the east Antarctic sheet by means of passive microwave remote sensing, *IEEE International Geoscience and Remote Sensing Symposium(IGARSS)*, 24-29 July 2011, Vancouver, BC, pp. 3859-3862.

Brown R. D., Brasnett, B. and Robinson, D., 2003, Gridded North American monthly snow depth and snow water equivalent for GCM evaluation, *Atmosphere-Ocean*, 41, pp. 1-14.

Brutsaert, W., 1975, On a derivable formula for long wave radiation from clear skies, *Water Resource Research*, 11, 742–744.

Buck, A. L., 1981, New equations for computing vapor pressure and enhancement factor, *Journal of Applied Meteorology*, 20, pp. 1527-1532.

Bühler, Y., 2012, Remote sensing tools for snow and avalanche research, *Proceedings International Snow Science Workshop*, September 16-21 2012, Anchorage, Alaska, pp. 264-268.

Chai, H., Cheng, W., Zhou, C., Chen, X., Ma, X. and Zhao, S., 2011, Analysis and comparison of spatial interpolation methods for temperature data in Xinjiang Uygur Autonomous Region, China, *Natural Science*, 3 , pp. 999-1010.

Chavez, P. S. Jr., 1988, An improved dark object subtraction technique for atmospheric scattering correction of multispectral data, *Remote Sensing of Environment*, 24, pp. 459–479.

Chavez, P. S. Jr., 1989, Radiometric calibration of Landsat Thematic Mapper multispectral images, *Photogrammetric Engineering and Remote Sensing*, 55, pp. 1285-1294.

Chavez, P. S. Jr., 1996, Image based atmospheric corrections revisited and improved, *Photogrammetric Engineering and Remote Sensing*, 62, pp. 1025 – 1036.

Chang, A. T. C., Foster, J. L. and Hall, D. K., 1987, Nimbus-7 derived global snow cover parameters, *Annals of Glaciology*, 9, pp. 39-44.

Chang, T. Y., Liou, Y. A., Lin, C. Y., Liu, S. C. and Wang, Y. C., 2010, Evaluation of surface heat fluxes in Chiayi plain of Taiwan by remotely sensed data, *International Journal of Remote Sensing*, 31, pp. 3885–3898.

Che, T., Li, X., Jin, R., Armstrong, R. and Zhang, T., 2008, Snow depth derived from passive microwave remote sensing data in China, *Annals of Glaciology*, 49, pp. 145-154.

Chehbouni, A., Nichols, W. D., Njoku, E. G., Qi, J., Kerr, Y. H. and Cabot, F., 1997, A three component model to estimate sensible heat flux over sparse shrubs in Nevada, *Remote Sensing Reviews*, 15, pp. 99-112.

Civco, D. L., 1989, Topographic normalization of Landsat Thematic Mapper digital imagery, *Photogrammetric Engineering and Remote Sensing*, 55, pp. 1303-1309.

Colby, J. D., 1991, Topographic normalization in rugged terrain, *Photogrammetric Engineering and Remote Sensing*, 55, pp. 531-537.

Courault, D. and Monestiez, P., 1999, Spatial interpolation of air temperature according to atmospheric circulation patterns in Southeast France, *International Journal of Climatology*, 19, pp. 365-378.

Cresswell, M. P., 1999, Estimating surface air temperatures, from Meteosat land surface temperatures, using an empirical solar zenith angle. *International Journal of Remote Sensing*, 20, pp. 1125–1132.

Cuffey, K. M. and Paterson, W. S. B., 2010, *The Physics of Glaciers*, Fourth Edition, B H Elsevier, ISBN 978-0-12-369461-4, pp. 693.

Dai, L., Che, T., Wang, J. and Zhang, P., 2012, Snow depth and snow water equivalent estimation from AMSR-E data based on a priori snow characteristics in Xinjiang, China, *Remote Sensing of Environment*, 127, pp. 14-29.

Das, I. and Sarwade, R. N., 2008, Snow depth estimation over north-western Indian Himalaya using AMSR-E, *International Journal of Remote Sensing*, 29, pp. 4237-4248.

Datt, P., Srivastava, P. K., Negi, P. S. and Satyawali, P. K., 2008, Surface energy balance of seasonal snow cover for snow-melt estimation in N-W Himalaya, *Journal of Earth System Science*, 117 (5), pp. 567–573.

Deardorff, J. W., 1968, Dependence of air-sea transfer coefficients on bulk stability, *Journal of Geophysical Research*, 73 (8), pp. 2549-2557.

Deems, J. S., Fassnacht, S. R. and Elder, K., 2006, Fractal distribution of snow depth from LIDAR data, *Journal of Hydrometeorology,* 7(2), pp. 285–297.

Deems, J. S. and Painter, T. H., 2006, Lidar measurement of snow depth: accuracy and error sources, *Proceedings of the International Snow Science Workshop,* 1–6 October, 2006, Telluride, Colorado, USA, pp. 30–38.

Deneke, H. M., Feijt, A. J. and Roebeling, R. A., 2008, Estimating surface solar irradiance from METEOSAT SEVIRI-derived cloud properties, *Remote Sensing of Environment*, 112, pp. 3131–3141.

Dewali, S. K., Snehmani, Singh, P. S. and Sarwade, R. N., 2009, A GIS-based avalanche hazard zonation scheme for NW Himalaya using topographical and meteorological variables, *Proceedings of International Symposium on Snow and Avalanches (ISSA-09)*, 6-10 April 2009, Manali, India, pp. 99-107.

Dilley, A.C., O'Brien, D.M., 1998, Estimating downward clear sky long-wave irradiance at the surface from screen temperature and precipitable water, *Quaterly Journal of Royal Meteorological Society,* 124, 1391–1401.

Doran, P. T., Mckay, C. P., Meyer, M. A., Andersen, D. T., Wharton JR., R. A. and Hastings, J. T., 1996, Climatology and implications for perennial lake ice occurrence at Bunger Hills Oasis, east Antarctica, *Antarctic Science*, 8, pp. 289-296.

Dozier, J., 1980, A clear sky spectral solar radiation model for snow-covered mountainous terrain, *Water Resource Research*, 16, 709–718.

Drewry, D. J., Jordan, S. R. and Jankowski, E., 1982, Measured properties of the Antarctic ice sheet: Surface configuration, ice thickness, volume, and bedrock characteristics, *Annals of Glaciology*, 3, pp. 83-91.

Duguay, C. R., 1993, Modelling the radiation budget of alpine snowfields with remotely sensed data: model formulation and validation, *Annals of Glaciology*, 17, pp.288-293.

Duguay, C. R., 1995, An approach to the estimation of surface net radiation in mountain areas using remote sensing and digital terrain data, *Theoretical and Applied Climatology*, 52, pp. 55-68.

Elder, K., Rosenthal, W. and Davis, R., 1998, Estimating the spatial distribution of snow water equivalence in a montane watershed. *Hydrological Processes* 12, 1793–1808.

Eldrandaly, K. A. and Abu-Zaid, M. S., 2011, Comparison of six GIS-based spatial interpolation methods for estimating air temperature in Western Saudi Arabia, *Journal of Environmental Informatics*, 18 , pp. 38-45.

Erxleben, J., Elder, K., Davis, R., 2002, Comparison of spatial interpolation methods for estimating snow distribution in the Colorado Rocky Mountains, *Hydrological Processes,* 16, pp. 3627–3649.

Fierz, C., Riber, P., Adams, E.E., Curran, A. R., Föhn, P.M.B., Lehning, M. And Plüss, C., 2003, Evaluation of snow-surface energy balance models in alpine terrain, *Journal of Hydrology*, 282, pp. 76-94.

Florio, E. N., Lele, S. R., Chang, Y. C., Sterner, R. and Glass, G. E., 2004, Integrating AVHRR satellite data and NOAA ground observations to predict surface air temperature: a statistical approach. *International Journal of Remote Sensing*, 25, pp. 2979–2994.

Foppa, N., Stoffel, A., and Meister, R., 2007, Synergy of in situ and space borne observation for snow depth mapping in the Swiss Alps, *International Journal of Applied Earth Observation and Geoinformation*, 9, pp. 294-310.

Foody, G. M. and Atkinson, P. M., 2002, *Uncertainty in remote sensing and GIS*, John Wiley & Sons Ltd., West Sussex, England , pp. 307.

Fountain, A. G., Nylen, T. H., MacClune, K. L. and Dana, G. L., 2006, Glacier mass balances (1993–2001), Taylor Valley, McMurdo Dry Valleys, Antarctica, *Journal of Glaciology*, 52, 451–462.

Gates, D. M., 1980, *Biophysical Ecology*, Springer-Verlag, New York.

Garcia, M., Fernandez, F., Villagarcia, L., Palacios-Orueta, A., Were, A., Puigdefabregas, J. and Domingo, F., 2008, Estimating latent and sensible heat fluxes using the temperature vegetation dryness index (TVDI) and MODIS data, *IEEE International Geoscience and Remote Sensing Symposium(IGARSS),* July 8-11, 2008, Boston, Massachusetts, USA.

Genthon, C., Lardeux, P. and Krinner, G., 2007, The surface accumulation and ablation of a coastal blue-ice area near Cap Prudhomme, Terre Adelie, Antarctica. *Journal of Glaciology*, 53, 635–645.

Giesen, R. H., Van den Broeke, M. R., Oerlemans, J., and Andreassen, L. M., 2008, Surface energy balance in the ablation zone of Midtdalsbreen, a glacier in southern Norway : Interannual variability and the effect of clouds, *Journal of Geophysical Research,* 113, D21111, doi:10.1029/2008JD010390, pp.1-17.

Grenfell, T. C., 2011, Albedo, *Encyclopedia of Snow, Ice and Glaciers (edited by Vijay P. Singh, Pratap Singh and Umesh K. Haritashya)*, Springer, pp. 1253.

Greuell, W. and Konzelmann, T., 1994, Numerical modelling of the energy balance and the englacial temperature of the Greenland ice sheet: calculation for the ETH-camp location (West Greenland, 1155 m a.s.l), *Global and Planetary Change*, 9, pp. 91–114.

Greuell, W., Reijmer, C. H. and Oerlemans, J., 2002, Narrowband-to-broadband albedo conversion for glacier ice and snow based on aircraft and near-surface measurements. *Remote Sensing of Environment*, 82, pp.48-64.

Greuell, W. and Oerlemans, J., 1986, Sensitivity studies with a mass-balance model including temperature profile calculations inside the glacier, *Z. Gletscherkd Glazialgeol.*, 22, pp.101-124.

Greuell, W. and Oerlemans, J., 2004, Narrowband-to-broadband albedo conversion for glacier ice and snow: equations based on modeling and ranges of validity of the equations. *Remote Sensing of Environment*, 89, pp.95-105.

Gr¨unewald, T., St¨otter, J., Pomeroy, J. W., Dadic, R., Moreno Ba˜nos, I., Marturi`a, J., Spross, M., Hopkinson, C., Burlando, P. and Lehning, M., 2013, Statistical modelling

of the snow depth distribution in open alpine terrain, *Hydrology and Earth System Science*, 17, pp. 3005–3021.

Gusain, H. S., Chand, D., Thakur, N., Singh, A., and Ganju, A., 2009a, Snow avalanche climatology of Indian Western Himalaya, *Proceedings International Symposium on Snow and Avalanches (ISSA-2009)*, Manali India, 6-10 April, pp. 85-93.

Gusain, H. S., Mishra, V. D., and Arora, M. K., 2014a, A four-year record of the meteorological parameters, radiative and turbulent energy fluxes at the edge of the East Antarctic ice sheet, close to Schirmacher Oasis, *Antarctic Science*, 26 (1), pp. 93-103.

Gusain, H. S., Mishra, V. D., and Arora, M. K., 2014b, Estimation of net shortwave radiation flux of western Himalayan snow cover during clear sky days using remote sensing and meteorological data, *Remote Sensing Letters*, 5(1), pp. 83-92.

Gusain, H. S., Mishra, V. D., and Negi, A., 2011, Comparative study of the radiative and turbulent energy fluxes during summer and winter at the edge of the Antarctic ice sheet in Dronning Maud Land –East Antarctica, *MAUSAM*, 62(4), pp. 557-566.

Gusain, H. S., Singh, A., Ganju, A. and Singh, D., 2004, Characteristics of the seasonal snow cover of Pir Panjal and Great Himalayan ranges in Indian Himalaya, *International symposium on snow monitoring and avalanches*, 12-16 April, 2004, Manali, India, pp. 97-102.

Gusain, H. S., Singh, K. K., Mishra, V. D., Srivastava, P. K. and Ganju, A., 2009b, Study of surface energy and mass balance at the edge of the Antarctic ice sheet during summer in Dronning Maudland, East Antarctica, *Antarctic Science*, 21(4), pp. 401-409.

Gustafsson, D., Stähli, M., Jansson, P.-E., 2001. The surface energy balance of a snow cover: comparing measurements to two different simulation models. *Theoretical and Applied Climatology*, 70, pp. 81-96.

Hall, D. K., 2011, Surface temperature of snow and ice, *Encyclopaedia of Snow, Ice and Glaciers (edited by Vijay P. Singh, Pratap Singh and Umesh K. Haritashya)*, Springer, pp. 1123-1125.

Hall, D. K., Riggs, G. A., and Salomonson, V. V., 1995. Development of methods for mapping global snow cover using Moderate Resolution Imaging Spectroradiometer (MODIS) data. *Remote Sensing of Environment*, 54, pp. 127–140.

Hall, D. K., Key, J. R., Casey, K. A., Riggs, G. A. and Cavalieri, D. J., 2004, Sea ice surface temperature product from MODIS, *IEEE Transactions on Geoscience and Remote Sensing,* 42, pp. 1076-1087.

Hall, D. K., Riggs, G. A., Salomonson, V. V., Digirolamo, N. E., and Bayr, K. J., 2002, MODIS snow cover products, *Remote Sensing of Environment*, 83, pp.181-194.

Hernandez, T., Nachabe, M., Ross, M. and Obeysekera, J., 2003, Modeling runoff from variable source areas in humid, shallow water table environments, *Journal of the American Water Resources Association*, 39 (1), pp. 75-85.

Hetrick, W.A., Rich, P. M., Barnes, F. J. and Weiss, S. B., 1993, GIS-based solar radiation flux models, *American Society of Photogrammetry and Remote Sensing Technical papers (GIS Photogrammetry and Modeling),* 3, pp. 132-143.

Hoffman, M., J., Fountain, A. G. and Liston, G. E., 2008, Surface energy balance and melt thresholds over 11 years at Taylor Glacier, Antarctica, *Journal of Geophysical Research*, 113, 10.1029/2008JF001029, pp. 1-12.

Hopkinson, C., Sitar, M., Chasmer, L. and Treltz, P., 2004, Mapping snowpack depth beneath forest canopies using airborne Lidar. *Photogrammetric Engineering and Remote Sensing,* 70, 323–330.

Idso, S. B., 1981, A set of equations for full spectrum and 8- to 14- μm and 10.5- to 12.5-μm thermal radiation from cloudless skies, *Water Resource Research*, 17, pp. 295–304.

IPCC, 2007 (Climate Change 2007): *Climate Change Impacts, Adaptation and Vulnerability, Working Group II Contribution to the Intergovernmental Panel on Climate Change - Fourth Assessment Report Summary for Policymakers*. Cambridge University Press: Cambridge and New York

Iqbal, M., 1983, *An Introduction to Solar Radiation*, Academic Press, 390 pp.

Jacobs, J. D., 1978, Radiation climate of Broughton Island, Energy budget studies in relation to fast-ice breakup processes In Davis Strait (Ed.). *Occas. Pap., FULL FORM vol. 26, Institute of Arctic and Alpine Research*, University of Colorado, Boulder, United States, pp. 105–120.

Jiang, L. and Islam, S., 2010, An intercomparison of regional latent heat flux estimation using remote sensing data, *International Journal of Remote Sensing*, 24, pp. 2221–2236.

Jonas, T., Marty C. and Magnusson J., 2009, Estimating the snow water equivalent from snow depth measurements in the Swiss Alps, *Journal of Hydrology*, 378, pp. 161-167.

Journée, M. and Bertrand, C., 2010, Improving the spatio-temporal distribution of surface solar radiation data by merging ground and satellite measurements, *Remote Sensing of Environment,* 114, pp. 2692–2704.

Kasten, F., 1962, *Table of solar altitudes for geographical latitudes±77°10'*, CRREL Special Report 57 U.S. Army Corps of Engineers, Hanover, New Hampshire, 169p.

Kelly, R. E., Chang, A. T., Tsang, L. and Foster, J. L., 2003, A prototype AMSR-E global snow area and snow depth algorithm, *IEEE Transactions on Geoscience and Remote Sensing*, 41 , pp.230-242.

Key, J. R., Collins, J. B., Fowler, C. and Stone, R. S., 1997, High-latitude surface temperature estimates from thermal satellite data, *Remote Sensing of Environment*, 61, pp. 302-309.

Key, J., Wang, X., Stroeve, J. and Fowler, C., 2001, Estimating the cloudy sky albedo of sea ice and snow from space, *Journal of Geophysical Research*, 106, pp. 12,489-12,497.

Kim, Y. and Lee, K., 2005, An experimental study on the image - based atmospheric correction method for high resolution multispectral data, *Proceedings Geoscience and Remote Sensing Symposium (IGARSS), 25-29 July 2005,*1, pp. 3.

King, J. C., Anderson, P. S. and Mann, G. W., 2001, The seasonal cycle of sublimation at Halley, Antarctica, *Journal of Glaciology*, 47, 1–8.

King, J. C., and Turner, J., 1997, *Antarctic Meteorology and Climatology*, Cambridge University Press*,* UK, pp. 409.

Klok, E. J., Nolan, M. and Van Den Broeke, M. R., 2005, Analysis of meteorological data and the surface energy balance of McCall Glacier, Alaska, USA, *Journal of Glaciology*, Vol. 51, No. 174, pp. 451-461.

Konzelmann, T. and Braithwaite, R. J., 1995, Variations of ablation, albedo and energy balance at the margin of the Greenland ice sheet, Kronprins Christian Land, eastern north Greenland, *Journal of Glaciology*, 41, pp. 174-182.

Kuipers Munneke, P., Van Den Broeke, M. R., King, J. C., Gray, T. and Reijmer, C. H., 2012, Near-surface climate and surface energy budget of Larsen C ice shelf, Antarctic Peninsula, *The Cryosphere*, 6, pp. 353-363.

Kulkarni, A. V., Singh, S. K., Mathur, P. and Mishra, V. D., 2006, Algorithm to monitor snow cover using AWiFS data of RESOURCESAT-1 for the Himalayan region, *International Journal of Remote Sensing*, 27 (12), pp. 2449-2457.

Kumar, S. K., Shashikumar, M. C. and Sivasankar, E., 2010, Spatial interpolation of air temperature in Himalayas, *IEEE Conference Proceedings on 'Recent Advances in Space Technology Services and Climate Change (RSTSCC)'*, 13-15 November, Chennai, pp. 74-76.

Kumar, V., Rao, Y. S., Venkataraman, G., Sarwade, R.N. and Snehmani, 2006, Analysis of Aqua AMSR-E derived Snow Water Equivalent over Himalayan Snow Covered Regions, *IEEE International Geoscience and Remote Sensing Symposium(IGARSS)*, July 31-August 4, Denver CO, pp. 702 - 705.

Kunkel, K. E., 1989, Simple procedures for extrapolation of humidity variables in the mountainous Western United States, *Journal of Climate*, 2, pp. 656-669.

Kustas, W. P. and Norman, J. M., 1996, Use of remote sensing for evapotranspiration monitoring over land surfaces, *Hydrological Sciences Journal*, 41, 495-516.

Kustas, W. P., Choudhury, B. J., Moran, M. S., Reginato, R. J., Jackson, R. D., Gay, L. W. and Weaver, H. L., 1989, Determination of sensible heat flux over sparse canopy using thermal infrared data. *Agricultural and Forest Meteorology,* 44, pp.197-216.

Laevastu, T., 1960, *Factors affecting the temperature of the surface layer of the sea*, Academic Book Store*,* Helsinki*,* 136 pp.

Lai, Y. J., Li, C. F., Lin, P. H., Wey, T. H. and Chang, C. S., 2012, Comparison of MODIS land surface temperature and ground-based observed air temperature in complex topography, *International Journal of Remote Sensing*, 33, pp. 7685-7702.

Lewis, K. J., Fountain, A. G. and Dana, G. L., 1998, Surface energy balance and melt water production for a Dry Valley glacier, Taylor Valley, Antarctica, *Annals of Glaciology*, 27, pp. 603-609.

Liang, S., Strahler, A. and Walthall, C., 1999, Retrieval of land surface albedo from satellite observations: A simulation study, *Journal of Applied Meteorology*, 38, pp. 712-725.

Liang, S., 2000, Narrowband to broadband conversions of land surface albedo I Algorithms, *Remote Sensing of Environment*, 76, pp. 213-238.

Liang, S., Shuey, C. J., Russ, A. L., Fang, H., Chen, M., Walthall, C. L., Daughtry, C. S. T. and Hunt Jr., R., 2002, Narrowband to broadband conversions of land surface albedo : II validation, *Remote Sensing of Environment*, 84, pp. 25-41.

Liang, S., 2003, A direct algorithm for estimating land surface broadband albedo from MODIS imagery, *IEEE Transaction of Geoscience and Remote Sensing*, 41, pp. 136-145.

Liang, S., Wang, K., Zhang, X. and Wild, M., 2010, Review on estimation of land surface radiation and energy budgets from ground measurement, remote sensing and model simulations, *IEEE Journal of Selected Topics in Applied Earth Observations and Remote Sensing*, 3, pp. 225-240.

Liang, S., Yu, Y., and Defelice, T. P., 2005, VIIRS narrowband to broadband land surface albedo conversion: Formula and validation, *International Journal of Remote Sensing*, 26, pp. 1019-1025.

Lindsay, R.W., 1998, Temporal variability of the energy balance of thick Arctic pack ice, *Journal of Climate*, 11, pp. 313-333.

Liu, J., Curry, J. A., Rossow, W. B., Key, J. R. and Wang, X., 2005, Comparison of surface radiative flux data sets over the Arctic Ocean, *Journal of Geophysical Research*, 110, C02015, doi:10.1029/2004JC002381, pp 1-13.

Lynch, A. H., Chapin, F. S., Hinzman, L. D., Wu, W., Lilly, E., Vourlitis, G. and Kim, E., 1999, Surface energy balance on the Arctic Tundra : Measurements and Models, *Journal of Climate*, 12, pp. 2585-2606.

Markham, B. L. and Barker, J. L., 1986, Landsat MSS and TM post-calibration dynamic ranges, exoatmospheric reflectances and at-satellite temperature, *EOSAT Technical Notes*, 1, pp. 3-8.

Marks, D. and Dozier, J., 1979, A clear-sky long wave radiation model for remote alpine areas, *Archive fur Meteorologie Geophysik und Bioklimatologie,* 27, pp. 159–178.

Marofi, S., Tabari, H. and Abyanech, H. Z., 2011, Predicting spatial distribution of snow water equivalent using multivariate non-linear regression and computational intelligence methods, *Water Resource Management*, 25, pp. 1417-1435.

Masuda, K., Leighton, H. G., and Li, Z., 1995, A new parameterization for the determination of solar flux absorbed at the surface from satellite measurements, *Journal of Climate*, 8, pp. 1615-1629.

Maykut, G. A. and Church, P. F., 1973, Radiation climate of Barrow, Alaska, 1962–66, *Journal of Applied Meteorology,*12, pp. 620–628.

Mc Clung, D., Schaerer, P., 1993, *The avalanche handbook, Mountaineers*, 1001 SW Klickitat Way, Seattle, USA, 342 pp.

Mishra, V. D., 1999. Albedo variations and surface energy balance in different snow-ice media in Antarctica, *Defence Science Journal*, 49, pp. 347–362.

Mishra, V. D., Gusain, H. S., Arora, M. K., 2012, Algorithm to derive narrow band to broad band albedo for snow using AWiFS and MODIS imagery of Western Himalaya-validation, *International Journal of Remote Sensing Applications*, 2(3), pp. 52-62.

Mishra, V. D., Negi, H. S., Rawat, A. K., Chaturvedi, A. and Singh, R. P., 2009, Retrieval of sub-pixel snow cover information in the Himalayan region using medium and coarse resolution remote sensing data, *International. Journal of Remote Sensing*, 30 (18), pp. 4707 – 4731.

Mishra, V. D., Sharma, J. K., and Khanna, R., 2010, Review of topographic analysis methods for the Western Himalaya using AWiFS and MODIS satellite imagery, *Annals of Glaciology*, 51, pp.1-8.

Mishra, V. D., Sharma, J. K., Singh, K. K., Thakur, N. K. and Kumar, M., 2009, Assessment of different topographic corrections in AWiFS satellite imagery of Himalaya terrain, *Journal of Earth System Science*, 118, , pp. 11-26.

Mito, C. O., Boiyo, R. K. and Laneve, G., 2012, A simple algorithm to estimate sensible heat flux from remotely sensed MODIS data, *International Journal of Remote Sensing*, 33, pp. 6109–6121.

Moody, E. G., King, M. D., Schaaf, C. B., Hall, D. K. and Platnick, S., 2007, Northern Hemisphere five-year average (2000-2004) spectral albedos of surfaces in the presence of snow: Statistics computed from Terra MODIS land products, *Remote Sensing of Environment*, 111, 337-345.

Moore, R. D., 1983, On the use of bulk aerodynamic formulae over melting snow, *Nordic Hydrol*ogy, pp. 193-206.

Moran, M. S., Jackson, R. D., Slater, P. N. and Teillet, P. M., 1992, Evaluation of simplified procedures for retrieval of land surface reflectance factors from satellite sensor output, *Remote Sensing of Environment*, 41, pp. 169–184.

Moreno, J. I. L'opez and Bravo, D. Nogu'es, 2006, Interpolating local snow depth data: an evaluation of methods. *Hydrological Processes*, 20, 2217-2232.

Moritz, R. E., 1978, A model for estimating global solar radiation, Energy budget studies in relation to fast-ice breakup processes in Davis Strait. *Occasional Paper of University Of Colorado, Institute of Arctic and Alpine Research,* 26, 121–142.

Munneke, P. K., Van Den Broeke, M. R., Reijmer, C. H., Helsen, M. M., Boot, W., Schneebeli, M. and Steffen, K., 2009, The role of radiation penetration in the energy budget of the snowpack at Summit, Greenland, *The Cryosphere*, 3, pp. 155-165.

Negi, H. S. and Kokhanovsky, A., 2011, Retrieval of snow grain size and albedo of Western Himalayan snow cover using satellite data, *The Cryosphere*, 5, pp. 831-847.

Negi, H. S., Kulkarni, A. V. and Semwal, B. S., 2009, Estimation of snow cover distrubution in Beas Basin, Indian Himalaya using satellite data and ground measurements, *Journal of Earth System Science*, 118, , pp. 525-538.

Negi, H. S., Snehmani and Thakur, N. K., 2008, Operational Snow Cover Monitoring in NW-Himalaya using Terra and Aqua MODIS Imageries, *Proceedings of International workshop on Snow, Ice, Glacier and Avalanches*, 07-09 Jan 2008, IIT Bombay, Mumbai, India.

Negi, H. S., Thakur, N. K., and Mishra, V. D., 2007, Estimation and validation of snow surface temperature using MODIS data for NW-Himalaya, *Journal of Indian Society of Remote Sensing*, 35, pp. 287 – 299.

Nichol, J., Hang, L. K. and Sing, W. M., 2006, Empirical correction of low Sun angle images in steeply sloping terrain: a slope matching technique, *International Journal of Remote Sensing,* 27, pp. 629–635.

Niemelä, S., Räisänen, P. and Savijärvi, H., 2001a, Comparison of surface radiative flux parameterizations Part I. Longwave radiation, *Atmospheric Research*, 58, pp. 1-18.

Niemelä, S., Räisänen, P. and Savijärvi, H., 2001b, Comparison of surface radiative flux parameterizations Part II. Shortwave radiation, *Atmospheric Research*, 58, pp. 141-154.

Niu, X., Pinker, R. T., and Cronin, M. F., 2010, Radiative fluxes at high latitude, *Geophysical Research Letters*, 37, L20811, pp. 1-5.

Nolin, A. W., 2010, Recent advances in remote sensing of seasonal snow, *Journal of Glaciology*, 56, pp. 1141-1150.

Nolin, A. W. and Dozier, J., 2000, A hyperspectral method for remotely sensing the grain size of snow, *Remote Sensing of Environment*, 74, pp. 207-216.

Oerlemans, J., 1992, A model for the surface balance of ice masses, Part1, Alpine glaciers. *Z. Gletscherkd Glazialgeol.*, 27-28, pp. 63-83.

Oerlemans, J. and Fotuin, J. P. F., 1992, Sensitivity of glaciers and small ice caps to green house warming, *Science*, 258, pp. 115-117.

Ohmura, A., 1982, Climate and energy balance on the arctic tundra, *Journal of Climatology,* Volume, 2(1), pp. 65-84.

Ohmura, A., 1984, Comparative energy balance study for Arctic Tundra, Sea Surface, Glaciers and Boreal Forests, *GeoJournal 8.3*, pp. 221-228.

Ohmura, A., 2012, Present status and variations in the Arctic energy balance, *Polar Science*, 6, pp.5-13.

Oke, T. R., 1970, Turbulent transport near the ground in stable conditions*, Journal of Applied Meteorology*, 9, pp. 778-786.

Oliphant, A., Susan, C., Grimmond, B., Schmid, H. P. and Wayson, C. A., 2006, Local-scale heterogeneity of photosynthetically active radiation (PAR), absorbed PAR and net radiation as a function of topography, sky conditions and leaf area index, *Remote Sensing of Environment*, 103, pp.324-337.

Painter, T. H., Rittger, K., McKenzie, C., Slaughter, P., Davis, R. E. and Dozier J., 2009, Retrieval of subpixel snow covered area, grain size and albedo from MODIS, *Remote Sensing of Environment*, 113, pp. 868-879.

Pandya, M. R., Singh, R. P., Babu, K. R., Murali, P. N., Kirankumar, A. S. and Dadhwal, V. K., 2002, Bandpass solar exo-atmospheric irradiance and Rayleigh optical thickness of sensors on board Indian Remote Sensing satellites - 1B, 1C, 1D and P4, *IEEE Transactions on Geoscience and Remote Sensing*, 40, pp. 714-717.

Paterson, W. S. B., 1994, The physics of glaciers, *3rd edition Elsevier*, *Oxford,* 480 pp.

Peng, G., Li, J., Chen, Y., Norizon, A. P., Tay, L., 2006, High-resolution surface relative humidity computation using MODIS image in Peninsular Malaysia, *Chinese Geographical Science*, 16, pp. 260-264.

Pinker, R. T., Frouin, R. and Li, Z., 1995, A review of satellite methods to derive surface shortwave irradiance, *Remote Sensing of Environment*, 51, pp. 108-124.

Plüss, C., Ohmura, A., 1996, Longwave radiation on snow-covered mountainous surfaces, *Journal of Applied Meteorology,* 36, 818–824.

Prasad, A. K. and Singh, R.P, 2007, Changes in Himalayan Snow and Glacier Cover Between 1972 and 2000, *EOS, Transactions of American Geophysical Union,* 88, pp. 326-329.

Prata, A. J., 1996, A new longwave formula for estimating downward clear-sky radiation at the surface, *Quarterly Journal of the Royal Meteorological Society*, 122, pp. 1127–1151.

Price, J. C., 1990, Using spatial context in satellite data to infer regional scale evapotranspiration, *IEEE Transactions on Geoscience and Remote Sensing*, 28, pp. 940–948.

Price, A. G. and Dunne, T., 1976, Energy balance computation of snowmelt in a sub Arctic area. *Journal of Resource*, 12, pp. 686–694.

Qin, Z. and Karnieli, A., 1999, Progress in the remote sensing of land surface temperature and ground emissivity using NOAA-AVHRR data. *International Journal of Remote Sensing*, 20, pp. 2367-2393.

Qu, J. J., Gao, W., Kafatos, M., Murphy, R. E. and Salomonson, V. V., 2006, *Earth Science Satellite Remote Sensing (Science and Instruments)*, 1, Tsinghua University Press, Springer, USA, 414pp.

Reijmer, C. H. and Oerlemans, J., 2002, Temporal and spatial variability of the surface energy balance in Dronning Maud Land, East Antarctica, *Journal of Geophysicacl Research*, 107(D24), 4759, doi:10.1029/2000JD000110, pp. 1-12.

Roland Stull, 2000, *Meteorology (For Scientists and Engineers)*, Brooks/Cole Thomson Learning, USA, pp. 502.

Romanov, P. and Tarpley, D., 2007, Enhanced algorithm for estimating snow depth from geostationary satellites, *Remote Sensing of Environment*, 108, pp. 97-110.

Roy, V., Goïta, K., Royer, A., Walker, A. E. and Goodison, B. E., 2004, Snow water equivalent retrieval in a Canadian Boreal environment from microwave measurements using the HUT snow emission model, *IEEE Transactions on Geoscience and Remote Sensing*, 42, 1850-1859.

Russell, P. B., Livingston, J. M., Dutton, E.G., Pueschel, R. F., Reagan, J. A., Defoor, T. E., Box, M. A., Allen, D., Pilewskie, P., Herman, B. M., Kinne, S. A. and Hoffman,

D. J., 1993, Pinatubo and Pre-Pinatubo optical depth spectra: Mauna Loa measurements, compositions, inferred particle distribution, radiative effects, and relationship to lidar data, *Journal of Geophysical Research*, 98, pp. 22969–22985.

Salomonson, V. V., Barnes, W. L., Maymon, P. W., Montgomery, H. E. and Ostrow, H., 1989, MODIS: Advanced Facility Instrument for Studies of the Earth as a System, *IEEE Transactions on Geoscience and Remote Sensing*, 27, pp. 145–153.

Samani, Z., Bawazir, A. S., Bleiweiss, M., Skaggs, R. and Tran, V. D., 2007, Estimating daily net radiation over vegetation canopy through remote sensing and climatic data, *Journal of Irrigation and Drainage Engineering*, 133 , pp. 291-297.

Sanjeevi, S. and Bhaskar, A. S., 2008, Satellite derived digital terrain and perspective model an aid to teach geological mapping, *Journal of Geological Society of India*, 71(2), pp. 214-224.

Saraf, A. K., Foster, J. L., Singh, P. and Tarafdar, S., 1999, Passive microwave data for snow-depth and snow-extent estimations in the Himalayan mountains, *International Journal of Remote Sensing,* 20,, pp. 83-95.

Schaaf, C., Gao, F., Strahler, A., Lucht, W., Li, X., Tsung, T., Strugll, N., Zhang, X., Jin, Y., Muller, P., Lewis, P., Barnsley, M., Hobson, P., Disney, M., Roberts, G., Dunderdale, M., Doll, C., D'Entremont, R., Hu, B., Liang, S., Privette, J. and Roy, D., 2002, First operational BRDF, albedo nadir reflectance products from MODIS, *Remote Sensing of Environment*, 83, pp. 135–148.

Schneider, C., 1999, Energy balance estimates during the summer season of glaciers of the Antarctic Peninsula, *Global and Planetary Change*, 22, pp. 117-130.

Schumugge, T. J., Kustas, W. P. and Humes, K. S., 1998, Monitoring land surface fluxes using ASTER observations. *IEEE Transactions on Geoscience and Remote Sensing*, 36, pp. 1421–1430.

Sharma, S. S. and Ganju, A., 2000, Complexities of avalanche forecasting in Western Himalaya an overview, *Cold Regions Science and Technology*, 31, pp. 95-10.

Sharma, V., Mishra, V. D. and Joshi, P. K., 2012, Snow cover variation and streamflow simulation in a snow-fed river basin of the Northwest Himalaya, *Journal of Mountain Science*, 9, pp. 853- 868.

Sharma, V., Mishra, V. D. and Joshi, P. K., 2014, Topographic controls on spatio-temporal snow cover distribution in Northwest Himalaya, *International Journal of Remote Sensing*, 35, pp. 3036-3056.

Shi, J. and Dozier, J., 2000, Estimation of snow water equivalence using SIR-C/X-SAR, Part II: Inferring snow depth and particle size, *IEEE Transactions on Geoscience and Remote Sensing*, 38, pp. 2475-2488.

Shrivastava, P. K., Asthana, R. and Roy, S. K., 2011, The ice sheet dynamics around Dakshin Gangotri glacier, Schirmacher oasis, East Antarctica vis-à-vis topography and meteorological parameters, *Journal of Geological Society of India*, 78, pp.117-123.

Sicart, J. E., Hock, R. and Six, D., 2008, Glacier melt, air temperature and energy balance in different climates: The Bolivian Tropics, the French Alps, and northern Sweden, *Journal of Geophysical Research*, 113, D24113, doi:10.1029/2008JD010406, pp 1-11.

Singh, K. K., Mishra, V. D. and Negi, H. S., 2007, Evaluation of snow parameters using passive microwave remote sensing, *Defence Science Journal*, 57, pp. 271-278.

Sofan, P., Sugiharto, T., Hasnaeni, 2007, Relative humidity estimation based on MODIS precipitable water for supporting spatial information over Java Island, *Remote Sensing and Earth Sciences*, 4, pp. 33-45.

Song, J., and Gao, W., 1999, An improved method to derive surface albedo from narrowband AVHRR satellite data: narrowband to broadband conversion, *Journal of Applied Meteorology*, 38, pp. 239-249.

Song, C., Woodcock, C.E., Seto, K.C., Lenney, M. P. and Macomber, A.S., 2001, Classification and change detection using Landsat TM data : when and how to correct atmospheric effects, *Remote Sensing of Environment*, 75, pp. 230 – 244.

Stahl, K., Moore, R. D., Floyer, J. A., Asplin, M. G., McKendry, I. G., 2006, Comparison of approaches for spatial interpolation of daily air temperature in a large region with complex topography and highly variable station density, *Agricultural and Forest Meteorology,* 139, pp. 224–236.

Stewart, J. B., Kustas, W. P., Humes, K. S., Nichols, W. D., Moran, M. S. and De Bruin, H. A. R., 1994, Sensible heat flux-radiometric surface temperature relationship for eight semiarid areas, *Journal of Applied Meteorology*, 33, pp. 1110-1117.

Strahler, A. H., Wanner, W., Schaaf, C., Li, X., Mullar, J.-P., Lewis, P. and Barnsley, M. J., 1999, *MODIS BRDF/Albedo product:ATBD*, version 5.0, April 1999, pp. 53.

Stroeve, J., 2001, Assessment of Greenland albedo variability from the advanced very high resolution radiometer Polar Pathfinder data set, *Journal of Geophysical Research*, 106, pp. 33989 - 34006.

Stroeve, J. and Nolin, A., 2002a, New methods to infer snow albedo from the MISR instrument with applications to the Greenland ice sheet, *IEEE Transactions of Geoscience and Remote Sensing*, 40, No.7, pp. 1616 – 1625.

Stroeve, J. and Nolin, A., 2002b, Comparison of MODIS and MISR derived surface albedo with in situ measurements in Greenland, *Proceedings of EARSeL-LISSIG-Workshop Observing our Cryosphere from Space,* Bern, March 11-13*,* 2, pp. 88-96.

Stroeve, J., Box, J. E., Gao, F., Liang, S., Nolin, A. and Schaaf, C., 2005, Accuracy assessment of the MODIS 16-day albedo product for snow: comparisons with Greenland *in situ* measurements, *Remote Sensing of Environment*, 94, pp.46-60.

Su, H., Wood, E. F., Wang, H. and Pinker, T., 2008, Spatial and temporal scaling behavior of surface shortwave downward radiation based on MODIS and *in situ* measurements, *IEEE Geoscience and Remote Sensing Letters*, 5 , pp. 542–546.

Takala, M., Luojus, K., Pulliainen, J., Derksen, C., Lemmetyinen, J., Kärnä, J-P., Koskinen, J. and Bojkov, B., 2011, Estimating northern hemisphere snow water equivalent for climate research through assimilation of space-borne radiometer data and ground-based measurements, *Remote Sensing of Environment*, 115, pp. 3517-3529.

Tang, B. and Li, Z. L., 2008, Estimation of instantaneous net surface longwave radiation from MODIS cloud-free data, *Remote Sensing of Environment*, 112, pp. 3482-3492.

Tang, B., Li, Z. L., Zhang, R., 2006, A direct method for estimating net surface shortwave radiation from MODIS data, *Remote Sensing of Environment*, 103, pp. 115-126.

Tasumi, M., Allen, R. G. and Trezza, R., 2008, At-surface reflectance and albedo from satellite for operational calculation of land surface energy balance, *Journal of Hydrologic Engineering*, 13 (2), pp. 51-63.

Town, M. S. and Walden, V. P., 2009, Surface energy budget over the South Pole and turbulent heat fluxes as a function of an empirical bulk Richardson number, *Journal of Geophysical Research*, 114, D22107, doi:10.1029/2009JD011888*,* pp.1-15.

Tyagi, A., Singh, U. P. and Mohapatra, M., 2011, Weather & weather systems at Schirmacher Oasis (Maitri) during recent two decades – A review, *MAUSAM*, 62, pp. 513 – 534.

Ulaby, F. T., Moore, R. K. and Fung, A. K., 1990, *Microwave remote sensing fundamentals and radiometry*, Vol. I, Book-Mart Press, Inc. North Bergen. N J., USA, 365p.

Upadhyay, D. S., 1995, *Cold climate hydrometeorology*, New AGE International, New Delhi, 218p.

U S Army Corps of Engineers, 1956, *Summary report on the snow investigations - snow hydrology*, Portland, OR: North Pacific Division, Corps of Engineers, US Army, 434p.

Van As, D., Van Den Broeke, M. and Van De Wal, R., 2005, Daily cycle of the surface layer and energy balance on the high Antarctic Plateau, *Antarctic Science*, 17, 121-133

Van de Wal, R.S.W. and Russell, A. J., 1994, A comparison of energy balance calculations, measured ablation and melt water runoff near Sondre Stromfjord, West Greenland, *Global and Planetary Change*, 91, pp. 29-38.

Van Den Broeke, M., Reijmer, C. H. and Van De Wal, R. S. W., 2004a, A study of the surface mass balance in Dronning Maud Land, Antarctica, using automatic weather stations. *Journal of Glaciology,* 50, pp 565-582.

Van den Broeke, M., Reijmer, C. and Van de Wal, R., 2004b, Surface radiation balance in Antarctica as measured with automatic weather stations, *Journal of Geophysical Research*, 109, D09103, doi:10.1029/2003JD004394, pp. 1-17.

Van Den Broeke, M., Reijmer, C., Van As, D., Van De Wal, R. and Oerlemans, J., 2005, Seasonal cycles of Antarctic surface energy balance from automatic weather stations, *Annals of Glaciology*, 41, pp.131–139.

Van Den Broeke, M., Reijmer, C., Van As, D. and Boot, W., 2006, Daily cycle of the surface energy balance in Antarctica and the influence of clouds. *International Journal of Climatology*, 26, pp. 1587–1605.

Van Der Meer, F., 1996, Spectral mixture modeling and spectral stratigraphy in carbonate lithofacies mapping, *ISPRS Journal Photogrammetric and Remote Sensing*, 51, pp. 150 – 162.

Vihma, T., 2011, Atmosphere-snow/ice interactions, *Encyclopedia of Snow, Ice and Glaciers (edited by Vijay P. Singh, Pratap Singh and Umesh K. Haritashya)*, Springer, pp. 1253.

Vihma, T., Johansson, M. M. and Launiainen, J., 2009, Radiative and turbulent surface heat fluxes over sea ice in the western Weddell Sea in early summer, *Journal of Geophysical Research*, 114, pp. 1-18.

Wagnon, P., Sicart, J. E., Berthier, E. and Chazarin, J. P., 2003, Wintertime high-altitude surface energy balance of a Bolivian glacier, Illimani, 6340 m above sea level, *Journal of Geophysical Research*, 108, D6, doi:10.1029/2002JD002088, pp. 1-14.

Wan, Z., 1999, *MODIS Land-Surface temperature algorithm theoretical basis document (LST ATBD), version 3.3,* Institute for Computational Earth System Science, University of California, Santa Barbara, pp. 1-77.

Wan, Z. and Dozier, J., 1996, A generalized split-window algorithm for retrieving land surface temperature measurement from space, *IEEE Transactions on Geoscience and Remote Sensing*, 34, pp. 892–905.

Wang, H., and Pinker, R. T., 2009, Shortwave radiative fluxes from MODIS: model development and implementation, *Journal of Geophysical Research*, 114, D20201, doi:10.1029/2008JD010442, pp. 1-17.

Wang, W. and Liang, S., 2009, Estimation of high-spatial resolution clear-sky longwave downward and net radiation over land surfaces from MODIS data, *Remote Sensing of Environment*, 113, pp. 745-754.

Wang, X. and Zender, C. S., 2010, MODIS snow albedo bias at high solar zenith angles relative to theory and *in situ* observations in Greenland, *Remote Sensing of Environment*, 114, 563-575.

WMO (World Meteorological Organization), 2003a, *Manual on the Global Observing System*. Volume I-Global Aspects, WMO-No 544, Geneva, pp. 50.

WMO (World Meteorological Organization), 2008, *Guide to meteorological instruments and methods of observations*, WMO-No 8, Geneva, pp. 681.

Xu, Y., Qin, Z. and Shen, Y., 2012, Study on the estimation of near surface air temperature from MODIS data by statistical methods, *International Journal of Remote Sensing*, 33, pp. 7629-7643.

Yang, K., Koike, T. and Ye, B., 2006, Improving estimation of hourly, daily and monthly solar radiation by importing global data sets, *Agricultural and Forest Meteorology*, 137, pp.43-55.

Zillman, J. W., 1972, *A study of some aspects of the radiation and heat budgets of the southern hemisphere oceans*, Meteorological Study No. 26, Commonwealth Bureau of Meteorology, Canberra, Australia, pp. 562.

Zhou, M., Zhang, Z., Zhong, S., Lenschow, D., Hsu, H. M., Sun, B., Gao, Z., Li, S., Bian, X. and Yu, L., 2009, Observations of near-surface wind and temperature structures and their variations with topography and latitude in East Antarctica, *Journal of Geophysical Research*, 114, D17115, doi:10.1029/2008JD011611, pp. 1-8.

Journals

Gusain, H. S., Mishra, V. D., and Arora, M. K., 2014, A four-year record of the meteorological parameters, radiative and turbulent energy fluxes at the edge of the East Antarctic ice sheet, close to Schirmacher Oasis, *Antarctic Science*, 26 (1), pp. 93-103.

Gusain, H. S., Mishra, V. D., and Arora, M. K., 2014, Estimation of net shortwave radiation flux of Western Himalayan snow cover during clear sky days using remote sensing and meteorological data, *Remote Sensing Letters*, 5(1), pp. 83-92.

Gusain, H. S., Mishra, V. D., and Negi, A., 2011, Comparative study of the radiative and turbulent energy fluxes during summer and winter at the edge of the Antarctic ice sheet in Dronning Maud Land –East Antarctica, *MAUSAM*, 62(4), pp. 557-566.

Mishra, V. D., **Gusain, H. S.**, Arora, M. K., 2012, Algorithm to derive narrow band to broad band albedo for snow using AWiFS and MODIS imagery of Western Himalaya-validation, *International Journal of Remote Sensing Applications*, 2(3), pp. 52-62.

Gusain, H. S., Arora, M. K. and Mishra, V. D., Operational algorithm for generation of snow depth maps from discrete data in Indian Western Himalaya. (To be communicated).

Gusain, H. S., Mishra, V. D. and Arora, M. K., Estimation of net radiation flux of Antarctic ice sheet during clear sky days using remote sensing and meteorological data. (To be communicated).

Conferences

Gusain, H. S., Mishra, V. D., and Arora, M. K., 2012, Estimation of net shortwave radiation flux of Western Himalayan snow cover during clear sky days using remote sensing and meteorological data, *International Conference 'Geomatrix-2012'*, CSRE, IIT Bombay, 26-29 February 2012.

Gusain, H. S., Mishra, V. D., and Negi, A., 2012, Study of radiative and turbulent energy fluxes of Antarctic ice sheet close to ice free area in Dronning Maud Land, East Antarctica, *International Symposium on Cryosphere and Climate Change,* SASE Manali, 2-4 April, 2012.